THESIS FOR THE DEGREE OF DOCTOR OF PHILOSOPHY

Nanomaterials tailored with Angiogenin and Angiogenin mimicking peptides for cancer therapy and wound healing

Lorena Maria Cucci

Supervisor: Prof. Cristina Satriano

PhD Coordinator: Prof. Salvatore Sortino

Department of Chemical Sciences

University of Catania

A.Y. 2019 / 2020

Abstract

In the last few years, the application of nanomaterials (NMs) as medical devices has gained great interest among the researchers due to their several advantages compared to the conventional drugs, including improved efficacy, bioavailability, targeting ability and safety. Indeed, NMs, owing to their small size, can freely diffuse across the tissues, pass biological barriers and mediate molecular interactions. Moreover, NMs can be efficiently loaded with active molecules, to protect against enzymatic degradation and to allow for their efficient trafficking to the target site.

According to such premises, this thesis deals with the synthesis and the physico-chemical characterization of hybrid organic/metallic nanomaterials at the interface with systems of biological interest (peptides, protein, lipid membranes, cells), specifically developed for the modulation of the angiogenic process, for application in cancer therapy and wound care.

In particular, this work has been addressed to the synthesis and characterization of spherical gold nanoparticles (AuNPs) and AuNP-graphene oxide (Au-GO) nanoassemblies. These platforms have been functionalized with the protein angiogenin (ANG), one of the most powerful angiogenic factors as well as with peptide fragments able to mimic some biological activities of the whole protein. Also, the synergic/antagonist role of copper, another known angiogenic factor, which can bind to ANG thus influencing its biological response, has been investigated.

The hybrid bio-interface between AuNP, GO, and ANG protein/peptides was scrutinized by a multi-technique approach which

relies on spectroscopic techniques (UV-visible, dynamic light scattering, circular dichroism) and microscopic methods (atomic force microscopy, laser scanning confocal microscopy).

The interaction with an artificial model of cell membrane, i.e., supported lipid bilayers, was inspected by means of the acoustic sensing technique Quartz Crystal Microbalance with Dissipation monitoring and by fluorescence recovery after photo-bleaching experiments.

Cellular experiments were carried out to investigate the interaction with both tumour and healthy cells. Specifically, human neuroblastoma (SH-SY5Y line), both undifferentiated and differentiated neuron-like cells, glioblastoma (A172 line), fibroblasts (MRC-5 and HFF1 lines) and endothelial (HUVEC line) cells were examined in their response towards the nanomaterials, in terms of cytotoxicity, cellular internalization, cell-migration and tubulogenesis.

The AuNP-GO-ANG (protein/peptide)-Cu hybrids, by combining the antiangiogenic and antioxidant action of the colloidal gold, the angiogenic properties of copper ions, the antibacterial action of GO and with the biological activity of angiogenin, may provide promising applications for the angiogenesis modulation in cancer and wound care.

Abbreviations

ABE	angiogenin-binding element
ALS	amyotrophic lateral sclerosis
ANG	angiogenin
CD	circular dichroism
CID	chemical interface damping
CrD	Crohn's disease
DNA	deoxyribonucleic acid
EC	endothelial cell
eNOS	endothelial nitric oxide synthase
EPR	enhanced permeability and retention effect
ERK1/2	extracellular signal-related kinase 1/2
ESI-MS	electrospray ionization mass spectrometry
FDA	Food and Drug Administration
Gln	glutamine
HAS	human serum albumin
His	histidine
HOMO	highest occupied molecular orbital
IGF-1	insulin-like growth factor-1

Ile	isoleucine
LB	Luria-Bertani broth
LSCM	laser scanning confocal microscopy
LUMO	lowest occupied molecular orbital
Lys	lysine
ME	β- mercaptoethanol
MRI	magnetic resonance imaging
NHS-activated PEG	succinimidyl propionyl polyethylene glycoldisulfide
NM	nanomaterial
NO	nitric oxide
NP	nanoparticle
PD	Parkinson's disease
Phe	phenylalanine
rDNA	ribosomal DNA
RES	reticuloendothelial system
RNA	ribonucleic acid
RNase	ribonuclease
ROS	reactive oxygen species
rRNA	ribosomal RNA
TGF	transforming growth factors
Thr	threonine

tiRNA	stress induced tRNA
TNF-α	tumour necrosis factor
tRNA	transfer RNA
VEGF	vascular endothelial growth factor

Table of contents

Overview and aim of this work

Population ageing reflects the wealth of a community and is a natural and largely irreversible consequence of the social and economic development of the countries. It takes place as a joint effect of increased life expectancy, which is primarily connected with the ease of accessibility to medical care, the advanced medical technologies and the modern therapeutics, together with the declining fertility rates. In 1980, the First World Assembly on Ageing estimated that 378 million people in the world were aged 60 years or over; such a number has risen up to 759 million in the past three decades and it is assumed to jump to 2 billion by 2050 [1]. However, a longer life brings, along with its opportunities, to unavoidable and progressive biological changes in the human organism, decline of physiological functions and accumulation of a wide variety of molecular and cellular damages over time, which are potential risk factors for the onset of several diseases [2]. Common pathological conditions in older age include osteoarthritis [3], chronic obstructive pulmonary diseases [4], dementia [5] and diabetes [6]. Along with these disorders, the demographic changes occurring in the world population take on the urgency and relevance for the treatment of angiogenesis-dependent diseases and among these the most common are cancer [7] and chronic wounds [8].

Cancer is a complex genetic disease, which involves mutations in oncogenes and tumour suppressor genes, leading normal cells to gain malignant properties, that include primarily dedifferentiation, fast proliferation, resistance to apoptosis and immune defence [9]. Its progression and invasion into local tissues mostly depends on the ability

to form new blood vessels, which supply oxygen and nutrients to the cancer cells [10]. Several factors can be related to the neoplastic transformation, like inherited genetic defects, environmental exposure to chemical and physical agents and above all age. On the cellular level, indeed, ageing is associated with genomic instability, epigenetic alteration, qualitative and quantitative protein changes as well as cell organelle dysfunctions, which may result into irreparable damages to essential physiological processes, such as the gene repair ability, giving rise to malignant tumours [11]. Data from the National Cancer Institute Surveillance reveal that the number of new cases of cancer in one year are 439.2 per 100,000 men and women and among these, 56% of cancer diagnosis and 71% of cancer deaths occur in patients older than 65 years of age [12].

As to cutaneous wound healing, it is a complex process involving several overlapping events, which include coagulation, inflammation, re-epithelialization and tissue remodelling. Within this framework, angiogenic capillaries sprout plays a key role, providing a continuing source of immune cells, cytokines and nutrients to sustain cell metabolism and further allowing the reconstruction of the damaged tissues [13]. The demographic ageing, increasing the incidence of pathological conditions such as diabetes (over 23 million cases only in US) and dementia (according to data from the Global Burden Disease, increased by 117% between 1990 and 2006) and consequently the number of vulnerable patients, including people in wheelchair and bedridden as well as elderly, gives rise the prevalence of chronic or acute wounds [14] showing an incidence of 2.21 per 1,000 population [15].

From an economic perspective, the impact of an ageing population has dramatically risen the health care costs over the last several decades and currently approaches 2 trillion dollar annually, including 200 billion for cancer drugs [16], 1 billion for wound healing treatments and an additional burden of 12 billion per year due to the wounds consequences as skin scarring [8].

These high health and socioeconomic burdens highlight the need for a rigorous investigation to develop new, low cost, non-invasive, with high efficacy and reduced side effects, therapeutic strategies. In this context, nanotechnology and nanosystem-based approaches have introduced excellent novel advances in the treatment and diagnosis of cancer [17] as well as in wound care [18]. Nanoscale devices, indeed, owing to their small size, can readily interact with cells, for instance by 'perturbative' interactions with their surface (i.e., a phospholipid bilayer) as well as at the intracellular level, upon their uptake and accumulation in the nuclei or other intracellular organelles, such as lysosome and mitochondria, which can be difficult to be reached by hydrophilic drugs [19].

To be noted, due to their high surface to volume (S/V) ratio, nanoscale devices can be efficiently loaded with active molecules and so be used as drug delivery carriers, to improve the drug diffusion within the body and, at the same time, to reduce their enzymatic degradation thus ensuring their efficient trafficking to the target site [20].

In the wide class of biocompatible nanomaterials, gold nanoparticles (AuNPs) due to their size-related electronic [21], magnetic [22] and optical [23] properties, as well as their straightforward functionalization [24], represent an ideal theranostic platform for the treatment of cancer [25] (i.e., system displaying both imaging and therapeutic capabilities [26]) and

an innovative method to control the wound healing process [27]. Besides, AuNPs show intrinsic biological properties, being able to block pro-angiogenic factors by the selective interaction with heparin-binding glycoproteins and the further inhibition of their biological activity [28].

Accordingly, this inorganic anti-angiogenic nanosystem could overcome the limited clinical efficacy and the occurrence of a variety of adverse reactions related to the classical anti-angiogenic drugs, such as monoclonal antibodies, inhibitor of VEGF and related pathways, but also substrates of tyrosine kinase receptors, offering an alternative way for the angiogenesis modulation [29].

Graphene is made up of monoatomic sp^2 carbon atoms layers, hexagonally arranged into a honeycomb lattice structure [30]. Among the graphene derivatives, the most employed, especially at the biointerfaces, are graphene oxide (GO) and reduced GO (r-GO) [31], which form stable colloidal dispersions in water due to the presence of 'defective' sp^3 carbon atoms, bound to oxygen-containing hydrophilic groups, such as carboxylic (–COOH), hydroxyl (C–OH), carbonyl (C=O), and epoxide groups (C–O–C) [32]. These functional groups, localised both at edges and on the basal planes of the nanosheets, allow for an easy functionalization strategy, e.g., by immobilizing linker groups, molecules with an aromatic tail or a reactive end, like proteins and drugs [33]. Along with its application as a drug carrier, GO, due to its high biocompatibility and its intrinsic biological properties, being able to control the angiogenesis [34] and the function of immune cells [35], provides additional advantages in the modulation of the angiogenic process.

Angiogenesis is the new blood vessels formation from pre-existing vascular structures. It is a dynamic process, essential for providing oxygen

and nutrients to tissues and cells and to remove their metabolic waste [36] and is involved in several physiological conditions, namely wound healing, action of female reproductive organs namely ovulation, follicular release and corpus luteum formation as well as embryonic and foetal development [37]. Under these conditions, angiogenesis is highly regulated by the action of soluble angiogenic stimulators, that initiate the process and specific inhibitors able to stop it. The alteration of the balance between pro and anti-angiogenic factors results in a shift from physiological to pathological angiogenesis, which contributes to the pathogenesis of several diseases. Thus, the over-proliferation of blood vessels is mainly involved in tumour growth [38], psoriasis [39], arthritis [40], retinopathies [41], atherosclerosis [42] and wound repair [13], while impaired angiogenesis plays a key role in the hearth and brain ischemia [43], neurodegeneration [44] and osteoporosis onset [45]. Accordingly, stimulation of angiogenesis can be therapeutic in ischemic attack, peripheral arterial disease, Alzheimer's disease and wound healing, whereas the inhibition of the vessel's growth could be a promising strategy for the treatment of cancer and rheumatoid arthritis.

The tumour environment is well-known to be characterized by an enhanced permeability and retention effect (EPR), as a consequence of the excess of vessel growth during the carcinogenesis. The EPR phenomenon increases the capability of the cancer tissue to sequester chemotherapeutic agents with respect to healthy tissues [46]. This passive targeting strategy allows the nanoparticles to accumulate in the tumour cells and thus a targeted release of the desired active agent, which reduces non-specific delivery with unwanted side effects [47].

Many recent studies have demonstrated that nanoparticles in the range of 50–200 nm, could enhance the EPR effect by limiting the return of nanoparticles to the systemic circulation [48]. Likewise, graphene derived nanomaterials with a size of about 50 nm can be efficiently accumulated at higher concentration in tumour site compared to conventional drugs via the enhanced permeability and retention effect [49, 50]. Moreover, GO induces the intracellular ROS generation [51] that alter the chemical structure as well as the physiological function of macromolecules, including proteins, cell membrane lipids, deoxyribonucleic acid (DNA), and ribonucleic acid (RNA). This, in turn, result in the activation of signal transduction pathways that contribute to cytotoxicity effect on cancer cells leading to cellular apoptosis [52].

As to the **wound healing**, the biggest advantage of AuNP in tissue repair, is the high S/V ratio, the small diameter (< 100 nm) [53], which match with the natural tissue fibres of the skin. Furthermore, their mechanical properties, such as hardness (hardness value of 1.72 GPa and elastic modulus of 100 GPa [54]) and low molecular weight ($1.0 \cdot 10^4$ kDa, for spherical AuNP with a diameter of 12 nm [55]), prevent the compression of the injured tissue i*n situ* [56]. Gold nanoparticles also exhibit potent anti-oxidative effects, being able to quench the action of reactive oxygen species (ROS) like hydroxyl (OH), hydrogen peroxide (H_2O_2) and nitric oxide (NO) [57]. Their large surface area, indeed, allows the nanostructures to easily accept electrons from ROS, leading to their deactivation thereby playing a central role in the wound care treatment [58]. Indeed, during the healing process, the immune system produces a large amount of ROS, which inhibit cell growth and cause damages to

DNA, RNA and proteins, thus impairing and slowing down the physiological wound repair [59]. As to GO, many research studies highlighted its antibacterial activity associated with bacterial membrane damage [60] and ROS-dependent oxidative stress [61], that can significantly facilitate the wound repair by eradicating bacteria in wounds and may offer an alternative to the use of antibiotics in the wound care treatment [62]. Moreover, GO surface properties promote cell adhesion, migration and even induce proliferation [63], thus enhancing wound closure, increasing the strength of the formed new tissue and further reducing the scar formation.

Therefore, AuNPs, used in conjunction with graphene-based nanostructures may offer additional highly desirable chemical and biological properties in comparison to the two materials alone [64].

Based on these premises, the aim of this thesis work was the fabrication of angiogenin (protein and/or peptides)-functionalised gold nanoparticles **(PAPER I-II-III)** or the hybrid assembly of AuNP-graphene oxide **(PAPER IV-V)** and their physicochemical/biological characterization.

Specifically, in order to create hybrid nanoplatforms for the angiogenesis modulation with potential application in cancer therapy and wound healing, we combined the antiangiogenic and antioxidant action of the colloidal gold as well as the angiogenic properties and the antibacterial action of GO together with the biological activity of: 1) peptide fragments able to mimic some biological activity of angiogenin (ANG) protein **(PAPER I)**; 2) the whole ANG protein **(PAPER II-III-V).**

Three sequences encompassing the putative cell binding fragment (60-68) of the protein were used, namely: the "simple" $Ang_{60–68}$ sequence, its cysteine-conjugated Ang_{60-68}Cys and the fluorescein-labelled analogous

Fam-Ang$_{60–68}$, respectively. As to the protein three variants of ANG were used: *i)* the recombinant protein, rANG; *ii)* the wild-type angiogenin, wtANG; *iii)* the new mutant, S28CANG, with a cysteine substitution of the serine at the residue 28, for high affinity binding to the metal surface, through Au-S bonds.

The physico-chemical characterization was performed by a multi-technique approach, which includes: 1) UV-visible spectroscopy, to investigate the effective coating of the nanoparticles and the different arrangement of the peptides and the three variants of ANG at the AuNP interface, by following the absorbance and the wavelength shifts of the plasmon peak; 2) atomic force microscopy (AFM) and dynamic light scattering (DLS) measurements, to inspect the morphological features of the bare AuNPs and the hybrids Au-peptide/protein, Au-GO, Au-GO-ANG; 3) circular dichroism (CD), to investigate the conformational structures of the fragment peptides and the expressed proteins, before and after the Cu(II) complex formation. In the process of angiogenesis, indeed, copper ions play also a key role and have been recognized as angiogenic factors [65]. During angiogenesis, copper ions transfer from the cells to the extracellular matrix where bind to proteins involved in the vessel's growth, such as ANG, thereby affecting its biological activity. Hence, the influence of copper ions which differently bind to the two proteins isoforms (rANG and wtANG) through distinctive coordination environments and make complexes with the peptide fragments Ang$_{60-68,}$ Ang$_{60-68}$Cys and Fam-Ang$_{60-68,}$ were also scrutinized.

As to the biochemical/biological characterization, the interaction of the peptide molecules, the free proteins and the nano-platforms Au-peptide/protein, Au-GO, Au-GO-ANG with artificial model of cell

membrane, made of supported lipid bilayers (SLBs), was inspected by means of the acoustic sensing technique Quartz Crystal Microbalance with Dissipation (QCM-D) monitoring or by fluorescence recovery after photo-bleaching (FRAP) experiments. Cellular experiments were carried out to investigate their interaction with tumour cells (undifferentiated neuroblastoma, SH-SY5Y cell line; tumour glioblastoma cells, A172) and normal cells (fibroblasts, MRC-5 and HFF1 cell lines; differentiated neuroblastoma d- SH-SY5Y), in terms of cytotoxicity, through MTT assay, and cellular internalization, cytoskeleton rearrangements and lysosomal effects, through laser scanning confocal microscopy (LSM), after the treatment of cells with the studied systems. Moreover, wound closure experiments and tube formation assays were carried out to investigate the cell-migration effects and the angiogenic response induced by the synthetized systems, on HFF1 human foreskin fibroblasts and HUVEC endothelial cells respectively, which provide ideal cell model systems to assess both the wound healing and angiogenic properties.

Chapter 1- Introduction

1.1 Nanomaterials: classification and applications

Nanotechnology is one of the most exciting advances in the fields of both fundamental and applied science and it is defined as the synthesis, characterization and application of materials, structures and systems at the nanometer scale (1 to 100 nm). Hence the term “nanomaterial” (NMs) refers to materials at the nano-scale, which can be classified, based on their origin, as natural or synthetic [66]. Natural NMs are produced either by biological species or through anthropogenic activities; they are present in living organism such as bacteria, algae and virus, but also plants, insect and animals [67, 68]. Insects, for instance, use nano-wax coating in their lightweight wings [69]; plants contain nanostructures, which allow for insects sliding, enhance their mechanical stability and increase visible light and UV reflection and radiation adsorption [70]. As to the humans and animals, mechanical properties of organs, such as bones, are based on the interaction of their micro and nanoscale components [71]. On the other hand, artificial NMs can be fabricated via different synthetic strategies, classified as “bottom up” or “top down” approaches. The “bottom up” techniques, including chemical precipitation and self-assembly, are based on the building of the nano-structures atom by atom or molecule by molecule, through covalent or supramolecular interactions. On the other hand, the “top down” strategy involves mechanical grinding and erosion techniques, whereby a piece of material is gradually eroded until the desired shape and size is achieved [72]. Such strategies are further classified in three categories:

i) physical methods [73], including laser ablation [74], inert gas condensation, electron beam lithography [75], plasma enriched vapour deposition [76] and electro spraying [77];

ii) chemical methods, including sol-gel synthesis [78], chemical reduction [79], microemulsion [80] and hydrothermal synthesis [81];

iii) bio-assisted methods, which rely on biological systems like bacteria, fungi, viruses, yeast and plant extracts, for the NMs synthesis [82-84].

Based on the fabrication material, artificial NMs can be categorized into:

i) carbon-based nanomaterials, including fullerenes, carbon nanotubes, carbon nanofiber and graphene sheets [85];

ii) inorganic nanomaterials, which include metal and metal oxide nanoparticles (i.e., gold, silver, TiO_2, ZnO nanoparticles) [86], but also semiconductors like silicon and ceramics [87];

iii) organic nanomaterials, represented by dendrimers, micelles, liposomes and polymers [88];

iv) composite nanomaterials, represented by multiphase systems, which combine one nano-meter scale phase (i.e nanoparticles) with any different forms of metal, ceramic as well as lager or polymer bulk-type materials, depending on the required features and applications [89].

Moreover, according to their geometrical dimensions NMs can be classified as: 0 dimensional (0-D), which includes materials with all the three dimensions (x-y-z) smaller than 100 nm (e.g nanoparticles); 1 dimensional (1-D), if the material shows two dimensions (x,y) inside the nanoscale and one dimension (z) outside (e.g. nanofibers, nanotubes, nanorods); 2 dimensional (2-D), represented by plate-like shapes material

with only one dimension at the nanoscale (e.g. graphene sheets, nanocoating, thin films) [90] (Figure 1).

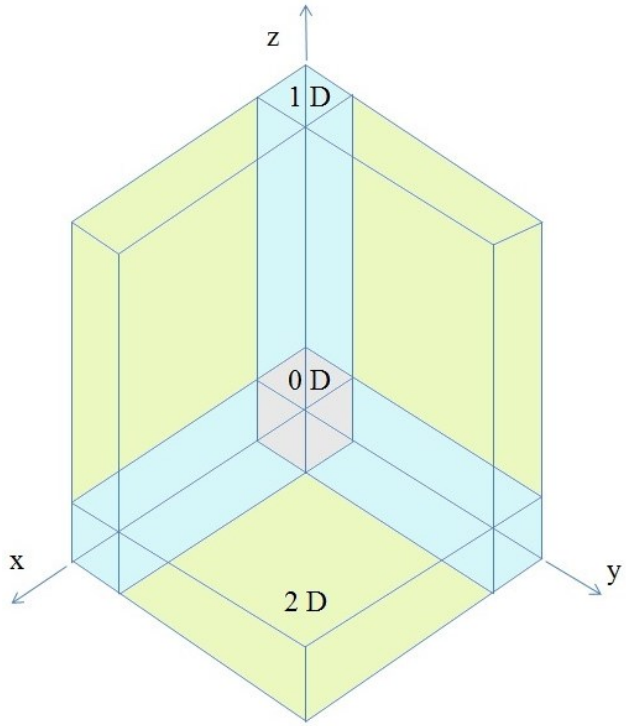

Figure 1- Classification of NMs based on their dimensions.

Owing to their tuneable physicochemical properties, including the size, the shape, the chemical composition, the melting point, wettability, thermal and electrical conductivity, the absorption of light and light scattering, NMs represent an attractive field of research with a high techno-economic impact in electronics [91], energy conversion and storage [92], miniaturized scale manufacture and water purification [93], molecular imaging and (bio)sensors [94] as well as biomedicine [95, 96]. Dye-sensitized solar cells with enhanced light-harvesting, have been developed using photo-electrochemical devices based on mesoporous

nanocrystalline TiO_2 layer [97]. Carbon-based nano-absorbents are currently used as substitute of active carbon for the removal of organic contaminants and heavy metals from water and wastewater [98, 99]. NMs functionalized with bio-receptor units likely DNA strands, proteins and antibody, due to the high surface area, are used for bio-sensing applications with increased sensitivities and low detection limit [100]. Nanotechnology has also great potential for applications in the agri-food sector, since NMs are used for the fabrication of high-performance agriculture-pesticide and fertilizer [101]; as enhancers of food processing-encapsulation of flavours or odours [102]; to improve food textural or quality, as well as gelation or viscosifying/suspension agents [103]; as sensors of food packaging-pathogen [104]; to allow for UV-protection [105] or supply nutrients with higher stability and bioavailability [106].

Among these applications, given that most of the biological pathways involved into both pathological and physiological processes are at the molecular or nanoscale levels (mutated genes, bacteria or viral infections, misfolded proteins), NMs are also potentially useful in medical applications for the prevention, treatment and diagnosis of several kind of diseases, in the field of the well-known “nanomedicine” [107]. NMs can be designed to specifically deliver therapeutic agents and biomolecules in the active site, since they can be engineered to easily pass biological barriers and mediate molecular interactions and can also detect molecular changes in a highly sensitive manner. Thus, new-generation drug-delivery vehicles, contrast agents and diagnostic systems, have been developed and some of them are currently undergoing clinical trials or have been already approved by the Food and Drug Administration (FDA) for human use (Table 1) [107].

Table 1- Examples of NMs in clinical use [107].

Nanomaterial	***Trade name***	***Application***	***Target***
Iron Oxide	Feridex	MRI* contrast	Liver
	Resovist	MRI contrast	Liver
	Combidex	MRI contrast	Lymphnodes
	NanoTherm	Cancer therapy	Various forms
Gold	Verigene	In vitro diagnostics	Genetic
	Aurimmune	Cancer therapy	Various forms
Nanoshells	Auroshell	Cancer therapy	Various forms
Quantum Dots	Qdots	Fluorescent contrast	Tumours cells
Polymer	Oncaspar	Cancer therapy	Acute lymphoblastic leukemia
	CALAA-01	Cancer therapy	Various forms
Liposome	Doxil	Cancer therapy	Various forms
Micelle	Genexol-PM	Cancer therapy	Neuropathy, Neutropenia
Dendrimer	VivaGel	Microbicide	Cervicovaginal

*MRI (magnetic resonance imaging)

1.2 Physicochemical properties of NMs at the biointerface

The physicochemical properties of NMs, including size, shape, aspect ratio, surface area, surface chemistry and roughness, influence their clinical applications and biological effects.

1.2.1 The effect of NM size and shape

The nanomaterial size plays a key role in the organism response upon their administration [108]. Materials with a smaller size and a higher surface to volume ratio, indeed, show an enhanced reactivity on itself and to the contiguous milieu when compared to bigger particles, consequently increasing their cytotoxic effects [90]. Moreover, the decrease in the size of NMs is also associated with fast endocytosis, improved interactions with cell organelles, such as lysosomes, mitochondria, endoplasmic reticulum [109] and macromolecules, namely proteins and nucleic acids, leading to a variation of their chemical structure and thus interfering with critical biological functions [110].

Accordingly, some studies on AuNPs demonstrated a higher cytotoxic effect for the lower size of the particles, so that gold nanospheres in the size range of 4-28 nm, as determined by Woźniak et al., reduce the viability of HeLa cells (a cervical cancer cell line) while, larger gold nanoparticles (diameter of >130 nm) are relatively safe [111]. Similarly, Liang et al. demonstrated that spherical AuNPs with diameters < 5 nm exhibit enhanced cytotoxicity on normal human liver cells and fibroblasts, with respect to the larger 30 nm and 15 nm size AuNPs, respectively, [112, 113].

As to carbon-based NMs, it has been proven that spherical carbon structures smaller than 14 nm show a higher oxidative capacity with respect to larger particles (> 60 nm), leading to cell damages and apoptosis [114]. Likewise, graphene oxide sheets with a lateral size smaller than 100 nm cause severe toxicity on stem cells with respect to the bigger sheets with a later size of around 500 nm, while GO with a diameter in the range of 5-10 nm can also enter the nucleus of the cells, thus further inducing genotoxic effects [115].

The NM size not only influences the cellular uptake, but also dictates the pharmacokinetic profile of the material, namely adsorption, bio-distribution and elimination processes [116]. In this regard, *in vivo* experiments demonstrated that spherical nanoparticles with diameters in the range of 15-50 nm, are able to pass the blood-brain barrier and accumulate in the brain tissue as well as in liver, lung and spleen, thus showing a high distribution volume, while particles greater than 50 nm are mostly retained by the reticuloendothelial system (RES) undergoing to a rapid excretion [117, 118]. As to graphene oxide, literature data showed that GO sheets of 10–30 nm in length, are mainly distributed in liver and spleen, while larger GO sheets (50-800 nm) mainly accumulate in the lung [119].

In respect to the shape, NMs can be synthesized in different forms namely fibres, rings, tubes, spheres and planes. Generally, shape influences the membrane wrapping process during endocytosis and phagocytosis, leading to different grades of cytotoxicity [120]. Thus, it has been demonstrated that endocytosis of spherical NPs is easier and faster compared to rod-shaped or fibre-like nanomaterials, that due to a larger contact area with the cell membrane when compared to spherical NPs,

slow down and impair the internalization process [121]. In accord, it has been shown that the higher is the aspect ratio (the ratio between the material's length and width) the more is the toxicity of the material [122].

In this respect, recent works revealed that spherical AuNPs show the fastest internalization rate followed by cubic, rod and disk-like shaped particles [123]. Accordingly, it has been demonstrated that gold nano-rods induce higher cytotoxicity compared to spherical particles with the same size (10-100 nm) [124]. As to the carbon-based materials, it has been similarly shown that rod-shaped structures exhibit significant cytotoxicity on mammalian cells with respect to the spherical carbon fullerenes, most likely due to their interaction with the K^+ ion channels on the cell membrane [125]. Such an effect increases with the aspect ratio, so that carbon nanotubes with a length higher than 20 μm are highly toxic and induce inflammatory responses in mice, than shorter carbon tubes with a length in the order of 5 μm [126].

1.2.2 Effect of NMs surface properties: charge and surface functionalization

Surface chemistry including the surface charge and the functionalization of the nanomaterials are additional critical factors, which influence the response of biological systems to NMs.

The surface charge, indeed, regulates the ability of NMs to go through the cell membrane and the biological barrier (e.g. brain-blood barrier) as well as the pharmacokinetics [127] and the adsorption of ions and biomolecules [128].

Positively charged nanoparticles undergo faster endocytosis with respect to neutral and negative particles [129], since the cell membrane is

slightly negative charged and the cellular uptake is driven by electrostatic attractions, that enhance the material adhesion upon the cellular surface [130]. However, it has been also observed that positively charged materials adsorbed on the cell membrane, increase the membrane fluidity creating defective areas on the lipid bilayers, which can lead to the formation of hydrophilic pores that further impair its structure [131]. Negatively charged nanosystems, instead, may cause local gelation of the lipid membrane [132].

Accordingly, it has been demonstrated that both positively and negatively charged AuNPs exhibit higher cytotoxicity than neutral nanoparticles leading to a marked variation of the cell morphology [133]. Similarly, the negatively charged acid functionalized carbon nanotubes exhibit embryo toxic effects rather than pristine carbon tubes [134].

Surface modifications and functionalization of NMs also affect their biological behaviour, influencing the physicochemical features of the materials and their chemical reactivity [135]. For instance, graphene is able to disrupt the function and the structure of cell membranes [136], but in its oxidized form, namely GO, it shows lower cytotoxicity, due to the high oxygen content, smoother edges and higher hydrophilicity, which allow its ease internalization in comparison with graphene that, on the contrary, is merely adsorbed and aggregate at the cell surface.

Moreover a proper surface functionalization can stabilize the particle dispersion avoiding the agglomeration, but also can prevent the release of toxic ions and, depending on the physico-chemical properties, can retard their cellular uptake due to the steric hindrance or, on the contrary, facilitate the NP endocytosis [137]. In this regard, it has been found that functionalization employing hydrophilic and flexible polymers, such as

polyethylene glycol (PEG), can both increase the stability of the nanosystems into biological environments and the biocompatibility [138, 139]. Thus, AuNPs (diameter of 4 nm) functionalized with PEG have been shown to penetrate the nucleus of HeLa cells without causing severe cytotoxicity with respect to the bare nanosystems of comparable size and can be efficiently used as a nuclear drug delivery carrier [140]. Likewise, gold nanoparticles functionalized with peptides and proteins improve their biocompatibility and attain further biological functions acting as drug carriers and even cellular targeting systems [141].

1.2.3 Protein corona formation and NMs influencing properties

The interface interaction between NMs and biological systems is complex and requires a holistic understanding. Biological environments, indeed, consist of several kind of biomolecules, namely lipids, nucleic acids, metabolites and most of all proteins (the blood plasma contains 3,700 identified proteins at the concentration of 60-80 g/L [142]), which immediately (< 30 s) interact with the NM surface resulting in the formation of a "corona" made up of multiple layers of molecules [143]. Since the "corona" is the outer layer on the NMs surface, which firstly interacts with the biological systems, it markedly affects the physiological response to the materials and their cytotoxicity [144].

The NMs-protein corona interaction is a dynamic process, which involves a continue competitive exchange of molecules through H-bonds, van del Waals and electrostatic attractions, as well as hydrophobic and π-π stacking interactions with the NM surface [145]. Highly bound proteins contribute to the formation of the so-called "hard-corona", while weakly

bound and exchangeable layer of molecules form the “soft corona” [146]. This phenomenon is described by the “Vroman effect”, which explains how high abundant molecules with smaller molecular weight and lower affinity adsorb first to the material surface, but are later replaced by larger molecules [147]. Large proteins, indeed, even though show a low diffusion coefficient, are able to replace earlier adsorbed molecules, due to their higher surface affinity and the numerous surface contacts, which allow for a strength adhesion onto the surface [148].

The physicochemical properties of NMs such as size, shape, surface charge and coating are critical factors in determining the interaction, affinities and the species of the proteins adsorbed on the material surface into biological milieu. In this regard, it has been demonstrated that the protein layer formed on small citrate-stabilized AuNPs with a diameter in the range of 3-10 nm, is thinner compared with the corona formed on AuNPs with diameters >150 nm, resulting into an increased binding constant and a faster adsorption kinetic of human serum albumin (HSA) [149]. From a bio-clinical point of view, the protein corona reduces the direct contact of the particles with the cell membrane affecting the cellular uptake. Thus, the thin layer of protein adsorbed on smaller AuNPs does not significantly alter the particle internalization while, markedly decrease the particle uptake for AuNPs with a size > 50 nm [150].

As to the shape, the interaction with curved NM surface can induce deformation of the secondary and tertiary structure of the adsorbed proteins, leading to aggregation effect and inducing autoimmune reactions. In this regard, circular dichroism (CD) measurements revealed that the secondary structure of HAS more significantly changes after its adsorption on triangle shaped gold nanoparticles, with a higher loss of helicity, in

comparison with the structure modification induced by the interaction with spherical gold nanoparticles [151].

Moreover, literature data evidence that NM shape also influences the "corona" composition and the binding affinity between the proteins and the NM surface. Thus, mass spectrometry analysis highlighted that the "corona" layer formed on 40 nm gold nanostars, injected in rodents by intravenous administration, is complex and includes a large amount of proteins with a molecular weight < 20 kDa and a slightly larger abundance of proteins with a molecular weight in the range of 20–40 kDa, than the "corona" formed on gold nanorod surface with a comparable size, that mainly includes big proteins. Such a difference is most likely due to the higher surface area and the presence of the spikes on the star-shaped particles which allow for an easier protein exchange and protein interaction [152]. As to graphene sheets, studies revealed that GO exhibits an extremely higher protein adsorption capacity with respect to carbon nanotubes, due to the formation of more stable π-π stacking interactions with the aromatic residues of the proteins. Such protein layer formed on the sheets limits the physical interaction of GO with the cell membrane, thus reducing the cellular morphological damage on HeLa, monocyte (THP-1) and lung carcinoma (A549) cells [153, 154].

The surface chemistry, like the charge, the hydrophobicity or hydrophilicity, as well as the surface coating and the functionalization are other critical factors in determining the protein corona formation. In this respect PEG-coating has been mostly used to reduce the protein adsorption on the particle surface. Hence, it has been demonstrated that 60 nm PEG-coated AuNPs weakly interact with the environmental proteins leading to a thin "corona" layer with respect to citrate-capped AuNPs with a similar

size [155]. Noteworthy, the size of the ligand on the particle surface influences the “corona” formation as well, so that it has been demonstrated that AuNPs functionalized with a large proteins results in a greater adsorption of plasma proteins with respect to AuNPs functionalized with fragment peptides, thus further leading to a different influences on the targeting ability of the nanosystems [156].

1.3 Nanomedicine for angiogenesis modulation

1.3.1 Angiogenesis

Mechanism of angiogenesis consists of a sequence of steps namely, enzymatic degradation of the capillary basement membrane, endothelial cell (EC) proliferation and migration, tube formation, vessel pruning and pericyte stabilizations [157]. Under physiological condition, angiogenesis starts when a low level of oxygen is detected in poorly perfused tissues, which require the formation of new vessels to satisfy their metabolic activity. Such tissues respond to the oxygen demand by secreting proangiogenic factors and among them the vascular endothelial growth factor (VEGF-A) [158]. VEGF-A activates the vascular endothelial receptor 2 (VEGFR-2) expressed on the surface of the long and thin cellular processes, known as “filopodia, of some endothelial cells called “tip cells [159]. Tip cells, due to the VEGF-A stimulation, secrete proteolytic enzymes, which digest the extracellular matrix (ECM) allowing for the EC migration and invasion [160] and induce the production of the Delta-like-4 (DLL4) ligand, which through a cell-cell signalling system, activates the Notch receptors of neighbouring cells, the endothelial “stalk” cells, prompting their proliferation [161]. These latter

cells give rise to the elongation of the capillary sprout and formation of the trunk of the new vessel, through which the blood can start to flow (Figure 2). The final step consists of the inhibition of stalk cells proliferation and migration and the maturation and stabilization of the newly formed capillaries by the construction of vessel walls through the recruitment of perivascular cells, pericytes and vascular smooth cells, which surround EC and the deposition of ECM [162]. Such latter process is mostly directed by the platelet-derived growth factor β (PDGF-B) and its receptor, that similarly to the VEGF receptor, is a transmembrane protein with tyrosine kinase domains in its intracellular region [163].

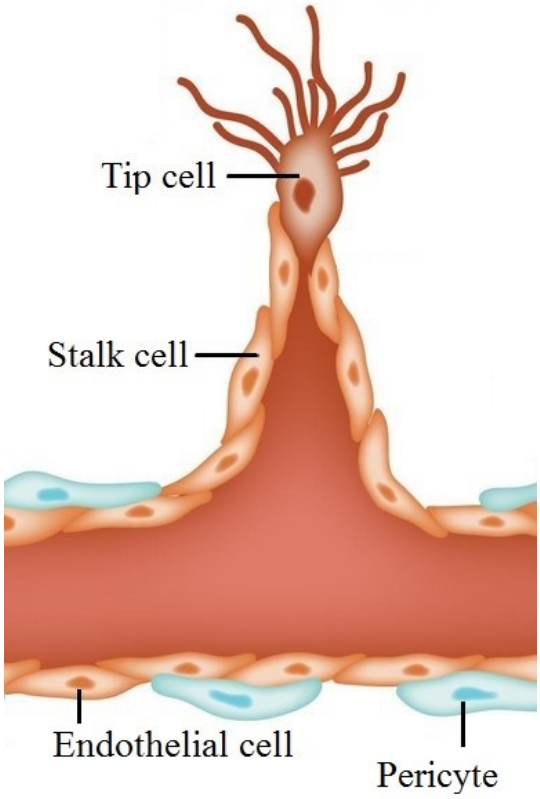

Figure 2- New blood vessel formation from "tip cells" and "stalk cells". *Modified from G. Fitzgerald et al. Front. Cell Dev. Biol., 2018* [164].

Although VEGF-A appears to be the main pro-angiogenic factor involved in proliferation, sprouting and vessels formation, other angiogenesis inducers have been identified including angiopoietins, transforming growth factors (TGF), tumour necrosis factor α (TNF-α), interleukins and above all a cytoplasmic protein, member of the ribonuclease (RNase) family, known as "angiogenin" (ANG). Previous works reported that ANG is able to induce vessels growth in chicken embryo chorioallantoic membrane at the concentration of 0.5 ng/mL [165], promotes cell proliferation and invasion of several cell models [166] and in zebrafish, angiogenesis and yolk extension are controlled by a ANG homolog gene [167]. Moreover, ANG gene silencing in HeLa cells, even though the high level of VEGF-A, reduces angiogenesis in athymic mice, thus demonstrating the crucial role of ANG, as permissive factor, in the neovascularization induced by VEGF-A [168].

Interestingly, metal ions are also involved in the angiogenic process and among them copper ions are known to stimulate the new vessels growth both directly, acting as cofactor of pro-angiogenic molecules like ANG and indirectly, by modulating expression and release of several proteins and cytokines [169].

1.3.2 Nanomaterials to control angiogenesis

The medical treatment of pathological angiogenesis as well as the modulation of the physiological vessels growth, through traditional therapies, based on anti and pro-angiogenic drugs such as monoclonal antibodies, inhibitors or activators of VEGF and related pathways, but also substrates of tyrosine kinase receptors, has shown limited clinical efficacy and the occurrence of a variety of adverse reactions [29]. Nanomaterials

provide a novel potential therapeutic approach, due to their intrinsic properties and being able to specifically and efficiently deliver the drug in the active site, thus further reducing the associated adverse effects.

Among the wide variety of nanomaterials, polymers, micelles, liposomes, graphene and above all inorganic nanoparticles, especially gold nanoparticles, are extensively investigated to modulate angiogenic processes. Polymeric NPs showed high stability and functionalization efficiency, being able to load drugs whether inside the polymer matrix or upon their surface. Furthermore, the polymeric structure allows the sustained release of the active principle in the target site [170]. Based on these advantages several polymer therapeutics have been developed, for instance, the FDA approved, biodegradable and biocompatible poly(lactic-co-glycolic) acid (PLGA), loaded with the anti-tumour drug oseltamivir phosphate (OP) has been proved to inhibit neovascularization and tumour growth [171]. Along with artificial polymers, natural polymers in particular chitosan, a cationic polysaccharide, has been found to inhibit vessels growth on mouse models of hepatocellular carcinoma, exhibiting an anti-angiogenic action [172]. Lipid-based nanocarriers, like liposomes and micelles, were also developed to control the angiogenic process [173]. Such nanomaterials are highly biocompatible and can be easily functionalized with both hydrophilic and hydrophobic compounds [174], thus offering a wide perspective for the synthesis of new therapeutics nanosystems. Solid lipid nanoparticles loaded with paclitaxel, for instance, exhibited anti-angiogenic activity by inhibiting HUVEC cells proliferation and tube-like formation [175], while PEGylated liposomes loaded with doxorubicin efficiently block tumour growth and pathological angiogenesis. Moreover, gene therapy based on cationic liposomes, which

deliver negative therapeutic genes, has also demonstrated promising activity in the angiogenesis regulation [176].

Among the NMs, inorganic nanoparticles and specifically gold nanoparticles, due to their distinctive size dependent optical, electrical, photothermal and intrinsic properties [23], which are not achievable with the above discussed polymer and lipid-based nanosystems, as well as the carbon-based NMs, including graphene oxide sheets, owing to their high stability, low toxicity, environmental friendliness and their intrinsic properties, have raised considerable attention, among the researchers, for the treatment of pathological angiogenesis [177].

1.3.3 Gold nanoparticles: physico-chemical-biological properties

1.3.3.1 Optical properties of Gold nanoparticles: SPR principle and application

Spherical AuNPs exhibit advantageous size-dependent optoelectronic properties, which allow their application in the field of bio-nanotechnology. The prominent spectroscopic feature of AuNPs is the surface plasmon resonance (SPR), which gives rise to an intense absorption band in the visible region, thus conferring the distinctive bright-red colour to the dispersion of nanoparticles with a diameter of around 20 nm.

SPR is based on the collective oscillation of excited conduction electrons by electromagnetic waves. According to the Fermi model, gold nanoparticle can be depicted as a lattice of ionic cores surrounded by a "sea" of free conduction electrons (Fermi sea) and in analogy to the real "plasma", the net charge of such a system is neutral. The electron field of

an incident light induces the displacement of the negatively charged electron cloud, also known as “plasmon”, toward the nanoparticle surface, thus accumulating the free electrons far from the positively charged ions and thereby creating an electric dipole. Such electric dipole generates an electric field along the particles, that is opposite to the electric field of the incident light and which also acts as “restoring force”, allowing the electrons to turn back to the equilibrium state [178] (Figure 3).

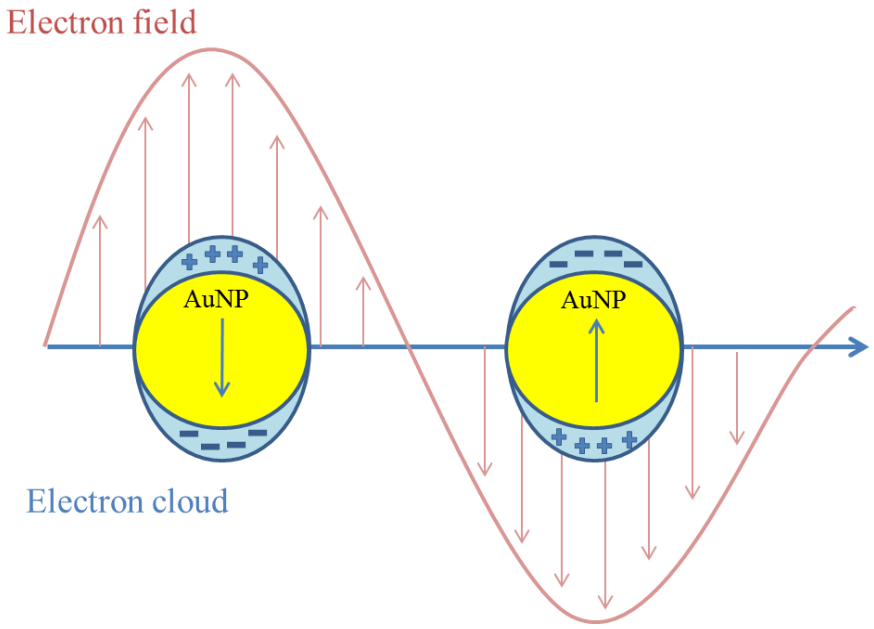

Figure 3- Schematic illustration of the surface plasmon resonance in gold nanoparticles.

The restoring force is proportional to the movement of the plasmon from the equilibrium to the excited state and the NP behaviour can be compared with a linear oscillator. In view of that, the removal of the applied electric field results in the oscillation of the negative electron cloud, with a frequency known as “plasmonic frequency” [179]. When an

alternating force is applied to the gold colloidal dispersion, plasmon starts to oscillate with the same frequency, but with amplitude and phase depending on the intrinsic parameters of the nanoparticles. Thus, at the plasmonic frequency, the amplitude shows the maximum value and the electrons are easily displaced.

It is possible to indirectly determine the electrons oscillating amplitude, since SPR requires an increase of both kinetic and electrostatic energies associated with the dipole electric field. Such energy, in accordance with the "conservation energy principle" is provided by the incident light, which is extinguished when electrons are excited. Hence, the higher is the oscillation, the higher is the light extinction and the absorption spectrum allows to detect the SPR. Based on this mechanism, SPR can be simply described as an electronic process, in which the absorption of light leads to the promotion of electrons, from their equilibrium state to the excited level.

The plasmon frequency for AuNPs corresponds to UV-vis light and in particular, spherical gold nanoparticles with a size range between 1 and 100 nm show an absorption band from 500 to 550 nm [180, 181]. Overlapped with this strong absorption band, associated to the SPR, the UV-vis spectrum of AuNPs shows also, other small electronic absorptions, due to interband transitions, namely the electron excitation from the occupied 5d level to the unoccupied 6s and 6p levels of the metal [182] (Figure 4).

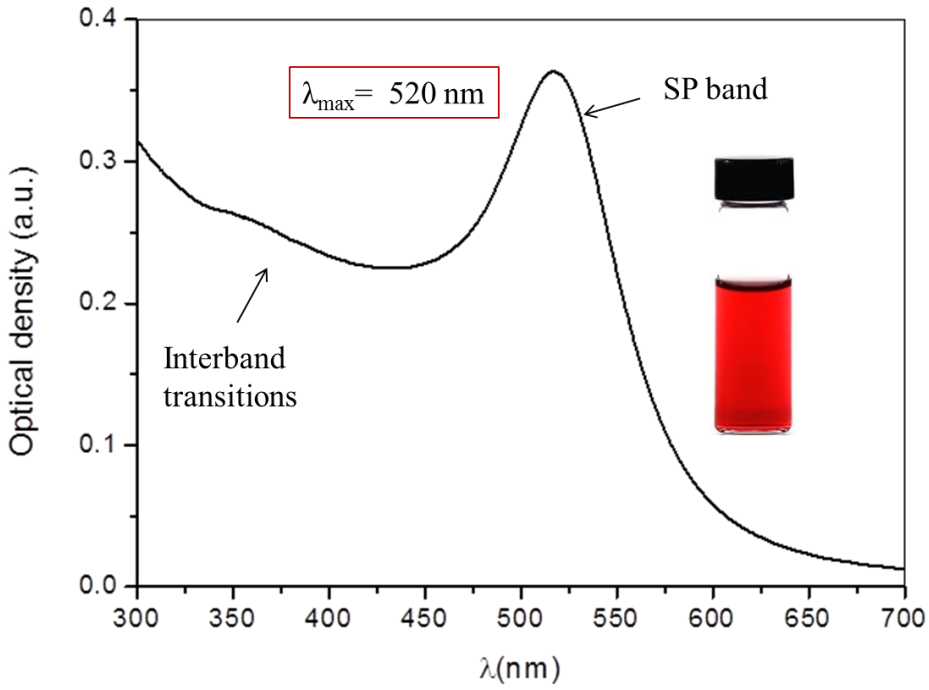

Figure 4- UV-vis spectrum of gold nanoparticles dispersion with a diameter of 12 nm.

Interestingly, the intensity of SPR extinction band increases along with the number of free conduction electrons involved and since each gold atom contributes with one electron [183], the plasmon absorption and so the extinction coefficient of the AuNPs dispersion is extremely high, almost 10^5 times more, compared to the molar absorptivity of any organic chromophore [184].

Modelling of the optical properties

A detailed comprehension of the AuNPs optical properties is essential to optimize their application. To this end, several analytical and theoretical models have been proposed, but nowadays there is not a

universal method able to ensure optimal results for all the nanoparticle structures and the associated physico-chemical phenomena.

Among these, Mie theory provides the optical properties of spherical AuNPs not interacting with each other, with any size and optical constant. Such a theory is based on both the multipole expansion of the electromagnetic field and the solution of the Maxwell equation, which allows to accurately determine the concentration and the size of the god colloidal dispersion using the optical absorption spectrum of AuNPs [185, 186]. In this case, the plasmon extinction is given by the following equation (eqn. 1):

$$\sigma_{ex} = \frac{2\pi}{|k^2|} \sum_{L=1}^{\infty} (2L+1) \cdot Re\,[a_L + b_L] \qquad (1)$$

where L is the electric charge of the NPs, k is wave-vector of the light in the dielectric medium, $x = |k| \cdot R$ and R is the nanoparticles radius. As to a_L and b_L, they are defined by the following equations (eqn. 2-3):

$$a_L = \frac{m\,\Psi_L(mx)\cdot\Psi_L'(x) - \Psi_L'(mx)\cdot\Psi_L(x)}{m\,\Psi_L(mx)\cdot\eta_L'(x) - \Psi_L'(mx)\cdot\eta_L(x)} \qquad (2)$$

$$b_L = \frac{\Psi_L(mx)\cdot\Psi_L'(x) - m\Psi_L'(mx)\cdot\Psi_L(x)}{\Psi_L(mx)\cdot\eta_L'(x) - m\Psi_L'(mx)\cdot\eta_L(x)} \qquad (3)$$

where Ψ_L and η_L refer to the cylindrical Bessel-Ricatti functions, $m = \frac{n}{n_m}$, while n and n_m are the refraction index of the gold and the dielectric medium respectively.

Since these equations are complicated to handle, computer codes can be applied to perform Mie calculations.

Factors influencing SPR

Particle size, shape and the surrounding environment affect the SPR of gold nanoparticles.

As to the size, a retardation effect associated with multipolar excitation modes increases along with the dimension of the nanoparticles, leading to a broadening and red-shifted SPR peak. In view of that, the diameter d of spherical gold nanoparticles, knowing the maximum of absorption of the SPR peak, can be calculated according to the following equation (eqn. 4) [187]:

$$d = \frac{\lambda \max - 515.04}{0.3647} \quad (4)$$

Such an effect is more evident for AuNPs with a diameter larger than 60 nm, whereas a dipolar oscillation mode characterized particles smaller than 25 nm [184].

As to the shape, it affects the width and the absorption maximum of the surface plasmon peak. Spherical particles, for instance, show a unique localized plasmon peak, while gold nanorods exhibit two strong absorptions corresponding to the displacement of the negative electron cloud along the two axes of the rod and resonating at different wavelengths. Furthermore, increasing the aspect ratio of the rod, a red shift of the SPR referred to the longitudinal excitation is observed [188].

The SP excitation process not only depends on the physico-chemical properties of AuNPs, but it is also influenced by chemical and physical effects induced by the surrounding media. Chemical effects refer to the chemical interface damping (CID) mechanism, which involves the adsorption, both chemisorption and physisorption, of molecules on the

particle surface that, providing new relaxation pathways to the free electrons on the metal nano-systems, leads to a widen and red-shifted SPR peak [189]. A possible explanation of CID was developed by Persson and concerns the coupling of the metal free conduction electrons with the unoccupied molecular orbitals (LUMOs) of the absorbed molecules on the particle surface. When the electron field is applied, such electrons can transfer into the LUMOs giving rise to a fast loss of coherence with the other excited electrons, thus modifying the SPR signal. Such an SPR variation depends on the physico-chemical properties of the adsorbates, which showing distinctive LUMO positions, further lead to different electron coupling [189]. As to the physical effects, the dielectric properties of whether the environment or the ligand layer upon the nanoparticle surface, modify the SPR peak in its absorbance maximum, width and intensity. In particular, surrounding medium with a high refractive index as well as nanoparticle coating layer with high polarizability (e.g. protein layer [190]) cause a gain of the SPR intensity, a red-shift and an increase of the full width at half maximum (FWHM) value of the plasmon peak [191]. The linear relationship between the wavelength at the maximum of absorption, $\lambda_{max,}$ of the surface plasmon peak and the environment refractive index is given by eqn. 5 [178]:

$$\lambda_{max} = \frac{2\,\pi\,c}{\omega_p}\sqrt{2n_m^2 + 1} \qquad (5)$$

where, $n_m = \sqrt{\epsilon_m}$, n_m is the environmental refractive index, ε_m is the dielectric constant of the surrounding medium, c is the light speed and $\omega_p$is the bulk plasma frequency.

Noteworthy, based on the SPR variation in response to the local refractive index, it is possible to calculate the fraction of molecules absorbed on the nanoparticle surface. Accordingly, the fraction of molecules over the total particles, g, depends on the λ_{max} variations, by considering the functionalized nanoparticles as core-shell spheres with a metallic core of d diameter, corresponding to the uncoated nanoparticles and a molecules shell surrounding the metal core, as follows (eqn.6) [192]:

$$\frac{g}{1+\alpha_s} = \left(\frac{\lambda_p^2(\varepsilon_s-\varepsilon_m)}{\Delta\lambda\cdot\lambda_{max,0}} + 2\alpha_s\right)^{-1} \quad (6)$$

where λ_p is the free electron oscillation wavelength ($\lambda_p = 131\,nm$ for gold [193]), $\varepsilon = n^2$ and correspond to the dielectric constant, $\lambda_{max,0}$ is the wavelength at the maximum of absorption for un-functionalized AuNPs and $\alpha_s = \frac{(\varepsilon_s-\varepsilon_m)}{(\varepsilon_s+2\varepsilon_m)}$ is the polarizability of a sphere with a shell dielectric constant ε_s in a medium with dielectric constant ε_m, where 's' and 'm' indices refer to the shell and environmental medium, respectively.

Biomedical applications of SPR

The optical properties of gold nanoparticles specifically the intense plasmon absorption, the highly sensitive spectral response to the local surface environment as well as the photostability, offer a wide range of applications in the field of biomedicine [194]. Thus, the ability to modify SPR in response to small changes in the surrounding environment, allows AuNPs to be used as an excellent signal transducer for the development of biosensors [195]. Accordingly, the surface plasmon resonance has been applied to develop DNA sequencer based on the spatial detection of

AuNPs functionalized with target DNA chains [196] as well as for the colorimetric detection of a variety of compounds like metals ions [197], organic molecules [198] and proteins [199]. SP process is also helpful to specifically label tissues, organelles and cells, such as cancer cells. To this purpose, AuNPs functionalized with biomolecules exhibiting a high affinity for particular cell factors and structures are detected into the screening tissue or in the cultured cells, by the optical microscopy at the SPR wavelength [200]. Along with the applications of SPR for imaging and detection of target cells and tissues, the optical properties of AuNPs allow for the controlled activation of physical processes, such as the conversion of light into heat, which is used in biomedicine as an innovative strategy for cancer treatment [201]. The photothermal heating strategy is based on the generation of local heating produced by the absorption of light associated with the SPR of gold nanoparticles, specifically functionalized to bind to cancer cells. To this purpose, gold nanorods, which show a strong optical resonant absorption of the near-infrared (NIR) light, are particularly used. Thus, the irradiation of gold nanorods-treated tumour mass induces a local increase of temperature, which selectively promotes proteins denaturation and cell cytoskeleton disruption, leading to the destruction of tumour cells and minimizing damages to the healthy tissues [202].

The local generation of heat is also applied for a controlled drug delivery [203]. This strategy uses gold nanoparticles properly functionalized with active principles and able to selectively interact with the target tissue. Once the nanoparticles reach the target site, the local increase of temperature, due to the excitation of the conduction electrons

of AuNPs, provides the required energy for the drug release process, not involving the healthy tissues [204].

Surface functionalization

Most of the biomedical applications of AuNPs, as biosensors and drug delivery systems, require their functionalization with biomolecules such as proteins, nucleic acids, peptide fragments as well as active principles and biolinkers, thus allowing the nanosystems to specifically interact with target compounds, cells and tissues. AuNPs, indeed, together with their easy synthesis, possess the advantages of a straightforward and efficient surface modification compatible with biomolecules [205].

Efficient bio-functionalization of AuNPs can be achieved by physical and chemical adsorptions, respectively.

Physical adsorption involves non-covalent interactions, namely electrostatic attractions between the negatively charged AuNPs surface and the positively charged groups of the absorbent molecules [206], hydrophobic attractions, Van del Waal force and π-π stacking interactions [207]. The non-covalent conjugation is the most simple technique to bind to molecules on the nanoparticle surface and is widely used for the development of drug delivery systems, due to the ease release and reversible nature [208]. Along with these advantages, physisorption shows also several weak points, as the requirement of a high concentration of the absorbent molecule and its random orientation on the nanoparticle surface, which can influence the biological behaviour of the ligand. Moreover, physisorbed molecules can be easily replaced by other compounds present in the biological environment, making the biological response difficult to control [209].

As to the chemical adsorption, it involves a covalent interaction between the biomolecule and the nanoparticle. The covalent binding leads to an ordered and highly reproducible layer of ligands upon the metal surface and the functionalised nanosystems have advantages in terms of stability and unspecific physisorption. Chemical adsorption can be achieved using several bio-conjugation techniques, which include the use of thiol derivatives, bifunctional linkers as well as adapter molecules like streptavidin and biotin. Among these, the thiol-gold system is the most used, being able to create robust and stable linkages on the particle surface. Gold, indeed, as soft acid, binds, with high-affinity, to soft bases like thiol groups, to form strong Au-S bonds (40-50 kcal/mol [210]). Such Au-S bonds exhibit both a covalent and donor-acceptor characters, due to the lone–pair electrons on the sulphur atoms and owing to their strong nature are able to replace the stabilizing agent shell (e.g. citrate shell) on the nanoparticle surface [211].

Other effective chemisorption strategies make use of coupling reactions between specific chemical groups on surface-derivatized AuNPs and functional groups of the ligand as well as bifunctional linkers. Succinimidyl propionyl polyethylene glycoldisulfide (NHS-activated PEG), for instance, is a linker which, acting as a bridge, is able to interact with both the primary amine of the ligand and the gold surface, by breaking its internal disulphide bond [22]. Biotinylated AuNPs are also used for the covalent adsorption, due to the specific and high affinity interaction of biotin with avidin/streptavidin glycoproteins [209].

Physical and chemical interactions between a general biomolecule like a protein and the AuNP surface are illustrated in figure 5.

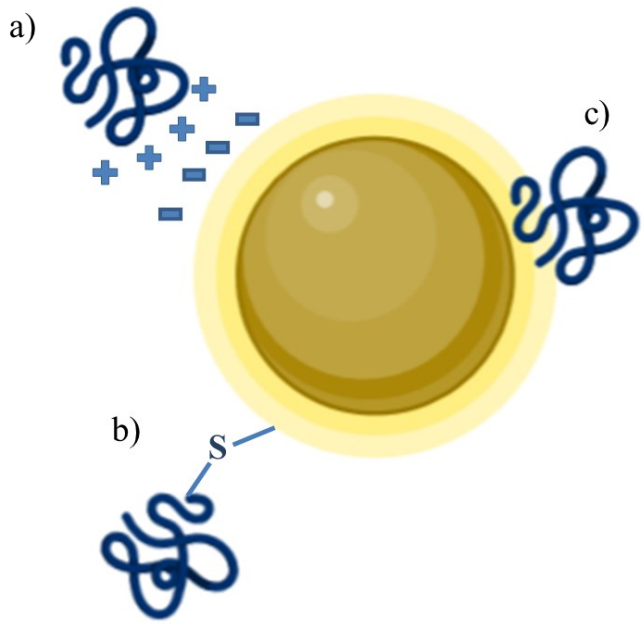

Figure 5- Physical and chemical interactions between a protein and the gold nanoparticle surface: a) ionic interaction, b) Au-S covalent bond, c) hydrophobic interaction.

1.3.3.2 Antiangiogenic and antioxidant properties of AuNPs

Along with the optoelectronic features, AuNPs exhibit intrinsic properties, such as antimicrobial [212], antioxidant [213] and antiangiogenic activities [214], which further allow for their biomedical applications. Among these, the ability of AuNPs to suppress the new blood vessels formation, provides a novel therapeutic strategy for the medical treatment of impaired angiogenesis, as well as to control the angiogenic process being, AuNPs, used as a platform for angiogenesis modulating compounds [215, 216]. AuNPs, indeed, can specifically interact with heparin-binding growth factors, such as VEGF-165 and FGF,

by binding to the cysteine residues present on their heparin-binding domain. Such an interaction changes the chemical conformation of the proteins, thereby inhibiting their angiogenic activity by blocking the interaction with their receptors [217]. Furthermore, AuNPs are able to induce structural reorganizations of the VEGF receptor (VEGFR-2) and inhibit the VEGF-induced phosphorylation [218]. Such anti-angiogenic activity of AuNPs depends on both the surface charge and the size of the gold nanosystems. Thus, the nanoparticle functionalization with thiolated tetraethleyene glycol reduces the interaction with VEGF, while bare citrate-capped AuNPs show the maximum inhibition effect [219]. As to the size, spherical AuNPs with diameters in range of 10-20 nm exhibit the most effective antiangiogenic action compared to the particle with diameters < 10 nm [219].

Based on these mechanisms, it has been demonstrated that AuNPs block both endothelial and fibroblast cells proliferation *in vitro* and reduce the VEGF-induced vascular permeability and angiogenesis *in vivo*, whether in mouse ear and mouse ovarian tumour models [28, 220]. Moreover, experiments performed on HUVEC cells evidenced the ability of AuNPs to suppress the capillary tube-like formation and the cell migration by affecting the cell cytoskeleton as well as by influencing the Akt phosphorylation pathway of VEGFR-2/PI3K [221]. As to the cytoskeleton, recent works demonstrated that AuNPs are able to reduce the actin networks and increase actin stress fibres thereby inhibiting the cell spreading of HUVEC cells [222]. Such an effect, as expected, is size-specific, thus spherical AuNPs with size in the order of 5 nm do not lead to cytoskeleton rearrangements, while particle with a size between 20-60 nm significantly impair the cytoskeleton of endothelial cells [223].

It has been also demonstrated a free radical scavenging activity of AuNPs that depends on the size and the surface/volume ratio of the nanosystems and increases with the concentration of the nanoparticle dispersion [57]. The antioxidant mechanism suggested involves an electron transfer from the gold colloidal dispersion to the free radicals which results in the intracellular ROS species quenching [57]. ROS species can damage biological structures including cell membranes, proteins and DNA and elevated levels of free oxygen radicals together with the alteration of redox balance are found in cancer cells owing to the high metabolic and peroxisomal activity as well as mitochondrial dysfunction of the tumour tissues [224]. Noteworthy excessive production of ROS or impaired ROS detoxification have been associated with slow healing process and chronic wounds [225]. In this perspective, the antioxidant protection of AuNPs provides a beneficial strategy for the medical treatment of the wounds.

1.3.4 GO: physico-chemical-biological properties

1.3.4.1 Graphene and GO: structure and synthetic methods

Graphene is a 2D material formed by a thick sheet of sp^2 carbon atoms arranged in a honeycomb-like structure [30] (Figure 6).

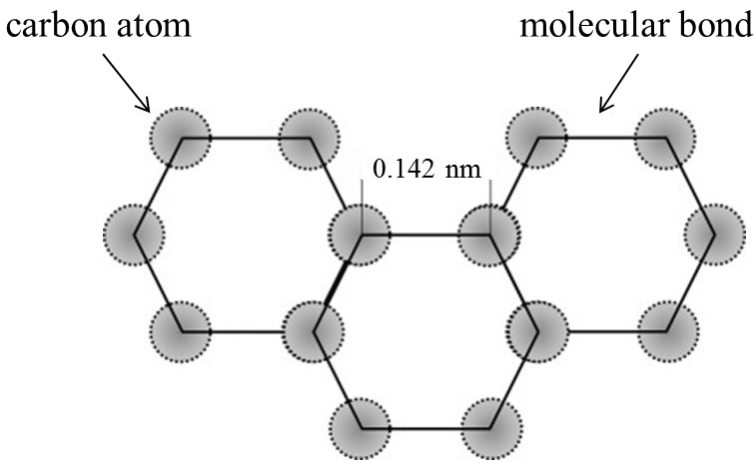

Figure 6- Chemical structure of graphene**.** *Modified from Z. Zheng et al. Graphene, 2018 [226].*

Each carbon atom establishes three covalent σ bonds on the 2D plane and one π bonds located above and below the two-dimensional plane, with the neighbour atoms, so that each hexagonal arrangement of atoms results in three π bonds with the π electrons delocalized over the whole structure. The σ bonds are rather strong and a high energy is required to break them; whereas the π bonds are weaker and are able to form Van der Waals interactions with the consecutive graphene layers. Such a material has risen great interest among the researcher due to its unique electrochemical properties including high thermal conductivity, density, chemical inertness, optical transmittance and hydrophobicity [227]. Graphene indeed, is a strong material with a high Young's modulus (~1.0 TPa) [228], it possesses a thermal conductivity of around 4.84-5.30 $kWm^{-1}K^{-1}$ [229] and an electron density of $2 \cdot 10^{11}$ cm^2 [230]. It can be produced by two different methods. The first approach is called top-down, through which

graphite is simply separated using mechanical or liquid exfoliation, to get the graphene layers. The second method is known as bottom-up procedure, which forms graphene by a chemical deposition. The top down methods produces high-quality graphene with small size while, the bottom up approach produces large graphene sheets with lower quality [231]. However, the pristine graphene has poor solubility [232] and, due to the hydrophobic interactions among the graphene layers, shows a pronounced tendency to agglomerate in solution [233]. As an alternative, its oxidized form, graphene oxide (GO), takes the advantages of graphene, with a similar hexagonal structure while also improving the water solubility and increasing the distance between the layers due to the presence of hydrophilic groups, such as hydroxyl (-OH), alkoxy (C-O-C) groups mostly present on the basal planes of the GO sheets and carbonyl (C=O) and carboxylic (-COOH) groups present near or on their edges [234, 235]. GO is mainly synthetized by using the Hummer's method which include oxidation of graphite by using potassium permanganate and sulphuric acid that lead to graphite salts, which act as a precursor for GO (Figure 7) [236].

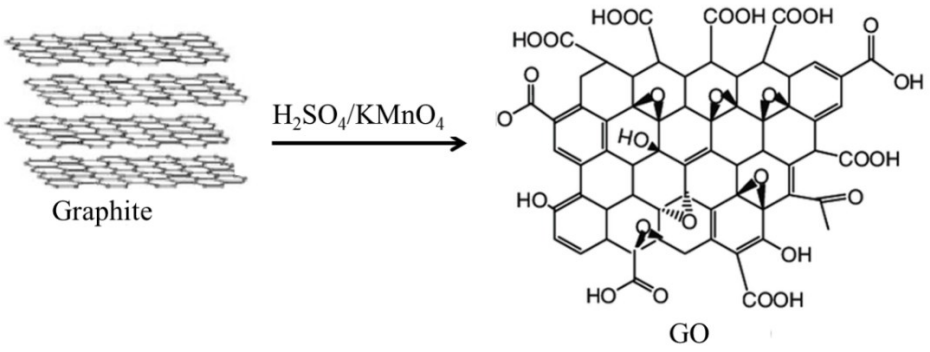

Figure 7- Schematic synthesis of GO using the Hummer's method. *Modified from A. Nafees et al. Journal of Plastic Film & Sheeting, 2015 [237].*

Owing to its chemical structure, GO shows unique intrinsic, physical and chemical properties including, fluorescence quenching capability, surface-enhanced Raman's scattering properties, high conductivity, good biocompatibility and can be efficiently functionalized [238]. Such features allow it to be used in bio-imaging [239], bio-sensing for biomolecules recognition [240], tissue engineering [241] and its biocompatibility and ease functionalization, in particular, make it a promising platform for drug delivery [242]. The hydrophilic functional groups of GO, like -COOH and -OH, indeed, make it acceptable for the immobilization of polymers, biomolecules and drug with no surface adjustments and no coupling reagents via covalent bonds or non-covalent interactions which include hydrogen bonds, ion-dipole or Van der Waal forces while the free surface π electrons are capable of forming π-π and CH-π and interactions.

1.3.4.2 GO: biomedical applications

Carbon-based NMs have gained the attention of many researcher due to their intrinsic biological properties, which allow for their potential clinical applications for the treatment of angiogenesis-dependent diseases.

Recent works demonstrated that GO exhibits pro or anti angiogenic effects depending on the used concentration which results in a variation of the intracellular generation of ROS induced by the carbon sheets. Indeed, ROS generation together with reactive nitrogen species and the activation of the phospho-eNOS pathway may be a plausible mechanisms for the GO modulation of angiogenesis [34]. Accordingly, lower concentration of GO leads to a controlled formation of ROS that enhance the angiogenesis [243], while high concentration of GO induces cell death through the formation of a large amount of ROS [244]. Based on this findings, it has

been determined that GO has pro angiogenic properties and enhances the expression of angiogenic proteins (i.e. VEGF and FGF) in human mesenchymal cells and endothelial cells at the lower doses (1-50 ng/mL), while shows anti-angiogenic activity at the higher concentrations (> 100 ng/mL) [34, 245].

Moreover, GO sheets are non-toxic and due to its nanotopography, are able to enhance proliferation and adhesion, of fibroblasts [246], osteoblasts and mesenchymal stromal cells, playing a significant role in the wound healing treatment [247]. Cells, indeed, are influenced by the impact with mechanical forces in the local environment to which, they can respond by activating nano-transduction pathways leading to their adaptation, proliferation, migration or even death [248]. Since the roughness and the stiffness of GO is able to mimic the architecture of the native extracellular matrix, its interaction with cells results in a spatial organization of the cells which leads to enhanced wound closure and increases the strength of the new formed tissue [249]. Moreover, the full detachment of the cells and so the dissolution of old adhesion which allows for the cell migration requires a great amount of energy, that derives from the mitochondrial activity, which has been found stimulated by the GO action [246, 250].

GO exhibits also antibacterial properties, which have been associated with ROS-dependent stress [61], bacterial membrane damages, due to the sharp edges of GO which can cause the disruption of the cellular integrity [60] and isolation of bacteria by wrapping/trapping them in a sheet-form blanket of GO, thus limiting their access to nutrients [251]. In this regard it has been found that E.coli cells lose their cellular integrity after 2.4 hours of incubation with 100 μg/mL GO nanosheets dispersion [252] while 250

μg/mL of GO are able to inhibit the growth of Salmonella enterica and Listeria monocytogenes by 100% [253].

The hemocompatibility of GO has been also investigated. In this regard, recent works showed that GO exhibits pro-thrombotic properties by activating intracellular pathways that induce the release of calcium ions from intracellular stores and which also depend on the surface charge distribution of the GO nanosheets [254].

Besides, GO is able to modulate the function of immune cells, such as macrophages [255], neutrophils [256] and dendritic cells [257] depending on their physicochemical features and functionalization [258].

1.3.5 Angiogenic factors: Angiogenin and copper

1.3.5.1 Biological structure of ANG

ANG is a 14,200 Da basic single-chain protein, member of the RNase family and physiologically present in the blood plasma at the concentration of 200-400 ng/mL [259]. It was firstly discovered and characterized by Vallee and colleagues at the Harvard University in the 1985 [260]. Its primary structure includes 123 amino acids with a 33% of sequence identity and 65% of sequence homology respect to the pancreatic ribonuclease A (RNase A). Similarly to RNase A, ANG shows a kidney-shaped structure consisting of three α-helices and seven β-sheets stabilized by three disulphide bridges [261]. Precisely, helix 1 (H1, residues 3-14), helix 2 (H2, residues 21-33), β-sheet 1 (B1, residues 41-47), helix 3 (H3, residues 49-58), β-sheet 2 (B2, residues 62-65), β-sheet 3 (B3, residues 69-73), β-sheet 4 (B4, residues 76-84), β-sheet 5 (B5, residues 93-101), β-sheet 6 (B6, residues 103-108), β-sheet 7 (B7, residues 111-116) and helix 3 (residues 117-121). Whereas, the three disulphide bridges involve the

residues Cys-26-Cys-8, Cys-39-Cys-82 and Cys-57-Cys-107, respectively [262]. Moreover, ANG, as well as RNAase A, contains both a catalytic centre, formed by the triad His-13, Lys 40 and His-114 [259] and a purine/pyrimidine binding site. Despite of these analogies, the enzymatic activity of ANG is 10^5-10^6 fold lower compared to the ribonucleolytic activity of RNase A. The rationale behind the low enzymatic activity of ANG is the obstruction of its pyrimidine base binding site by the glutamine residue, Gln-117, which forms two hydrogen bonds with the threonine residue, Thr-44 [263]. Such an obstructive position of Gln-117 is also permitted by intramolecular hydrophobic interactions, which involve the amino acid residues isoleucine, Ile-1 and Ile-19, and phenylalanine, Phe-120 [264]. Accordingly, mutation of the Gln-117 residue leads to an increase of the enzymatic activity of ANG [263]. Furthermore, ANG lacks the fourth disulphide bridge, respect to RNAse A, resulting in the formation of a loop region, including the amino acid sequence 60-68, that is involved in the endothelial cell-surface receptor interaction [265]. The ANG structure comprises, also, a nuclear localization sequence encompassing the amino acid sequence 30-35 [266].

The catalytic site, the receptor binding site and the nuclear translocation sequence constitute the three characteristic functional sites of ANG, which explain its unique RNase activity and allow for its distinctive biological functions, as key factor, in the blood vessel formation [168] (Figure 8). Interestingly, the integrity of all the three functional sites is essential for the maintenance of the biological activity of ANG, since it has been demonstrated that mutation of the His-114 residue causes the completely loss of both the enzymatic activity of the protein and its angiogenic action [267].

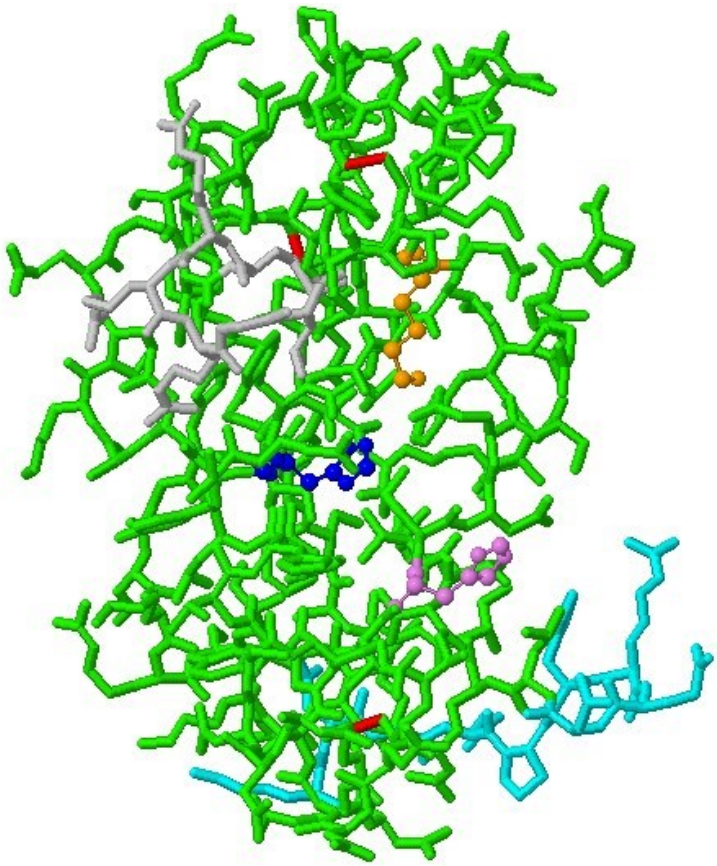

Figure 8- 3D biological structure of human ANG consisting of: three disulphide bridges (in red); a catalytic site formed by the triad His-13 (in blue), Lys-40 (in orange) and His-114 (in violet); the receptor binding site, sequence 60-68 (in cyan); the nuclear translocation sequence, 30-35 (in grey). (PDB ID 1ANG).

1.3.5.2 Mechanism of action of ANG

The angiogenic action of ANG, is based on protein-protein interactions through which angiogenin promotes endothelial cells growth, survival, migration and invasion. Based on literature data, ANG binds to a 170-kDa transmembrane receptor located on the surface of angiogenin-responsive endothelial cells. The interaction between ANG and its receptor induces

conformational changes in the protein, moving the Gln-117 residue from its obstructive position and allowing ANG to bind to its natural substrate RNA, and triggers several signal transduction pathways, through the activation of secondary messaging cascades [268]. Accordingly, available data demonstrated that ANG stimulates extracellular signal-related kinase 1/2 (ERK1/2) [269], protein kinase B/Akt [270] and stress-associated protein kinase/c-Jun N-terminal kinase (SAPK/JNK), [271] increasing the production of intracellular ribosomal proteins and enhancing cell growth and proliferation. In addition, through the activation of the phosphatidylinositol-3 kinase/Akt pathway (PI3K/Akt), ANG promotes synthesis and release of nitric oxide, a vasodilator factor, involved in the vascular physiology [272]. Along with the activation of extracellular transduction pathways, ANG is able to pass through the cell membrane, via the "receptor-mediated endocytosis" and accumulates into the nucleus or cytoplasm of endothelial cells, under growth or stress conditions, respectively. Data reveal that inside the nucleus, ANG promotes the ribosomal DNA (rDNA) transcription, thus increasing the 47S ribosomal (rRNA) levels by binding to the angiogenin-binding element (ABE) on the rDNA promoter, where angiogenin induces methylation and histone modification [273]. Besides, ANG enhances the messenger RNA (mRNA) transcription of several genes, since acts as chromatin remodelling activator [260]. In this regard, chromatin immunoprecipitation-chip assays identified 699 genes that could be regulated by nuclear ANG and most of these genes are significantly expressed in tumorigenesis [274]. On the other hand, the cytoplasmic ANG, following stress conditions (e.g. oxidative damages and starvation stress), cleaves transfer RNA (tRNA) molecules leading to the production of stress induced tRNA-derived

(tiRNA) [275], which guide the protein translation thereby promoting damage repair and cell survival [274].

It is also known that ANG, through the amino acid sequence encompassing the residues from 60 to 68, that are also part of the cell-surface receptor binding site, makes complex with the endothelial cell surface α-actin. The α-actin binding is a crucial step for the promotion of angiogenesis since this complex is able to activate the plasminogen activator/plasmin serine protease system leading to the plasmin (PLN) generation from plasminogen [276, 277]. Plasmin, indeed, is an enzyme able to degrade both laminin and fibronectin of the basement membrane and the extracellular matrix, thus promoting endothelial cell migration and invasion into the perivascular tissue, which is a crucial phase of the vessel growth [277, 278]. Furthermore, upon the interaction with actin, ANG induces changes in the cell cytoskeleton by inhibiting the polymerization of G-actin and changing the physical properties of F-actin, respectively [279]. These events severely alter the cells mechanical properties, thus inducing strong effects on the cellular structure and function [280], the tissue morphogenesis [281] as well as on the whole angiogenic process [282] (Figure 9).

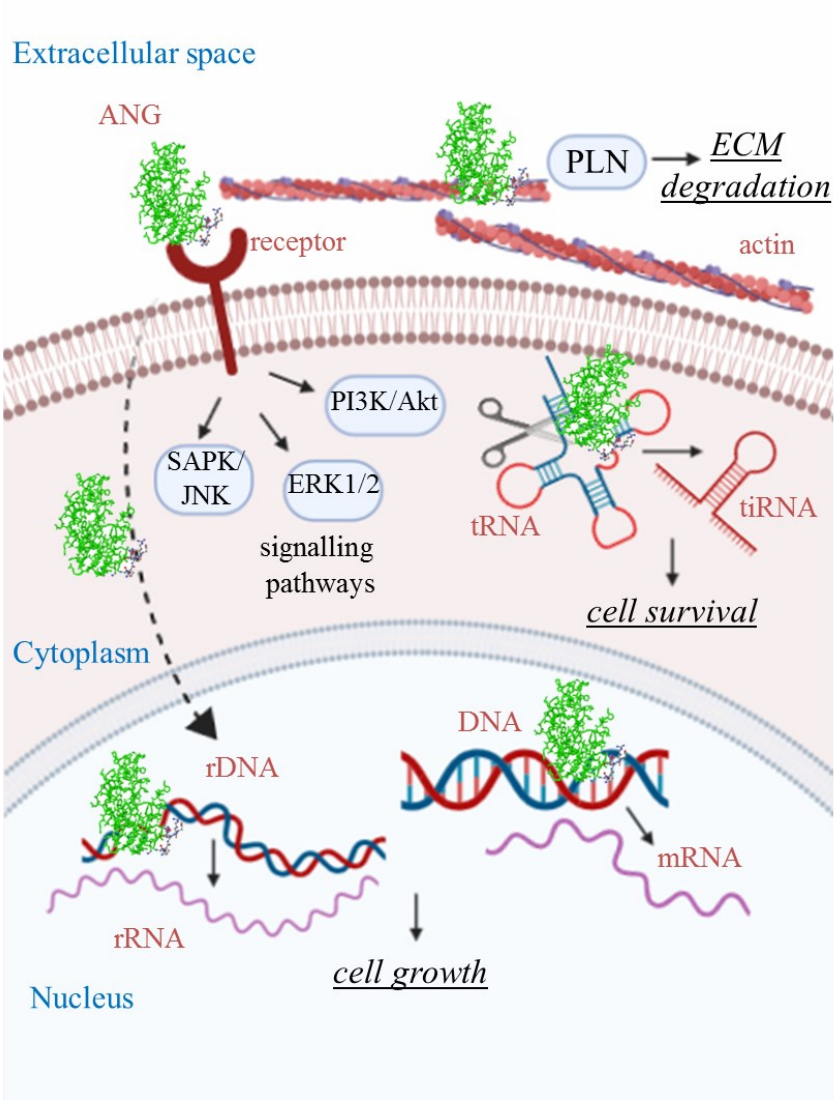

Figure 9- Mechanism of action of ANG. Extracellular ANG, through the interaction with a 170 kDa endothelial surface cell receptor, activates several signal transduction pathways, including ERK1/2, SAPK/JNK and PI3K/Akt thus promoting cell growth and differentiation. Moreover, extracellular ANG undergoes receptor-mediated endocytosis and accumulates into the cytoplasm, under stress condition or in the nucleus, under growth condition. Cytoplasmic ANG, in response to stress, cleaves tRNA molecules and generates tiRNA, which reprograms protein translation thus promoting damage repair and cell survival. Whereas, nuclear ANG stimulates both rRNA and mRNA transcription allowing

for the cellular growth. In addition, ANG interacts with the cell surface actin leading to ECM and basement membrane degradation thereby promoting cell migration and invasion.

1.3.5.3 Physio and pathological role of ANG: wound healing and tumorigenesis

The primary biological function of ANG is the blood vessel homeostasis regulation, through both the stimulation of the new vessel growth and the maintenance of the endothelial cell self-renewal. Nevertheless, the widespread expression of ANG in several human tissues and fluids, namely plasma [283], tumour micro-environment [284], amniotic [285] and cerebrospinal liquids [286] suggests its participation, not merely in the neovascularization but also in further physiological and pathological processes, including neuroprotection [287], inflammation [288], immune-response [289], micro biocidal activity [290] and reproduction [291]. Accordingly, mutation of the gene encoding for ANG, has been found in patients affected by neurodegenerative disorders, such as amyotrophic lateral sclerosis (ALS) [292] and Parkinson's disease (PD) [293], while increased concentration of ANG has been measured in patients with ulcerative and Crohn's diseases (CrD) [294]. Moreover, high level of ANG has been measured in wound fluids collected post-injury [295] and the upregulation of the ANG expression has been detected in different types of tumours i.e. breast, cervical, colon, liver, kidney as well as lymphoma and melanoma [296], thus proving its pivotal role in the wound healing of damaged tissue [297] and tumorigenesis [298], as well.

As to wound healing, it is an essential physiological process consisting of a sequence of molecular and cellular events, which occurs to restore lesions induced by specific trauma or pathological conditions that break

the physical continuity of functional tissues [299]. Cell and biochemical events in wound repair can be divided into four stages: bleeding and homeostasis, inflammatory reaction, cell proliferation and remodelling [300] (Figure 10).

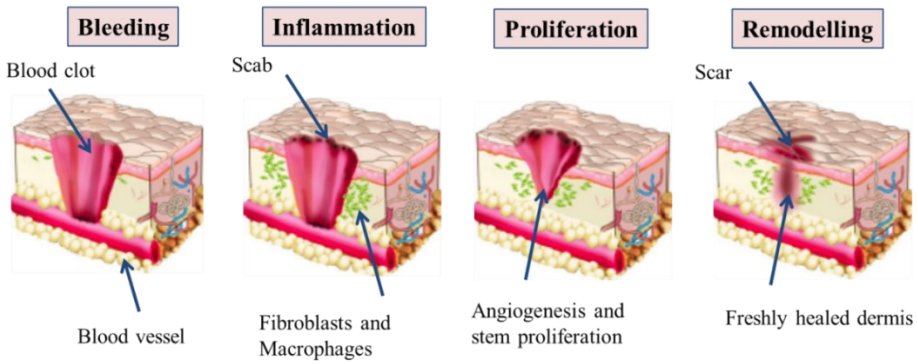

Figure 10- Phases of the wound healing process: haemostasis; inflammation; proliferation; remodelling. *Modified from P.H. Lin et al. Nutrients, 2018 [301].*

The former reaction of a tissue to a specific damage is the contraction of the lesioned vessels and the aggregation of platelets, thrombocytes and fibrins, allowing for the blood clot formation that is essential to maintain the homeostasis. Such a clot acts also as a barrier, which prevents the microorganism invasion and provides a temporary matrix for cell migration [302]. The immune response activation, during the inflammatory stage, indeed, requires the migration, in the wound area, of immune cells, namely mastocytes, Langerhans cells and gamma-delta cells, which release cytokines as well as lysosomal enzymes and ROS in the injury site, thus causing the appearance of the oedema and the erythema [303]. Such a tissue response plays a protective role against invading

agents and supports the removal of cell debris. In the latter stages of wound healing new capillaries invade the wound space allowing, the new tissue, to receive sufficient oxygen and nutrients [304]. This process involves several cell types, including fibroblasts, macrophages and endothelial cells, which play an interdependent activity in the wound management. In particular, macrophages provide cytokines essential to promote fibroplasia and angiogenesis; fibroblasts construct the ECM, which is indispensable to support the growing tissue; endothelial cells digest and penetrate the vascular basement membrane, invade the ECM and form tube-like structures, which continue to extend branches, thus creating new blood vessels networks [305]. These events require the action of several soluble molecules capable to regulate cells interactions and to stimulate wound angiogenesis. Among them, the FGF [306], VEGF [307], PDGF, several cytokines and chemokines and in particular ANG, the most abundant factor in the wound environment, play a pivotal role. Accordingly, it has been found that the high level of ANG in the wound fluids are able to induce endothelial cells proliferation and circular angiogenic cell (CAC) differentiation, while the antibody neutralization of ANG in equivalent wound fluids leads to a reduction of their angiogenic properties [308]. Such findings were also supported by further clinical data [308] and prove the positive correlation between ANG and the wound healing process.

As to tumorigenesis, it is the formation of an abnormal mass of malignant cells from normal cells, through a multistep process, which involves genetic and epigenetic modifications, as well as specific growth condition of the tumour mass [309]. Several studies suggest that ANG, as angiogenic factor, supports tumour growth, driving the new vessels formation whereby supplies oxygen and nutrients to the growing mass, but

also enhances the malignant cell migration and invasion thereby allowing for the metastasis formation [310, 311]. Cancer cells under suboptimal growth condition, indeed, release stress responsive proteins like ANG, which through the ubiquitination-mediated inactivation of p53 factor, can promote cell survival and proliferation [312]. In accord, increased levels of ANG has been detected, under hypoxic condition, in human malignant melanoma [313] and cervical cancer cell [314] growth media. Moreover, available data showed that the unleashed ANG, by glioblastoma cells, enhances the tube-like structure formation by endothelial cells [284], whereas the high level of ANG, in prostate cancer microenvironment, stimulates the malignant prostate fibroblasts migration and invasion [315]. Therefore, mastocytes, which are immune cells surrounding some solid tumours, are able to release ANG, thus prompting the angiogenesis cascade [316]. Besides ANG, acting also as immune suppression agent, may promote tumorigenesis by inhibiting the immune system function.

Such a findings highlight the close relationship between ANG and tumorigenesis process and may suggest its role as biomarker for the tumour progression and recurrence [317]. Accordingly, cohort studies revealed that patients with high serum levels of ANG are associated with aggressive form of cancer and poor prognosis [318].

1.3.5.4 The role of copper in physiological and pathological angiogenesis

Copper is an essential element in both human and animals and is crucial to the health of living organisms [319]. Several research works highlighted the distinctive biological role of copper ions in both neuronal and endothelial tissues that, despite the different biological structure, share

similar signalling pathways [320]. In the neuronal system, copper ions seem to play a pivotal role in post-synaptic transmission and its dyshomeostasis is involved in the aetiology of numerous neurologic disorders, such as ALS, prion encephalopathies, PD and Alzheimer's disease [321]. As to the interaction with the endothelial system, copper has been recognized as angiogenic factor. In accord, literature data demonstrated that copper ions are able to stimulate endothelial cell migration [322] and neovascularization in avascular rabbit corneas [323, 324], while its depletion, by Cu-chelators, such as penicillamine and trientine, *in vivo*, prevents the vessels formation [325]. Such an intersection between copper and angiogenesis supports the critical role of the metal in pathological and physiological angiogenic processes, such as cancer and wound repair. Accordingly, increased serum levels of copper have been found in patients with different types of tumours like brain cancer (157.88 μg/dL vs. 98.8 μg/dL for control patients [326]) and breast cancer (167.3 μg/dL vs. 98.8 μg/dL for control patients [327]), and have been connected to the tumour onset and progression [328]. Based on these findings, copper chelation therapies have been developed for cancer treatment and have proven their efficacy in the tumour regression [329]. On the other hand, the local modulation of copper pro-angiogenic effect provides a promising strategy to enhance tissue repair and regeneration [330] since, as expected, a higher concentration of copper ions (~ 30 μM) has been detected in the injured site with respect to the peri-wound areas [331].

1.3.5.5 Copper promotion of new vessels growth

The mechanism behind the pro-angiogenic activity of copper is the activation and amplification of the angiogenic response triggered by several cytokines and proteins including VEGF, FGF, and ANG, through a multiple action.

The intracellular uptake of copper ions, the efflux as well their trafficking within the cytoplasmic matrix are highly controlled by a complex proteins network, since copper shows a reactive nature, which could lead to severe oxidative damages, as long as the free cytosolic copper concentration exceeds the bio-recommended levels (10^{-18} M) [332]. Copper, indeed, can exist either in the reduced state, Cu^{+}, which shows a high affinity for the thiol and thioether groups of the proteins, or in the oxidized state, Cu^{2+}, which particularly binds to oxygen atoms and imidazole nitrogen. Although its double nature allows copper to interact with several proteins, thus controlling numerous biochemical processes, the passage between the two states, Cu^{+} and Cu^{2+}, can generate hydroxyl radicals [333].

Copper enters the cell through the copper transporters 1 and 2 (CTR1 and CTR2), which are membrane homotrimeric proteins with a channel-like structure, widely present in several cell types and tissues [334]. Before its transfer, to ensure an efficient transport across the cell membrane, Cu^{2+} is reduced to Cu^{+}, by membrane metal-reductases [335] and within the cell, the copper distribution to mitochondrial, nuclear and vesicular targets is mediated by several metal-chaperones, namely, glutathione (GSH), Menkes protein, copper chaperone for superoxide dismutase (SOD) and antioxidant-1 (ATOX-1) [336].

During the early stages of angiogenesis, the intracellular copper has been demonstrated to stabilize the hypoxia inducible factor-1 (HIF-1) structure, thereby promoting its transcriptional activity on angiogenic genes including VEGF and ceruloplasmin genes [337]. Ceruloplasmin, indeed, is a serum globulin protein which, by binding to copper ions, stimulates neovascularization, whereas its copper-deprived form is unable to induce blood vessels formation [324]. As to the VEGF, experiments on cultured human cardiomyocytes showed that copper ions, at the concentration of 5 μM, stimulate insulin-like growth factor-1 (IGF-1)-induced VEGF expression [338]. Moreover, copper ions have been found to promote vasodilation by activating the endothelial nitric oxide synthase enzyme (eNOS) and the nitric oxide (NO) release. In this regard, several studies suggest that the extracellular Cu^{2+} promotes transmembrane calcium ions influx, increasing the concentration of intracellular Ca^{2+} ions that via the calcium-calmodulin pathway, enhance the eNOS activity [339]. On the other hand, the intracellular copper, as cofactor of the cuproenzyme SOD, protects NO from the superoxide anion scavenging, thus increasing its half-life [340]. Furthermore, copper complexes of the fibroblast growth factor 1 (FGF-1) and the lysyl oxidase (LOX) [341], stimulate FGF secretion [342] and ECM degradation, respectively, thus promoting cell migration and proliferation. It is important to note that the copper-induced angiogenic effects are highly cell-type specific, since it has been demonstrated that copper ions are able to enhance proliferation of endothelial cells, while, at the same condition, no stimulating effects are shown on arterial smooth muscle cells and rather fewer effects are measured on cultured fibroblasts [343].

1.3.5.6 Copper modulates ANG activity

Copper ions amplify and promote vascular permeabilization as well as endothelial cells migration and proliferation by binding to several factors involved in the angiogenic process. Among the pro-angiogenic effectors, it has been found that copper controls and modulates the angiogenic response and the biological function of ANG [344]. Previous works reported that the complex formation between divalent copper and ANG decreases both the nuclear translocation of the protein and its ribonucleolytic activity [267]. Moreover, the interaction between ANG and calf pulmonary artery endothelial cells increases 4.3 fold, in the presence of copper ions [345].

The ANG-copper complex formation, the metal coordination environment as well as the copper-induced effect on ANG, mostly depend on the chemical structure of the protein and angiogenin, in particular, shows two different forms, the recombinant and the wild type. The recombinant form of ANG (rANG), expressed into bacterial vectors and typically used for research works, contains an extra methionine residue at the N-terminal domain. Differently, the wild-type angiogenin (wtANG), physiologically presents in human plasma, shows the glutamine, as the first residue, which spontaneously cyclized to a pyroglutamate ring. A recent research work showed that rANG and wtANG share a similar secondary structure rich in β-strands, but a different metal binding. Circular dichroism (CD) and electrospray ionization mass spectrometry (ESI-MS) experiments, indeed, suggest a 2:1 metal to ligand stoichiometry of the metal-protein complex for rANG while, a 1:1 metal to ligand stoichiometry for the copper-complex of wtANG, at physiological pH [346]. Furthermore, spectroscopic data revealed a strong ligand field

around the metal core of the rANG-Cu(II) complex, which involves 4 nitrogen donors in a planar arrangement [345]. Whereas, a low ligand field seems to characterize the wtANG-Cu(II) complex, which most likely involves two imidazole nitrogen atoms, one deprotonated nitrogen and one oxygen atom [346]. Further NMR measures, allowed to identify, at physiological pH, the N-terminal group of the methionine, the deprotonated amide nitrogen of Glu-1 and Asp-2 and the imidazole nitrogen of the His-8 residues in the coordination environment of the rANG-Cu(II) complex. On the other hand, His-114 and His-13, which also form the catalytic site of ANG, are the metal anchoring sites for the wtANG-Cu(II) complex formation (Figure 11). Accordingly, copper ions more efficiently influence the physiological form of ANG, with respect to the recombinant angiogenin, since the metal-protein complex involves its catalytic site. In this regard, in vitro experiments of capillary-like tube formation and the RNAase enzymatic assay evidenced that divalent copper decreases the activity of both the two proteins, but a higher concentration of Cu^{2+} is required for the rANG sample, to reach the same decrease of both tube formation and enzymatic action observed for wtANG [346].

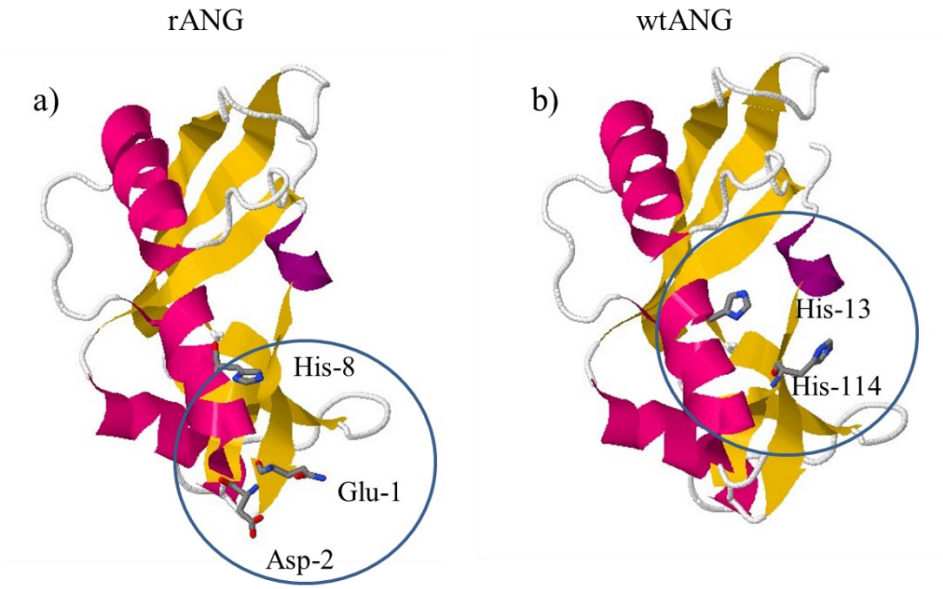

Figure 11- Putative anchor site of Cu^{2+} in a) rANG and b) wtANG copper complexes (PDB ID 1ANG).

Chapter 2- Synthesis and physicochemical characterization of nanomaterials

2.1 Synthesis and physicochemical characterization of AuNPs

Gold nanoparticles (AuNPs) were synthesized following the method pioneered by J. Turkevich, which uses the chemical reduction reaction of chloroauric acid by the action of trisodium citrate, that acts both as reducing agent and capping agent [347]. The chloroauric acid reduction reaction can be written as follows:

$$2AuCl_4^- + C_6H_5O_7^{-3} + 2H_2O \xrightarrow{100\ ^\circ C} 3\ CH_3O + 3CO_2 + 8Cl^- + 3\ H^+$$

The synthesis was carried out as follows. 20 µL of 1 M gold(III) chloride dihydrate solution were diluted in 20 mL of ultrapure MilliQ water in a 50 mL glass beaker at the final concentration of 1 mM. The solution was brought at the boiling point on a hot plate, under stirring and 2 mL of 1% (w/v) trisodium citrate dihydrate solution were quickly added to the final concentration of 3.08 mM citrate (Au^{3+}/citrate molar ratio of 1:3). As soon as the colour turned from yellow to deep red, AuNPs were formed and the beaker was removed from the hot plate (Figure 12).

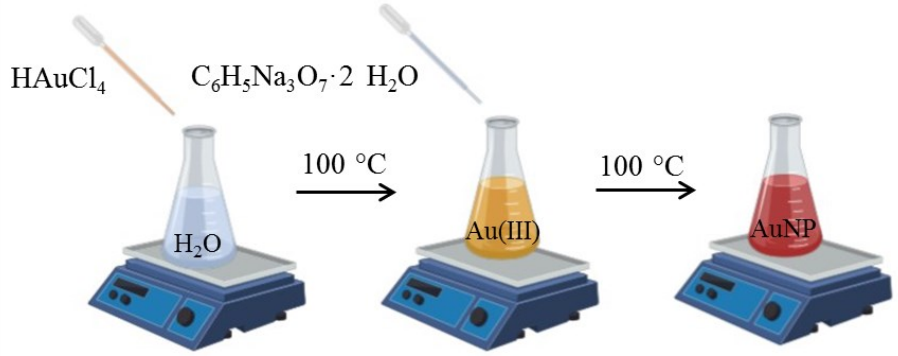

Figure 12- Graphic representation of the AuNPs preparation.

Such a synthetic method produces small particles with a diameter of ~12 nm and a plasmonic peak centred at 520 nm [348, 349]. By assuming the complete reduction of Au^{3+} from the chloroauric acid to Au^0, the calculated concentration of gold nanoparticles is expected to 19 nM (corresponding to $2.1 \cdot 10^8$ NP/mL [336]). The actual concentration of about 13 nM AuNPs ($9.5 \cdot 10^7$ NP/mL [350]) is determined by the UV–visible spectra using the Lambert-Beer equation (eqn. 7) (see table 2):

$$c = \frac{A}{\varepsilon \cdot b} \tag{7}$$

where c is the M concentration, ε is the extinction coefficient in $M^{-1}cm^{-1}$, b is the optical path length and A is the maximum of absorbance of the plasmon peak. As to the extinction coefficient value, it is determined using the following eqn. 8 [351]:

$$\varepsilon_{gold} = A d_{opt.}{}^{\gamma} \tag{8}$$

where A and γ are constants ($d \leq 85\ nm$: $A = 4.7 \cdot 10^4$, $\gamma = 3.30$; $d \geq 85\ nm$: $A = 1.6 \cdot 10^8$, $\gamma = 1.47$) and $d_{opt.}$ is the optical diameter of the nanoparticles (14 nm) calculated from the wavelength of maximum absorbance, λ_{max}, of the plasmon peak, according to the eqn.4 (see section 1.3.3.1) [187].

The resultant nanoparticles were washed with 1 mM 3-(N-morpholino) propanesulfonic acid (MOPS) buffer (pH=7.4) using two centrifugation steps (15 min, 6,010 RCF), in order to remove the excess of sodium citrate from the nanoparticles dispersion and to concentrate the nanosystems (Figure 13).

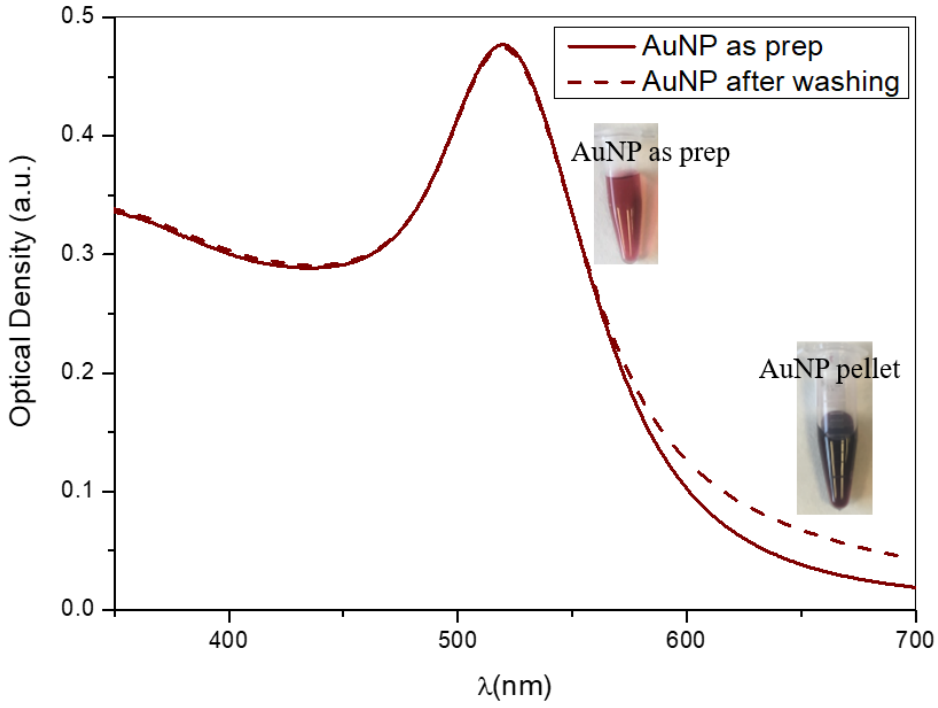

Figure 13- UV-vis spectra of citrate-capped bare nanoparticles (AuNP) as prepared in MilliQ water (13.4 nM, $9.5 \cdot 10^7$ NP/mL) and of the pellet (53.6 nM,

$3.8 \cdot 10^8$ NP/mL) (dashed curves) obtained after the two washing steps (6,010 RCF for 15 min) in 1 mM MOPS (pH=7.4).

The synthetized citrate-capped AuNPs show the distinctive plasmon peak centred at 520 nm of wavelength, with a full width at half maximum (FWHM), which is the parameter related to size distribution and polydispersity index [352] (see Figure 14), of about 50 nm. These findings are in agreement with the optical response of monodisperse (uniform in shape and size) spherical gold nanoparticles with a diameter of 14 nm [187, 353].

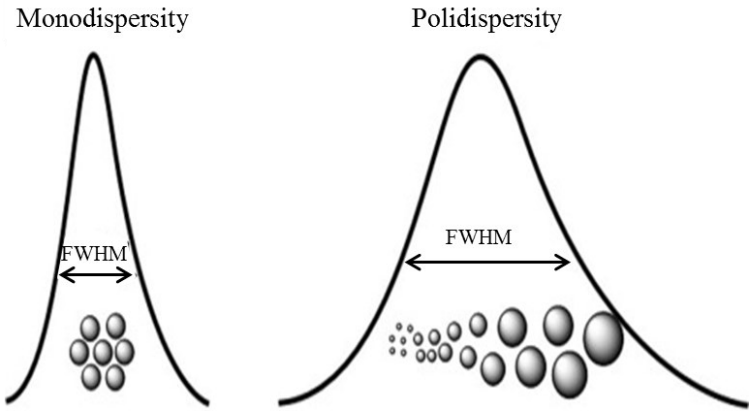

Figure 14- Absorption spectra of gold nanoparticles with different dispersity. Low values of FWHM indicates monodispersity, while higher values are indicative of polydispersity of the colloidal suspension. *Modified from J. Oliveira et al. Arab. J. Chem., 2017.*

As to the pellets, no significant changes can be observed for the washed and concentrated AuNPs with respect to the as prepared AuNPs, since both the wavelength at the maximum absorbance of the plasmon peak and the FWHM continue to maintain similar values of 520 nm and 50 nm, respectively (see table 2). This result highlights that no aggregation effect

occurs upon the washing procedure and that the re-suspended gold nanoparticle pellet preserves its stability and monodispersity.

Dynamic light scattering (DLS) measurements were carried out on both the as prepared AuNPs and the AuNPs pellet to assess the hydrodynamic sizes of the particles, taking into account not only the particle metallic "core" but also the solvation shell on the nanoparticles surface, as well as aggregation effect and dispersion stability before and after the washing procedure. As expected from the UV-vis data, the hydrodynamic diameter ($d_{hydrod.}$) for the aqueous dispersion of AuNPs ($9.5 \cdot 10^7$ NP/mL) is 29.3 ± 3 nm and not significantly changes for the obtained AuNP pellet ($3.8 \cdot 10^8$ NP/mL) that shows an hydrodynamic size of 30.4 ± 2 nm (Table 2).

Table 2- Optical properties: maximum of absorption (A_{max}), wavelength at the absorbance maximum (λ_{max}), extinction coefficient (ε), full width at half maximum (FWHM) value as well as the calculated optical diameters and the nanoparticles concentration in both nM and NP/mL for the as prepared AuNP in MilliQ water and the re-suspended pellet in 1 mM MOPS. Hydrodynamic size ($d_{hydrod.}$) .measured by DLS.

Sample	**A_{max}**	**λ_{max} (nm)**	**ε ($cm^{-1}M^{-1}$)**	**FWHM (nm)**	**d_{opt}**	**$d_{hydrod.}$ ±SD (nm)**	**[nM]**	**[NP/mL]**
AuNP as prep	0.477	520	$2.8 \cdot 10^8$	50	14	29.3 ± 3	13.4	$9.5 \cdot 10^7$
AuNP pellet	0.305	520	$2.8 \cdot 10^8$	50	14	30.4 ± 2	53.6	$3.8 \cdot 10^8$

AFM analysis in AC mode, in air, carried out on the synthetized citrate-capped AuNPs deposited on mica surface and the obtained height histograms (Z-scale), in agreement with the UV-vis parameter discussed

above, indicates that the maximum Z-averaged value (nanoparticle height) for the bare AuNPs core is 12 ± 2 nm (Figure 15).

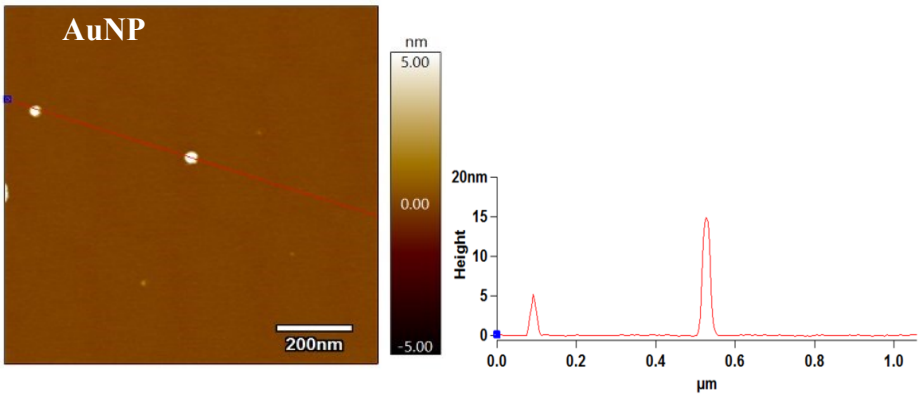

Figure 15- Atomic force microscopy micrographs of bare and washed AuNP, scale bar = 200 nm. The graphs on the right shows the section analysis plot corresponding to the drown line.

2.2 Synthesis and physicochemical characterization of Au-GO hybrid nanosystems (PAPER IV)

Au-GO hybrid nanosystems were prepared by chemical reduction of the chloroauric acid with trisodium citrate in the presence of GO aqueous dispersion as follows. The GO aqueous dispersion (4 mg/mL, Graphenea) was firstly diluted in MilliQ water (18.2 MΩ·cm resistivity at 25°C) at a final concentration of 0.4 mg/mL and then ultra-sonicated with a titanium cup-horn sonicator (Hielscher UP200Ht) at 200 W and 24 kHz in order to obtain laterally homogeneous nanosheets with a lateral size of about 200 nm. To separate the nanosheets, with a sub-micron size, from the bulky large sheets, samples were centrifuged at 17,949 RCF for 20 min and the concentration of GO into the collected supernatant, typically of around 0.3 mg/mL, was estimated by the UV–visible spectra [354]. For the synthesis of the hybrids Au-GO, 20 mL of gold(III) chloride di-hydrate solution (1 mM) in MilliQ water were brought to boil, under stirring, on a magnetic hot-plate. In the meanwhile, 1% (w/v) of trisodium citrate dihydrate was dissolved in 2 mL of the previously ultra-sonicated GO dispersion (0.3 mg/mL) and quickly added to the auric solution, under vigorous stirring, until the wine-red colour was observed (Figure 16).

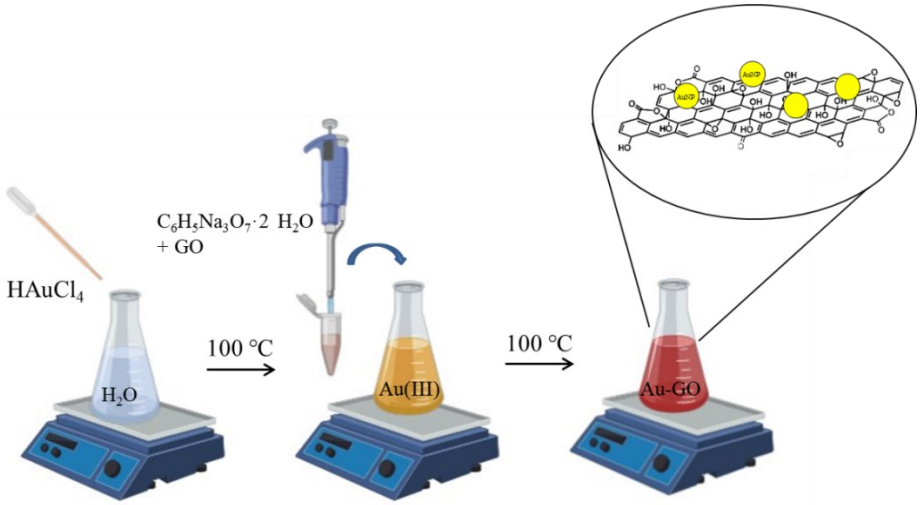

Figure 16- Graphic representation of the Au-GO hybrids preparation.

Finally, to remove the excess of reactants and the unbound or weakly bound GO-sheets, the synthetized hybrid systems were washed with MilliQ water twice by centrifuging at 6,010 RCF for 15 minutes.

UV-visible spectroscopy was used to study the characteristic optical properties of the hybrids Au-GO. Figure 17 shows two spectra for each sample (AuNP, Au-GO, GO) corresponding to the as prepared dispersions and the re-suspended pellets. GO shows a maximum absorption peak centred at 230 nm attributed to π–π* transitions of aromatic C=C bonds and a shoulder peak at about 300 nm attributed to *n*–π* transitions of C=O bonds [355]. On the other hand, AuNPs, as described above, present a plasmon peak centred at 520 nm, typical of 14 nm spherical gold nanoparticles [349]. The plasmonic response of AuNPs is very sensitive to the local environment, since variation of the dielectric properties of the surrounding medium as well as the adsorption of molecules on the particle

surface, providing new relaxation pathways to the free electrons on the metal nanosystems, modifies the SPR peak in its absorbance maximum, width as well as intensity [189, 356]. Such a variation of the plasmonic band gives information on the molecular layer adsorbed on the particle surface and provides novel applications in the field of bio-sensing, imaging and spectroscopy [357]. Accordingly, the UV-vis spectrum of the hybrid system Au-GO (see Figure 17) shows a red-shifted plasmon band centred at 525 nm, indicative of variation in the near environment of the gold nanoparticles, thereby revealing an effective interaction between AuNPs and GO nanosheets (see table 3). Moreover, an increase of the absorption at around 230 nm associated with the π–π* transition of GO can be observed for the hybrid Au-GO.

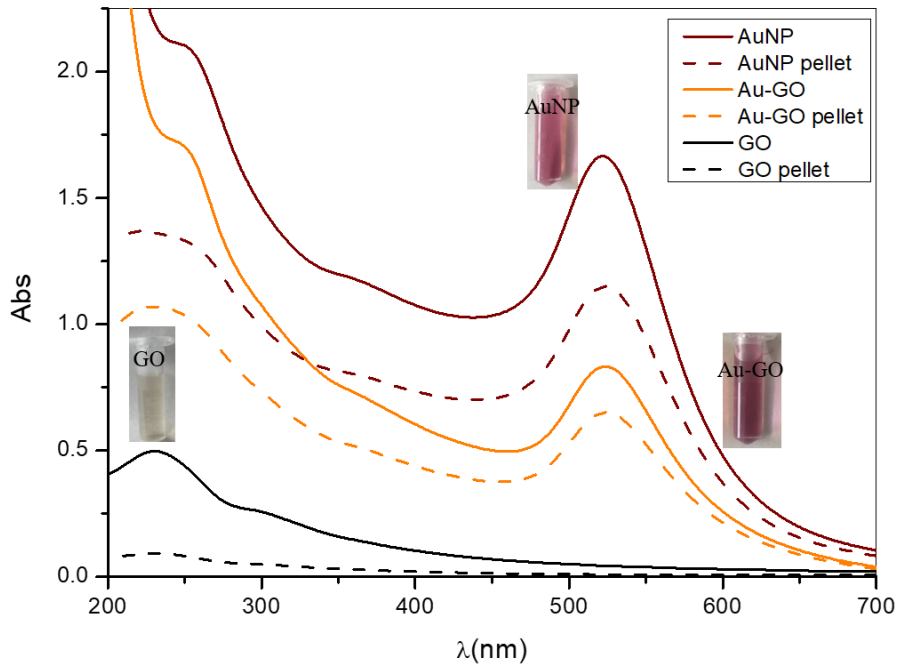

Figure 17- UV-visible spectra of the as prepared AuNPs (wine), Au-GO (orange) and of the pellets (dashed line) obtained after two rinsing steps in MilliQ water

(centrifugation at 6,010 RCF, 15 min). Spectra of GO (black) and of the pellet (dashed line) obtained after two rinsing steps in MilliQ water (17,949 RCF, 20 min).

The washing steps do not affect the particle size and no aggregation processes are evidenced owing also to the GO sheets which further act as stabiliser of the colloidal dispersion. Thus, only a minimal band broadening of about 3 nm is measured for the obtained Au-GO pellet. The characteristic UV-vis parameters for the synthetized systems before and after the centrifugation steps, the optical diameter and the hydrodynamic size measured by DLS are shown in Table 3.

Table 3- Optical properties: maximum of absorption (A_{max}), wavelength at the absorbance maximum (λ_{max}), extinction coefficient (ε), full width at half maximum (FWHM) value as well as the calculated optical diameters and the nanoparticles concentration in both nM and NP/mL and the GO concentrations for the as prepared Au-GO and the re-suspended pellet in in MilliQ. Hydrodynamic size ($d_{hydrod.}$) measured by DLS.

Sample	**A_{max}**	**λ_{max} (nm)**	**ε ($cm^{-1}M^{-1}$)**	**FWHM (nm)**	**d_{opt}**	**$d_{hydrod.}$ ±SD (nm)**	**[AuNP] nM**	**[AuNP] NP/mL**	**[GO] mg/mL**
Au-GO as prep	0.833	525	$2.5 \cdot 10^9$	50	27	-	0.7	$6.9 \cdot 10^5$	0.03
Au-GO pellet	0.651	525	$2.5 \cdot 10^9$	53	27	100 ± 14.4	5.2	$5.2 \cdot 10^6$	0.07

Figure 18 shows the Au-GO subtracted spectrum by the spectrum of the AuNPs, which definitely points out the charge transfer process in the gold core-GO shell nanostructure thus demonstrating the effective AuNPs-GO

interaction. The subtraction spectra (dotted line), indeed, show an increase of the signal at 300 nm and a red shift of peak at 230 nm of about 9 nm, indicative of the interaction of the metal surface and the GO sheets, that affects the conjugation of the electrons in the GO backbone [358]. Moreover, the subtracted spectrum, by considering the value of absorbance at 230 nm for GO, A_{230nm}=0.259, and the molar extinction coefficient ε = 37.81 ± 0.06 mL/mg·cm in MilliQ water, allows to calculate the amount of GO surrounding the gold nanoparticles, which is around $6.8 \cdot 10^{-2}$ mg/mL (see table 3).

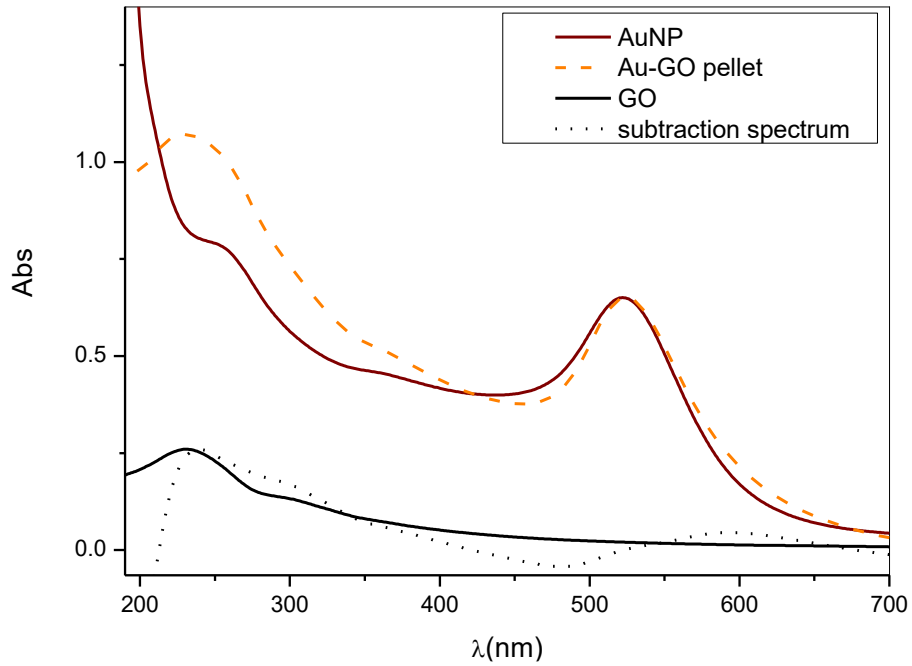

Figure 18- UV-vis spectra of AuNP (wine), Au-GO pellet (orange), GO (black) and of the GO calculated from the difference spectrum (Au-GO)-AuNP (dotted line).

AFM images of the hybrid Au-GO and the GO adsorbed on mica, recorded AC mode in air give evidence of the hybrid Au-GO formation (Figure 19). Spherical particles with a maximum Z-averaged value of around 20 nm are found associated with the GO single sheets, which show a dimension of around 1 nm in thickness and 300-400 nm in lateral size. Noteworthy a preferential position of the AuNPs in the basal plane of the GO layer can be noted.

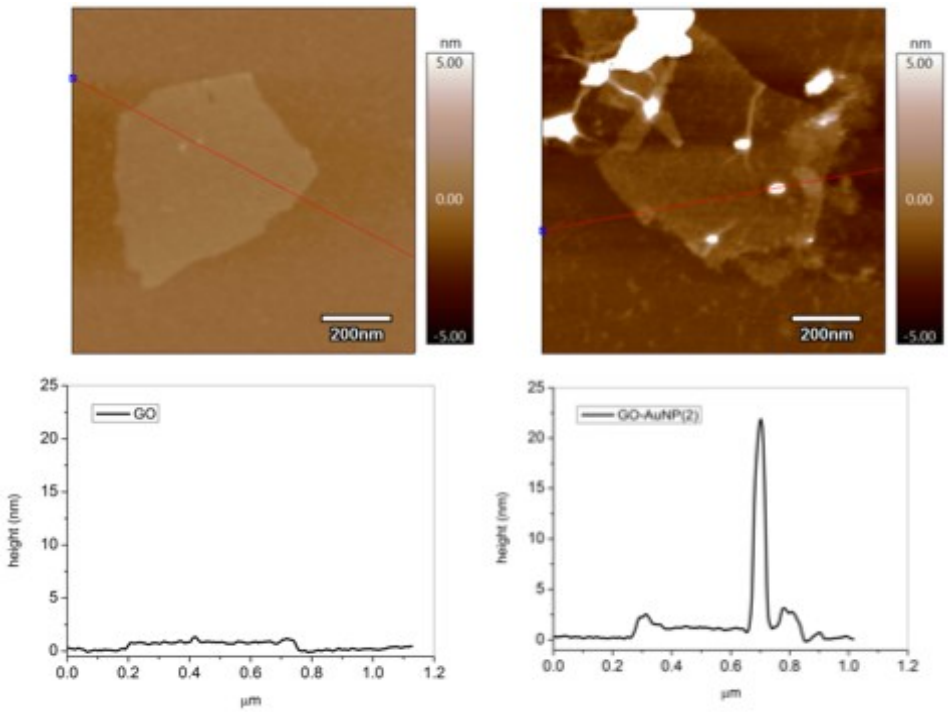

Figure 19- Atomic force microscopy micrographs of GO (left) and the hybrid Au-GO (right), scale bar = 200 nm. The graphs below each image show the section analysis plot corresponding to the drown line.

2.3 ANG fragment mimicking peptides and Cu(II) complex formation

The use of proteins as therapeutic agents is often associated with the induction of unnatural immune response and side effects [359]. To this respect a peptide sequence mimicking the biological activity of a protein, overcomes the limits related to the whole molecule, giving also the advantages of enhanced pharmacokinetic properties, increased receptor specificity and affinity as well as low cost [360, 361]. Based on these premises, we used the peptide-mimetic approach to promote the angiogenic process elicited by ANG. In particular, we inspected the sequence 60-NKNGNPHREN-68 of the protein, identified as a part of the endothelial cell receptor binding site and that is further involved in the cytoskeletal actin-binding, which is another crucial step for the angiogenesis promotion.

We used three different variants of the 60-68 sequence: the simple $Ang_{60–68}$ (Ac-KNGNPHSEN-NH_2); the analogous fluorescent peptide Fam-Ang_{60-68}, labelled with the 5,6-carboxyfluorescein unit (Fam) to inspect steric hindrance and charge effects; the analogous Ang_{60-68}Cys peptide with an additional cysteine residue at the N-terminal domain, which strongly binds to the metal surface, through Au-S bonds.

The fragment $Ang_{60-68,}$ including the amino acid sequence Ac-KNGNPHSEN-NH_2 (molecular weight, MW, of 1,105.5 g/mol, isoelectric point, PI, of 11.38), modified by N-terminal acetylation and the C-terminal amidation, was assembled by using the solid phase peptide synthesis strategy, on a Biotage initiator+ Alstra^{TM} fully automated microwave peptide synthesizer. Whereas, the fluorescent peptide, carboxyfluorescein-KNGNPHREN-NH_2 (Fam-Ang_{60-68}) and the peptides

Ac-KNGNPHRENC-NH_2 (Ang_{60-68}Cys) were purchased from CASLO (Lyngby,Denmark).

As discussed in section 1.3.4.6, ANG binds to copper ions and the copper complex formation affect the biological function of the protein by increasing both its expression and interaction with endothelial cells [346]. Previous work reported that the studied sequence 60-68 is one of the probable protein domain involved in the copper-binding and that the metal coordination could affect the whole Ang_{60-68} conformation [362]. However, if the cysteine residue in the Ang_{60-68}Cys peptide does not dramatically change the 60-68 sequence conformation and chemical structure, the introduction of the carboxyfluorescein moiety on the Fam-Ang_{60-68} peptide, owing to the steric hindrance and the charge effect, could change the copper-binding affinity and metal coordination environment changing also its biological properties. Hence, the copper complex species with the peptide encompassing the ANG sequence 60-68 was scrutinized by Circular Dichroism (CD) spectroscopy, in comparison with the Fam-Ang_{60-68} peptide, to assess the potential role of the Fam moiety on the Cu(II)-complex formation (Figure 20).

The Ang_{60-68} and Fam-Ang_{60-68} copper(II) complexes were studied under physiological condition (pH = 7.4) and basic condition (pH = 10.5).

As previously reported, at pH = 7.4, the copper(II) complex of Ang_{60-68} involves a bis-deprotonated species [$Cu(LH_{-2})H$] and the coordination environment includes one imidazole and two amide deprotonated nitrogen atoms [362]. Figure 20 shows in black the CD spectrum of the copper(II) complex of Ang_{60-68} obtained under physiological conditions. The spectrum displays a visible negative band, due to the copper d-d transitions, at the wavelength of 600 nm and a positive band at 338 nm due

to the $N^{-}\rightarrow Cu^{2+}$ energy transfer. At the same condition, the CD spectrum of the complex Fam-Ang_{60-68}-Cu(II) clearly shows a negative band at 600 nm (Figure 22b), even though the signal is highly noisy owing to the Fam moiety at the used concentration of 10^{-3} M in MilliQ water.

As to the basic condition (pH = 10.5), in red, it is shown, for both the peptides-Cu(II) complexes, an intensification of the $N^{-}\rightarrow Cu^{2+}$ charge transfer band at around 312 nm, thus indicating the involvement, in the metal binding environment, of a further deprotonated amide nitrogen atom, representative of a 4N coordination mode ($3N^{-},1N_{Im}$) [362]. Moreover, the CD spectrum of the Ang_{60-68}-Cu(II) complex shows a negative band at 495 nm and a positive band at 596 nm that are also clearly visible in the copper(II) complex with Fam-Ang_{60-68} (Figure 20 a-b).

As a results, the spectra referred to the Ang_{60-68}-Cu(II) complex in comparison with the spectra obtained for the Fam-Ang_{60-68}-Cu(II) complex seems to not display significant differences thereby confirming that the carboxyfluorescein moiety of Fam-Ang_{60-68} doesn't perturb the coordination environment of Cu(II) and most likely its biological behaviour.

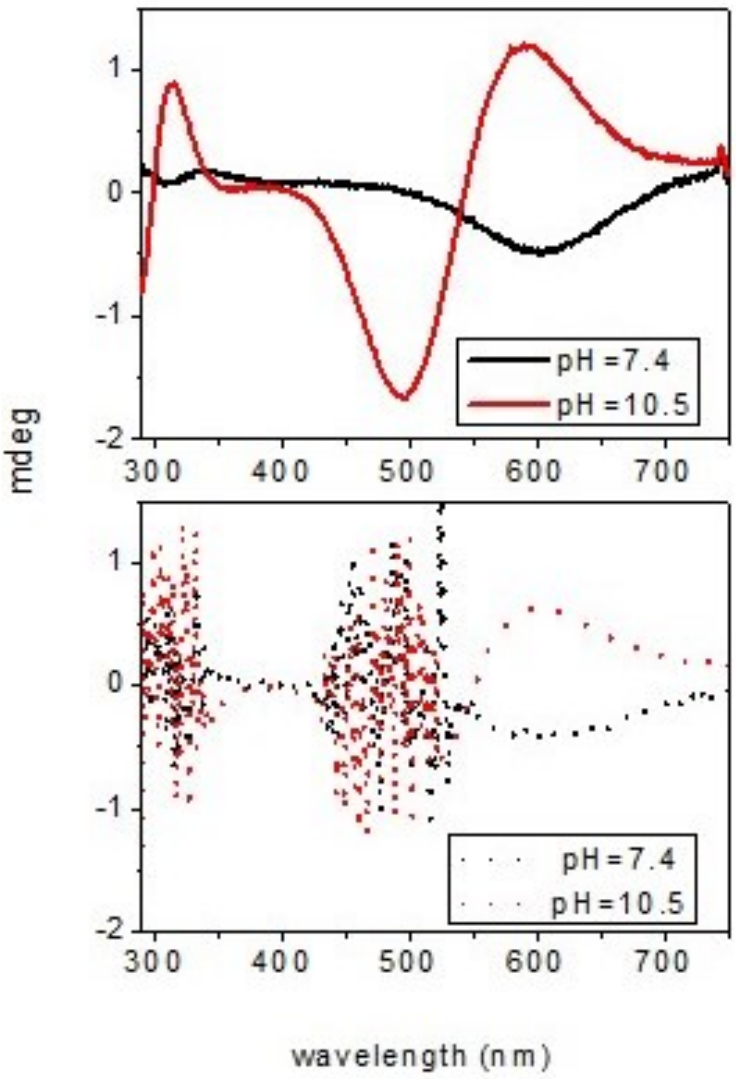

Figure 20- CD spectra of a) Ang_{60-68}-Cu(II) and b) Fam-Ang_{60-68}- Cu(II) recorded in MilliQ with 1:1 metal to ligand molar ratio at the peptide concentration of 10^{-3} M, under physiological condition (pH = 7.4) in black and basic condition (pH = 10.5) in red.

2.4 Expression and purification of human angiogenin (rANG and wtANG)

The human ANG expression was carried out following the method reported by Holloway et al. [363]. Briefly, the *E. Coli* (BL21(DE3)) expression strain was cultured at 37°C under shaking (180 r.p.m.) in 5 mL of terrific broth (12 g peptone, 24 g granulated yeast extract, 4 mL glycerol 87%, 900 mL of MilliQ water) supplemented with ampicillin (100 μg/mL). After 24 hrs of incubation the whole volume of the bacterial culture was inoculated in 1000 mL of fresh broth. When the density of the culture had reached the $OD_{600\ nm}$ value of 0.8, the ANG expression was induced by the addition of 1 mM isopropyl β-D-1-thiogalactopyranoside (IPTG) and the incubation was continued for additional 2 hrs. Afterwards, the cell culture was harvested by centrifugation (4,000 RCF for 15 min at 4°C, JLA 8,100) and cells were lysed with 30 mL of lysis buffer (50 mM Tris-HCl, 2 mM EDTA, pH = 8) by using the high-pressure homogenizer (Emulsiflex) and a sonication step (Qsonica Sonicator Q700). Lysate was, then, centrifuged (20,000 RCF for 40 min at 4°C, JA25.50) and the pellet was re-suspended in 25 mL of lysis buffer supplemented with 1% (v/v) Triton X-100. Sonication and centrifugation steps were repeated twice and the final pellet was dissolved in 30 mL of denaturation buffer (0.24 M guanidine hydrochloride (GdnHCl), 100 mM Tris-HCl, 1 mM ethylenediaminetetraacetic acid (EDTA), 4 mM NaCl, 0.4 mM 1,4-dithiothreitol (DTT)).

The expressed recombinant angiogenin (rANG) was refolded from inclusion bodies according to the procedure described by Jang et al. (2004) [364] and then purified by a cation exchange chromatography performed on an automated chromatographic workstation (Akta prime, GE

Healthcare) equipped with a 15 x 1.6 cm column packed with SP Sepharose Fast Flow (GE Healthcare). After a washing step with 25 mM Tris-HCl (pH = 8.0), rAng was eluted with 25 mM Tris-HCl, 1 M NaCl (pH = 8.0) buffer solution. To obtain wild-type angiogenin (wtANG), rANG was incubated with 1 nM *Aeromonas* aminopeptidase, at the concentration of $1 \cdot 10^{-5}$ M in 200 mM potassium phosphate buffer (pH = 7.2) (overnight at 37 °C under gentle shaking). This procedure allows for the specific removal of the N-terminal methionine residue (Met(-1)) in the primary sequence of rANG, thus obtaining the N-terminal glutamine residue (Glu1) that spontaneously cyclises to the pyroglutamate residue (PyrGlu1) that is characteristic of 'native' wtANG.

The reaction mixture was purified by dialysis (Spectra/por MWCO 6–8000 Da), which replaces PBS with 25 mM Tris-HCl (pH 7.4) buffer solution, followed by cation-exchange chromatography.

The native folding of wtANG was evaluated by testing the ribonucleolytic activity of the protein, according to the procedure reported by Shapiro et al. 1987, by measuring the production of perchloric-acid soluble fragments (Abs = 262 nm) from tRNA molecules induced by wtANG, at increasing concentration. [259]. As expected, the RNase activity of wtANG increases with the concentration of the protein, thus demonstrating that the conditions of expression and purification of wtANG do not influence the biological activity of the protein (Figure 21).

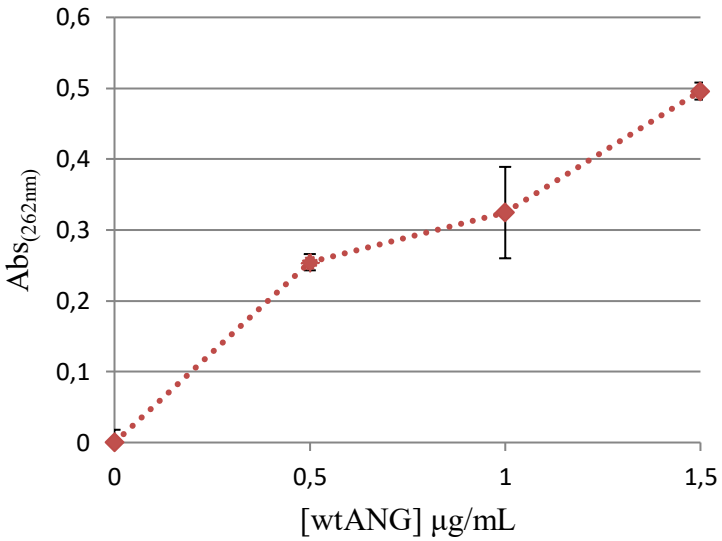

Figure 21- Ribonucleolytic activity of wtANG. Assay was performed at increasing protein concentration (0.5, 1, 1.5 µg/mL), in 33 mM MOPS buffer, at 37 °C for 2 hrs, with the addition of $6 \cdot 10^2$ µg/mL tRNA. Averaged values and standard deviation from three experiments.

To assess the purity of the protein sample and to evaluate the presence of dimers, that could influence the biological activity and the stability of wtANG [365, 366], sodium dodecyl sulphate polyacrylamide gel electrophoresis (SDS-PAGE) (Mini-PROTEAN TGX Precast gel, 4-20%, 15-well, BioRad) was carried out using both the native wtANG (without the addition of β-mercaptoethanol as reducing agent) and the reduced protein (wtANG + red, in the presence of 355 mM β-mercaptoethanol), respectively. In agreement with the enzymatic assay result, the SDS-PAGE clearly shows a strong band at around 14 kDa, under both reducing or not reducing condition, corresponding to wtANG (14.2 kDa), while no

other signals attributed to the presence sub-cellular products or dimers were found (Figure 22).

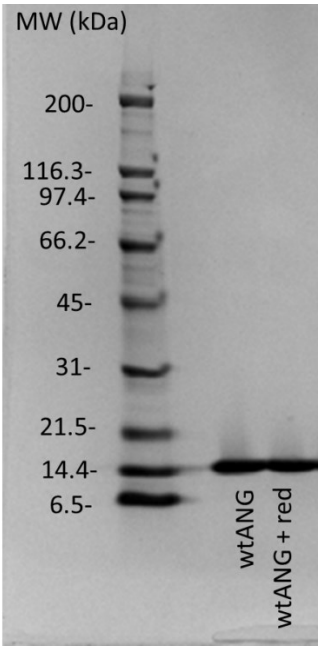

Figure 22- SDS-PAGE of the purified wtANG electrophoresed through a pre-cast 4-20% polyacrylamide gel under denaturing and both native and reducing (355 mM β-mercaptoethanol addition) conditions prior to staining with Coomassie brilliant blue R-250.

2.5 Site-directed mutagenesis of ANG: expression of the mutant S28CANG

Angiogenin is a member of the pyrimidine-specific pancreatic ribonuclease superfamily and boasts a specific ribonucleolytic activity [367].

The integrity of both its catalytic site, involving the residues His13, Lys40 and His114, and the receptor-binding domain (sequence 60-68) are required for the biological activity of the protein [293], which is also regulated by the interaction with copper ions [267].

In this work, a new variant of angiogenin, named S28CANG, with a cysteine instead of the serine at the residue 28, was expressed and purified for the high affinity binding to the gold nanoparticles surface through Au-S bonds. To this purpose, the serine 28 is an ideal residue for the cysteine substitution, since it is placed on the surface of the protein (Figure 23) and out of its active site pocket, thus the single point mutation at the serine permits to maintain the biological acvity of ANG as well as allows for a predominant covalent grafting of the protein onto the surface of the metal nanoparticle.

Moreover, serine and cysteine present a similar chemical structure and a comparable side-chain volume, since they differ only at the γ atom, namely oxygen for the serine and sulphur for the cysteine, respectively.

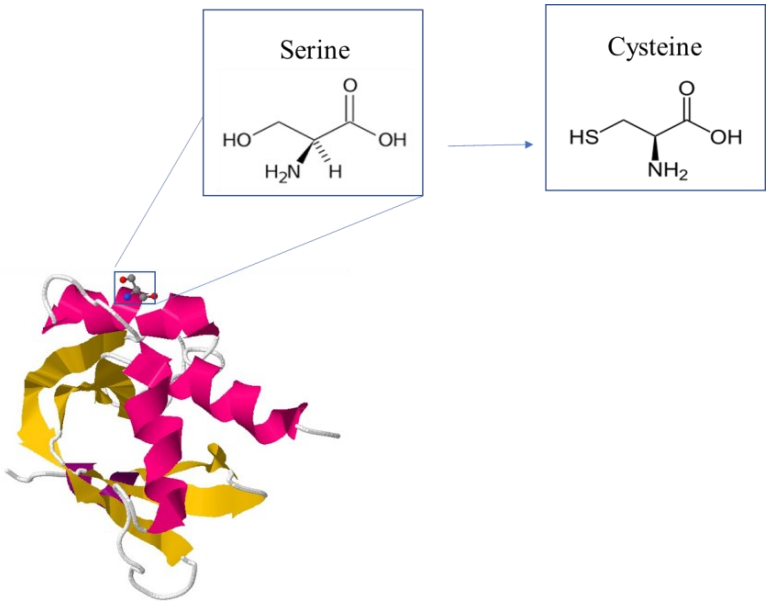

Figure 23- 3D-structure of human angiogenin ANG showing the serine 28 residue replaced with the cysteine in the mutant S28CANG protein.

To introduce the substitution in the ANG gene, the QuickChange Lightning site-directed mutagenesis kit was used. A pair of oligonucleotide primers (forward and reverse), homologous to the template DNA, were accurately designed according to the chosen mutation. Thus, the codon AGT (for Ser) was mutated to TGT (for Cys), and the oligonucleotide primers were constructed as follows:

(Forward) 5'-GAT CGC TAC TGT GAG **TGT** ATC ATG CGT CGT CGC GG-3'

(Reverse) 5'-CC GCG ACG ACG CAT GAT ACA CTC ACA GTA GCG ATC-3'

The designed primers were characterized by a melting temperature (T_m) of 82.6°C, as estimated by the following formula (eqn. 9):

$$T_m = 81.5 + 0.41\ (\%NG\ NC) + \left(\frac{675}{N}\right) - (\%\ mismatch) \qquad (9)$$

where N is the number of nucleotides ($N = 35$ in our case) and NG and NC are referred to the number of guanine ($NG = 12$ for the forward and 7 for the reverse) and cytosine ($NC = 7$ for the forward and 12 for the reverse) bases, contained within the sequence, respectively.

Polymerase chain reaction (PCR) was performed to conduct the mutagenesis process that consists of the following three steps: 1) the denaturation by heating of the template DNA molecules; 2) the annealing of the primers to the parental strands; 3) the amplification of the mutated plasmid by DNA polymerase (Figure 24).

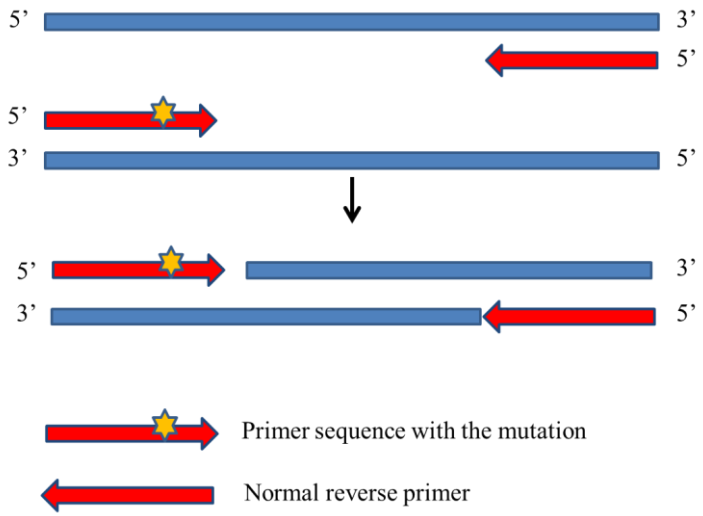

Figure 24- Graphic representation of the site-directed mutagenesis procedure.

PCR was carried out according to the manufacturer's instructions. Briefly, 5 µL of QuickChange buffer, 1 µL of deoxynucleotides (dNTPs), 100 ng of plasmid pET22b(+)-ANG, 125 ng of each primer, 1.5 µL of QuickSolution reagent and nuclease free-H_2O to reach a final volume of 50 µL, were sequentially added to the PCR-tube to prepare the sample reaction. Finally, 1 µL of PfuUltra high-fidelity DNA polymerase was rapidly added to the reaction mixture and the sample was thermo-cycled following the steps showed in the table below (Table 4).

Table 4– Specifications for the PCR steps.

Round	N. of cycles	Temperature (°C)	Time (sec)
1	1	95	120
2	18	95	20
		60	20
		68	480
3	1	68	350

To test the efficiency of the DNA mutation, a control reaction was similarly prepared by adding 25 ng of the plasmid pWhitescript 4.5-kb to the reaction mixture.

After the completion of the PCR cycling, the obtained products were treated with 2 µL of Dpn I restriction enzyme, which specifically digests the 5′-Gm6ATC-3′ sequence in the parental template DNA. The uncut mutated DNA sequences were used to transform the XL10-Gold ultra-competent cells. Thus, 2 µL of Dpn I-treated DNA from each control and

sample reaction were transferred to pre-chilled tubes containing 45 µL of cells and 2 µL of β- mercaptoethanol (ME) mix provided with the kit. The cell suspensions were incubated on ice for 30 min, heat-shocked in a 42 ºC water bath for 30 sec and finally placed on ice for 2 min. 250 µL of NZY+ broth (10 g/L NZ amine, 5 g/L NaCl, 5 g/L Yeast extract, 12.5 mM $MgCl_2$, 12.5 mM $MgSO_4$, 40 g/L glucose) were, subsequently, added to each tube and the cellular suspensions were incubated at 37°C for 1 hr with shaking at 225 r.p.m.

Afterwards, 200 µL of each transformation reaction were plated on Luria-Bertani (LB) agar plates supplemented with ampicillin, as the appropriate antibiotic for the used plasmid vector. In particular, I plated (Figure 25):

- XL10-Gold ultra-competent cells transformed with the plasmid pWhitescript, on LB + ampicillin agar plate as positive control (ctrl+);
- no transformed XL10-Gold ultra-competent cells, on LB-ampicillin agar plate as negative control (ctrl-);
- no transformed XL10-Gold ultra-competent cells, on LB + ampicillin agar plate as second negative control (ctrl-);
- XL10-Gold ultra-competent cells transformed with the plasmid pET22b(+)-S28CAng, on LB + ampicillin agar plate.

The prepared plates were incubated at 37°C overnight.

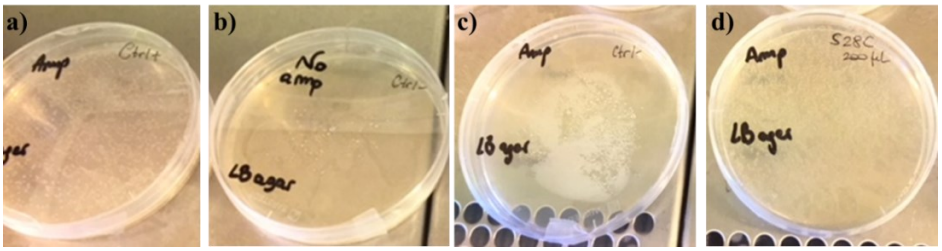

Figure 25- Colonies of: (a) XL10-Gold ultracompetent cells transformed with the control DNA and grown on LB+ampicillin agar plate; (b-c) no-transformed ultracompetent cells and plated on LB-ampicillin and LB+ampicillin agar plates; (d) XL10-Gold ultracompetent cells transformed with the mutated DNA and grown on LB+ampicillin agar plate.

After 24 hrs of incubation, a high presence of bacterial colonies was observed on all the tested plates and as expected no colonies of no transformed XL10-Gold ultra-competent cells grew in presence of ampicillin, thus verifying the effective cells transformation with the control and mutated DNA.

Individual colonies were transferred to 5 mL of LB broth supplemented with 0.1 mg/mL of ampicillin and subsequently incubated overnight, at 37 °C under shaking at 180 r.p.m. Afterwards, plasmid DNA purification was performed through the Gene Jet Plasmid Miniprep Kit (Thermo-Scientific) according to manufacturer's instructions and analysed by DNA sequencing (Eurofins MWG Operon, Germany).

Finally, BL21 cells, specifically studied to have a high-level expression of recombinant proteins, were transformed with the mutated plasmid by heat-shock method using the One Shot® BL21(DE3) Chemically Competent *E. coli* cells. The transformed bacterial culture was plated on LB + ampicillin agar plates for 24 hrs at 37°C and the obtained colonies

were transferred to grow into 5 mL of LB medium, supplemented with 0.1 mg/mL of ampicillin. Cells were incubated overnight at 37°C, under shaking at 225 r.p.m. and finally frozen after the addition of 10% (v/v) glycerol.

The S28CANG mutant protein was expressed and purified as described for the native protein in the paragraph 2.3. Noteworthy, to chemically remove the intermolecular S-S bridges formed between the free SH groups of the introduced Cys residue into the amino acid sequence of ANG, without destroying the intramolecular and rather buried disulphide bridges of ANG, the purified S28CANG protein was treated, according to the Levison M.E. et al. procedure, with tris(2-carboxyethyl)phosphine hydrochloride (TCEP) at 5-fold molar excess over the theoretical disulphide bridges concentration, for 20 min at room temperature [368].

RNase assay was performed to assess the influence of the S28C mutation on the enzymatic activity of ANG. As shown in Figure 24, the mutant S28CANG maintained its RNase activity, which increases with the protein concentration, showing a comparable trend to that observed for the wtANG (see Figure 20), thus confirming that the introduction of the mutation does not affect the biological features of the protein (Figure 26).

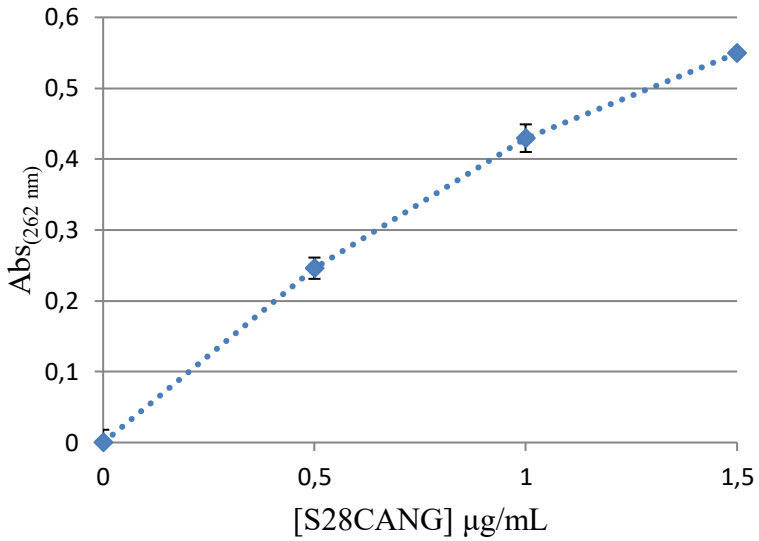

Figure 26- Ribonucleolytic activity of S28CANG. Assay was performed at increasing protein concentration (0.5, 1, 1.5 µg/mL), in 33 mM MOPS buffer, at 37 °C for 2 hrs, with the addition of $6 \cdot 10^2$ µg/mL tRNA. Averaged values and standard deviation from three experiments.

Finally, to verify the effective purification and the absence of protein dimers, SDS-PAGE was performed using both the native S28CANG (without the addition of β-mercaptoethanol as reducing agent) and the reduced protein (S28CANG + red, in the presence of 355 mM β-mercaptoethanol). The SDS-PAGE result shows the appearance of a strong protein band at around 14 kDa, under both reducing and not reducing condition, corresponding to ANG (14.2 kDa) and a very weak band at around 30 kDa attributed to a not significant presence of S28CANG dimers, under native condition, thus demonstrating the efficiency of both the expression procedure and the reduction of the intermolecular disulphide bridges of the mutant protein (Figure 27).

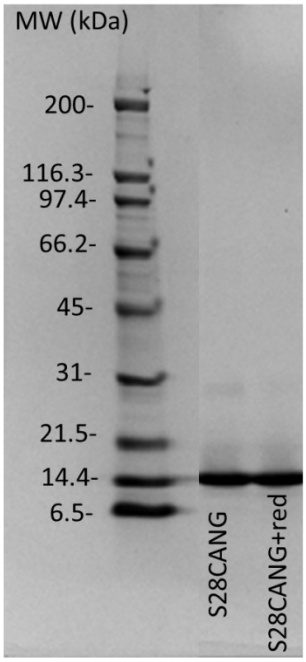

Figure 27- SDS-PAGE of the purified S28CANG electrophoresed through a pre-cast 4-20% polyacrylamide gel under denaturing and both native and reducing (355 mM β-mercaptoethanol addition) conditions prior to staining with Coomassie brilliant blue R-250.

CD experiments were carried out to scrutinize the conformational features of the three expressed variants of ANG in presence and in absence of copper ions. The recorded spectra of the free proteins (wtANG, rANG and S28CANG) at the concentration of $2 \cdot 10^{-6}$ M in 1 mM MOPS, before and after the addition of Cu(II) at the ANG:Cu(II) molar ratio of 1:1 and 1:2 are showed in Figure 28.

All three proteins display the typical CD spectrum of a secondary structure rich in β-strands [362], with the distinctive broad negative band centred at around 210 nm of wavelength [346]. This finding suggests that the methionine residue at the N-terminus domain in rANG and the Ser to

Cys mutation in S28CANG do not change the conformational features of the protein with respect to the physiological human wtANG. Interestingly, the addition of copper ions at equimolar (1:1) and excess molar (1:2) ratio with respect to the protein induces small changes in the CD signal of all the three ANG variants thus proving that the copper-complex formation further involves little structural rearrangements of the proteins.

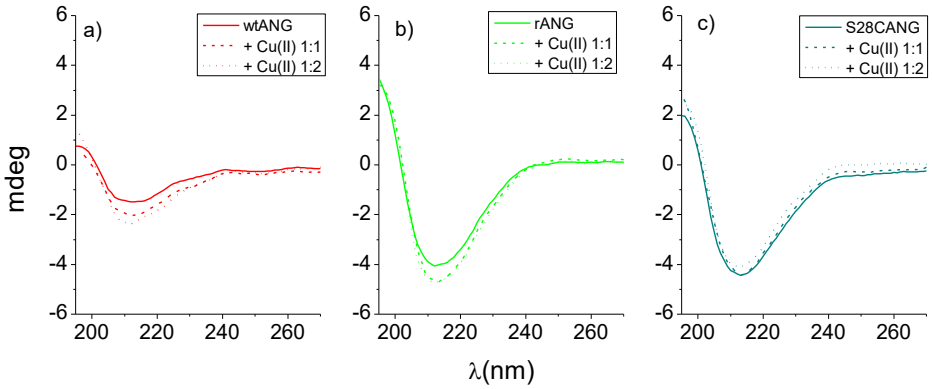

Figure 28- Far-UV CD spectra of a) wtANG (red, solid-line), b) rANG (green, solid-line), c) S28CANG (cyan, solid-line) before and after the addition of 1 and 2 Cu(II) equivalents (dash, dot line), at the protein concentration of $2 \cdot 10^{6}$ M in 1 mM MOPS buffer (pH=7.4).

2.6 Assembly of nano-bio interfaces and study with model cell membrane

2.6.1 Functionalization of AuNPs with ANG fragment peptides (PAPER I)

The hybrid assembly of AuNPs and peptides mimicking the biological function of ANG was used as a promising strategy to modulate the balance between the naturally secreted pro- and anti-angiogenic factors by combining the angiogenic properties of ANG and the anti-angiogenic activity of gold nanoparticles, for potential theranostic application. Such hybrid systems take the advantage of the peptide-mimetic approach, overcoming the limits associated to the therapeutic use of the whole proteins allowing also for the protection of the peptides, given their intrinsically vulnerable structure and their susceptibility to enzymatic degradation which often limits their clinical application [369].

Accordingly, we inspected three different variants of the 60-68 sequence: the simple $Ang_{60–68}$ (Ac-KNGNPHSEN-NH_2); the analogous fluorescent peptide Fam-Ang_{60-68}, labelled with the 5,6-carboxyfluorescein unit to inspect steric hindrance and charge effects; the analogous Ang_{60-68}Cys peptide with an additional cysteine residue at the N-terminal domain, which strongly binds to the metal surface, through Au-S bonds.

The immobilization of the three fragment peptides on the AuNPs surface was obtained by physisorption for $Ang_{60–68}$ and Fam-$Ang_{60–68}$ and a prevalent covalent grafting for Ang_{60-68}Cys. It is noticeable, in fact, that gold, being a soft acid, binds strongly with soft bases like thiols, creating, new and with high affinity, bonds between Au and S with the replacement of the citrate shell due to strong binding affinities [370].

The AuNPs functionalization was carried out through the gradual addition, in a concentration range from $5 \cdot 10^{-6}$ M up to $3 \cdot 10^{-5}$ M, of the three different peptides, to the washed AuNPs, re-suspended at the concentration of $1 \cdot 10^{-8}$ M ($7.2 \cdot 10^{7}$ NP/mL) in 1 mM MOPS-TCEP (molar ratio 1:1) and the titration experiment was scrutinized by UV–visible spectroscopy. Finally, to rinse off unbounded or weakly bound peptide molecules as well as to concentrate the nanoparticle dispersion, the hybrid systems were washed twice with 1 mM MOPS-TCEP by centrifugation at 6,010 R.C.F. for 15 min (Figure 29).

As described in the section 1.3.3.1, the absorbance and scattering of a particle depends on the local dielectric environment, which change upon the adsorption of molecules to the nanoparticles surface, since proteins/peptides have a higher refractive index than water [190, 371]. Such variations of absorption and scattering are manifested as changes to the wavelength of maximum absorption (λ_{max}) and peak absorbance (A_{max}) [25].

Figure 29 shows the UV−vis titration spectra of AuNPs after the addition of the three protein fragments in the 0.5-$3 \cdot 10^{-5}$ M concentration range. As expected the addition of $Ang_{60\text{-}68}$ produces maximum shifts in the wavelength and the absorbance of the plasmon of 3 nm and 0.07, respectively, with respect to the 12 nm, spherical, bare AuNPs, which show the distinctive plasmon peak centred at 520 nm of wavelength (see Figure 29a and Table 5) [348]. Such a spectral changes are immediately reached already after the peptide addition at the lowest concentration $0.5 \cdot 10^{-5}$ M (see the inset Figure 29a). This finding, meaning the immediate reaching of the equilibrium of saturation at the peptide-gold interface, suggesting the rapid formation, by pure physisorption mechanism, of a

stable and likely ‘disordered’, peptide shell around the nanoparticle surface.

As to $Ang_{60\text{-}68}Cys$, the addition of the peptide induces shifts of wavelength ($\Delta\lambda$) and absorbance (ΔA) reaching the maximum values respectively of $\Delta\lambda = 3$ nm and $\Delta A = 0.06$ after the addition of the $Ang_{60\text{-}68}Cys$ at the concentration of $1 \cdot 10^{-5}$ M. Noteworthy, although the measured shifts are comparable with those measured for the physisorption case, due to the cysteine residue, these spectral changes are gradually reached (see the inset Figure 29b). The peptide chemisorption, indeed, should occur with the formation of a strong thiol-gold bond that trigger an ‘ordered’ arrangement of the peptide molecules around the nanoparticles [372].

The addition of Fam-$Ang_{60–68}$ leads to a broader and red-shifted plasmon peak compared with the bare nanoparticles ($\Delta\lambda = 5$ nm, $\Delta A = 0.13$) (Figure 29c). In this case, the complete surface coverage is reached at the peptide saturation concentration of $2 \cdot 10^{-5}$ M. The observed differences can be related to an increased contribution of aggregation effects, due to the negatively charged carboxyfluorescein moiety and its steric hindrance.

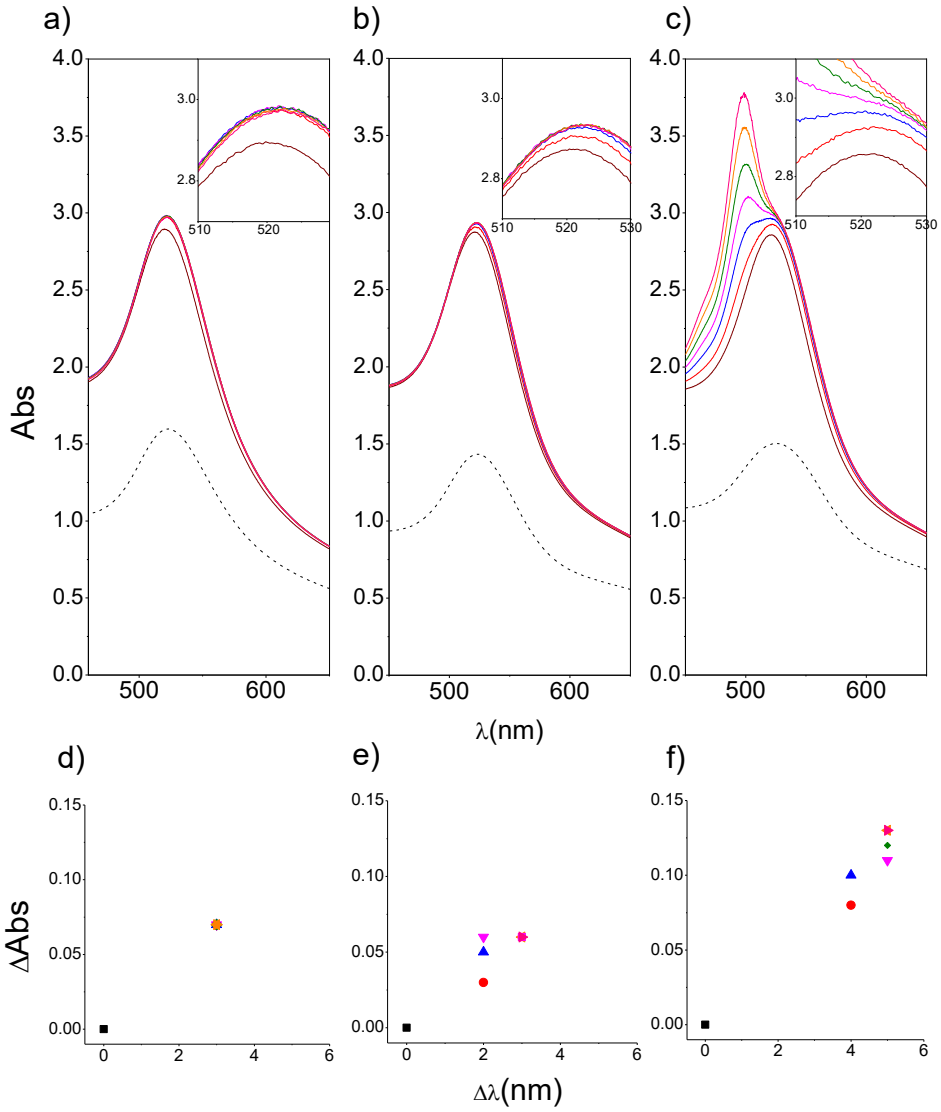

Figure 29- UV-visible spectra of $7.2 \cdot 10^7$ NP/mL AuNPs in MOPS-TCEP 1mM (pH=7.4) before (wine) and after the addition of a) $Ang_{60\text{-}68}$, b) $Ang_{60\text{-}68}Cys$, c) Fam-$Ang_{60\text{-}68}$ at increasing concentrations: $5 \cdot 10^{-6}$ M (red), $1 \cdot 10^{-5}$ M (blue), $1.5 \cdot 10^{-5}$ M (magenta), $2 \cdot 10^{-5}$ M (green), $2.5 \cdot 10^{-5}$ M (orange) and $3 \cdot 10^{-5}$ M (pink); the dashed
curves refer to the re-suspended pellet after the rinsing steps. In panel d), e), f) are shown the shifts in absorbance (ΔAbs) and wavelength (Δλ) of the plasmon peak after the addition of the of d) $Ang_{60\text{-}68}$, e) $Ang_{60\text{-}68}Cys$, f) Fam-$Ang_{60\text{-}68}$ to the

AuNPs dispersion at increasing concentrations with respect to the bare nanoparticles (black).

Table 5 summarizes the optical parameters calculated for each synthetized hybrid system, showing that, for all three cases, as expected from the wavelength shift, the peptides addition induces an increase of the calculated optical diameter ($d_{opt} = 22$ nm for both Au-Ang$_{60\text{-}68}$ and Au-Ang$_{60\text{-}68}$Cys and 27 nm for Au-Fam-Ang$_{60\text{-}68}$) associated also with a slight increase of the FWHM value (2 nm for Au-Ang$_{60\text{-}68}$, 3 nm for Au-Ang$_{60\text{-}68}$Cys and 17 nm for Au-Fam-Ang$_{60\text{-}68}$).

In general, the peak broadening points to the polydispersity of the colloidal suspension, i.e., the presence of several size populations of nanoparticles, owing to the actual size increase upon the adsorption of molecules, as also confirmed by the higher values of the optical size [373].

Table 5- Optical properties: shifts of the maximum of absorption (A_{max}) and of the wavelength at the absorbance maximum (λ_{max}), full width at half maximum (FWHM) values and optical diameters obtained upon the adsorption of the three ANG peptides on the AuNPs surface.

Sample	**ΔA**	**Δλ (nm)**	**FWHM (nm)**	**d_{opt}**
AuNP	-	-	50	14
Au- Ang$_{60\text{-}68}$	0.07	3	52	22
Au- Ang$_{60\text{-}68}$Cys	0.06	3	53	22
Au-Fam-*Ang$_{60\text{-}68}$*	0.13	5	67	27

Theoretical predictions show how the local refractive index environment of the particle affects its absorption spectrum.

By assuming the peptide-coated nanoparticles as core-shell spheres with a metallic core of d_{opt} diameter, corresponding to the uncoated nanoparticles, and a homogeneous spherical proteinaceous shell, the fraction of protein over the total particle, g, is related to the changes of λ_{max}, as given by the following equation (eqn. 10):

$$g = (1 + \alpha_s)\left(\frac{\lambda_p^2(\varepsilon_s - \varepsilon_m)}{\Delta\lambda \cdot \lambda_{max,0}} + 2\alpha_s\right)^{-1} \quad (10)$$

where λ_p is the free electron oscillation wavelength (which is 131 nm for gold [193]), ε is a dielectric constant or relative permittivity (equal to the squared refractive index), the 's' and 'm' subscripts refer to the shell and surrounding medium, respectively; $\lambda_{max,0}$ is the wavelength of maximum absorption for uncoated colloid and $\alpha_s = \frac{(\varepsilon_s - \varepsilon_m)}{(\varepsilon_s + 2\varepsilon_m)}$ is the polarizability of a sphere of shell dielectric constant ε_s in a medium of dielectric constant ε_m. By considering the refractive index values (n) at 550 nm respectively of 1.335 [374] for water and 1.38 [375] for a pure protein, a protein fraction shell of $g = 0.74$ for Au-Ang$_{60\text{-}68}$ and Au-Ang$_{60\text{-}68}$Cys and $g = 1.2$ for Au-Fam-Ang$_{60\text{-}68}$, could be calculated.

According to the following equation (eqn. 11), which refers to the shell thickness (s):

$$s = \frac{d}{2}\left[\frac{1}{(1-g)^{1/3}} - 1\right] \quad (11)$$

and using the Feijter's formula in the equation below (eqn. 12):

$$\Gamma = s\frac{n_s - n_m}{dn/dc} \quad (12)$$

where, Γ is the coverage and dn/dc is the refractive index increment (typically 0.19 mL·g^{-1} for a protein [376]), the mass of protein absorbed per unit area are calculated to be about 90 ng/cm^2 for Au-Ang$_{60\text{-}68}$ and Au-Ang$_{60\text{-}68}$Cys and 450 ng/cm^2 for Au-Fam-Ang$_{60\text{-}68}$, respectively.

Given the molecular weight of Ang$_{60\text{-}68}$ (MW=1,105 g/mol) and the diameter $d_{opt} = 14\ nm$ for each spherical AuNP, the corresponding Γ in terms of molecular coverage is calculated as follows: ~3·10^2 molecules of Ang$_{60\text{-}68}$ (or Ang$_{60\text{-}68}$Cys) and ~1.5·10^3 molecules of Fam-Ang$_{60\text{-}68}$ per each NP. Since the average molecular dimensions of the three peptides are 1.7x1.5x3.2 nm^3 for Ang$_{60\text{-}68}$, 1.6x1.4x1.9 nm^3 for Ang$_{60\text{-}68}$Cys and 1.4x1.2x3.7 nm^3 for Fam-Ang$_{60\text{-}68}$, respectively, the ideal monolayer coverage of the peptide molecules in the two *end-on* and *side-on* limit configurations are of the order of 2-3·10^2 molecules/NP and 1-2·10^2 molecules/NP, respectively. Accordingly, at nanoparticle surface it can be figured out a monolayer coverage of Ang$_{60\text{-}68}$ (or Ang$_{60\text{-}68}$Cys), whereas a multilayer is most likely formed by Fam-Ang$_{60\text{-}68}$ at the interface with the gold nanoparticle.

These findings suggest that different adsorption modes are expected for the three peptides.

In particular, both Ang$_{60\text{-}68}$ and Fam-Ang$_{60\text{-}68}$ interact with the AuNP surface by a 'pure' physisorption process, leading to a "disordered" molecular monolayer at the nanoparticles interface for Ang$_{60\text{-}68}$ and a multilayer of peptides in the case of Fam-Ang$_{60\text{-}68}$, most likely due to the electrostatic interactions that occur between the negatively charged

carboxyfluorescein group of the peptide and the positively charged Arg residue of the 60-68 sequence.

As to the Au-Ang$_{60\text{-}68}$Cys, the cysteine residue prompts a mixed chemisorption/physisorption process, with the formation of strong thiol-gold bonds, which trigger "ordered" domains of molecules around the nanoparticle, likely in a close-packed arrangement [377].

Figure 26 shows also the spectra of the hybrid Au-peptides systems after the two rinsing steps (dashed curves). Noteworthy, the distinctive plasmon peak shift is maintained ($\Delta\lambda$ =3 nm for Ang$_{60\text{-}68}$, $\Delta\lambda$ =3 nm for Ang$_{60\text{-}68}$Cys and $\Delta\lambda$ =5 nm for Fam-Ang$_{60\text{-}68}$) with respect to the bare AuNPs, indicating that no significant loss of peptides occurs after the washing steps thereby confirming the effective and irreversible coating of the three peptides on the gold surface (see Table 6).

According to the wavelength shifts, the optical size of the hybrids does not change ($d_{opt} = 22$ nm for both Au-Ang$_{60\text{-}68}$ and Au-Ang$_{60\text{-}68}$Cys and 27 nm for Au-Fam-Ang$_{60\text{-}68}$) while, as expected for AuNPs coated with a layer of molecules, increased FWHM values (5 nm for Au-Ang$_{60\text{-}68}$, 2 nm for Au-Ang$_{60\text{-}68}$Cys and 11 nm for Au-Fam-Ang$_{60\text{-}68}$) are maintained for the hybrids with respect to the uncoated AuNPs.

Table 6- Optical properties: maximum of absorption (A_{max}), shift of the wavelength at the absorbance maximum ($\Delta\lambda$), extinction coefficient (ε), full width at half maximum (FWHM) value as well as the calculated optical diameters and the nanoparticles concentration in both nM and NP/mL for the re-suspended pellets in 1 mM MOPS-TCEP (molar ratio 1:1).

Sample	**A_{max}**	**$\Delta\lambda$ (nm)**	**ε ($cm^{-1}M^{-1}$)**	**FWHM (nm)**	**d_{opt}**	**[nM]**	**[NP/mL]**
AuNP pellet	0.9	-	$2.8 \cdot 10^8$	50	14	31.6	$2.2 \cdot 10^8$
Au-Ang$_{60-68}$ pellet	1.6	3	$1.3 \cdot 10^9$	55	22	12.6	$2.3 \cdot 10^7$
Au- Ang$_{60-68}$Cys pellet	1.4	3	$1.3 \cdot 10^9$	52	22	11.4	$2.1 \cdot 10^7$
Au-Fam-*Ang$_{60-68}$ pellet*	1.5	5	$2.5 \cdot 10^9$	61	27	7.8	$7.7 \cdot 10^6$

To verify the actual chemisorption process of thiol derivatives on the gold surface through the Au-S interaction, Fourier Transform Infrared Spectroscopy (FT-IR) is often used by detecting the decrease or disappearance of whether the SH stretching vibration signal at 2,546 cm^{-1} of the Cys residue or the asymmetric COO- stretching mode at 1640-1560 cm^{-1} attributed to the citrate shell, owing to the formation of the Au-S bonds [360, 361] and the displacement of the adsorbed citrate layers [370]. Accordingly, we recorded ATR-IR spectra for both the uncoated- citrate stabilized AuNPs, and the hybrid Au-Ang$_{60-68}$Cys, in the comparison with the free peptide Ang$_{60-68}$Cys (see Figure 30). As it is noticeable, the ATR-IR spectrum of citrate stabilized AuNPs displays a broad peak between 2500–3600 cm^{-1} attributed to the OH stretch and a signal at around 1600 cm^{-1} due to the carbonyl peaks, C=O stretch. These signals are indicative of gold nanoparticles stabilized by citrate ions. In contrast, the hybrid Au-

$Ang_{60\text{-}68}Cys$ spectrum shows an attenuation of the hydroxyl broad peak intensity and a slightly perceptible peak at around 1600 cm^{-1}, thus proving the displacement of the citrate shell by the Cys-peptide and so the presence of the Au-S interaction on the gold nanoparticles surface.

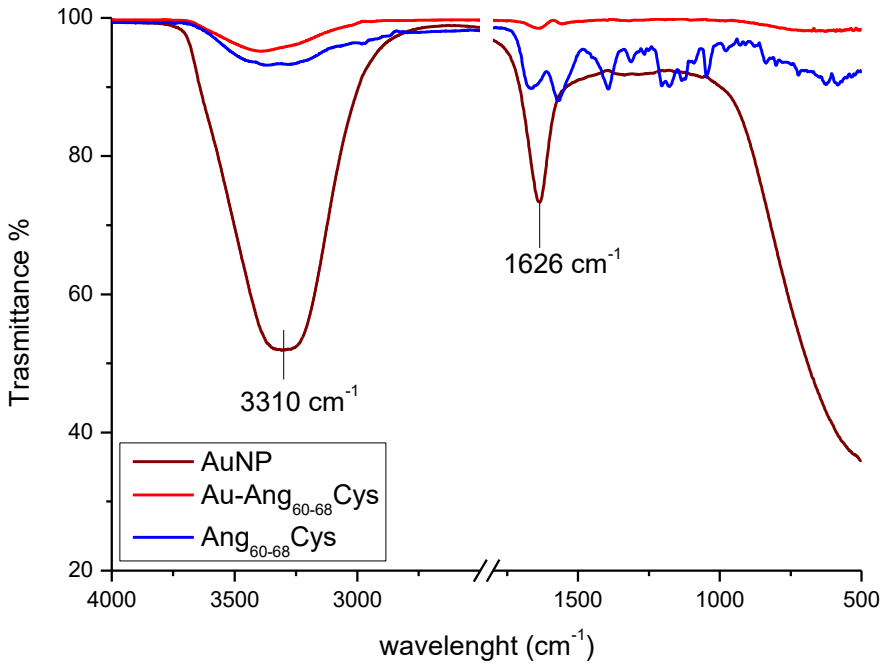

Figure 30- ATR-IR spectra of citrate stabilized AuNPs (wine) 31.6 nM ($2.2 \cdot 10^{8}$ NP/mL) compared with the hybrid Au-$Ang_{60\text{-}68}Cys$ (red) 11.4 nM ($2.1 \cdot 10^{7}$ NP/mL) and the free peptide $Ang_{60\text{-}68}Cys$ $3 \cdot 10^{-5}$ M (blue) re-suspended pellet in 1 mM MOPS-TCEP obtained after two rinsing steps by centrifugation at 6,010 R.C.F. for 15 min.

AFM analysis in AC mode in air were carried out on the bare AuNPs and the synthetized hybrids Au-peptides (Figure 31). The recorded images and the obtained height histograms (Z-scale), indicate that the maximum height for the bare gold nanoparticles is around 9 ± 3 nm whereas, as

expected from the UV-visible data, slightly increases up to around 15 ± 4 nm for Ang_{60-68}, 10 ± 3 nm for $Ang_{60-68}Cys$, and 15 ± 4 nm for Fam-Ang_{60-68}. Such a data further prove the peptide immobilisation on the AuNPs surface, even if a collapse of the peptide layer, most likely due to the de-wetting process required for the AFM sample preparation, can be observed, especially for $Ang_{60-68}Cys$, thus underestimating the real size of the hybrids and giving similar values for the Au-Ang_{60-68} and Au-Fam-Ang_{60-68} samples.

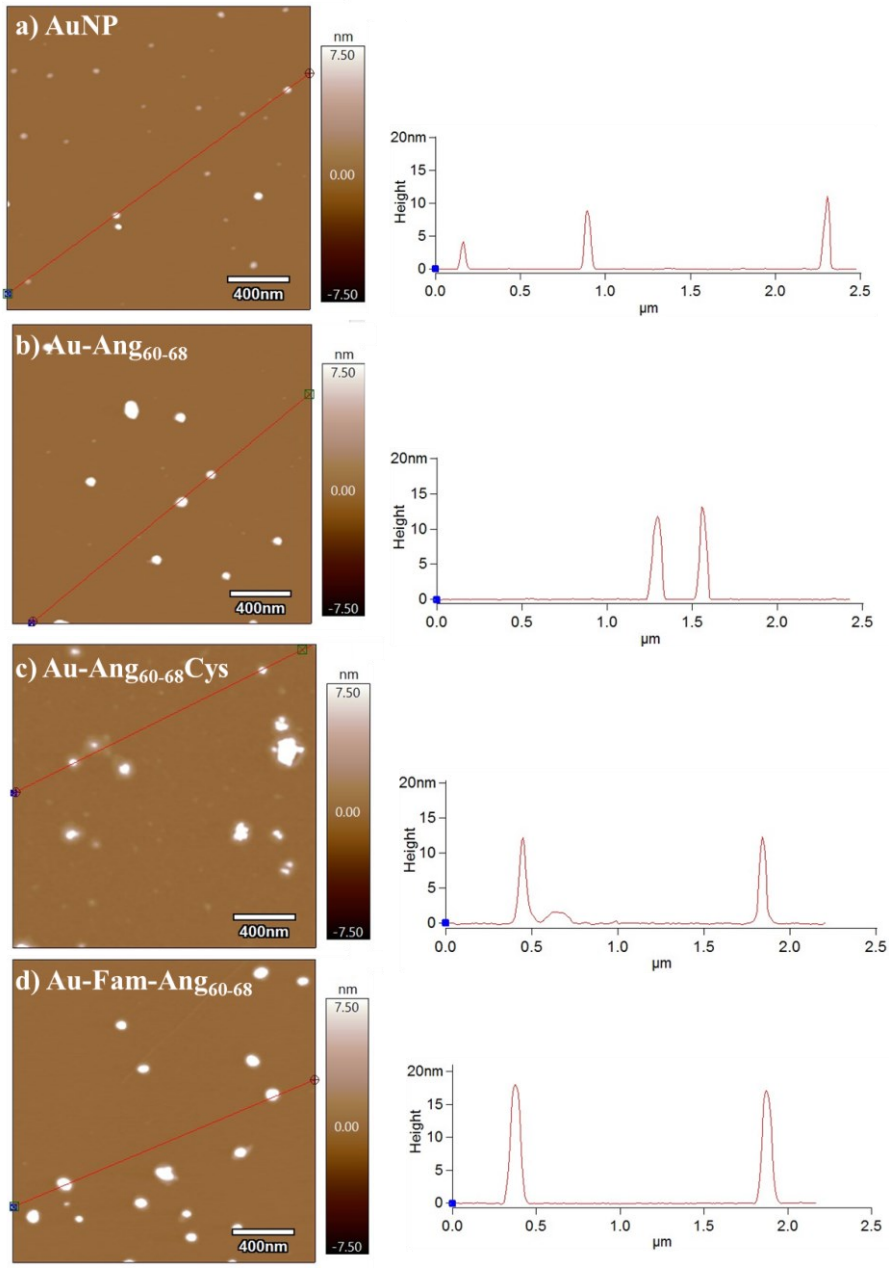

Figure 31-Atomic force microscopy micrographs of bare AuNPs a) and Au-Ang: $Ang_{60\text{-}68}$ b), $Ang_{60\text{-}68}$Cys c), Fam-$Ang_{60\text{-}68}$ (d); scale bar = 400 nm. The graphs below each image show the histograms calculated for Z max.

Supported lipid bilayers (SLBs) were used to scrutinize, by FRAP experiments, the interaction of the three ANG peptides immobilised on the gold nanoparticles surface with model artificial membranes.

Figure 32 displays the confocal micrographs recorded before and after the photobleaching. As it is noticeable from the graph (Figure 29f), the lipid bilayers continue to maintain its fluidity properties after the exposure of SLBs to the hybrid Au-Ang$_{60–68,}$ and the recovery of emission is around the 98% compared with the pre-bleach value. Conversely, the fluidity is significantly affected after the treatment with Au-Ang$_{60–68}$Cys and Au-Fam-Ang$_{60–68,}$ with a recovery of fluorescence of 94% and 96%, respectively. Noteworthy, after the treatment with the bare AuNPs the lipids diffusion is even more reduced, thus leading to a recovery of about 90%. In the optical bright field images merged with the rhodamine emission confocal images, all the three Au-peptides aggregates are visible as dark spots. However, only for the bilayer exposed to the bare AuNPs, the photobleaching creates quenched zone around the aggregates and in that point the recovery does not take place. This phenomenon is most likely due to the insertion of the bare AuNPs into the 5 nm-thick membrane which markedly affect the lipid diffusion. Whereas the peptide functionalised nanoparticles, owing to the peptide sequence 60-68, that is physiologically involved in the interaction with the cell membrane [279], predominantly stay on the top leaflet of the lipid bilayers.

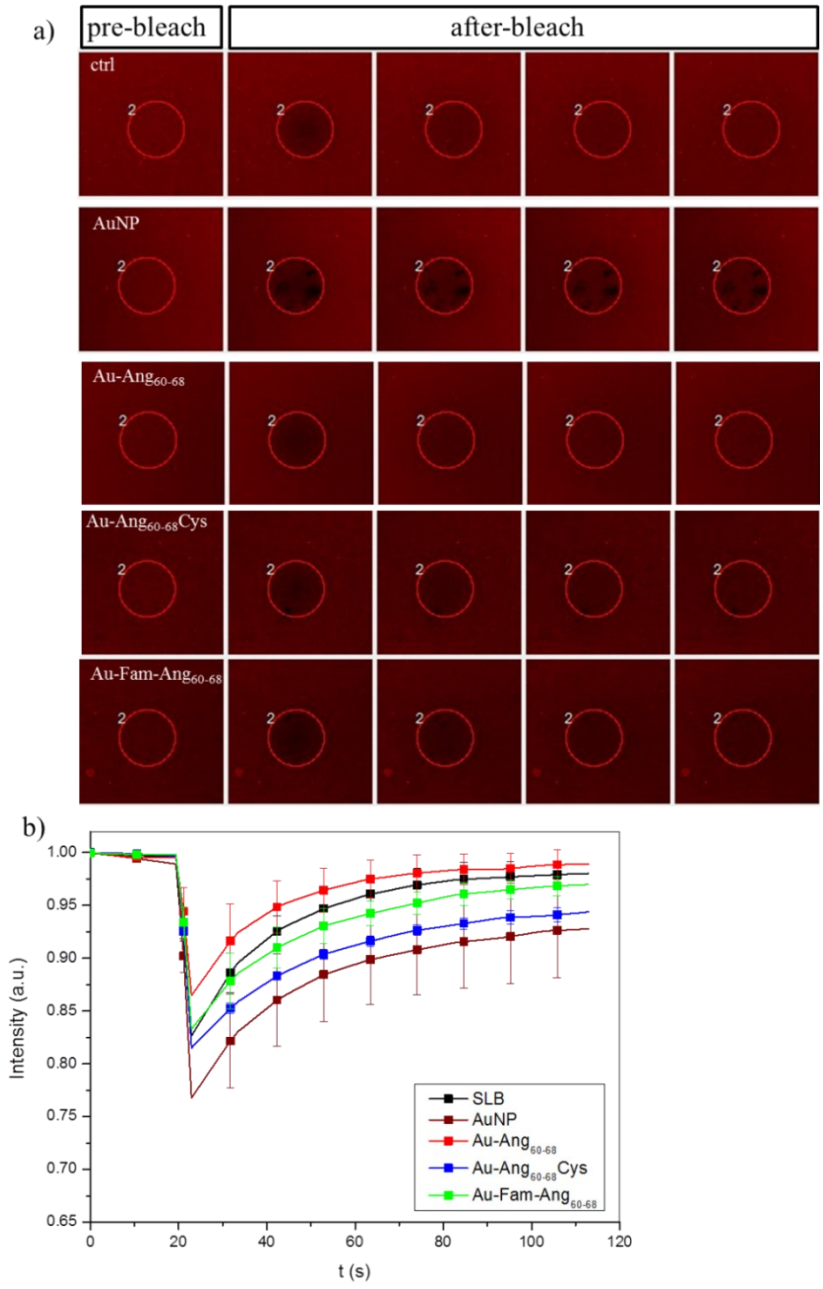

Figure 32- LSM merged optical bright field and red fluorescence ($\lambda_{ex/em}$= 543/550-600 nm) for rhodamine-labelled POPC SLBs untreated and after 30 min incubation with: AuNP, Au-Ang$_{60–68}$, Au-Ang$_{60–68}$Cys and Au-Fam-Ang$_{60–68}$.

The graph in b) shows the corresponding fluorescence recovery curves. Each curve represents the average (± standard deviation) of the emission intensities recorded in FRAP runs on five randomly chosen areas of the sample. Experiments were repeated in triplicate.

2.6.2 Functionalization of AuNPs with ANG (PAPER II-III)

Together with their anti-angiogenic activity, AuNPs show potent anti-oxidative effects, being able to quench the action of reactive oxygen species (ROS) like hydroxyl (OH), hydrogen peroxide (H_2O_2) and nitric oxide (NO) [57, 378]. Their large surface area, indeed, allows the nanostructures to easily accept electrons from ROS, leading to their deactivation (see section 1.3.3.2). In this perspective, AuNPs offer an advantageous strategy for the treatment of acute and chronic wounds since the increased production of ROS, during healing process, inhibits cell growth and causes damages to DNA, RNA and proteins, impairing and slowing down the physiological wound repair [58].

Based on these premises and knowing the pivotal role of ANG in the angiogenic process as well as in the wound management (see section 1.3.4.2), it has been synthetized a protein delivery system made of gold nanoparticles functionalized with the whole ANG (Au-ANG) to control the angiogenic process for wound care application. Such hybrid system, together with the intrinsic proprieties of the gold colloidal dispersion, offers the advantage of an improved selective delivery of the protein as well as enhanced therapeutic outcomes by increasing the membrane permeability of ANG, limiting its endosomal escape and the enzymatic degradation thereby leading to a prolonged half-life of the protein [379].

In particular, three variants of ANG were inspected: *i)* the human wild-type angiogenin, wtANG; *ii)* the recombinant protein, rANG, typically expressed into bacterial vectors and commonly used for research works, which owing to the extra methionine residue at the N-terminal domain differently binds to copper ions with respect to the human wtANG. Such a relevant difference between rANG and wtANG in the copper binding would influence the biological properties of the proteins (see section 1.3.4.6); *iii)* the new mutant, S28CANG, with a cysteine instead of the serine at the residue 28, for the high affinity binding to the metal surface, through Au-S bonds. Accordingly, a predominant chemisorption mechanism is expected at the interface with AuNPs for the mutant protein S28CANG, while a "pure" physisorption process would occur for both wtANG and rANG, respectively.

The hybrid Au-ANG systems were synthetized as follows. The three variants of ANG, namely wtANG, rANG and S28CANG, were added to the colloidal dispersion of gold nanoparticles in 1 mM MOPS buffer (pH=7.4) and the actual metal nanoparticle/protein optical interface was scrutinized by UV–visible spectroscopy. Figure 33 shows the UV−visible spectra of AuNPs (at the concentration of $1 \cdot 10^{-8}$ M, $7.2 \cdot 10^{7}$ NP/mL), before and after the addition of the three proteins at the concentration of $5 \cdot 10^{-8}$ M for wtANG and S28CANG and $2 \cdot 10^{-8}$ M for rANG. Such values correspond to the limit concentration of protein mixed with the AuNP dispersion, that ensures the maximum coverage of the nanoparticle before reaching the aggregation of the nano-systems. Finally, in order to rinse off unbounded or weakly bound proteins, the functionalized nanoparticles were washed by two centrifugation steps (6,010 RCF, 15 min) in 1 mM MOPS.

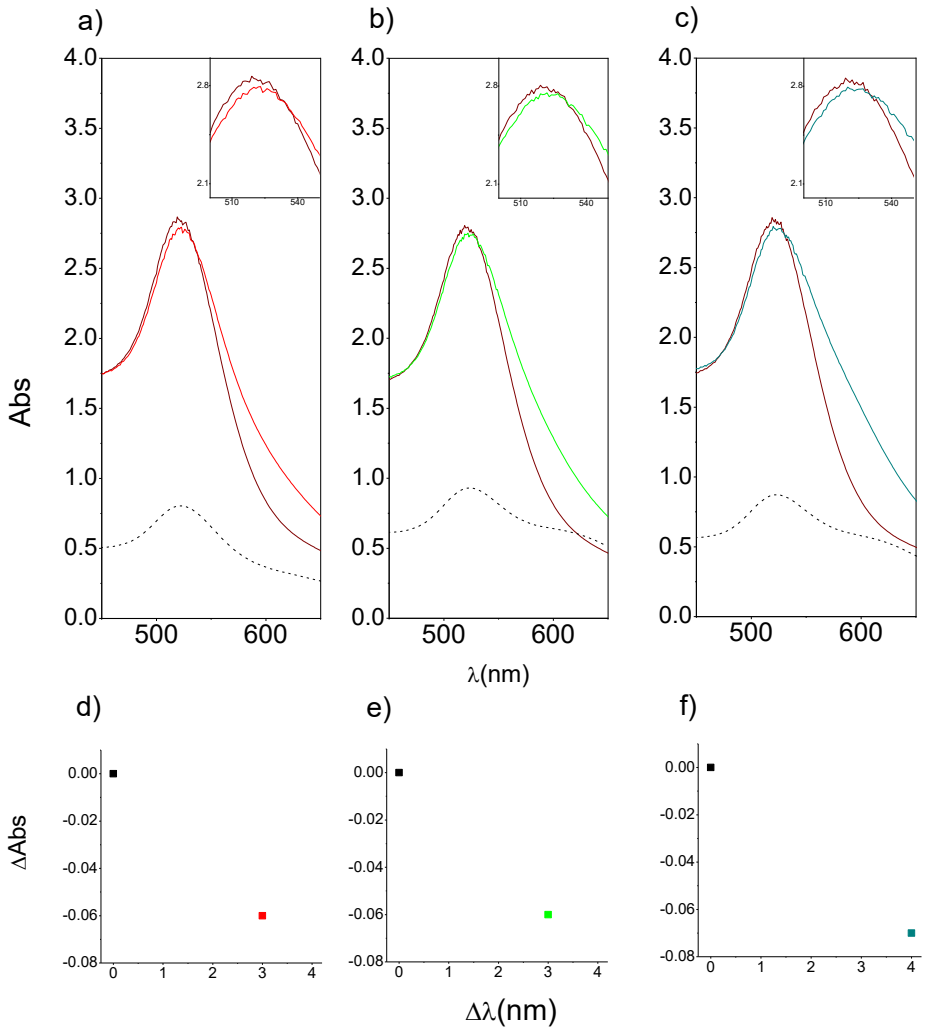

Figure 33- UV-visible spectra of $7.2 \cdot 10^{7}$ NP/mL AuNPs in 1mM MOPS (pH=7.4) before (wine) and after the addition of a) $5 \cdot 10^{-8}$ M wtANG (red), b) $2 \cdot 10^{-8}$ M rANG (green), c) $5 \cdot 10^{-8}$ M S28CANG (cyan); the dashed curves refer to the re-suspended pellet after the rinsing steps. In panel d), e), f) are shown the shifts in absorbance (ΔAbs) and wavelength (Δλ) of the plasmon peak after the addition of the of d) wtANG (red), e) rANG (green), f) S28CANG (cyan) to the AuNPs dispersion with respect to the bare nanoparticles (black).

As expected for spherical nanoparticles with a diameter of about 14 nm the bare AuNPs show the characteristic plasmon peak centred at 520 nm of wavelength, with a FWHM of about 54 nm [348].

For all three cases, the protein addition (Figure 33a-b) induces a change of the plasmon peak, with a small increase in the FWHM (2 nm for Au-wtANG; 6 nm for Au-rANG and 8 nm for Au-S28CANG) and red shifts ($\Delta\lambda \sim 3$ nm for both wtANG and rANG; 4 nm for S28CANG), respectively. No significant changes in the maximum of absorbance are instead observed ($\Delta A \sim -0.06$ for both wtANG and rANG; $\Delta A \sim -0.07$ for S28CANG) (Figure 33d-f, Table 7).

Table 7- Optical properties: shifts of the maximum of absorption (A_{max}) and of the wavelength at the absorbance maximum (λ_{max}), full width at half maximum (FWHM) values and optical diameters obtained upon the adsorption of the three variants of ANG on the AuNPs surface.

Sample	**ΔA**	**Δλ (nm)**	**FWHM (nm)**	**d_{opt}**
AuNP	-	-	54	14
Au- wtANG	-0.06	3	56	22
Au- rANG	-0.06	3	60	22
Au-S28CANG	-0.07	4	62	25

The UV-vis spectra of the hybrids Au/protein after two rinsing steps (Figure 33a-b dashed line) show that the distinctive plasmon peak shift is maintained ($\Delta\lambda \sim 2$ nm for Au-wtANG and 3 nm for both Au-rANG and Au-S28CANG; $\Delta FWHM \sim 2$ nm, 6 nm, 8 nm for Au-wtANG, Au-rANG and Au-S28CANG, see Table 8) in comparison to the bare AuNPs. However, differently from the UV-vis response observed for the Au-peptides hybrids (see section 2.6.1), a shoulder at around 620 nm of

wavelength is evident, indicative to the occurrence of nanoparticle aggregation to some extent owing to the washing steps. This effect is especially evident for Au-rANG and Au-S28CANG, respectively.

Table 8- Optical properties: maximum of absorption (A_{max}), shift of the wavelength at the absorbance maximum ($\Delta\lambda$), extinction coefficient (ε), full width at half maximum (FWHM) value as well as the calculated optical diameters and the nanoparticles concentration in both nM and NP/mL for the re-suspended pellets in 1 mM MOPS.

Sample	**A_{max}**	**$\Delta\lambda$ (nm)**	**ε ($cm^{-1}M^{-1}$)**	**FWHM (nm)**	**d_{opt}**	**[nM]**	**[NP/mL]**
AuNP pellet	0.867	-	$1.3 \cdot 10^7$	54	14	60.9	$4.3 \cdot 10^8$
Au-wtANG pellet	0.803	2	$7.8 \cdot 10^8$	55	19	10.3	$2.9 \cdot 10^7$
Au- rANG pellet	0.930	3	$1.3 \cdot 10^9$	60	22	7.4	$1.4 \cdot 10^7$
Au-S28CANG *pellet*	0.872	3	$1.3 \cdot 10^9$	62	22	6.9	$7.3 \cdot 10^6$

The peak broadening is indicative of an increase of the polydispersity of the colloidal suspension due to the presence of several size populations of nanoparticles associated with aggregation effects [380, 381] as well as the effective size increase upon the molecule adsorption [373].

As to the aggregation, upon the interaction between the positively charged groups at the physiological pH of the protein (namely lysine, arginine, histidine as well as the free N-terminus group for rANG) and the citrate-capped negatively charged AuNPs, the electrostatic stabilisation mechanism of the colloidal dispersion is expected to be partially or even

totally nullified, with consequent polydispersity of the suspension [382]. Such an effect is particularly evident after the washing step.

As to the adsorption of molecules on the nanoparticle surface, as expected, it induces variations on the local dielectric environment, manifested as changes to the wavelength of maximum absorption (λ_{max}) and peak absorbance (A_{max}). To this respect, theoretical calculations were used to explain how the local refractive index environment of the particle affects its absorption spectrum [192].

In particular, by assuming the protein-coated nanoparticles as a spheres with a metallic core of d_{opt} diameter surrounded by an homogeneous spherical proteinaceous shell, using eqn. 10 (see section 2.6.1) a protein fraction shell of $g = 0.74$ for Au-wtANG and Au-rANG and $g = 0.97$ for Au-S28CAng, could be calculated.

From the g value and using the eqn. 11-12, the calculated mass of protein absorbed on the synthetized hybrid Au-protein per unit area is about 80 ng/cm^2 for Au-wtANG and Au-rANG, and of 320 ng/cm^2 for Au-S28CANG, respectively.

Thus, given the molecular weight of ANG (MW=14,200 g/mol) and the diameter d = 14 nm for each spherical AuNP, the corresponding Γ in terms of molecular coverage is calculated as follows: 20.9 molecules of wtANG (or rANG) and 83 molecules of S28CANG per each NP. Since the average angiogenin molecular dimensions are (70x62x32) Å^3 [383] the ideal monolayer coverage (Figure 34) of the protein in the two *end-on* and *side-on* limit configurations is about 10.4 and 22.8 molecules/nanoparticle, respectively. Accordingly, at nanoparticle surface it can be figured out a bilayer coverage of wtANG, rANG and a multilayer of S28CANG, most likely in the *side-on* configuration.

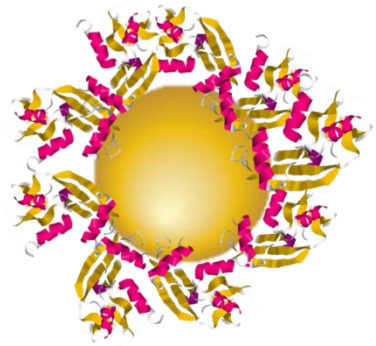

Figure 34- Representative ideal monolayer coverage of ANG on the gold nanoparticles surface.

As to the pellets recovered after the washing steps, according to the equations 10-12, for Au-wtANG pellet 2 ($\Delta\lambda \sim 2$ nm), the theoretical protein fraction shell is $g = 0.5$, corresponding to a coating thickness of s =1.54 nm and a mass of protein absorbed of $\Gamma = 36$ ng/cm^2. On the other hand, for both Au-rANG and Au-S28CANG pellets 2 ($\Delta\lambda \sim 3$ nm), the calculated values are: $g = 0.74$, $s = 3.36$ nm and $\Gamma = 79$ ng/cm^2. Therefore, the washing steps cause a loss of unbound and/or weakly bound proteins respectively of about 55% for Au-wtANG and 75% for Au-S28CAng. As to Au-rANG, apparently no significant loss of protein is detected since the shift in the wavelength at the maximum absorbance is similar to that before the nanoparticle rinsing ($\Delta\lambda \sim 3$ nm). These findings suggest that different adsorption modes are expected for the cysteine-mutated protein with respect to the wild type and to the recombinant angiogenin.

As to the Au-S28CAng, indeed, the substitution of the serine with the cysteine residue, as described for the $Ang_{60\text{-}68}$Cys peptide, leads to a mixed chemisorption and physisorption process, involving the formation of

strong thiol-gold bonds, which further trigger “ordered” domains of protein around the nanoparticle [372].

On the contrary, both wtANG and rANG interact with the AuNP surface by a physisorption process, leading to a “disordered” molecular layer at the nanoparticles interface. However, in the case of rANG, the presence of an extra positively charged group at the N-terminal methionine residue can drive a weaker immobilisation of the protein molecules at the interface with the gold surfaces in comparison with wtANG. Hence, after the rinsing, more homogeneous ‘protein patches’ at the AuNP surface are expected for Au-wtANG than Au-rANG. It is postulated that a ‘disordered’ protein coating of gold nanoparticles can contribute to the optical spectra in a similar way than a thick shell [192]; accordingly, the use of eqn. 10-12 for Au-rANG may result in an overestimation of the actual protein coverage [384].

Given the increased polydispersity of the systems obtained after the functionalization procedure, it was possible to calculate the component peaks referred to the protein-coated AuNPs and to nanogold aggregates by a Gaussian fit of the UV-vis spectra as shown in Figure 35.

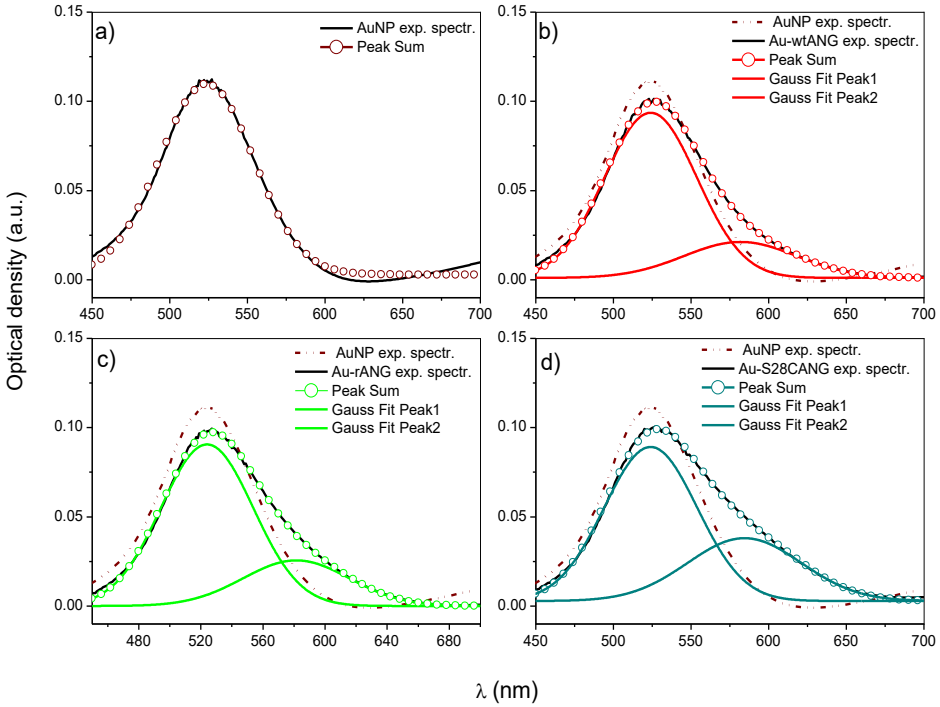

Figure 35- a) UV-vis spectra (experimental and curve fittings) of $7.2 \cdot 10^{7}$ AuNP/mL in 1 mM MOPS (pH=7.4) for: a) citrate-capped bare nanoparticles; b) in red, AuNP + $5 \cdot 10^{-8}$ M wtAng; c) in green, AuNP + $2 \cdot 10^{-8}$ M rAng; d) in cyan, AuNP + $5 \cdot 10^{-8}$ M S28CAng. In b-d the spectra of uncoated AuNP (dash-dotted lines) are shown as reference.

The two absorption peaks obtained from the spectral deconvolution and centred at 524 nm (peak 1) and 585-620 nm (peak 2) can be assigned to the protein-functionalised AuNPs and to the clusters of AuNP aggregates of about 150 nm in size, respectively [385].

Noteworthy, the peak related to the aggregated nanoparticles increases after the rinsing steps, especially for Au-rANG and Au-S28CANG (Figure 36) but a component of at least 50% of the overall population related to the protein-coated AuNPs is maintained (Figure 37).

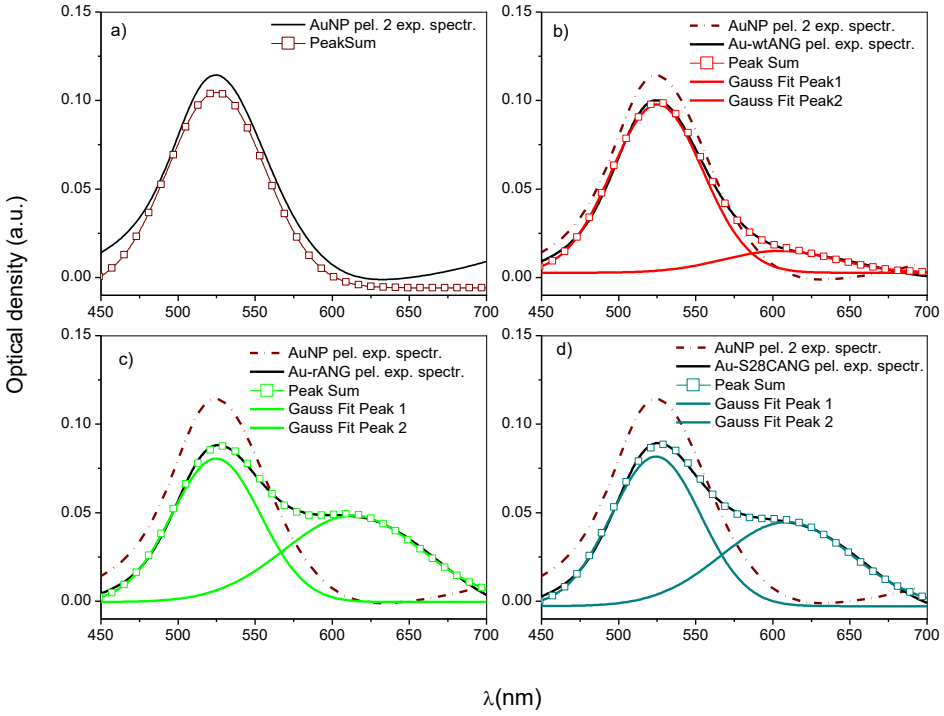

Figure 36- a) UV-vis spectra (experimental and curve fittings) of the second re-suspended pellets in 1 mM MOPS (pH=7.4) for: a) citrate-capped bare nanoparticles; b) in red, Au-wtANG; c) in green, Au-rANG; d) in cyan, Au-S28CANG. In b-d the spectra of uncoated AuNP (dash-dotted lines) are shown as reference.

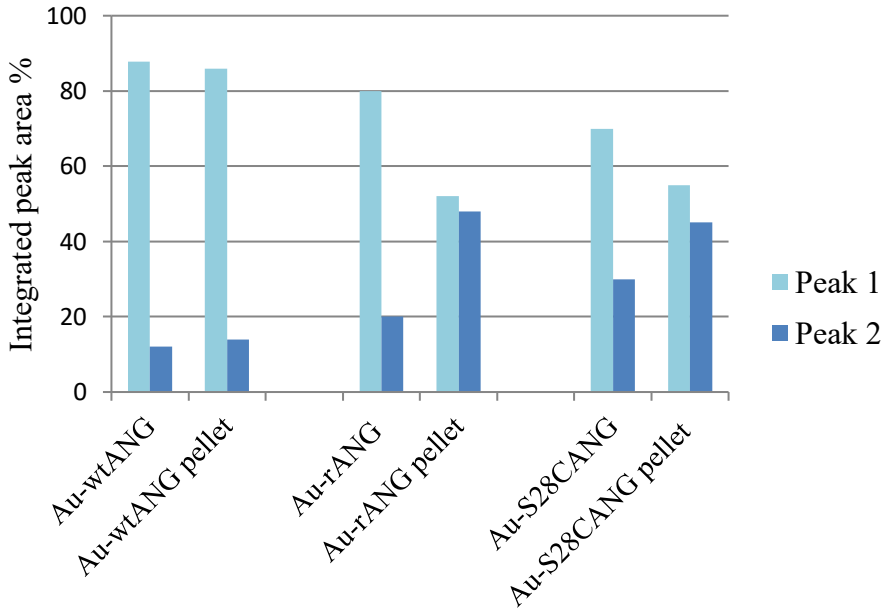

Figure 37- Percentage of the integrated area for the calculated plasmonic peak components (peak 1 and peak 2) by a Gaussian fit of the UV-vis spectra for the suspensions Au-wtAng, Au-rAng and Au-S28CAng and the second re-suspended pellets of the Au-protein hybrids.

DLS measures were carried out on the synthetized hybrid systems to assess the hydrodynamic diameter, which depend on both the single particle and/or clusters of aggregates "core" size and the proteins and solvation shell on the nanoparticles surface. Figure 38 shows, in agreement with the UV-vis spectra, that the measured hydrodynamic size for uncoated AuNPs is 35±5 nm, while the particles size increases up respectively to 51±1 nm for Au-wtANG, to 72±1 for Au-rANG and to 103±12 nm for Au-S28CANG thus also proving the presence of big cluster

of nanogold aggregate together with the AuNP-protein hybrids in particular for the Au-rANG and Au-S28CANG samples.

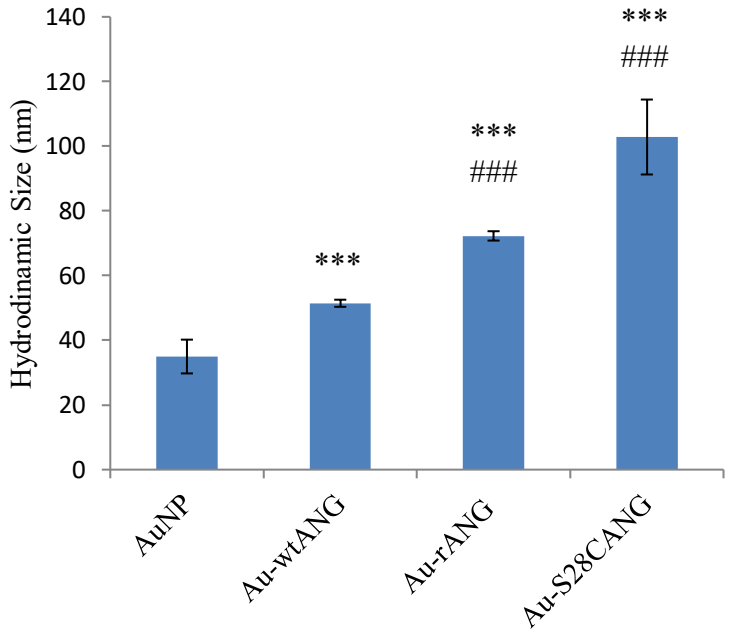

Figure 38- Hydrodynamic size of the bare AuNP ($4.3 \cdot 10^8$ NP/mL) and the functionalized nanosystems Au-wtANG ($2.9 \cdot 10^7$ NP/mL), Au-rANG ($1.4 \cdot 10^7$ NP/mL), Au-S28CANG ($7.3 \cdot 10^6$ NP/mL), measured by dynamic light scattering. (***) = $p < 0.001$ vs. AuNP; (###) = $p < 0.001$ vs. Au-wtANG (one-way ANOVA).

AFM analysis in AC mode in air were carried out on the bare AuNPs and the hybrids Au/protein (Figure 39). The maximum Z-averaged value (nanoparticle height) for the bare gold nanoparticles core is 12±2 nm, according to the UV-vis spectra discussed above. As to the washed pellets obtained for Au-wtANG, Au-rANG and Au-S28CANG, the measured values were respectively of 17±2 nm, 14±1 nm and 18±2 nm. Such data

clearly refer to the single protein-coated nanoparticles thus confirming the effective and irreversible protein immobilisation at the gold surface with different arrangement modes, while no clusters of aggregates were observed, probably because of their easier removal from the mica surface after washing procedure.

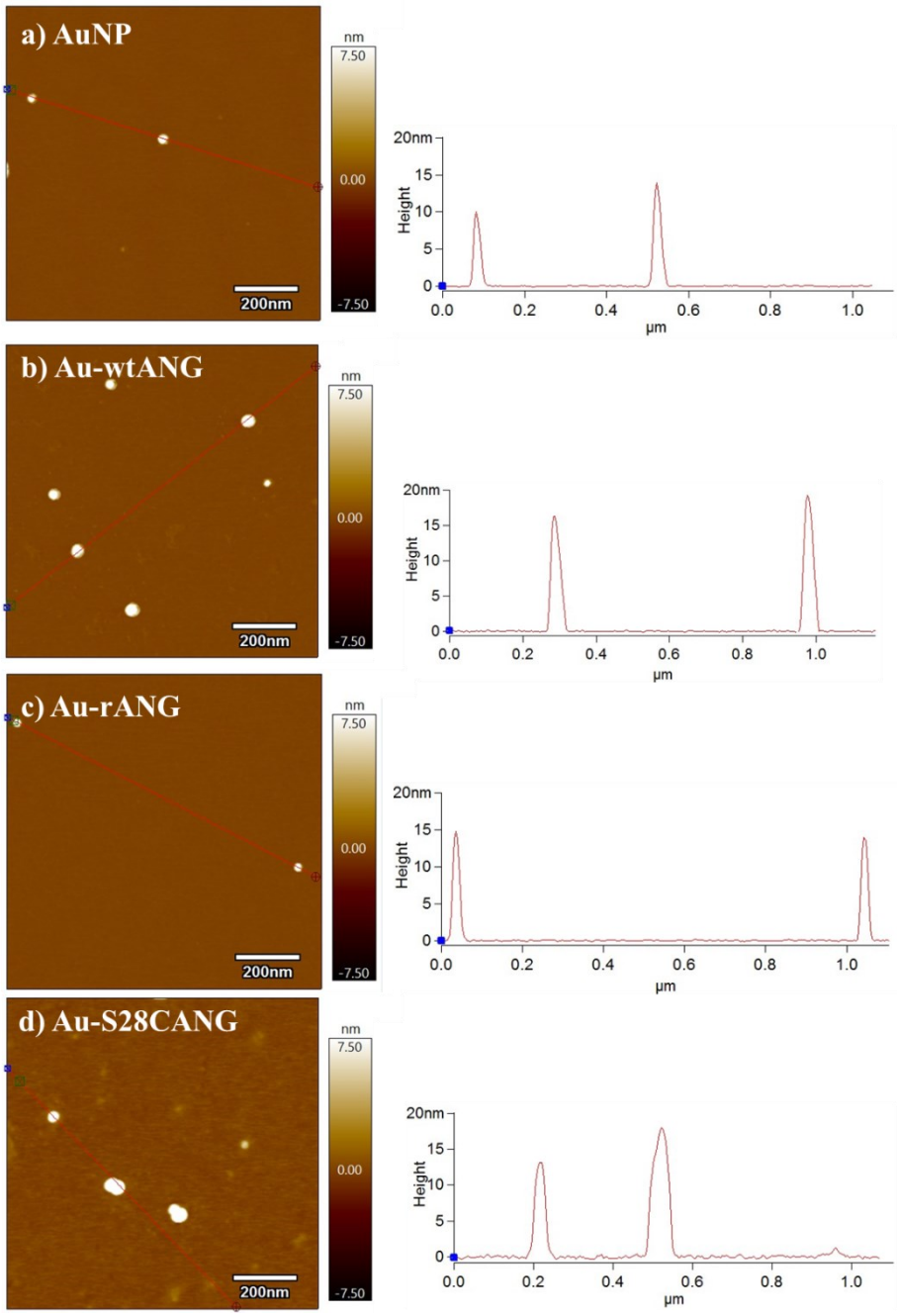

Figure 39- Atomic force microscopy micrographs of a) bare AuNP, b) Au-wtANG, c) Au-rANG and d) Au-S28CANG; scale bar = 200 nm. The graphs below each image show the histograms calculated for Z max.

QCM-D experiments were performed to investigate the interaction of the functionalized nanoparticles in comparison with the bare AuNPs and the free ANG protein, with model cell membranes made of supported lipid bilayers.

In the QCM-D experiment, quartz crystal sensor oscillates at the resonance frequency (5 MHz) when an alternating potential is applied. Since the resonance frequency (f) changes upon mass adsorption on the crystal surface, when rigid adlayers are formed, the deposited mass can be calculated from the Sauerbrey's equation, eqn. (13) [386].

$$\Delta m = \frac{C}{n} \cdot \Delta f \tag{13}$$

where f is the frequency, m the mass adsorbed and n the harmonic number. $C = \frac{t_q \cdot \rho_q}{f_0}$, with t_q and ρ_q being the thickness and the density of quartz, respectively. Such a value corresponds to ~ 17.7 Hz ng/cm^2 for a 5 MHz crystal.

Besides the deposited mass, QCM-D allows for monitoring a second parameter related to the energy loss, the dissipation (D), turning off the driving potential and monitoring the decay of the crystal oscillations. Such a parameter gives meaningful information about the viscoelastic properties of the film adsorbed, which are useful to characterize the interaction of SLBs with different molecules and nanosystems [387].

The QCM-D response observed after the addition of small unilamellar vesicles (SUVs) on 2D-SiO_2 crystals displays a typical two-phase process. The first phase reflects the adsorption of the vesicles on the silica surface until the minimum in frequency shift (increase in coupled mass) and the

maximum in dissipation shift (viscoelastic properties of the vesicles) are reached. This point corresponds to a critical coverage of the intact vesicles on the SiO_2 surface. The second phase reflects the vesicles disruption followed by the formation of a regular SLB. Typical values of Δf~-26 Hz and $\Delta D < 0.5 \cdot 10^{-6}$ indicate the formation of a homogeneous and stable lipid bilayer, in agreement with literature data [388].

In this work, QCM-D curves of Δf and ΔD are shown after the adsorption of zwitterionic SUVs made of POPC-NBD, followed by the addition of $2.3 \cdot 10^7$ NP/mL ($3 \cdot 10^{-9}$ M) bare AuNP, $2.5 \cdot 10^6$ NP/mL ($9 \cdot 10^{-10}$ M) Au-wtANG, $1.6 \cdot 10^6$ NP/mL ($9 \cdot 10^{-10}$ M) Au-rANG, $1.6 \cdot 10^6$ NP/mL ($9 \cdot 10^{-10}$ M) Au-S28CANG, and the proteins at the concentration of $5 \cdot 10^{-8}$ M wtANG and S28CANG, and $2 \cdot 10^{-8}$ M rANG, in 1mM MOPS buffer solution.

For all cases, the first part of the experiments displayed in Figure 40, clearly point to the successful formation of a SLB following the adsorption, rupture/fusion of the SUVs at the sensor surface. The next step of solvent exchange, from PBS to MOPS buffer, exhibits shifts in both the curves of frequency and dissipation, due to density and viscosity changes of the liquid layer at the interface with the sensor. Upon the addition of the protein (Fig. 40a) the frequency and the dissipation values of the QCM-D curves do not significantly change except than in the case of the mutant S28CANG, which induces a slight shift of the frequency of about -2.02 Hz. Thus, the obtained results do not provide evidence, at the studied conditions, of interactions between the proteins and the lipid membrane system, which remains stable on the SiO_2 surface.

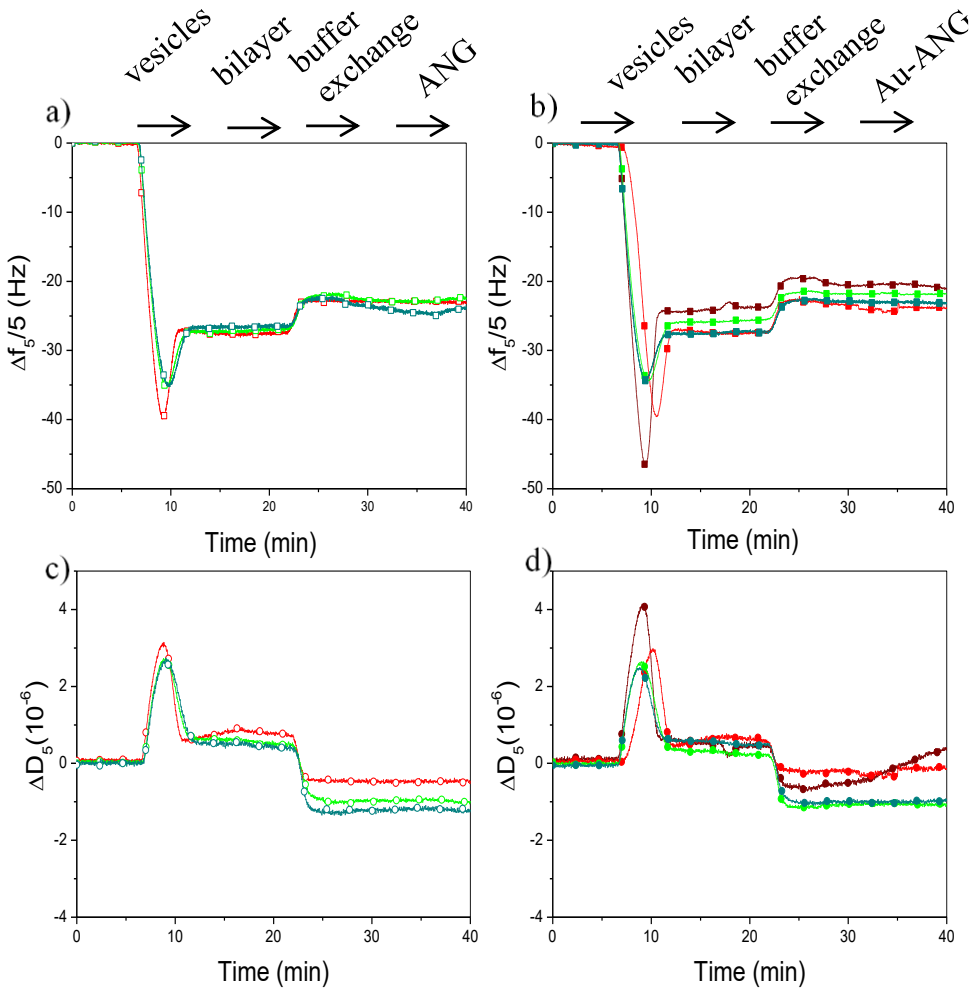

Figure 40- QCM-D curves of frequency and dissipation shifts corresponding to the overtones n=5 for vesicles POPC adsorption on 2D silica surfaces after the addition of (a-c) the free proteins at the concentration of $5 \cdot 10^{-8}$ M: wtANG (red); rANG (green); S28CANG (dark cyan) (open symbol); and (b-d) $2.3 \cdot 10^{7}$ AuNP/mL for citrate-capped bare nanoparticles (wine); $2.5 \cdot 10^{6}$ Au-wtANG (red); $1.6 \cdot 10^{6}$ Au-rANG (green); $1.6 \cdot 10^{6}$ Au-S28CANG (dark cyan) (solid symbol). Experiments were performed in 1 mM MOPS buffer (pH = 7.4).

Likewise, the addition of the functionalized Au-protein hybrids (Figure 40 b-d) does not perturb the lipid bilayer and only a no significant

reduction of the frequency, $\Delta f \sim -0.9$ Hz, is detected for all the studied systems. Noteworthy, the addition of the bare AuNPs, does not induce relevant frequency shifts, but significantly increases the dissipation value that, not reaching the equilibrium, reflects complex structural changes in the SLB and significant modifications of the viscoelastic properties of the model membrane systems [389]. These experimental findings provide evidence of the effective AuNPs functionalization with the studied proteins, which exhibit a comparable behaviour against the model membrane systems, both as free-molecules and ANG-adsorbed on the nanoparticles surface.

2.6.3 Functionalization of the nanoplatform Au-GO with wtANG (PAPER V)

Following an approach of increased complexity, the synthetized Au-GO hybrids were used as multifunctional nanoplatform for the delivery of wtANG, thus combining the antiangiogenic [28] and antioxidant [57] action of the colloidal gold as well as the pro-angiogenic [63] and antibacterial [61] features of GO together with the biological activity of the protein. Such an hybrid nanoplatform taking also the advantages of the selected nanomaterials, such as their high volume to surface area ratio, their electric, optical and mechanical properties [21, 23] along with the high specific delivery of the active molecule to the target site and its protection from the action of proteolytic enzymes [379], was studied as potential system to control the angiogenic process in the wound treatment (see section 1.3).

The functionalization of the hybrid platform Au-GO by a “pure” physical adsorption of wtANG was carried as follows. Briefly, the whole human angiogenin, wtANG, was added at the final concentration of $5 \cdot 10^{-8}$ M to the washed Au-GO hybrids in 1 mM MOPS (pH=7.4) (see section 2.2) and re-suspended at the concentration of $4.3 \cdot 10^{5}$ NP/mL ($6 \cdot 10^{-9}$ M). Finally, to rinse off unbounded proteins and to remove the excess of reactants, the functionalized nanohybrids were rinsed by two centrifugation steps (6,010 RCF, 15 min) in 1 mM MOPS. Figure 41 shows the UV-vis spectra recorded for the hybrids Au-GO before and after the addition of wtANG along with the UV-vis spectrum of the obtained Au-GO-wtANG pellet.

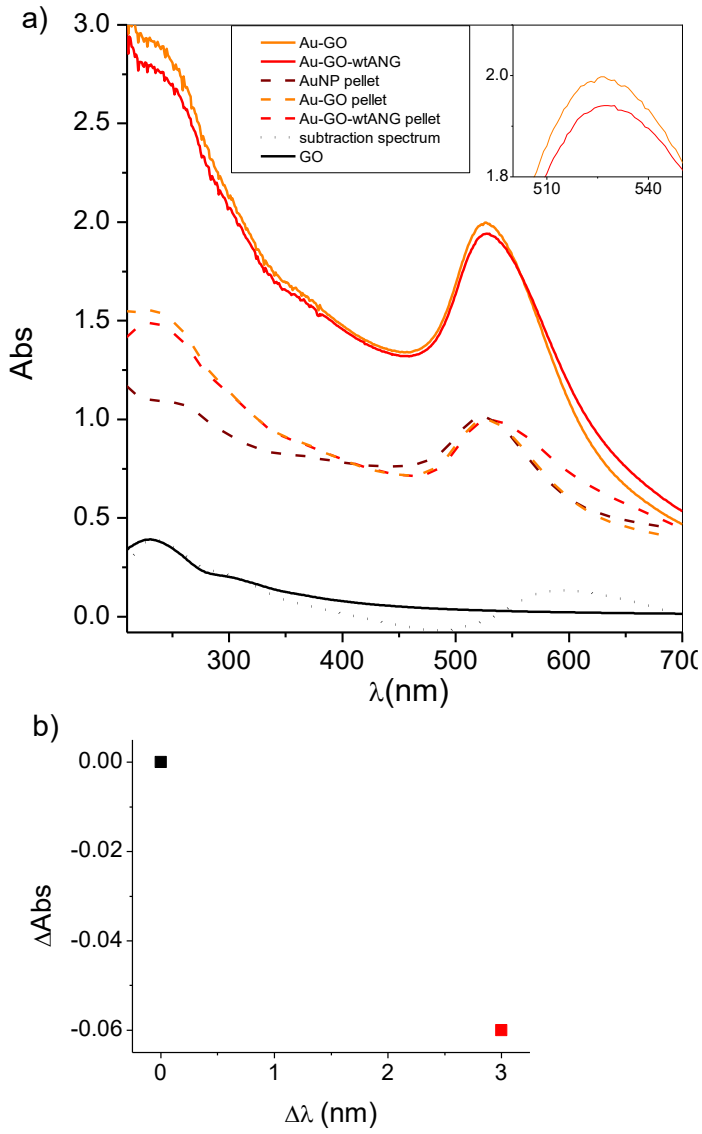

Figure 41- a) UV-visible spectra of $4.3 \cdot 10^5$ NP/mL Au-GO hybrids in 1mM MOPS (pH=7.4) before (orange) and after the addition of $5 \cdot 10^{-8}$ M wtANG (red); the dashed curves refer to the re-suspended pellet of AuNP (wine), as reference, Au-GO (orange) and Au-GO-wtANG (red), after the rinsing steps. In black is shown the UV-vis spectrum of GO and of the GO calculated from the difference spectrum (Au-GO)-AuNP (dotted line). In panel b) are shown the shifts in absorbance (ΔAbs) and wavelength (Δλ) of the plasmon peak after the addition of wtANG to the Au-GO hybrids with respect to the bare systems (black).

As described in section 2.2, the UV-vis spectrum of Au-GO, due to the interaction between AuNP and GO sheets, that changes the local dielectric environment of the gold nanoparticles, shows a red-shifted plasmon band ($\Delta\lambda$= 3 nm) with respect to the characteristic plasmon peak of spherical AuNPs with a diameter of about 14 nm [348]. Moreover, an absorption band at around 230 nm associated with the π–π^* transition of GO can be observed [355]. As to the functionalized system, Au-GO-wtANG, the addition of the protein, as expected, induces a variation of the plasmon peak, with red shifts and an increase of the FWHM value, of about 3 nm and 4 nm, respectively (Table 9). No significant changes in the maximum of absorbance are instead observed ($\Delta A \sim -0.06$). Moreover, the subtracted spectrum, by considering the molar extinction coefficient $\varepsilon = 37.81 \pm 0.06$ mL/mg·cm for GO, it is possible to calculate the presumable amount of GO surrounding the AuNPs, which is around $10.8 \cdot 10^{-2}$ mg/mL.

Table 9- Optical properties: shifts of the maximum of absorption (A_{max}) and of the wavelength at the absorbance maximum (λ_{max}), full width at half maximum (FWHM) values and optical diameters obtained upon the adsorption of ANG on the Au-GO surface.

Sample	**ΔA**	**Δλ (nm)**	**FWHM (nm)**	**d_{opt}**
Au-GO	-	-	63	30
Au-GO- wtANG	-0.06	3	67	38

The UV-vis spectrum of the hybrid Au-GO-wtANG after two rinsing steps (Figure 41, Table 10) shows that the distinctive plasmon peak shift

is maintained (Δλ ~ 3 nm) in comparison to the bare Au-GO hybrids and a significant increase of FWHM ~ 11 nm is further observed.

Table 10- Optical properties: maximum of absorption (A_{max}), shift of the wavelength at the absorbance maximum (Δλ), extinction coefficient (ε), full width at half maximum (FWHM) value as well as the calculated optical diameters and the nanoparticles concentration in both nM and NP/mL and the GO concentrations for the re-suspended pellets in 1 mM MOPS.

Sample	A_{max}	Δλ (nm)	ε ($cm^{-1}M^{-1}$)	FWHM (nm)	d_{opt}	[AuNP] nM	[AuNP] NP/mL	[GO] mg/mL
Au-GO pellet	0.589	-	$3.5 \cdot 10^9$	61	30	4.1	$2.9 \cdot 10^6$	0.147
Au-GO-wtANG pellet	0.995	3	$7.9 \cdot 10^9$	74	38	1.1	$3.9 \cdot 10^5$	0.108

Such an increase of the FWHM is indicative of a higher polydispersity of the colloidal suspension, due to the presence of several size populations of nanoparticles associated with both aggregation effects and the adsorption of the biomolecules on the hybrid Au-GO surface.

In regard to the aggregation, as shown for the hybrids Au-ANG (see section 2.6.2), it is most likely due to the interaction between the positively charged groups at the physiological pH of ANG, such as lysine, arginine and histidine, and the negatively charged citrate-capped AuNPs, that reduces the electrostatic stabilisation mechanism of the colloidal dispersion leading to bigger clusters of nanoparticles. Such an effect is particularly evident after the rinsing steps, through which we removed not only the weakly bound proteins but also the excess of citrate molecules, which additionally act as stabilizer of the nano-systems. Differently, the bare hybrids Au-GO, lacking of the positive groups of the protein, after

the washing procedure maintain their stability, since comparable values of both the wavelength at the absorbance maximum and FWHM are observed (Figure 41, Table 9-10).

As to the adsorption of molecules on the nanoparticle surface, using equations 10-12 (see section 2.6.1) [192] a protein fraction shell of $g = 0.74$ for Au-GO-wtANG could be calculated. From the g value, the calculated mass of protein absorbed on the hybrid Au-GO-wtANG per unit area is about 82 ng/cm^2. Thus, given the molecular weight of ANG (MW=14,200 g/mol) and the diameter d_{opt} = 30 nm for the hybrids Au-GO considered as core-shell spheres, the corresponding coverage in terms of molecules/NP is calculated as follows: 97 molecules of wtANG per each Au-GO system. Since the average angiogenin molecular dimensions are (70x62x32) Å^3 [383] the ideal monolayer coverage of the protein in the two *end-on* and *side-on* limit configurations is about 142 and 65 molecules/NP, respectively. Accordingly, at nanoparticle surface it can be figured out a disordered monolayer coverage of wtANG, most likely in the *side-on* configuration. Noteworthy, since the shift in the wavelength at the maximum absorbance is similar to that before the nanoparticle rinsing ($\Delta\lambda \sim 3$ nm) no significant loss of protein is detected for the Au-GO-wtANG pellet (Table 10).

Given the increased polydispersity of the systems obtained after the functionalization procedure, it was possible to calculate the component peaks referred to the protein-coated AuNPs and to nanogold aggregates by a Gaussian fit of the UV-vis spectra as shown in Figure 42.

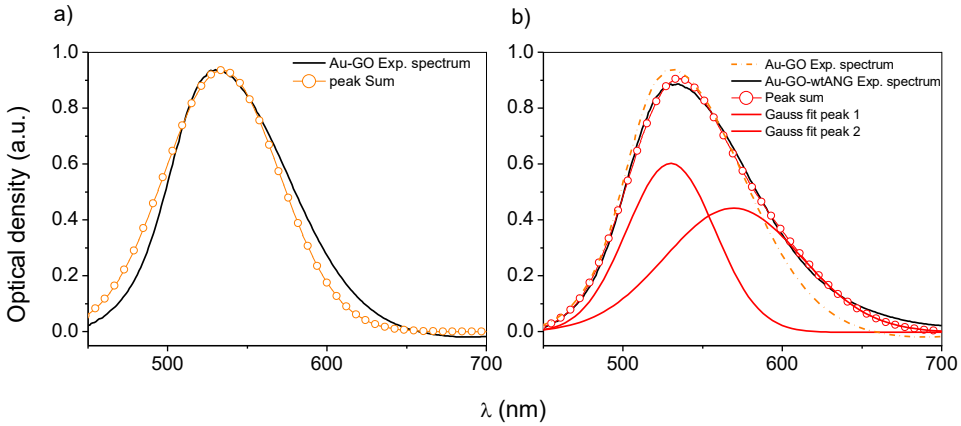

Figure 42- a) UV-vis spectra (experimental in black and curve fittings in orange or red) for: a) $4.3 \cdot 10^5$ NP/mL Au-GO bare nanoparticles (orange) in 1 mM MOPS (pH=7.4); b) $1.1 \cdot 10^5$ NP/mL Au-GO-wtANG (red); In b the spectrum of uncoated Au-GO (orange dash-dotted line) is shown as reference.

The two absorption peaks obtained from the spectral deconvolution and centred at 530 nm (peak 1) and 569 nm (peak 2) can be assigned to the protein-coated Au-GO and to the clusters of Au-GO aggregates of about 150 nm in size, respectively. Noteworthy, even if the percentage of the integrated area for the calculated peak 1 and peak 2 does not change after the rinsing steps, the peak 2 related to the aggregated nanoparticles is red-shifted after the washing procedure, thus indicating the presence of bigger Au-GO aggregates of around 180 nm (Figure 43) but a component of at least 50% of the overall population related to the protein-coated hybrid system is maintained (Figure 44).

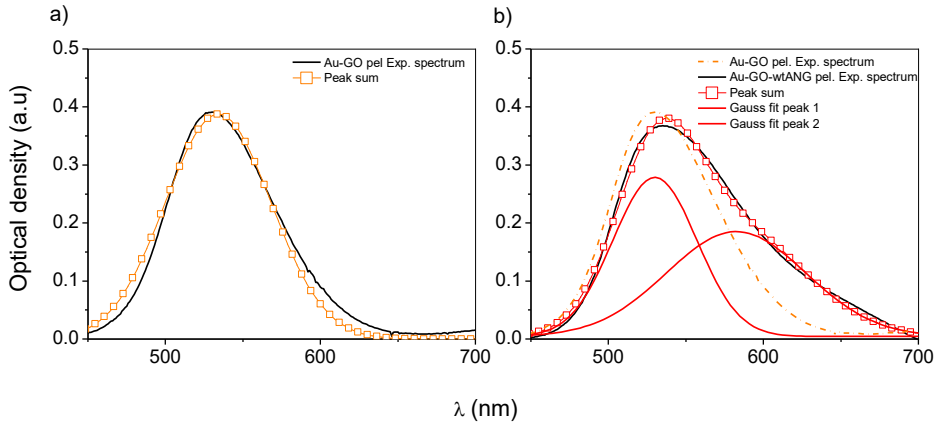

Figure 43- a) UV-vis spectra (experimental in black and curve fittings in orange or red) of the second re-suspended pellets in 1 mM MOPS (pH=7.4) for: a) $2.9 \cdot 10^6$ NP/mL Au-GO hybrid (orange); b) $3.9 \cdot 10^5$ NP/mL Au-GO-wtANG (red); In b the spectrum of uncoated Au-GO (orange dash-dotted line) is shown as reference.

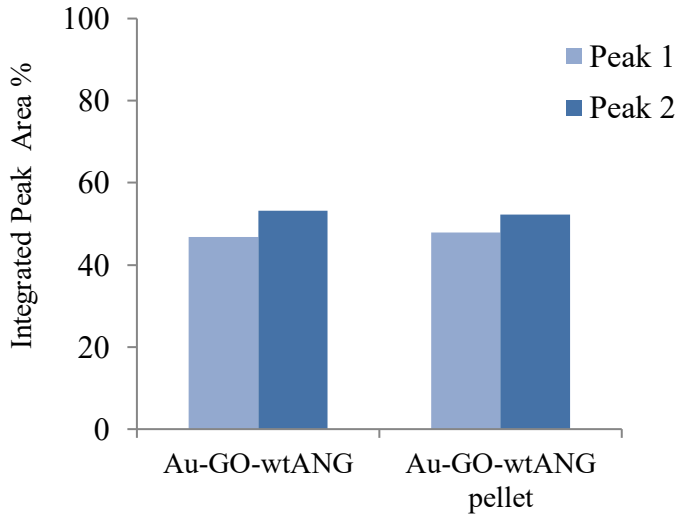

Figure 44- Percentage of the integrated area for the calculated plasmonic peak components (peak 1 and peak 2) by a Gaussian fit of the UV-vis spectra for the dispersion Au-GO-wtANG and the second re-suspended pellets of the hybrid.

DLS measures were carried out on the synthetized systems to detect the average hydrodynamic size of the particles, considering both the single particle and/or clusters of aggregates "core" size and the proteins-coated hybrids. Figure 45 shows, in agreement with the UV-vis spectra, that the measured hydrodynamic size for monodisperse and uncoated AuNPs is 23 ± 1 nm, and increases up to 27 ± 1 for the hybrid Au-GO. As to the Au-GO-wtANG sample, the particles size increases up to 204 ± 34 nm, thus proving the presence of big clusters of nanogold aggregates, in agreement with the Gaussian fit of the UV-vis spectrum. Such an aggregate component, with an optical diameter of about 180 nm, represents at least the 50% of the overall particle population, thus explaining the high average value of hydrodynamic diameter obtained.

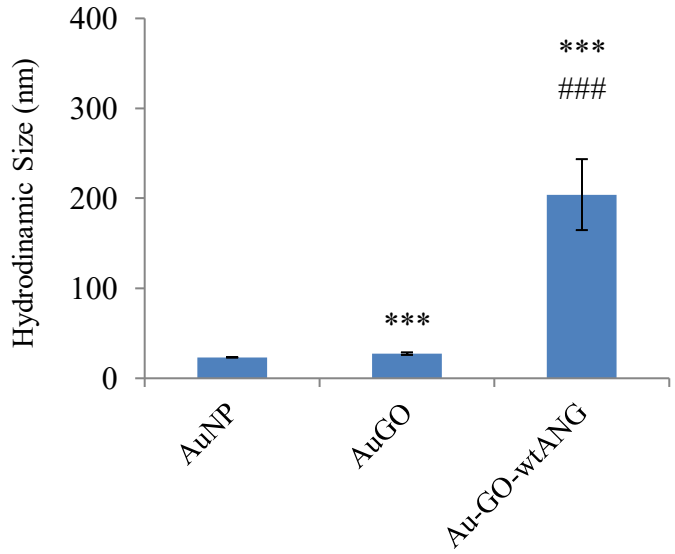

Figure 45- Hydrodynamic size of the bare AuNP ($2.5 \cdot 10^7$ NP/mL), the hybrid Au-GO ($2.9 \cdot 10^6$ NP/mL) and the functionalized nanosystems Au-GO-wtANG

(3.9 $\cdot 10^5$ NP/mL) measured by dynamic light scattering. (***) = $p < 0.001$ vs. AuNP; (###) = $p < 0.001$ vs. Au-GO-wtANG (one-way ANOVA).

QCM-D experiments (see section 2.6.2) were performed to investigate the interaction of the synthetized hybrid systems Au-GO-wtANG in comparison with the bare Au-GO and the free wtANG protein, with model cell membranes made of supported lipid bilayers.

QCM-D curves of Δf and ΔD are shown after the adsorption of zwitterionic SUVs made of POPC-Rhod, followed by the addition of $5.1 \cdot 10^5$ NP/mL ($7 \cdot 10^{-10}$ M) Au-GO, $2.2 \cdot 10^4$ NP/mL ($6 \cdot 10^{-11}$ M; GO ~ $20 \cdot 10^{-3}$ mg/mL) Au-GO-wtANG, and wtANG and GO, as reference, at the concentration of $5 \cdot 10^{-8}$ M and $30 \cdot 10^{-3}$ mg/mL, respectively, in 1 mM MOPS buffer solution.

As shown in figure 46, the QCM-D response observed after the addition of small unilamellar vesicles (SUVs) on 2D-SiO_2 crystals displays the typical two-phase process and the formation of an homogeneous and stable lipid bilayer is confirmed by the frequency and dissipation shifts of $\Delta f \sim$-26 Hz and $\Delta D < 0.5 \cdot 10^{-6}$, respectively [388]. The following step of solvent exchange, from PBS to MOPS buffer, exhibits the typical shifts in both the curves of frequency and dissipation, due to density and viscosity changes of the liquid layer at the interface with the sensor. Upon the addition of the protein (Fig. 46a-c) the frequency and the dissipation values of the QCM-D curves do not significantly change, thus confirming that, at the studied conditions, no interactions between the proteins and the lipid membrane system occurs and the SLB remains stable on the SiO_2 surface. Differently, the addition of GO induces an increase of the dissipation value, not reaching the equilibrium, thus reflecting complex structural changes in the SLB [389] mostly due to the interaction of the hydrophobic domains of

GO and the lipid tails of the bilayer [390], as expected from its biological effect on the cellular membrane [391]. Noteworthy, the addition of the hybrid Au-GO, as shown for the AuNPs nanosystems (Figure 40 b-d) slightly reduces the frequency, $\Delta f \sim -1.7$ Hz and increases the dissipation value ($\Delta D = 0.13 \cdot 10^{-6}$) which, in this case, rapidly reaches the equilibrium. Such data further confirm the effective conjugation of the gold nanosystems and the GO sheets, that due to the presence of AuNPs differently interacts with the lipid bilayer.

Interestingly, similarly to the free protein case, the addition of the functionalized hybrid Au-GO-wtANG (Figure 60 b-d) does not perturb the lipid bilayer and only a no significant reduction of the frequency, $\Delta f \sim -1$ Hz, is detected. These experimental findings provide evidence of the effective Au-GO functionalization with wtANG, which exhibit a comparable behaviour against the model membrane systems, both as free-molecules and ANG-adsorbed on the hybrids Au-GO.

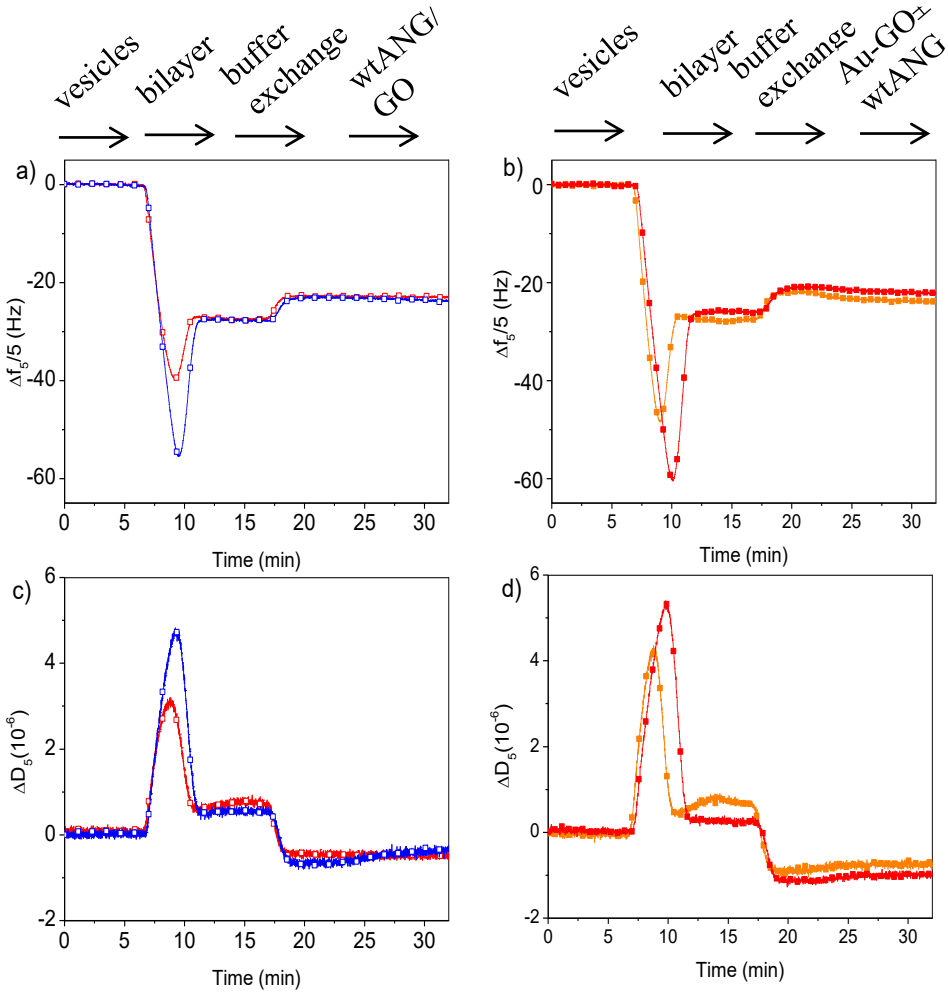

Figure 46- QCM-D curves of frequency (a-b) and dissipation (c-d) shifts corresponding to the overtones n = 5 for vesicles POPC adsorption on 2D silica surfaces after the addition of (a-c) the free protein at the concentration of $5 \cdot 10^{-8}$ M wtANG ((open square) red), $30 \cdot 10^{-3}$ mg/mL GO (open square in blue) and (b-d) $5.1 \cdot 10^{5}$ NP/mL for Au-GO (solid square in orange); $2.2 \cdot 10^{4}$ NP/mL wtANG-added Au-GO hybrids (solid square in red); Experiments were performed in 1 mM MOPS buffer (pH = 7.4).

Chapter 3- Cellular Assays

3.1 Anticancer effects

The effective ability of the synthetized hybrid systems to control the pro/anti-angiogenic processes for potential application in cancer treatment was investigated, for an initial screening, by means of in vitro cellular experiments on tumour and normal cells. In particular, human neuroblastoma (SH-SY5Y cell line) and human glioblastoma (A172 cell line) were chosen as experimental models of cancer, while normal cells like differentiated neuroblastoma d-SHSY5Y and fibroblasts (MRC-5 cell line) were used as control. SH-SY5Y cells were originally isolated from a metastatic bone tumour biopsy of a 4-year old child affected by neuroblastoma, which is a rare form of nerve cancer [392]. Whereas A172 cells were isolated from the glioblastoma, that is an aggressive brain cancer, of a 53-year old male [393]. These solid forms of tumour, that affect the human central nervous systems, are widely investigated owing to the elevated incidence, their highly malignant nature and invasive properties as well as their high chemo-resistance and difficult to access for the surgical resection, that often lead to a poor prognosis [394, 395]. Moreover, from an experimental point of view, such cell lines grow and adhere to the culture flasks and show high proliferation rate that allows their large-scale expansion with relative ease to culture and a straightforward use as cellular models for in vitro experiments [393, 396]. Noteworthy, the treatment of SH-SY5Y cells with retinoic acid allows for their de-differentiation to mature, non-tumour and neuron-like phenotype cells, d-SHSY5Y, giving the advantage to compare the response of malignant and normal brain cells with similar features [397]. Several

studies demonstrated significant differences between SH-SY5Y cells in their undifferentiated and differentiated states. Undifferentiated SH-SY5Y cells rapidly proliferate and appear to be non-polarized, with very few and short processes [396]. On the other hand, d-SH-SY5Y are characterized by long, branched processes and a decreased growth rate. Moreover, these cells are able to express markers of mature neurons, thus representing an ideal homogeneous model of human neurological cells [398].

Fibroblast cell line MRC-5 was also used as in vitro model of non-cancer cell. Fibroblasts are mesenchymal-derived cell types, crucial for several physiological processes such as synthesis of the extracellular matrix, epithelial differentiation as well as regulation of inflammation and wound healing, being involved in the secretion of several growth factors [399, 400]. In particular the MRC-5 cell line derives from the lung tissue of a 14 week old aborted male foetus and similarly to the SH-SY5Y and the A172 cells, are adherent cells, easy to culture and to maintain in vitro [401].

The cellular response was studied in term of cytotoxicity and proliferation by using the MTT assay. Moreover, cellular internalization, lysosomal endocytosis and cytoskeleton rearrangement were studied by means of laser scanning confocal microscopy. Lysosomes, indeed, are cellular organelles involved in the digestion of materials derived from both outside and inside the cells during endocytosis, phagocytosis and autophagy and their function is indispensable for maintaining cellular homeostasis [402]. To this regard, it was demonstrated that AuNPs accumulate into lysosomes thus leading to lysosome enlargement and further causing impairment of their degradation capability [403]. As to the cytoskeleton, it is known that ANG, through the amino acid sequence (60-

68) [276], is able to interact with actin, which is the most abundant cytoskeletal protein, thus inducing cytoskeleton rearrangements that are crucial for the angiogenesis promotion [277]. Cell cytoskeleton, indeed, is responsible for the morphology and movements of the cells showing a pivotal role in vessel growth, which involves migration, proliferation and finally differentiation of endothelial cells [404] as well as in tumour invasion and metastasis so that it is also a key target for cancer therapy [405].

3.1.1. Cellular response to the hybrid Au-ANG peptides/protein

3.1.1.1 Response of SH-SY5Y and MRC-5 cells to Au-Ang peptides in terms of cell viability and interaction with cellular organelles (cytoskeleton and lysosomes) (PAPER I)

Cell viability and proliferation experiments on undifferentiated neuroblastoma (SH-SY5Y) and fibroblast (MRC-5) cell lines, were carried out to evaluate the cellular response to the three different peptides ($Ang_{60-68}Cys$, Ang_{60-68}, FAM-Ang_{60-68}) and the hybrids Au-Ang, while bare AuNPs were used as control.

MTT assay was performed incubating the cells, for 24 and 40 hrs, with the samples at two different concentrations namely $3.5 \cdot 10^7$ NP/mL ($5 \cdot 10^{-9}$ M) and $7.1 \cdot 10^7$ NP/mL ($1 \cdot 10^{-8}$ M) for AuNPs; $1.6 \cdot 10^6$ NP/mL ($9 \cdot 10^{-10}$ M) and $3.7 \cdot 10^6$ NP/mL ($2 \cdot 10^{-9}$ M) for both Au-Ang_{60-68} and Au-$Ang_{60-68}Cys$; $4.9 \cdot 10^5$ NP/mL ($5 \cdot 10^{-10}$ M) and $9.9 \cdot 10^5$ NP/mL ($1 \cdot 10^{-9}$ M) for Au-Fam-Ang_{60-68} hybrid; and the free peptides at the concentration of $3 \cdot 10^{-5}$ M.

Literature data demonstrated that the AuNPs cytotoxicity mostly depends on the size of the nanosystems. Thus, smaller AuNPs that more easily reach intracellular organelles such as nucleus, are often considered dangerous. In this regard, it has been shown that AuNPs with a diameter of about 1 nm induce high cytotoxicity to neuroblastoma cells compared to gold nanoparticles with a diameter of about 15 nm that are no-toxic up to 100-fold higher concentration [406]. On the other hand, no cytotoxic effects were observed after the treatment of fibroblast MRC-5 with 10-40 nm AuNPs [407]. Along with the size, the surface properties of the nanosystems, such as charge, roughness as well as coating, significantly

affect the physiological interaction with cells thus changing their cytotoxic effect [222]. Noteworthy, such cytotoxic effects are considerably cell-specific, so that citrate-capped gold nanoparticles (13 nm in diameter) were found to be toxic to a human carcinoma lung cell line but not to human liver carcinoma cell line at same dosage [408].

As to the interaction with neuroblastoma cells, our results (Figure 47a) do not show any significant effects in term of cytotoxicity and proliferation for all the free peptides at the studied conditions. The bare AuNPs (d_{opt} = 14 nm), in agreement with literature data, do not show cytotoxicity after 24 hrs of treatment, while after 40 hrs of incubation, it is shown a reduction of the cell viability of 10% and 18%, at the two studied concentrations, respectively.

As to the functionalized Au-Ang systems, it is found that all the three hybrids, at longer time incubation, slightly decrease the cell viability, in particular $Ang_{60-68}Cys$ and $Au\text{-}Ang_{60-68}$ at the higher concentration of $3.7 \cdot 10^6$ NP/mL ($2 \cdot 10^{-9}$ M) and $Au\text{-}Fam\text{-}Ang_{60-68}$ after 24 hrs incubation at the concentration of $4.9 \cdot 10^5$ NP/mL ($5 \cdot 10^{-10}$ M). No proliferative effects are showed at all the tested condition after 20 and 40 hrs incubation on neuroblastoma cells.

On the other hand, general proliferative effects were found after the treatment of fibroblasts with the studied nanosystems. In particular AuNPs slightly increase cell proliferation, after both 24 and 40 hrs of incubation, at the two tested concentration and similar effects were shown for the functionalized systems, $Au\text{-}Ang_{60-68}$ and $Au\text{-}Fam\text{-}Ang_{60-68}$, while only the treatment with $Au\text{-}Ang_{60-68}Cys$ shows significant cytotoxicity at the highest concentration of $3.7 \cdot 10^6$ NP/mL ($2 \cdot 10^{-9}$ M). As to the peptides, none of the samples, Ang_{60-68}, $Ang_{60-68}Cys$, $Fam\text{-}Ang_{60-68}$ seems to

influence the fibroblast proliferation and only Ang_{60-68}, after 40 hrs of treatment, increases the viability of about 15%.

In summary, the MTT assay results, according to literature data, demonstrate that the incubation time as well as the cell line and the different AuNPs functionalization, have a crucial role in determining cytotoxicity and cell damage [409]. Thus, a reduction of the cell viability, at longer time incubation, is found on cancer cells treated with the synthetized nanosystems, while proliferative effects are shown on normal cells. These results prove the efficacy of the synthetized hybrids as anti-cancer platform at longer incubation time. Moreover, the controlled modification of the surface properties, obtained through the two different functionalization approaches and so "pure" physisorption for Ang_{60-68} and Fam-Ang_{60-68}, and prevalent chemisorption for Ang_{60-68}Cys, differently modulate the interaction of the biomolecules immobilized on the gold surface and cellular organelles, and so their response in term of cytotoxicity and proliferation.

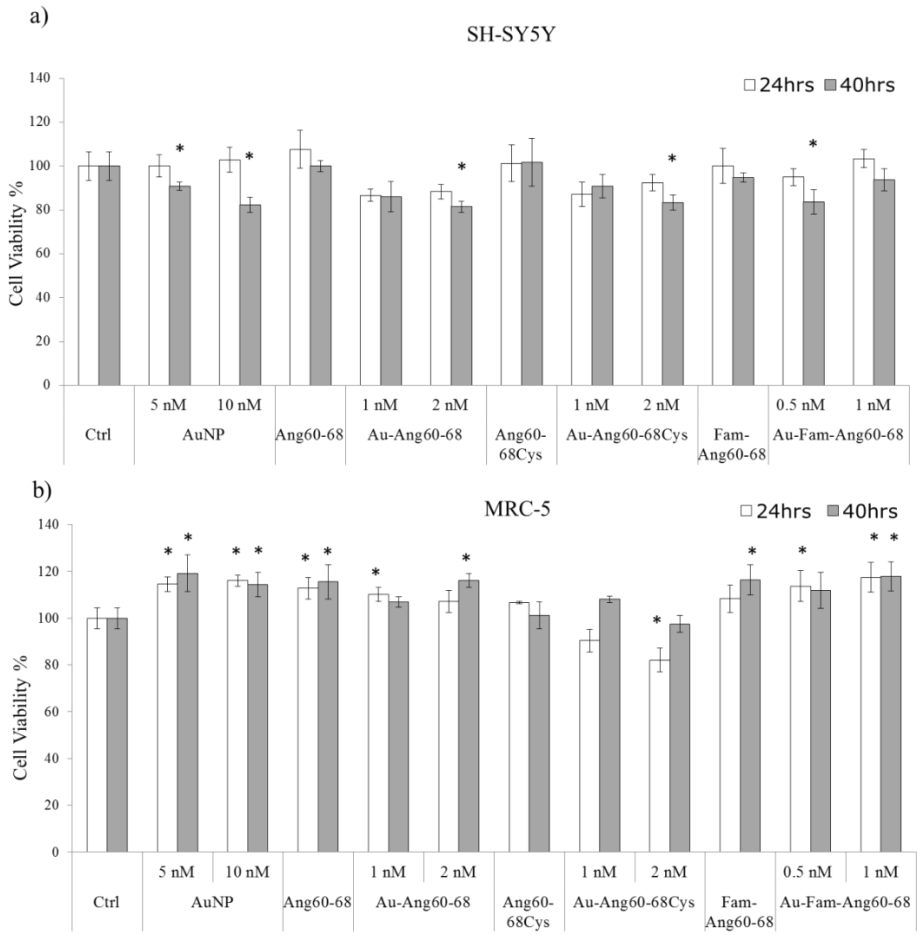

Figure 47- MTT experiment on different cell lines: a) SH-SY5Y (neuroblastoma) and b) MRC-5 (fibroblast). Cells were incubated for 24 and 40 hrs with AuNPs, Au-Ang$_{60–68}$, Au-Ang$_{60–68}$Cys, Au-Fam-Ang$_{60–68}$, and the free peptides Ang$_{60–68}$, Ang$_{60–68}$Cys, Fam-Ang$_{60–68}$. The concentrations were 5 nM and 10 nM for AuNPs and 30 μM for the peptides. Results are presented as mean ± SEM from experiments in triplicate and normalized with respect to the control untreated cells. Asterisk (*) represents the correlation significant at the $p \leq 0.05$ vs. Ctrl.

As to the interaction with cellular organelles, confocal microscopy and optical micrographs of neuroblastoma and fibroblast cell lines were shown in Figures 48-50.

Figure 48 displays the recorded micrographs of neuroblastoma cells after 2 hrs of treatment with the three ANG peptides (Figure 48b-d), the bare AuNPs (Figure 48e) and the functionalized systems (Figure 4 f-h).

In the control, globular actin aggregates are well noticeable and the filaments are regular and homogeneously distributed, whereas the lysosomal staining shows the typical spotted distribution. The incubation with Ang_{60-68} (Figure 48 b) leads to thinner actin filaments, that appear, mostly condensed along the cell membrane. A similar effect was obtained after the treatment with Ang_{60-68}Cys (Figure 48 c), but with a more effective actin activation, confirmed by the higher intensity of the green emission (Figure 49 a). The incubation with Fam-Ang_{60-68} (Figure 48 d) induces a significant intensification of the green fluorescence, with respect to the control, also due to the carboxyfluorescein moiety contribution, nevertheless the actin activation can be well perceptible and associated with the green dot spots. In regard to the lysosomal staining, all the three peptides significant increase the intensity of signal with respect to the control, thus proving an effective up-take of the biomolecules, which further interact with the intracellular organelles (Figure 49 b).

As to the nanosystems, AuNPs (Figure 48 e), well visible in optical bright field as dark spots, are rather diffuse within the cytoplasm, thus confirming their effective ability to enter the cells via endocytosis, even if AuNPs do not induce relevant cytoskeleton changes with respect to the control (Figure 49 a).

As to the interaction with lysosomes, it is well-known that gold nanoparticles accumulate into these cellular organelles, thus causing impairment of their degradation capability and lysosomes enlargement [403]. Accordingly, the lysosomal staining, after the incubation with

AuNPs, shows an increase of the organelles volume detected as an enhancement of the red spotted signal of the stained organelles.

The treatment with the hybrid Au-Ang$_{60-68}$ (Figure 48 f) more markedly increases the intensity of the actin staining in comparison with the other two hybrids Au-Ang$_{60-68}$Cys and Au-Fam-Ang$_{60-68}$ and the actin filaments are well-defined, regular and particularly condensed on the cellular membrane. Moreover, Ang$_{60-68}$ seems to enhance the AuNPs internalization that appear spread into the cells and co-localized with the actin filaments. Lysosomes are larger and activated with respect to the control (Figure 49 b).

The incubation with Au-Ang$_{60-68}$Cys (Figure 48g) leads to a different reorganization of the cell cytoskeleton with respect to the Au-Ang$_{60-68}$ and in particular green points, due to presence of the globular actin, are markedly visible. Moreover, the covalently bound peptide seems to more efficiently direct the localization of the hybrid nanosystems on the cell membrane, thus reducing the interaction with lysosomes that seem to be less stimulated with respect to the Au-Ang$_{60-68}$ treated cells.

The treatment with Au-Fam-Ang$_{60-68}$ leads to a less actin activation with respect to the free peptide Fam-Ang$_{60-68}$ which more easily seems to interact with the cytoskeleton protein filaments (Figure 48 h). Interestingly, the optical image displays the presence of bigger AuNPs aggregates into the cells, associated to an higher cellular stress and lysosomes activation.

The finding results, clearly demonstrate the maintenance of the biological properties, in terms of interaction with the cellular cytoskeleton, of the peptides immobilized on the gold surface, leading to a relevant reorganization of the actin, with respect to the control. Noteworthy, in the

hybrids, in agreement with the MTT assay, the physisorbed (Ang_{60-68}, $Fam\text{-}Ang_{60-68}$) and the chemisorbed ($Ang_{60-68}Cys$) peptides differently affect the cellular organelles, most likely due to their distinctive adsorption modes which further affect their biological behaviour.

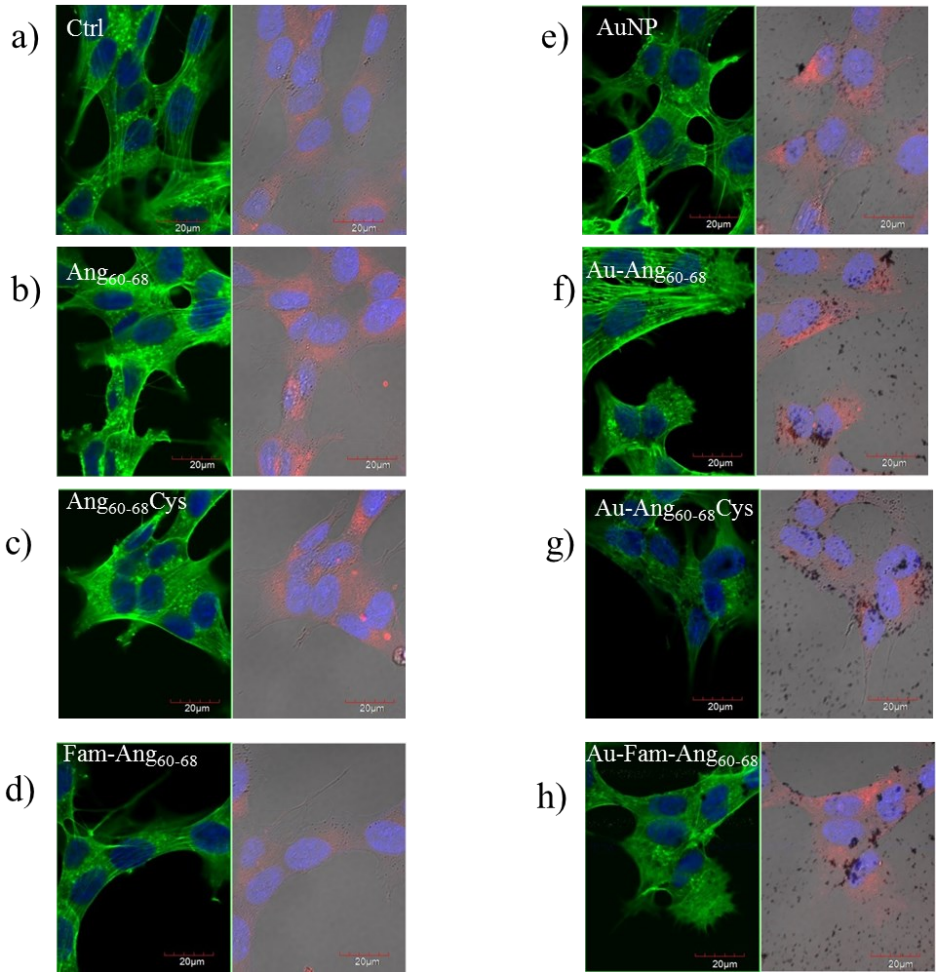

Figure 48- LSM merged optical bright field and fluorescence (in blue, nuclear staining, $\lambda_{ex/em}$=405/425–475nm; in green, actin staining and Fam moiety, $\lambda_{ex/em}$=488/500–530 nm; in red, LysoTracker deep red, $\lambda_{ex/em}$=633⁄650-700) images of SH-SY5Y neuroblastoma cells after 2 hrs of incubation with: (a)

control, (b) $3 \cdot 10^{-5}$ M Ang_{60-68}, (c) $3 \cdot 10^{-5}$ M $Ang_{60-68}Cys$, (d) $3 \cdot 10^{-5}$ M Fam-Ang_{60-68}, (e) $3.5 \cdot 10^{7}$ NP/mL ($5 \cdot 10^{-9}$ M) AuNP, (f) $1.6 \cdot 10^{6}$ NP/mL ($9 \cdot 10^{-10}$ M) Au-Ang_{60-68}, (g) $1.6 \cdot 10^{6}$ NP/mL ($9 \cdot 10^{-10}$ M) Au-$Ang_{60-68}Cys$, (h) $4.9 \cdot 10^{5}$ NP/mL ($5 \cdot 10^{-10}$ M) Au-Fam-Ang_{60-68}. Scale bar = 10 µm.

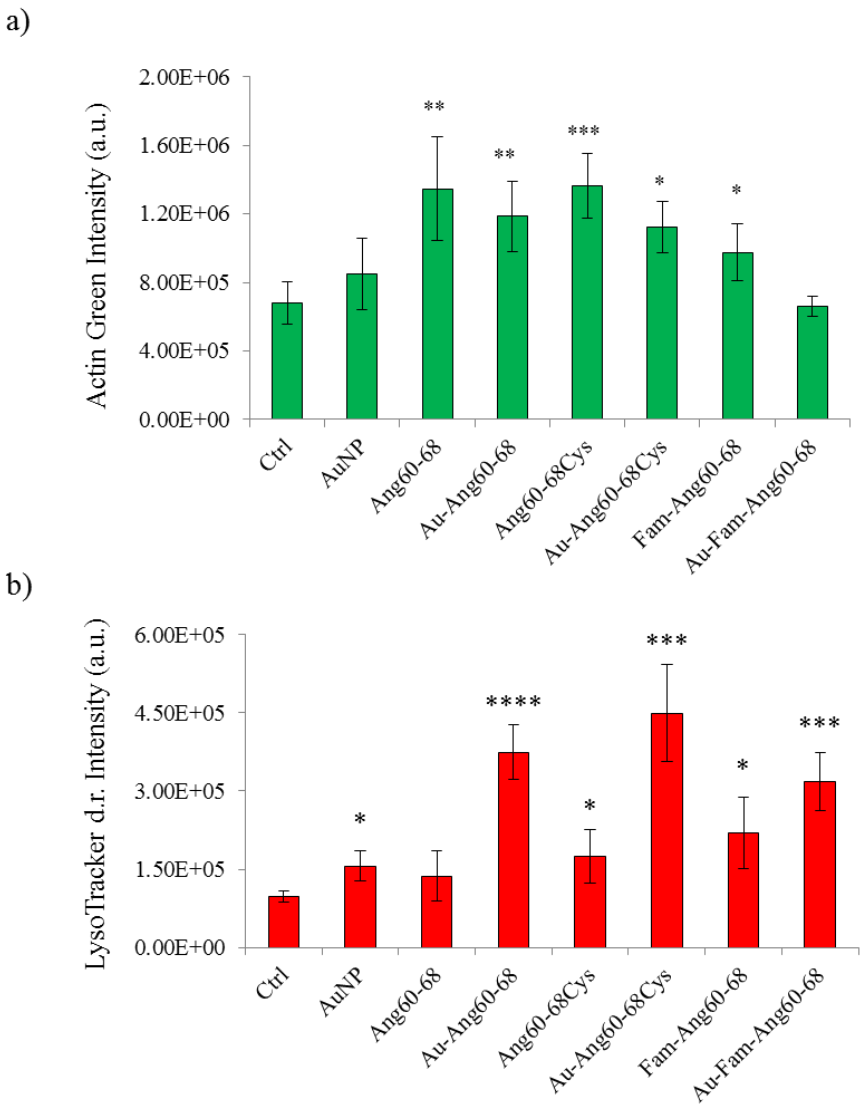

Figure 49- Intensity value of fluorescence corresponding to the a) Actin Green and b) LysoTracker deep red. Bars represent means ± SEM of at least 5

experiments. (*) p <0.05, (**) p <0.01, (***) p<0.001, (****) p<0.0001 vs. Ctrl. (One-way ANOVA).

Figure 50 shows the confocal microscopy micrographs and optical images of the lysosomes and actin-stained fibroblast cell line.

In the control, the filament of actin are well-defined, regular and elongated, while differently to the trend observed on neuroblastoma, the treatment with Ang_{60-68} (Figure 50 b) induces a more marked actin activation (Figure 51 a) and the fibres appear dense and spread compared to the Ang_{60-68}Cys, which leads to thinner actin fibres more confined along the cellular membrane (Figure 50 c). As to the lysosomes, Ang_{60-68} and Ang_{60-68}Cys no significantly affect this cellular organelle with respect to the untreated control (Figure 51 b). The incubation with Fam-Ang_{60-68} (Figure 50 d), instead, leads to a general increase of the signals referred to the stimulation actin fibres and lysosomes with respect to the control.

In regard to the nanosystems, in contrast with the response showed for neuroblastoma cells, the incubation with AuNPs (Figure 50 e) increases the actin-stained intensity and the protein filaments appear widespread and thin. Moreover, in the optical image it is possible to observe the effective internalization of AuNPs with a consequent increase of the lysosome activation (Figure 51 b). The treatment with Au-Ang_{60-68} (Figure 50 f) induces the formation of thin actin filaments that appear diffused and widespread in the whole cell. The nanoparticles are internalized, but lysosomes staining is comparable to the control. Indeed, optical image shows the presence of big clusters of AuNP aggregates that are not able to efficiently interact with the intracellular organelles.

As to the hybrid Au-Ang_{60-68}Cys (Figure 50 g) it is found to strongly stimulate the actin cytoskeleton through the formation of dense and

elongated fibres, that appear mostly confined near the cell membrane where the nanoparticles are largely localized. Lysosomes, instead, appear bigger and swelled (Figure 51 b).

The biological response to the Au-Fam-Ang$_{60-68}$ hybrids (Figure 50 h) is similar to that observed for the Au-Ang$_{60-68}$ system. Noteworthy, the actin staining observed is completely different with respect to signal obtained after the treatment with the free peptide Fam-Ang$_{60-68}$, thus suggesting an unmistakable nanoparticle effect.

The obtained results highlight the cell-specific action of the synthetized systems, which differently affect the two studied cell lines in term of cytoskeleton rearrangement and lysosomes stimulation, as confirmed by the MTT results. Moreover, the preferential localization of the hybrids system along the cellular membrane, especially found for the Au-Ang$_{60-68}$Cys sample, additionally prove the role of the 60-68 ANG sequence in the binding to the cell membrane.

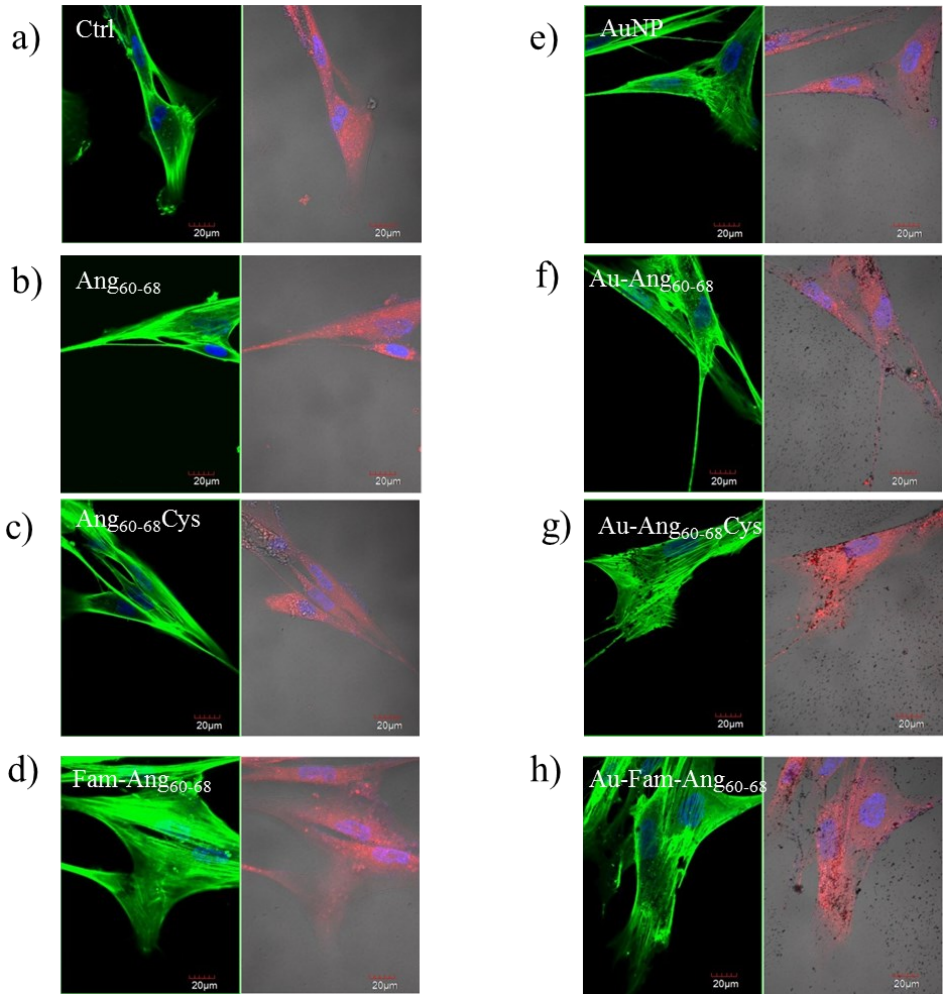

Figure 50- LSM merged optical bright field and fluorescence (in blue, nuclear staining, $\lambda_{ex/em}$=405/425–475nm; in green, actin staining and Fam moiety, $\lambda_{ex/em}$=488/500–530 nm; in red, LysoTracker deep red, $\lambda_{ex/em}$=633/650-700) images of MRC-5 fibroblast cells after 2 hrs of incubation with: a) control, b) $3 \cdot 10^{-5}$ M Ang_{60-68}, c) $3 \cdot 10^{-5}$ M $Ang_{60-68}Cys$, d) $3 \cdot 10^{-5}$ M Fam-Ang_{60-68}, e) $3.5 \cdot 10^{7}$ NP/mL ($5 \cdot 10^{-9}$ M) AuNP, f) $1.6 \cdot 10^{6}$ NP/mL ($9 \cdot 10^{-10}$ M) Au-Ang_{60-68}, g) $1.6 \cdot 10^{6}$ NP/mL ($9 \cdot 10^{-10}$ M) Au-$Ang_{60-68}Cys$, h) $4.9 \cdot 10^{5}$ NP/mL ($5 \cdot 10^{-10}$ M) Au-Fam-Ang_{60-68}. Scale bar = 10 μm.

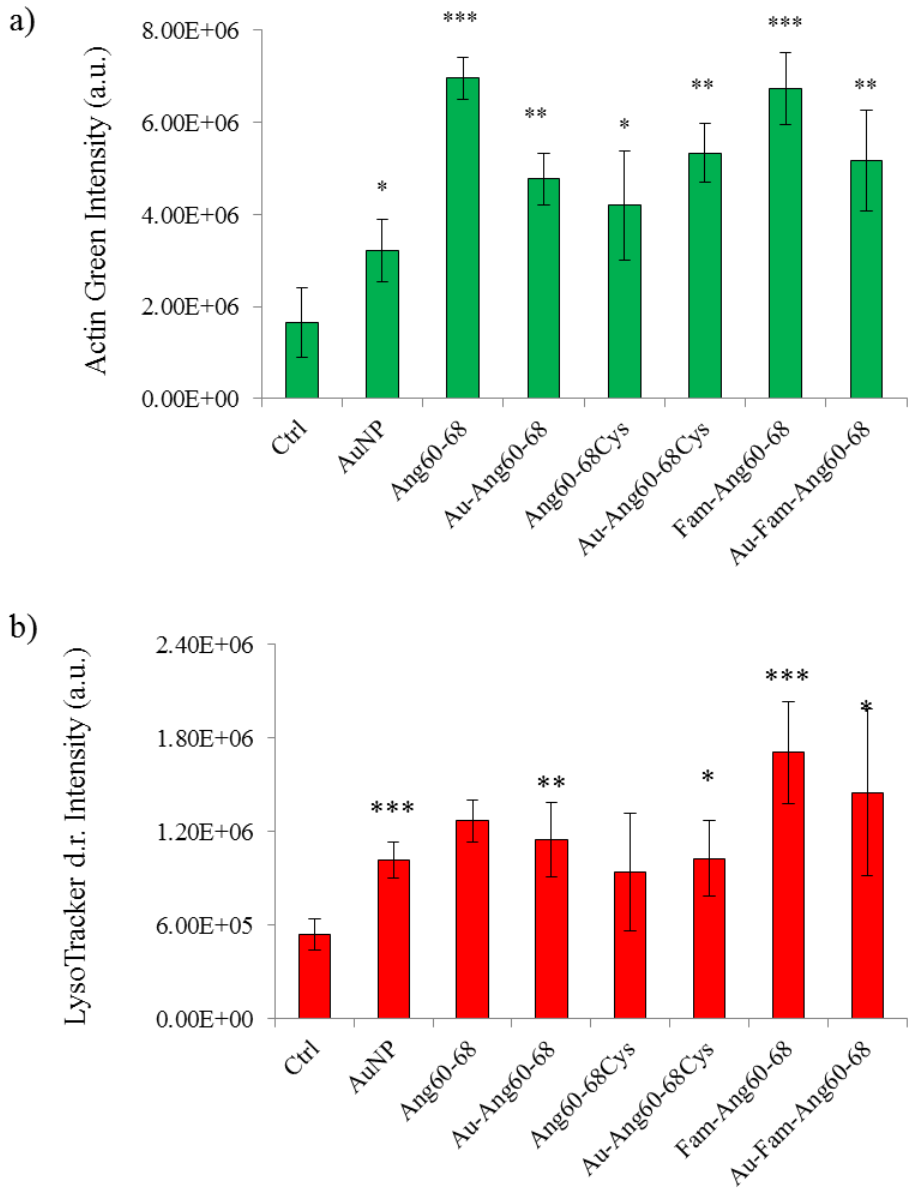

Figure 51- Intensity value of fluorescence corresponding to the a) Actin Green and b) LysoTracker deep red. Bars represent means ± SEM of at least 5 experiments. (*) p <0.05, (**) p <0.01, (***) p<0.001 vs. Ctrl. (One-way ANOVA).

3.1.1.2 Effect of the ANG peptides-copper(II) complexes on the cellular response of SH-SY5Y differentiated and undifferentiated

Copper is an essential metal, crucial to the health of all living organisms. Owing to its role as cofactor of numerous enzymes, indeed, it is involved in several physiological processes [410]. Among these, copper ions show a pro-angiogenic action by stimulating both endothelial cell migration [322] and new vessels formation [323, 324]. Such angiogenic activity is mostly associated with its ability to bind to ANG, thus affecting the biological function of the protein by increasing both its expression and interaction with endothelial cells [346]. Previous work reported that the studied sequence 60-68, also involved in the cellular actin binding, is one of the probable protein domain involved in the copper-binding and that the metal coordination could affect the whole Ang_{60-68} conformation [362].

In view of that, we performed cell experiments to study the cellular response in terms of cytotoxicity and cytoskeleton rearrangement on the two different cell lines, differentiated SH-SY5Y as model of normal cells and undifferentiated SH-SY5Y as model of cancer cells, in the presence and absence of copper ions. Cells were treated for 24 hrs with the nanosystems at two different concentrations namely $3.6 \cdot 10^7$ NP/mL ($5 \cdot 10^{-9}$ M) and $7.1 \cdot 10^7$ NP/mL ($1 \cdot 10^{-8}$ M) for the bare AuNPs; $1.5 \cdot 10^6$ NP/mL ($8 \cdot 10^{-10}$ M) and $2.6 \cdot 10^6$ NP/mL ($1.6 \cdot 10^{-9}$ M) for Au-Ang_{60-68}; $4.9 \cdot 10^5$ NP/mL ($5 \cdot 10^{-10}$ M) and $8.9 \cdot 10^5$ NP/mL ($9 \cdot 10^{-10}$ M) for Au-$FamAng_{60-68}$; the free peptides, Ang_{60-68} and $FamAng_{60-68,}$ at the concentration of $3 \cdot 10^{-5}$M, in presence or not of $2 \cdot 10^{-5}$ M $CuSO_4$.

Our results (Figure 52 a-b) show that Cu(II) not significantly affects the viability of both undifferentiated and differentiated neuroblastoma after 24 hrs incubation in comparison with the control. Whereas, in complex with

the two peptides, Ang_{60-68} and Fam-Ang_{60-68}, Cu(II) shows significant cytotoxicity in both the two studied cell lines with a reduction of the cell viability of about 35%. Differently, the treatment with the free peptides does not induce cytotoxic effect on both the two cell lines. Interestingly, no significant reduction of cell viability is observed after the treatment with the synthetized nanosystems at the studied conditions, whether on SH-SY5Y or d-SH-SY5Y. These results are in agreement with the previous experiment on SH-SY5Y cells (Figure 45), that showed cytotoxic effect on neuroblastoma cells only after a longer incubation period. Moreover, these findings highlight the ability of copper to modulate the biological behavior of ANG, probably promoting, conformational changes of the peptide structure, thus affecting the interaction between the biological molecules and the cells. Interestingly, such an effect is not displayed for the peptides immobilized on the gold surface, which seem to be protected from the conformation changes induced by the copper complex formation.

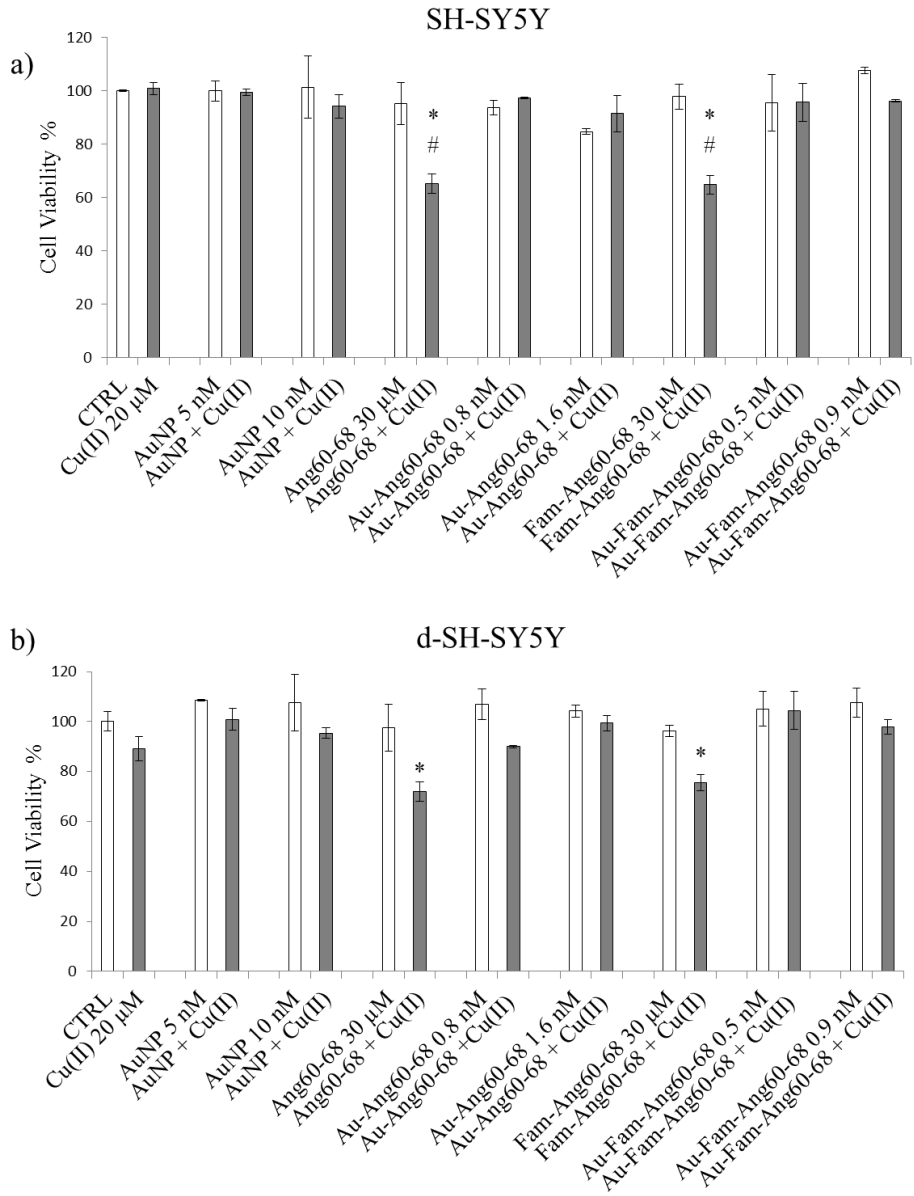

Figure 52- Cell viability assay (MTT) on a) undifferentiated and b) differentiated neuroblastoma cells after 24 hrs treatment with: $3.6 \cdot 10^{7}$ NP/mL ($5 \cdot 10^{-9}$ M) and $7.1 \cdot 10^{7}$ NP/mL ($1 \cdot 10^{-8}$ M) AuNPs; $1.5 \cdot 10^{6}$ NP/mL ($8 \cdot 10^{-10}$ M) and $2.6 \cdot 10^{6}$ NP/mL ($1.6 \cdot 10^{-9}$ M) Au-$Ang_{60\text{-}68}$; $4.9 \cdot 10^{5}$ NP/mL ($5 \cdot 10^{-10}$ M) and $8.9 \cdot 10^{5}$ NP/mL ($9 \cdot 10^{-10}$ M) Au-$FamAng_{60\text{-}68}$; the peptides at the concentration $3 \cdot 10^{-5}$ M; in the absence or presence of $2 \cdot 10^{-5}$M $CuSO_4$. Results are presented as mean ± SEM

from experiments in triplicate and normalized with respect to the control untreated cells. (*) $p < 0.05$ level: (*) = vs. Ctrl, (#) $p < 0.05$ vs. 20 μM $CuSO_4$. (One-way ANOVA)

The cellular response of SH-SY5Y and d-SH-SY5Y to the ANG peptides-Cu(II) complexes was also investigates in terms of cytoskeleton re-organization induced by the two peptides as free molecules and molecule immobilized on the nanoparticle surface.

Figure 53 displays the confocal microscopy micrographs of actin-stained undifferentiated and differentiated neuroblastoma cells, after 2 hrs of treatment.

The untreated control of both the cell lines displays regular and homogeneously distributed actin filaments and globular actin aggregates are distinguishable as well (Figure 53 a-a'). As to the copper ions, it has been demonstrated that the Cu(II) supplementation on neuronal cells can damage their F-actin and tubulin network leading to a drastic reduction of the typical actin protrusion of neuronal cells [411]. Accordingly, our data confirm a general reduction of the actin-stained fluorescence after the treatment with Cu(II). Such an effect is markedly evident for the free ANG peptide + Cu(II) complexes (Figure 53 i-m-53 i'-m') as expected from the MTT results, thus indicating significant cytoskeleton impairments. Moreover, the reduction of the actin-stained signal is more appreciable for undifferentiated cell line with respect to the differentiated neuroblastoma. The differentiation process, basically, alters the susceptibility of neuroblastoma cells to stress signals, thus conferring selective survival advantages to the cell line [412] that can also protect the cells from the cytoskeleton impairment induced by the copper supplementation.

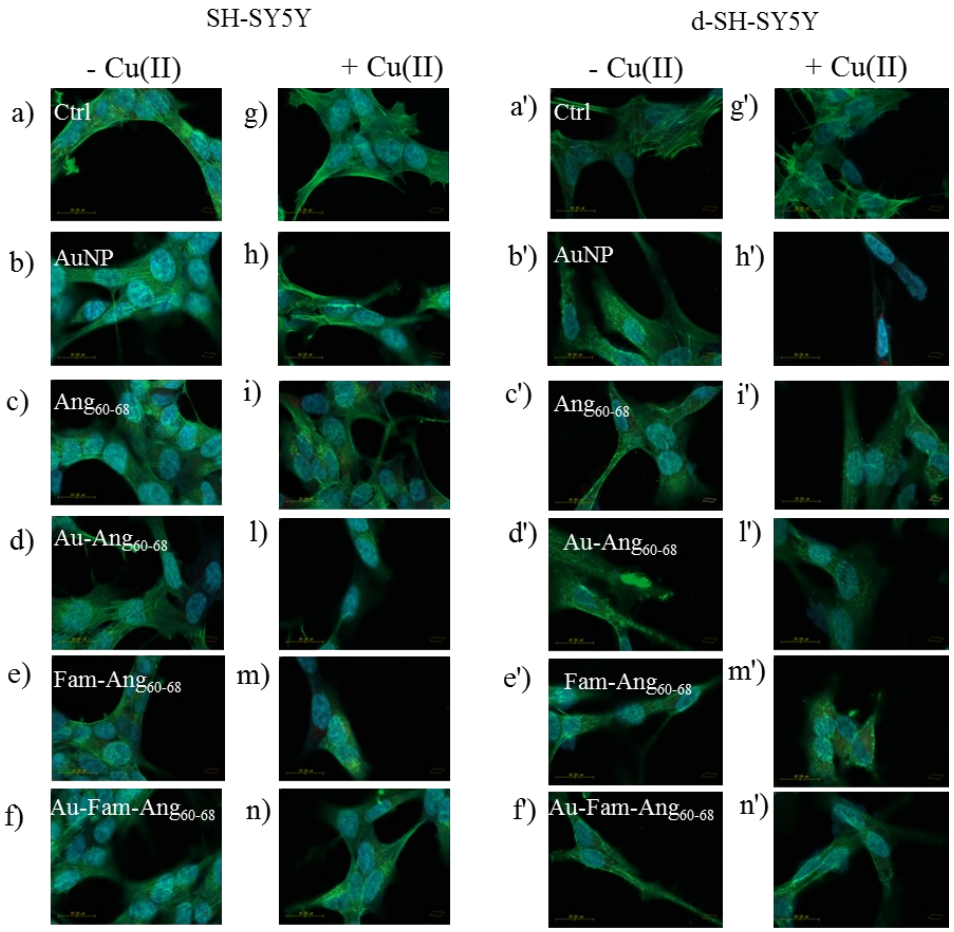

Figure 53- LSM fluorescence (in blue, nuclear staining, $\lambda_{ex/em}$=405/425–475nm; in green, actin staining and FAM, $\lambda_{ex/em}$=488/500–530 nm) images of undifferentiated SH-SY5Y cells (left) and differentiated d-SH-SY5Y cells after 2 hrs of incubation with: a-a') control, b-b') AuNP, c-c') Ang_{60-68}, d-d') Au-Ang_{60-68}, e-e') Fam-Ang_{60-68}, f-f') Au-Fam-Ang_{60-68}, g-g') $CuSO_4$, h-h') AuNP + Cu(II); i-i') Ang_{60-68} + Cu(II) l-l') Au-Ang_{60-68} + Cu(II); m-m') Fam-Ang_{60-68}, n-n') Au-Fam-Ang_{60-68} + Cu(II). The concentrations were $3.6 \cdot 10^7$ NP/mL ($5 \cdot 10^{-9}$ M) for AuNPs, $1.5 \cdot 10^6$ NP/mL ($8 \cdot 10^{-10}$ M) for Au-Ang_{60-68}, $4.9 \cdot 10^5$ NP/mL ($5 \cdot 10^{-10}$ M) for Au-Fam-Ang_{60-68}; $3 \cdot 10^{-5}$ M the peptides, $2 \cdot 10^{-5}$ M $CuSO_4$. Scale bar = 20 μm.

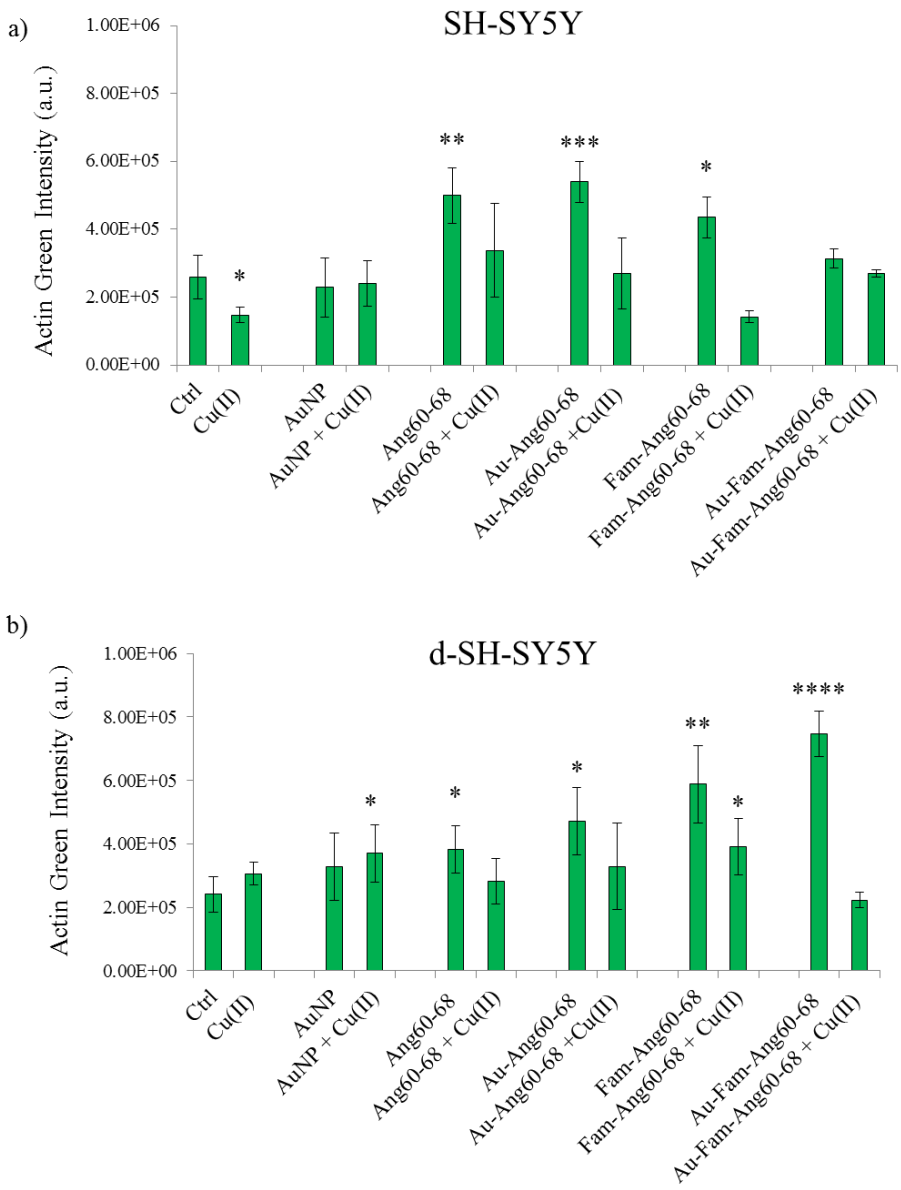

Figure 54- Intensity value of fluorescence corresponding to the Actin Green staining of a) undifferentiated SH-SY5Yand b) differentiated SH-SY5Y. Bars represent means ± SEM of at least 5 experiments. (*) $p < 0.05$, (**) $p < 0.01$, (***) $p < 0.001$, (****) $p < 0.0001$ vs. Ctrl. (One-way ANOVA).

3.1.1.3 Response of glioblastoma A172 cells to the hybrid Au-Ang/ANG in terms of cell viability and interaction with cell cytoskeleton (PAPER III)

AuNPs functionalised with Ang_{60-68} and its analogous having a cysteine residue in the C-terminus, $Ang_{60-68}Cys$, in comparison with the whole human wtANG protein were also scrutinised as potential nanomedicine platforms towards the human glioblastoma brain cancer of (A172 cell line). In this regard, MTT assay was firstly carried out to assess the cellular response in terms of cell viability (Figure 55) to both the free peptides or protein and the corresponding functionalized nanosystems, in the absence or presence of copper ions, owing to their key role in the modulation of the biological activity of ANG. To this purpose, A172 cells were treated for 24 hrs with the nanosystems at the concentrations of $1.4 \cdot 10^{8}$ NP/mL ($9.4 \cdot 10^{-9}$ M) for AuNP, $4.0 \cdot 10^{6}$ NP/mL ($1.4 \cdot 10^{-9}$ M) for Au-Ang_{60-68}, $4.0 \cdot 10^{6}$ NP/mL ($1.4 \cdot 10^{-9}$ M) for Au-$Ang_{60-68}Cys$ and $3.4 \cdot 10^{6}$ NP/mL ($1.2 \cdot 10^{-9}$ M) for Au-wtANG; the free peptides (Ang_{60-68}, $Ang_{60-68}Cys$) or protein wtANG at the concentration of $3 \cdot 10^{-5}$ M and $1 \cdot 10^{-11}$ M, respectively; in presence or absence of $2 \cdot 10^{-5}$ M $CuSO_4$.

The obtained results show a significant increase of the cell viability after the treatment with the whole protein, wtANG, both in absence and in presence of Cu(II). Whereas, the treatment with the free peptides, Ang_{60-68} and $Ang_{60-68}Cys$, in the presence or absence of Cu(II) do not induce cytotoxicity, differently to the cellular response observed, after 24 hrs, on the other scrutinized model of brain cancer, namely neuroblastoma (Figure 52 a). As to the nanosystems, it has been found that the incubation with bare AuNPs, both in the absence and presence of Cu(II), does not change the cell viability with respect to the control, while the functionalized Au-

Ang_{60-68} reduces the cell viability of A172 cells of about 20–25%, both in the absence and in the presence of copper ions, with respect to the free peptide. Noteworthy, the same sample does not induce significant cytotoxic effects on neuroblastoma cells (Figure 52). As to the Au-Ang_{60-68}Cys, it leads to a reduction of the glioblastoma viability in the absence of Cu(II), while no significant differences with respect to the control have been found in the presence of copper. Similar response is observed for the protein-functionalized nanoparticles, Au-wtANG.

Such results point out a strongly cell-dependent response to the studied systems, most likely due to the activation of different intracellular signalling pathways as well as the overexpression of different receptors on the membrane of the scrutinized cell lines [413]. Thus, experiment on tumour glioblastoma cells show very promising anti-cancer capabilities of both the Au-peptide and Au-ANG functionalized nanoparticles, being able to reduce the viability of such tumour cells in comparison to the free peptide/proteins as controls. No cytotoxicity, instead, was observed on neuroblastoma cells treated with the same samples after short incubation time. Interestingly, this effect is almost nullified in the presence of copper ions which confirms its ability to bind to the protein/peptide, inducing conformational changes and thereby controlling their biological behaviour.

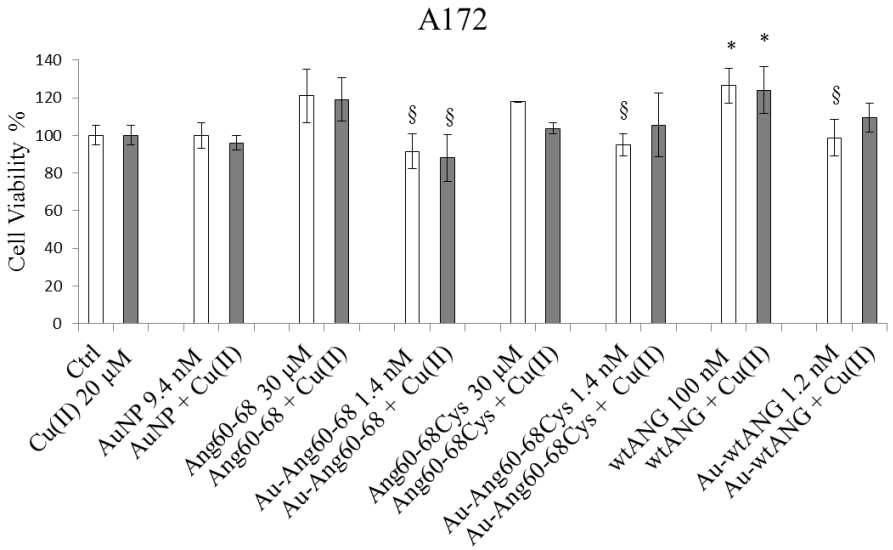

Figure 55- Cell viability assay (MTT) on A172 cells treated for 24 hrs with: $1.4 \cdot 10^{8}$ NP/mL ($9.4 \cdot 10^{-9}$ M) AuNP, $4.0 \cdot 10^{6}$ NP/mL ($1.4 \cdot 10^{-9}$ M) Au-Ang$_{60\text{-}68}$, $4.0 \cdot 10^{6}$ NP/mL ($1.4 \cdot 10^{-9}$ M) Au-Ang$_{60\text{-}68}$Cys, $3.4 \cdot 10^{6}$ NP/mL ($1.2 \cdot 10^{-9}$ M) Au-wtANG; Ang$_{60\text{-}68}$ ($3 \cdot 10^{-5}$ M), Ang$_{60\text{-}68}$Cys ($3 \cdot 10^{-5}$ M); wtANG ($1 \cdot 10^{-11}$ M) in presence or absence of $2 \cdot 10^{-5}$ M $CuSO_4$. The bars represent means ± SD of three independent experiments performed in triplicate (S.D. = standard deviation). Statistically significant differences, determined by one-way analysis of variance ANOVA are indicated: (*) $p < 0.05$ vs. Ctrl; (§) $p < 0.05$ vs. the respective treatment with free peptides/protein.

The cellular response of glioblastoma A172 cell line to the synthetized hybrid systems in the presence or absence of Cu(II) was also investigates in terms of cytoskeleton re-organization.

Figure 56 displays the confocal microscopy micrographs and the optical images of the actin-stained glioblastoma A172 cell line after 2 hrs of treatment with, AuNP ($9.4 \cdot 10^{-9}$ M, $1.4 \cdot 10^{8}$ NP/mL), Au-Ang$_{60\text{-}68}$ ($1.4 \cdot 10^{-9}$, $4.0 \cdot 10^{6}$ NP/mL), Au-Ang$_{60\text{-}68}$Cys ($1.4 \cdot 10^{-9}$, $4.0 \cdot 10^{6}$ NP/mL), Au-wtANG ($1.2 \cdot 10^{-9}$, $3.4 \cdot 10^{6}$ NP/mL); and the peptides (Ang$_{60\text{-}68}$ and Ang$_{60\text{-}68}$Cys) or

protein at the concentration of $3 \cdot 10^{-5}$ M and $1 \cdot 10^{-11}$ M, respectively. All the sample were used in the presence or absence of $2 \cdot 10^{-5}$ M $CuSO_4$.

The recorded images show, for the untreated cells, thin filaments of actin with lamellipodial projection, typical of glioblastoma cells [414]. The treatment with the free peptides and the protein leads to a diffuse staining of actin that mostly appears in the globular form. Interestingly, the addition of Cu(II) markedly changes the cytoskeletal actin organization induced by the free peptides Ang_{60-68} and $Ang_{60-68}Cys$ and the whole protein ANG, by increasing the presence of thick filaments of actin and reducing the globular form of this protein. As to the nanosystems, the treatment with bare AuNPs both in the presence and absence of Cu(II) leads to the appearance of actin dots rather than long fibres, correlated with the presence of AuNPs in the cytosol which are thought to cause de-polymerization of actin [415]. As to the hybrids, instead, Au-Ang_{60-68} and Au-wtANG both in the absence and in the presence of copper, induce a similar cellular response in terms of cytoskeleton reorganization with respect to the free Ang_{60-68} and wtANG. Differently, the incubation with Au-$Ang_{60-68}Cys$, in the absence and presence of copper seems to impair the A172 cell cytoskeleton leading to a reduction of the actin signal (Figure 57).

These findings further highlight the ability of both the peptide sequence 60-68 and the whole protein wtANG to bind to actin, thus inducing a marked reorganization of the cell cytoskeleton by inhibiting its polymarization [279]. Such reorganization is essential for the migration and proliferation of the cells as well as for the tumour invasion and metastasis. On the other hand, AuNPs affect the cell cytoskeleton structure, leading to an increase of globular actin and reducing the

thickness of the fibres. Such an effect is rather modulated in the hybrids owing to the immobilization of the biomolecules. Moreover, Cu(II) seems to no significantly affect the A172 cytoskeleton in comparison to the untreated control, while as observed for SH-SY5Y cells (Figure 54) there is a reduction of the F-actin fibres signal after the treatment with the free peptides Ang_{60-68} and $Ang_{60-68}Cys$ in complex with Cu(II) (Figure 57), thus further proving the conformational changes triggered by the copper complex formation, which also affect the biological behaviour of the peptides.

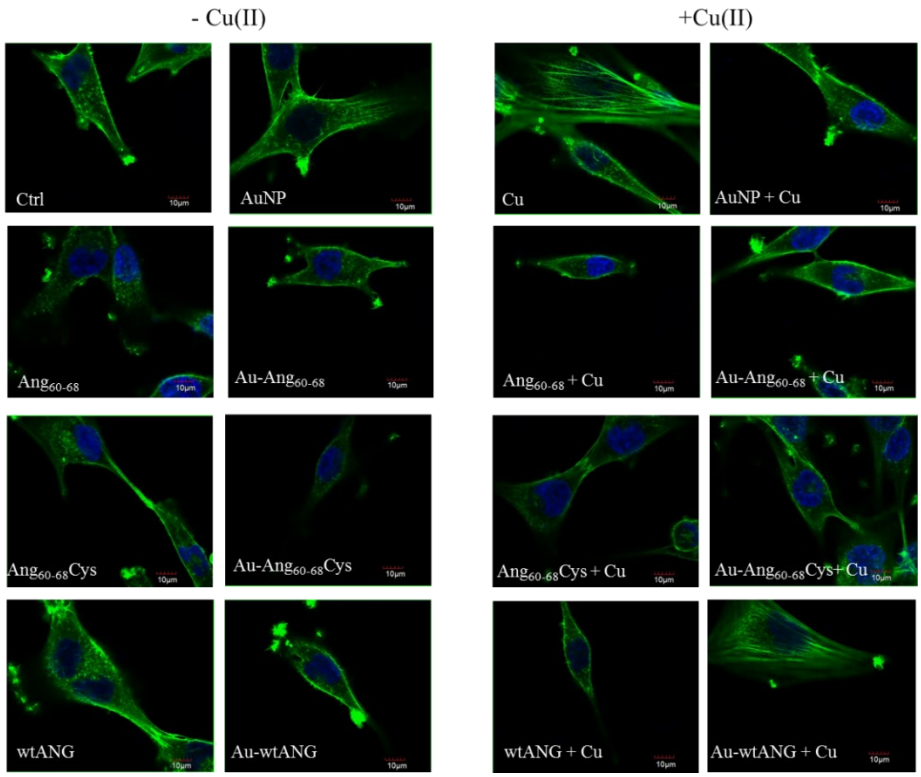

Figure 56- Confocal micrographs of A172 cells stained with Actin Green 488 (in green, $\lambda_{ex/em}$= 488/500–530 nm) and Hoechst33342 (in blue, $\lambda_{ex/em}$ =405/425–475 nm) untreated and after the treatment with $1.4 \cdot 10^{8}$ NP/mL ($9.4 \cdot 10^{-9}$ M) AuNP, $4.0 \cdot 10^{6}$ NP/mL ($1.4 \cdot 10^{-9}$ M) Au-Ang_{60-68}, $4.0 \cdot 10^{6}$ NP/mL ($1.4 \cdot 10^{-9}$ M) Au-Ang_{60-}

$_{68}$Cys, $3.4 \cdot 10^{6}$ NP/mL ($1.2 \cdot 10^{-9}$ M) Au-wtANG; Ang_{60-68} ($3 \cdot 10^{-5}$ M), Ang_{60-68}Cys ($3 \cdot 10^{-5}$ M); wtANG ($1 \cdot 10^{-11}$ M) in presence or absence of $2 \cdot 10^{-5}$ M $CuSO_4$. Scale bar = 10 μm.

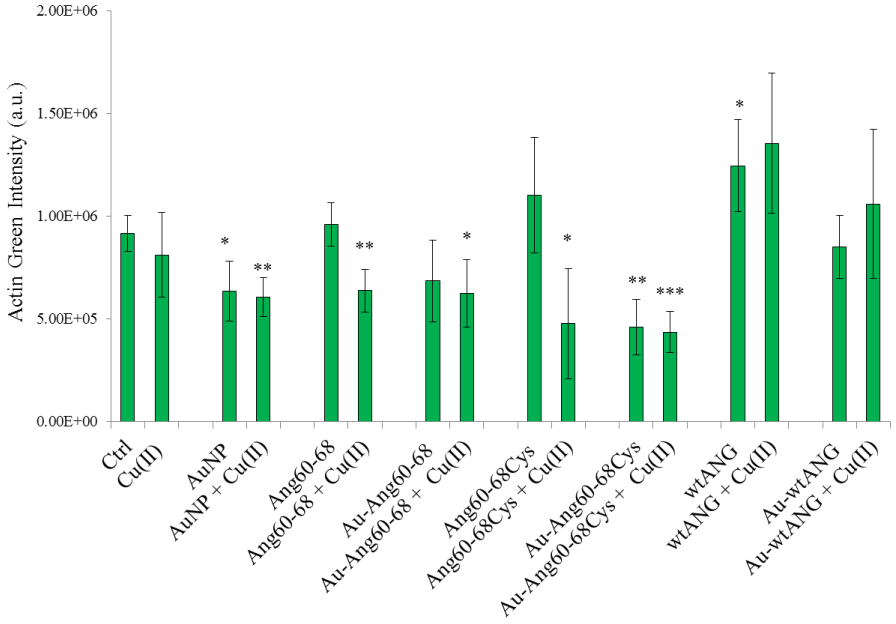

Figure 57- Intensity value of fluorescence corresponding to the Actin Green staining of A172 cells. Bars represent means ± SEM of at least 5 experiments. (*) $p < 0.05$, (**) $p < 0.01$, (***) $p < 0.001$ vs. Ctrl. (One-way ANOVA).

3.1.2. Potential anti-cancer properties of Au-GO nanohybrids (PAPER IV)

Cellular experiments on human neuroblastoma cell line, SH-HY5Y, were carried out to scrutinize the anti-cancer properties of the synthetized nanoplatform Au-GO, made of gold nanoparticles and graphene oxide. Accordingly, MTT assay was performed to assess the cytotoxic effect induced by Au-GO in comparison with the bare AuNPs and GO sheets on the studied model of brain cancer cells while, their effect on the mitochondrial dysfunctions was studied by measuring the cellular ROS production. Mitochondria, indeed, are intracellular organelles involved in the energy metabolism, showing a central role in the adenosine triphosphate (ATP) synthesis, which is based on the proton gradient produced across their inner membrane by the electron transport chains [416]. Mitochondria dysfunctions, owing to the leaking of ROS from their electron transport chains, causes severe oxidative damages to DNA and proteins and are often associated with the activation of cell death processes [417]. Previous work demonstrated that GO displays an effective anti-cancer activity being able to inhibit migration and invasion of cancers cells by impairing their mitochondrial functions through the disruption of their electron transfer complexes, thus further leads to an increase of intracellular ROS [418]. In this respect, it has been shown that GO causes a significant reduction of the viability of neuroblastoma cells at high concentration (> 100 mg/mL) [419]. On the other hand, AuNPs with a diameter of 14 nm, as showed above, do not display any cytotoxicity on SH-SY5Y cells up to the studied concentration of $7.1 \cdot 10^{7}$ NP/mL ($1.0 \cdot 10^{-8}$ M).

In this work, cell viability assay (MTT) was carried out by treating the cells for 24 hrs with the samples at different concentrations: $3.4 \cdot 10^7$ NP/mL ($5 \cdot 10^{-9}$ M), $7.1 \cdot 10^7$ NP/mL ($1.0 \cdot 10^{-8}$ M), $1.1 \cdot 10^8$ NP/mL ($1.5 \cdot 10^{-8}$ M) of AuNPs; 5, 10, 20 μg/mL of GO into the hybrids; 5, 10, 20 μg/mL of GO alone.

MTT results (Figure 58), in accord with literature data, show that both the synthetized bare AuNPs and GO sheets, don't exhibit significant dose-dependent cytotoxicity at the tested conditions. Differently, the hybrids Au-GO show a clearly dose-depended cytotoxicity on neuroblastoma cell line with a significant cell viability reduction after the treatment with 10 μg/mL of GO into the nanocomposites. These findings suggest that the combination of GO and AuNPs in the synthetizes hybrid increase the cytotoxic effect induced by GO, most likely due to the presence of AuNPs that most likely enhances the entrance of GO sheets into the cells and so their interaction with organelles such as mitochondria, thus leading to cytotoxic effects.

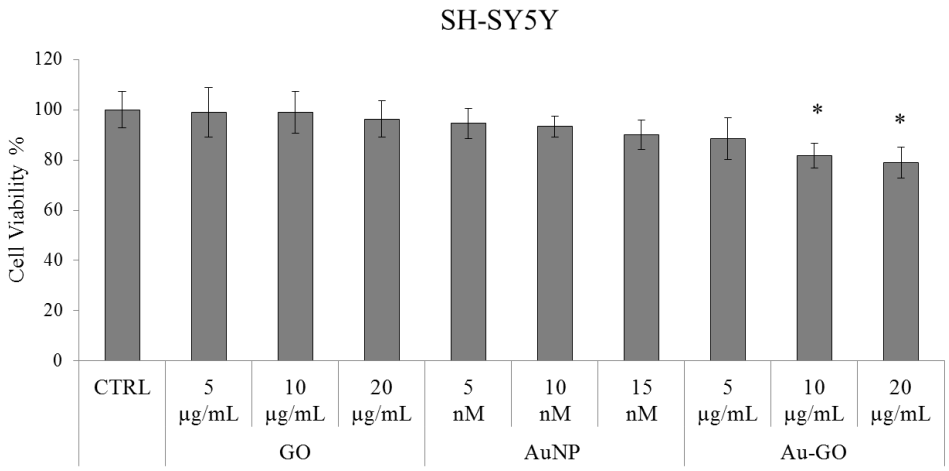

Figure 58- Dose response experiment on neuroblastoma SH-SY5Y cell line. Cells were incubated for 24 with AuNPs, Au-GO, and free GO nanosheets, at different concentrations: $3.4 \cdot 10^7$ NP/mL ($5 \cdot 10^{-9}$ M), $7.1 \cdot 10^7$ NP/mL ($1.0 \cdot 10^{-8}$ M), $1.1 \cdot 10^8$ NP/mL ($1.5 \cdot 10^{-8}$ M)of AuNPs; 5, 10, 20 µg/mL of GO into the hybrids; 5, 10, 20 µg/mL of GO alone. Results are presented as mean ± SEM from experiments in triplicate and normalized with respect to the control untreated cells. (*) $p < 0.05$ vs. Ctrl (One-way ANOVA).

To verify that the effective biological mechanism involved in the toxicity of the hybrid Au-GO is based on the mitochondrial dysfunction and so on the ROS production, MitoSOX and DCF assays were performed on neuroblastoma cells treated with the studied compounds. These assays, indeed, allow for the evaluation of mitochondrial and total ROS intracellular concentration, respectively. The experiments were carried out by treating neuroblastoma cells for 24 hrs with $3.4 \cdot 10^7$ NP/mL ($5 \cdot 10^{-9}$ M), $7.1 \cdot 10^7$ NP/mL ($1.0 \cdot 10^{-8}$ M), $1.1 \cdot 10^8$ NP/mL ($1.5 \cdot 10^{-8}$ M) of AuNPs; 5, 10, 20 µg/mL of GO into the hybrids corresponding to $3.1 \cdot 10^5$ NP/mL ($3.0 \cdot 10^{-10}$ M), $6.4 \cdot 10^5$ NP/mL ($6.0 \cdot 10^{-10}$ M), $1.3 \cdot 10^6$ NP/mL ($1.3 \cdot 10^{-9}$ M)

AuNPs; 5, 10, 20 μg/mL of GO sheets and the results are shown in figures 58-59.

In agreement with literature data, the obtained results show that the cellular treatment with GO sheets increases the MitoSOX signal, related to the mitochondrial ROS concentration, in a dose-depended manner (Figure 59). Interestingly, the incubation with the hybrids Au-GO more significantly increases the ROS production, supporting the hypothesis that the presence of the AuNPs improve the entrance of GO sheets into the cancer cells. As expected from the MTT results, AuNPs do not increase the ROS production with respect to the control at the tested conditions.

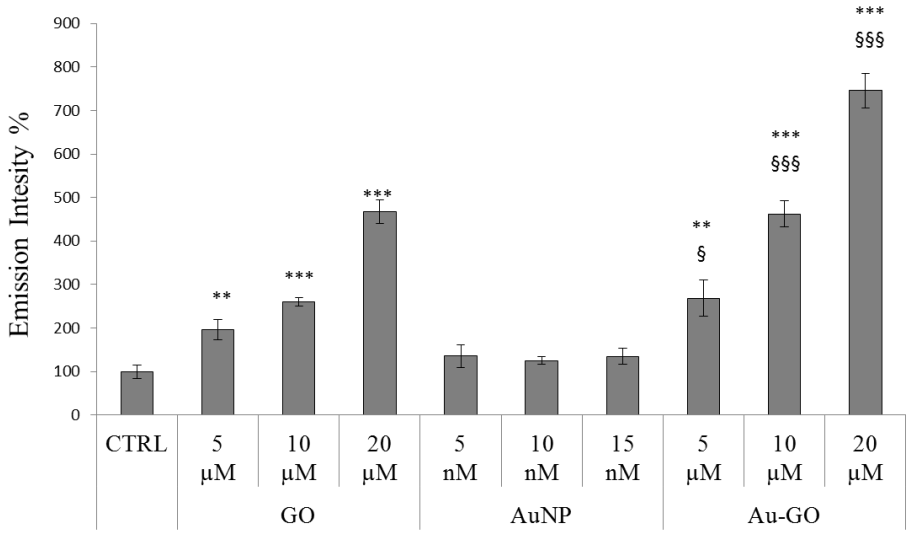

Figure 59- MitoSOX experiment on neuroblastoma SH-SY5Y cell line. Cells were incubated for 24 hrs with $3.4 \cdot 10^7$ NP/mL ($5 \cdot 10^{-9}$ M), $7.1 \cdot 10^7$ NP/mL ($1.0 \cdot 10^{-8}$ M), $1.1 \cdot 10^8$ NP/mL ($1.5 \cdot 10^{-8}$ M) of AuNPs; 5, 10, 20 μg/mL of GO into the hybrids corresponding to $3.1 \cdot 10^5$ NP/mL ($3.0 \cdot 10^{-10}$ M), $6.4 \cdot 10^5$ NP/mL ($6.0 \cdot 10^{-10}$ M), $1.3 \cdot 10^6$ NP/mL ($1.3 \cdot 10^{-9}$ M) AuNPs; 5, 10, 20 μg/mL of GO sheets. Results are presented as mean ± SEM from experiments in triplicate and

normalized with respect to the control untreated cells. (**) p <0.01, (***) p<0.001 vs. Ctrl; (§) p< 0.05, (§§§) p<0.001 vs. GO (One-way ANOVA).

As to DCF assay, it allows for the determination of the total intracellular ROS concentration which is useful to determine the real relationship between mitochondrial dysfunction and ROS species generation, which can also involve other cellular compartments and processes such as oxidase activity, protein folding, thymidine and polyamine catabolism [420].

The obtained results (Figure 60) show a slight increase of the total ROS after the treatment with AuNPs, while the incubation with GO at the concentration of 10 and 20 μg/mL raise the total ROS production on neuroblastoma cells showing a trend comparable to that observed with the MitoSOX (Figure 59), thus confirming that GO sheets cytotoxicity is mainly due to a mitochondrial dysfunctions.

Interestingly, the cell treatment with the hybrids Au-GO leads to a more significant increase of the total ROS concentration with respect to GO, thus suggesting that the ROS species generation involves different biological pathways together with the mitochondrial damage probably, due to combined role of AuNPs and GO into the hybrids.

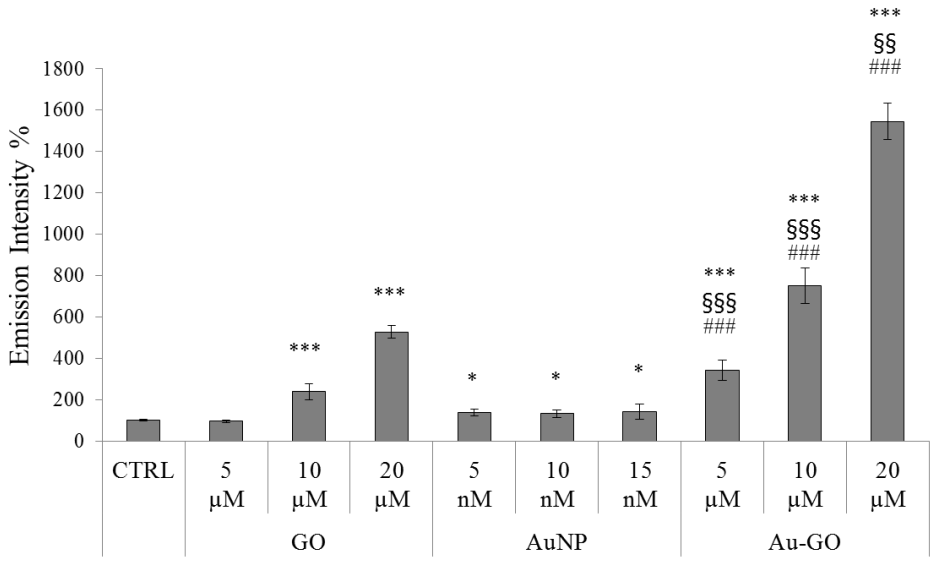

Figure 60- DCF experiment on neuroblastoma SH-SY5Y cell line. Cells were incubated for 24 hrs with $3.4 \cdot 10^{7}$ NP/mL ($5 \cdot 10^{-9}$ M), $7.1 \cdot 10^{7}$ NP/mL ($1.0 \cdot 10^{-8}$ M), $1.1 \cdot 10^{8}$ NP/mL ($1.5 \cdot 10^{-8}$ M) of AuNPs; 5, 10, 20 µg/mL of GO into the hybrids corresponding to $3.1 \cdot 10^{5}$ NP/mL ($3.0 \cdot 10^{-10}$ M), $6.4 \cdot 10^{5}$ NP/mL ($6.0 \cdot 10^{-10}$ M), $1.3 \cdot 10^{6}$ NP/mL ($1.3 \cdot 10^{-9}$ M) AuNPs; 5, 10, 20 µg/mL of GO sheets. Results are presented as mean ± SEM from experiments in triplicate and normalized with respect to the control untreated cells. (*) $p < 0.05$, (***) $p < 0.001$ vs. Ctrl; (§§) $p < 0.01$, (§§§) $p < 0.001$ vs. GO; (###) $p < 0.001$ vs. AuNP (One-way ANOVA).

Finally, intracellular imaging by laser scanning confocal microscopy, was carried out to assess the effective cellular internalization of the studied systems and the involvement of lysosomes in the cellular stress induces by the treatment.

Figure 61 shows the representative confocal microscopy, stained with lysotracker deep red and the optical images, of untreated neuroblastoma cells and after 2 hrs of incubation with $1.1 \cdot 10^{8}$ NP/mL ($1.5 \cdot 10^{-8}$ M) AuNPs, 20 µg/mL GO and the hybrid Au-GO at the GO concentration of

20 μg/mL. The recorded bright field images clearly evidence the presence of the AuNPs, as dark spots, and GO for the Au-GO hybrids as dark blots of aggregates, inside the cells thus confirming their ability to pass through the cell membrane also reaching the nuclei. Noteworthy, no aggregate nanomaterials are observed inside the cells after the treatment with GO, thus proving that the presence of AuNPs into hybrids improve the entrance of GO sheets into the cells.

As to the lysosomal staining (Figure 61-62), in the control lysosomes exhibits the characteristic dot distribution, while a lysosomal expansion is shown after the treatment with Au-GO and GO with respect to the bare AuNPs, thus indicating lysosomes activation and stress response of the cells, as expected from the MTT, MitoSOX and DCF results.

These preliminary results, provide evidence of an effective anti-cancer activity of the synthetized nanoplatform Au-GO, which show enhanced cytotoxic effects on neuroblastoma cells after 24 hrs of treatment, with respect to the GO alone, further involving ROS production due to mitochondrial dysfunctions and probably many other intracellular processes that in complex lead to a significant reduction of the cancer cell viability.

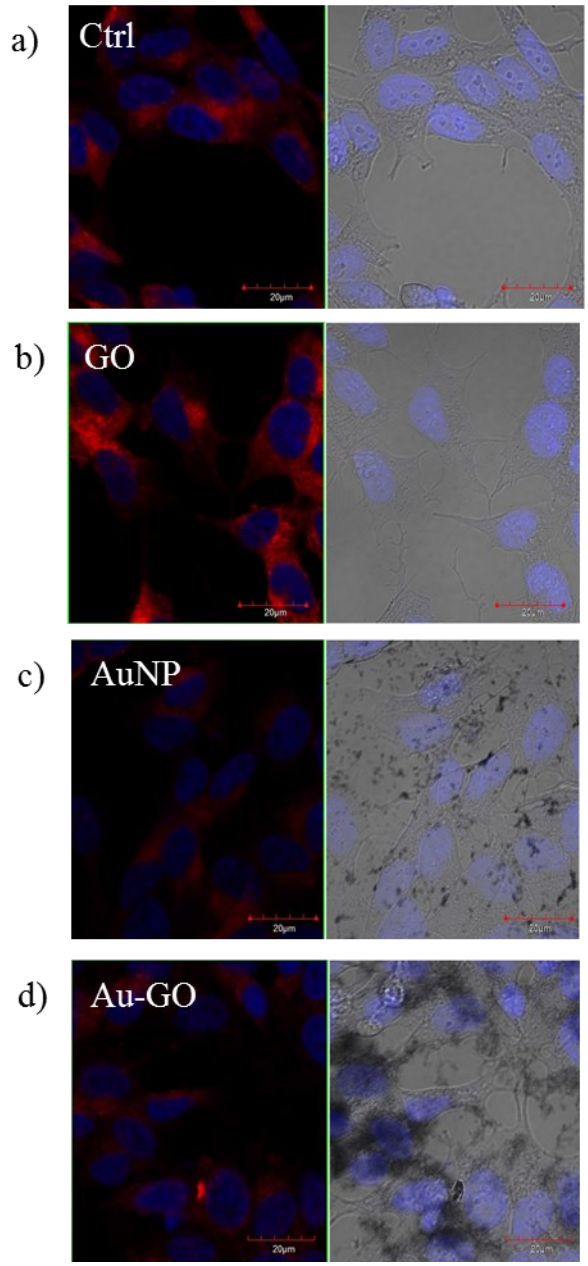

Figure 61- LSM merged optical bright field and fluorescence (in blue, nuclear staining, $\lambda_{ex/em}$=405/425–475 nm; in red, LysoTracker deep red, $\lambda_{ex/em}$=633⁄650-700) micrographs of SH-SY5Y neuroblastoma cells after 2 hrs of incubation with the different samples: a) control, b) GO 20 μg/mL, c) $1.1 \cdot 10^{8}$ NP/mL ($1.5 \cdot 10^{-8}$

M) AuNP, d) Au-GO ([GO]= 20 µg/mL; [AuNP] = $1.3 \cdot 10^{6}$ NP/mL or $1.3 \cdot 10^{-9}$ M)). Scale bar = 20µm.

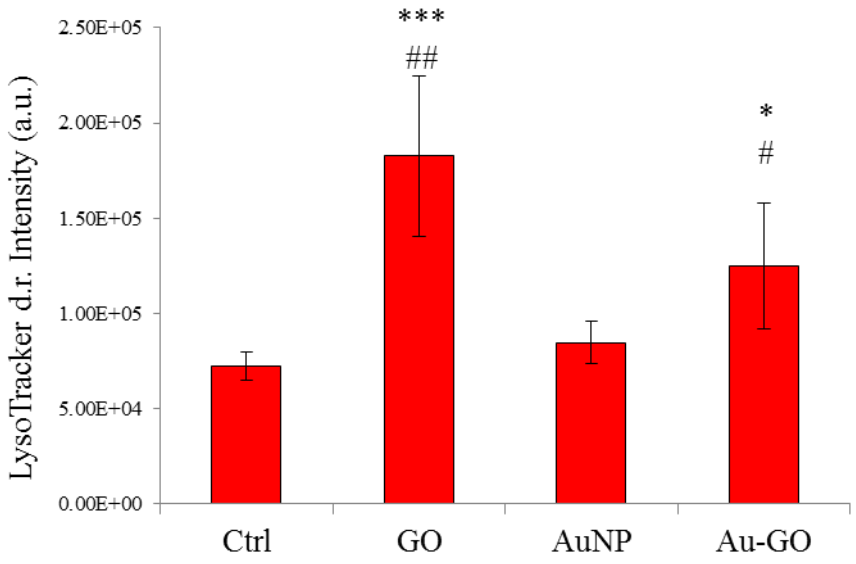

Figure 62- Intensity value of fluorescence corresponding to the LysoTracker deep red. Bars represent means ± SEM of at least 5 experiments. (*) $p < 0.05$, (***) $p < 0.001$ vs. Ctrl;
(#) $p < 0.05$, (##) $p < 0.01$ vs. AuNP (One-way ANOVA).

3.2 Wound healing properties

Dermal wound healing involves several interacting events, including inflammation, tissue contraction, remodelling and above all angiogenesis. During these processes, a large amount of ROS are generated by the immune system, causing the inhibition of cell growth and slowing down the physiological wound repair [59]. AuNPs, among their intrinsic properties, show strong anti-oxidative effects accepting electrons from ROS and leading to their deactivation [378]. In this respect, AuNPs could offer great advantages in wound care treatment. On the other hand, high levels of ANG were found in human burn wounds and deep thickness lesions [421], thus supporting a central function of this protein in the wound management, owing to its main role in the angiogenic process. Furthermore, the high biocompatibility of GO toward dermal fibroblasts [35] and its ability to promote cell adhesion, migration and proliferation [63], allows this carbon-based nanomaterial to enhance wound closure, by increasing the strength of the formed new tissue and further reducing the scar formation.

Based on these premises following an approach of increased complexity, in this work, we scrutinized the ability of the synthetized hybrid nanoplatforms, Au-ANG, Au-GO-ANG to modulate angiogenesis and to induce cell migration for potential wound healing treatments.

Crucial to all of the healing phases, indeed, is the migration to the wound site of several cell types including white blood cells, endothelial cells and in particular dermal fibroblasts. The main function of fibroblasts is the maintenance of tissue homeostasis and when tissues are injured, their migration is critical in supporting the healing process [422]. In the wound

site, in fact, fibroblasts are activated and differentiate into myofibroblasts, which play a pivotal role in the fibrin clot dissolution and its replacement with a collagen matrix, that all the migrating cells use as scaffolding to crawl along and restore the physiological features of the skin [423]. Accordingly, fibroblasts are the best cellular model for in vitro wound healing studies.

Thus, the wound healing properties of Au-ANG and the Au-GO-ANG, in comparison with the bare AuNPs and GO sheets as controls, were scrutinized on human foetal foreskin fibroblasts (HFF1 cell line), in terms of cell viability and cell migration assay. Moreover, laser confocal images of the treated cells were recorded to study the effective up-take of the nanosystems and their interaction with the cytoskeleton, lysosomes and mitochondria, through the actin green, the lysotracker and mitotracker staining, respectively.

3.2.1. Cellular response to the hybrid Au-ANG (PAPER II)

AuNPs functionalised with the whole protein ANG and its analogies, namely the recombinant protein, rANG, with a methionine at the N-terminus domain and the new mutant, S28CANG, with a cysteine instead of the serine at the residue 28 for the high-affinity binding to the gold surface, were investigated for potential application in wound healing. In this regard, cell proliferation assay was firstly carried out to assess the cellular response in terms of cell viability and proliferation to both the free proteins and the corresponding functionalized nanosystems, in the absence or presence of copper ions, owing to their key role in the modulation of the biological activity of ANG.

Cell proliferation was evaluated by a fluorimetric method based on the Hoechst 33342 dye, which is a non-toxic specific vital stain for DNA. The detected fluorescence resulting from the interaction of cell chromatin DNA with Hoechst 33342 is a linear function of the number of cells per well and allows estimation of cell division, growth and viability after the treatment with the free proteins and the hybrids Au-ANG in the presence or not of copper ions, with respect to the untreated control.

To this purpose, HFF1 cells were treated for 24 hrs with the nanosystems at the concentrations of $3.2 \cdot 10^{7}$ NP/mL ($4.5 \cdot 10^{-9}$ M) for AuNP, $2.7 \cdot 10^{6}$ NP/mL ($1.1 \cdot 10^{-9}$ M) for Au-wtANG, $1.8 \cdot 10^{6}$ NP/mL ($9.0 \cdot 10^{-10}$ M) for Au-rANG and $2.3 \cdot 10^{6}$ NP/mL ($1.1 \cdot 10^{-9}$ M) for Au-S28CANG; the free proteins at the concentration of $2 \cdot 10^{-8}$ M; in the presence or absence of $1 \cdot 10^{-7}$ M $CuSO_4$.

Cell proliferation assay results (Figure 63), in accord with literature data, show that none of the studied systems displays cytotoxicity on HFF1

cells in terms of IC-50 at the tested conditions. Noteworthy, while the recombinant protein increases cell proliferation of around 18%, compared to the control, neither wtANG nor S28CANG significantly affects the cell rate growth. In agreement with previous works, the obtained results show a significant stimulation of the fibroblasts proliferation induced by copper ions [424]. Copper, indeed, activates MAPK and PI3K-dependent intracellular signalling pathways, which are involved in the cell survival mechanisms and enhances fibroblast proliferation, into a concentration range of 1-100 μM, even though copper concentrations up to 200 μM stabilize fibronectin cables for wound care, without inducing cell toxicity [425]. Interestingly, both the copper complexes wtANG + Cu(II) and rANG + Cu(II) improve fibroblasts proliferation; no significant differences are instead found for S28CANG + Cu(II) with respect to the control, thus further proving the ability of Cu(II) to modulate the ANG activity, confirming the biological relevance of the ANG-Cu(II) complex formation.

The uncoated AuNPs slightly reduce the cell viability of about 8%, while except for the Au-rANG, which maintains a proliferative activity (about 15% increase of cell viability vs. control), no significant differences are found for the other two protein-coated nanoparticles with respect to the control, suggesting a higher biocompatibility of the proteins-coated nanoparticles, than the naked systems.

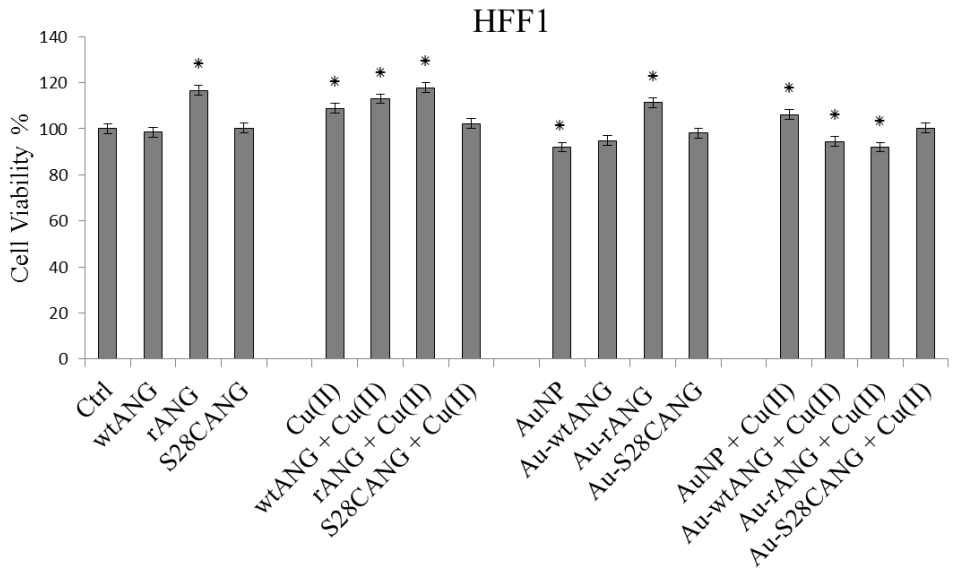

Figure 63- Cell proliferation assay on HFF1 cells treated for 24 hrs with: $3.6 \cdot 10^7$ NP/mL ($4.5 \cdot 10^{-9}$ M) AuNP; $2.7 \cdot 10^6$ NP/mL ($1.1 \cdot 10^{-9}$ M) Au-wtANG; $1.8 \cdot 10^6$ NP/mL ($9.0 \cdot 10^{-10}$ M) Au-rANG; $2.3 \cdot 10^6$ NP/mL ($1.1 \cdot 10^{-9}$ M) Au-S28CANG; the free proteins at the concentration of $2 \cdot 10^{-8}$ M; in the presence or absence of $1 \cdot 10^{-7}$ M $CuSO_4$. (*) $p<0.05$, (**), $p<0.01$, (****), $p< 0.0001$ vs. Ctrl. (One-wayANOVA).

Wound closure assay was carried out to study the wound repair properties of the synthetized systems in the absence or presence of copper ions.

For the assay, fibroblasts were grown in complete cell culture medium in 48-multiwell plates until reaching the confluence. Afterwards, a cell-free 'line' was traced on the plate by scratching the cell monolayer using a sterile plastic tip and following a gentle wash with pre-warmed medium (37 °C) to remove any cell debris, two optical micrographs per scratched well were recorded (experiments performed in duplicate) to get the starting

time (t=0). Therefore, cells were incubated up to 20 hrs of treatment time with the uncoated or protein-coated gold nanoparticles at the concentrations of $3.2 \cdot 10^7$ NP/mL ($4.5 \cdot 10^{-9}$ M) for AuNP, $2.7 \cdot 10^6$ NP/mL ($1.1 \cdot 10^{-9}$ M) for Au-wtANG, $1.8 \cdot 10^6$ NP/mL ($9.0 \cdot 10^{-10}$ M) for Au-rANG and $2.3 \cdot 10^6$ NP/mL ($1.1 \cdot 10^{-9}$ M) for Au-S28CANG; the free proteins at the concentration of $2 \cdot 10^{-8}$ M; in the presence or absence of $1 \cdot 10^{-7}$ M $CuSO_4$. Optical micrographs were collected at the incubation times of 6 hrs and 20 hrs and the wound area was calculated by using the MRI Wound Healing Tool on the ImageJ software (Figure 64- 65).

Noteworthy, after 6 hrs of incubation, the treatments with wtANG + Cu(II) and the synthetized hybrids Au-rANG, Au-wtANG + Cu(II) and Au-rANG + Cu(II) exhibit a statistically significant increase of cell migration with respect to the negative control.

On the other hand, after 20 hrs, in general, most of the treatments exhibit a significant increase of cell migration with respect to the untreated cells. In fact, the three variants of ANG show an increased capability in the wound closure, especially rANG that induces the total closure of the scratch after 20 hrs, while for the negative control the estimated closure is only around 80%. These experimental findings evidence a comparable behaviour of the wtANG and the mutant S28CAng, thus proving evidence on the fact that the amino-acid substitution does not affect the biological behaviour of the protein, as previously described in terms of the enzymatic activity (see section 2.5).

Moreover, in accordance with literature data, copper ions enhance the migration of HFF1 cells, thus leading to a total closure of the scratch site after 20 hrs of treatment [267]; similar considerations hold for the copper-protein complexes. As to the hybrid Au-ANG samples, in the absence of

copper ions only the Au-rANG show a significant improvement of the wound closure in comparison to the negative control; in the presence of copper, the wound closure after 20 hrs is also found for AuNP + Cu(II) and Au-wtANG + Cu(II), thus providing evidence of the metal pivotal role in the wound healing process.

In summary, the obtained results highlight enhanced wound closure capability, at short time of incubation, of the investigated hybrids synthetized by a pure physisorption process of the proteins, rANG and wtANG, on the gold surface in the presence of copper ions. Such systems, indeed, significantly increase the migration rate of HFF1 cells with respect to the free proteins and the naked AuNPs after 6 hrs. Whereas after 20 hrs all the tested systems show a higher wound closure capability with respect to the untreated control in the presence of copper ions. As to Au-S28CANG, the cellular treatment neither after 6 hrs nor after 20 hrs leads to a different response with respect to the control. Probably the small conformational changes induced during the chemisorption process influence the copper complex formation, further changing the biological response of the hybrid.

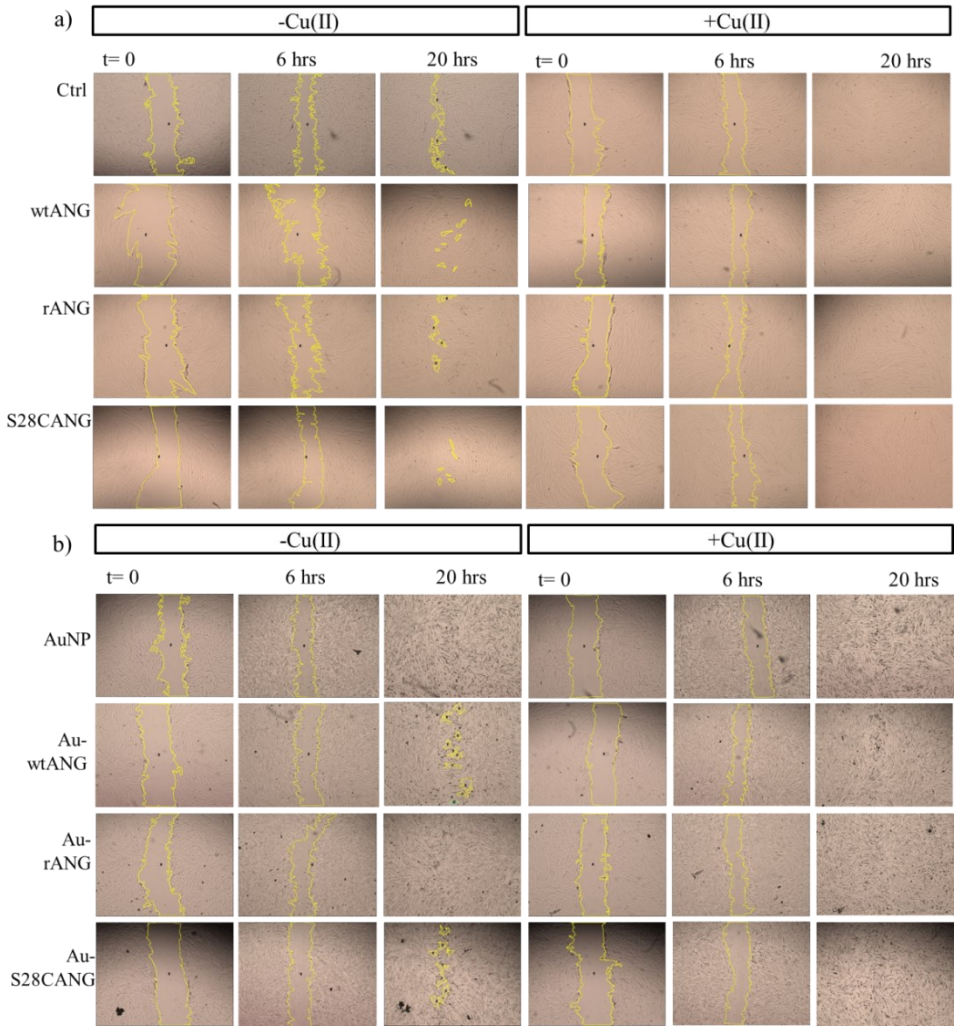

Figure 64- Bright-field optical images of fibroblasts (HFF1) cell line acquired after 6 hrs and 20 hrs of treatment with a) the free proteins (wtANG, rANG, S28CANG) at the concentration of $2 \cdot 10^{-8}$ M; b) the bare AuNPs and the hybrids Au-ANG at the concentration of $3.2 \cdot 10^{7}$ NP/mL ($4.5 \cdot 10^{-9}$ M) for AuNP, $2.7 \cdot 10^{6}$ NP/mL ($1.1 \cdot 10^{-9}$ M) for Au-wtANG, $1.8 \cdot 10^{6}$ NP/mL ($9.0 \cdot 10^{-10}$ M) for Au-rANG and $2.3 \cdot 10^{6}$ NP/mL ($1.1 \cdot 10^{-9}$ M) for Au-S28CANG, in the presence or not of $1 \cdot 10^{-7}$ M copper sulphate.

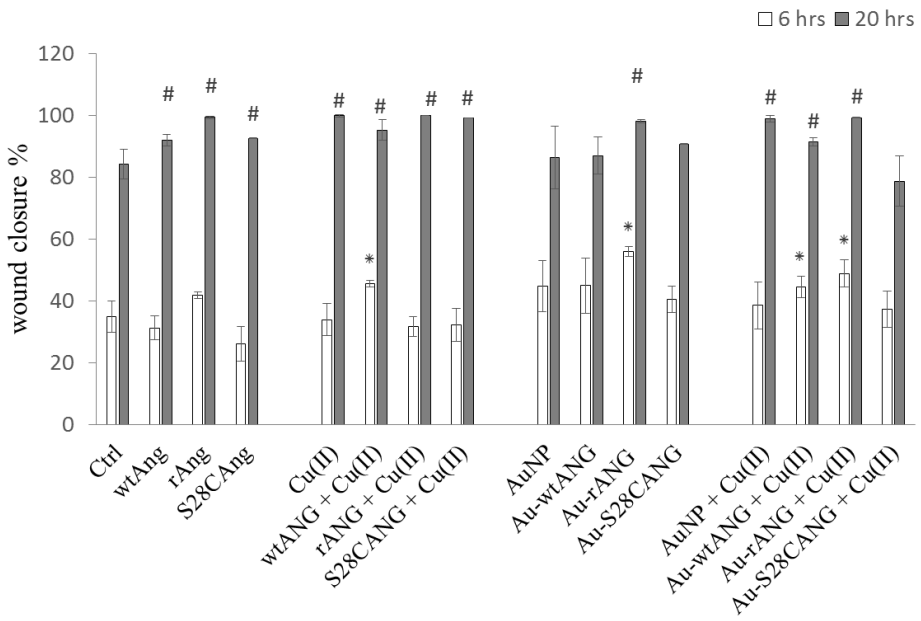

Figure 65- Percentage of wound closure after 6 hrs and 20 hrs of treatment of HFF1cells with the free proteins (wtANG, rANG, S28CANG) at the concentration of $2 \cdot 10^{-8}$ M; the bare AuNPs and the hybrids Au-ANG at the concentration of $3.2 \cdot 10^{7}$ NP/mL ($4.5 \cdot 10^{-9}$ M) for AuNP, $2.7 \cdot 10^{6}$ NP/mL ($1.1 \cdot 10^{-9}$ M) for Au-wtANG, $1.8 \cdot 10^{6}$ NP/mL ($9.0 \cdot 10^{-10}$ M) for Au-rANG and $2.3 \cdot 10^{6}$ NP/mL ($1.1 \cdot 10^{-9}$ M) for Au-S28CANG, in the presence or not of $1 \cdot 10^{-7}$ M copper sulphate. (*) = $p < 0.05$ vs. Ctrl after 6 hrs of treatment; (#) = $p < 0.05$ vs. ctrl after 20 hrs; n=3 (one-way ANOVA).

Since the growth of new vessels is an essential phase of the healing process, we studied the angiogenic activity of the synthetized hybrids by means of an in vitro assay, the tube formation assay, which allows for the development of three-dimensional vessels using human umbilical vein endothelial cells (HUVEC). To perform the assay HUVEC cells were treated with the free proteins wtANG and S28CANG at the concentration of $5 \cdot 10^{-8}$ M, the bare AuNPs and the functionalized Au-wtANG and Au-

S28CANG at the concentrations of $6.8 \cdot 10^6$ NP/mL ($2.2 \cdot 10^{-9}$ M), $2.9 \cdot 10^6$ NP/mL ($1.6 \cdot 10^{-9}$ M), $1.3 \cdot 10^6$ NP/mL ($1.0 \cdot 10^{-9}$ M), respectively. After 2 hrs of incubation, to assess the formation of the tube-like structures, optical images from each sample were captured by using a Leika microscope equipped with a digital camera.

Preliminary results show that after 2 hrs incubation, as expected, the angiogenic proteins wtANG and the mutant S28CANG display higher ability to induce capillary-like tube formation with respect to the untreated control, thus further proving that the Ser to Cys mutation in S28CANG does not affect the biological behaviour of the protein. Interestingly, the treatment with the bare AuNPs, in accord to their antiangiogenic activity, does not lead to the formation of capillary-like structures, while the functionalized hybrids display significant angiogenic activity compared to both the naked nanosystems and the control. Such findings highlight the ability of the hybrids to modulate the angiogenic process, thus combining the proangiogenic activity of the ANG and antiangiogenic intrinsic property of the gold nanosystems.

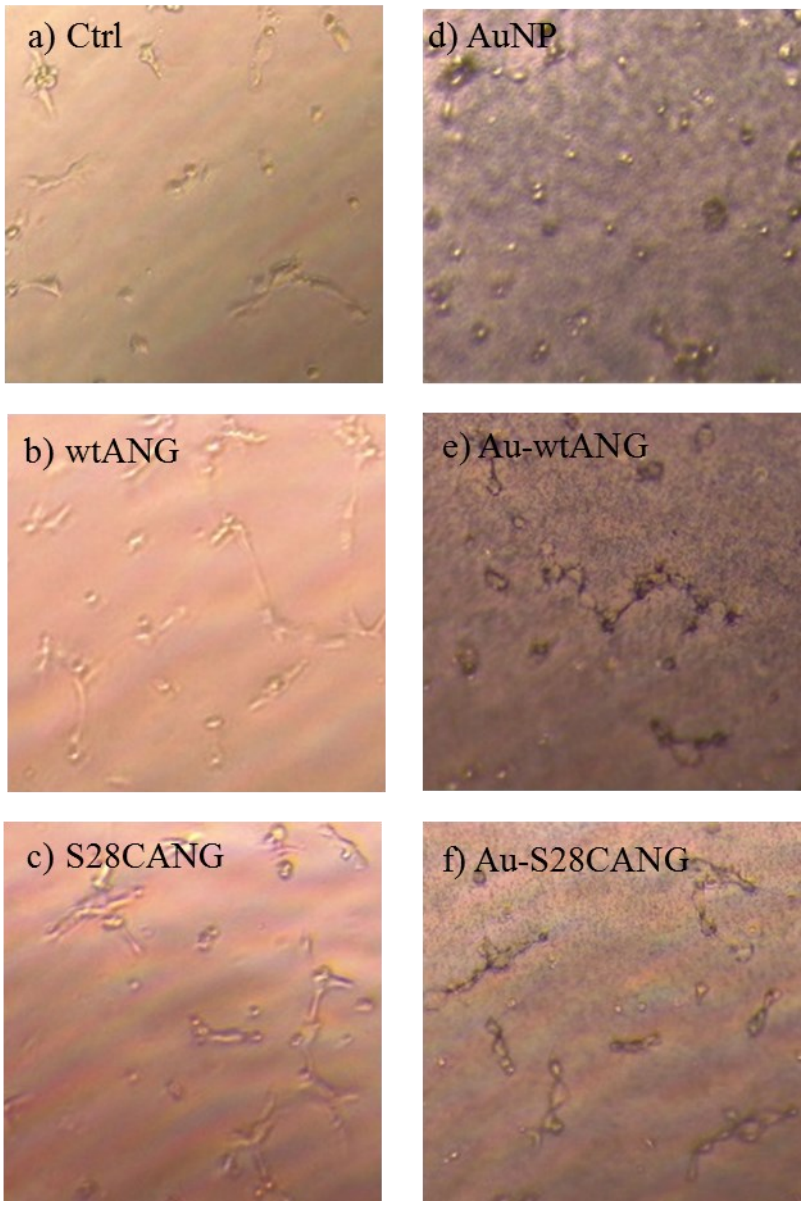

Figure 66- Tube formation assay. Representative bright-field optical images of HUVEC cells cultured on Matrigel matrix and a) untreated or treated for 2 hrs with the free proteins b) wtANG and c) S28CANG at the concentration of $5 \cdot 10^{-8}$ M, d) the bare AuNPs and the functionalized e) Au-wtANG and f) Au-S28CANG at the concentrations of $6.8 \cdot 10^{6}$ NP/mL ($2.2 \cdot 10^{-9}$ M), $2.9 \cdot 10^{6}$ NP/mL ($1.6 \cdot 10^{-9}$ M), $1.3 \cdot 10^{6}$ NP/mL ($1.0 \cdot 10^{-9}$ M), respectively.

Intracellular imaging by laser scanning confocal microscopy, was carried out to assess the cellular up-take of the studied systems on the investigated HFF1 cell line. Moreover, to verify that the effective biological mechanism involved into the improved wound healing capability of the hybrids Au-wtANG and Au-rANG, at short time of incubation, is related to the presence of copper ions which also affect the biological activity of the protein, the intracellular Cu(I) distribution was evaluated by using the CS1 copper probe selective for intracellular copper ions under basal condition, on cells treated with the copper chelator BCS as negative control ($5 \cdot 10^{-5}$ M), the free proteins ($2 \cdot 10^{-8}$ M), the bare AuNP and the hybrids Au-protein at the concentration of $3.2 \cdot 10^{7}$ NP/mL ($4.5 \cdot 10^{-9}$ M) for AuNP, $2.7 \cdot 10^{6}$ NP/mL ($1.1 \cdot 10^{-9}$ M) for Au-wtANG, $1.8 \cdot 10^{6}$ NP/mL ($9.0 \cdot 10^{-10}$ M) for Au-rANG and $2.3 \cdot 10^{6}$ NP/mL ($1.1 \cdot 10^{-9}$ M) for Au-S28CANG.

Figure 67 shows the representative bright-field optical and fluorescence micrographs (in blue, nuclear staining; in green, CS1 copper sensor probe) of HFF1 cells after 1 hr incubation with the different samples. All the samples treated with the nanosystems show small aggregates of AuNPs inside the cells, visible as dark dots, thus proving the effective entrance of the nanoparticles within the HFF1 cells. Interestingly the bare AuNPs aggregates appear bigger in comparison to the aggregates observed for the hybrids Au-ANG, that seems to reach also the nuclei. As to the intracellular copper staining, the obtained results reveal a significant enhancement of the Cu(I) intracellular concentration, after the treatment with the free proteins, with respect to the negative control (Figure 68). These findings highlight the ability of ANG, as free protein, to bind to extracellular copper ions, allowing for its trafficking within the cells.

Noteworthy, the three hybrids Au-Au-ANG, show an increased, capability to deliver copper inside the cells, with respect to the free proteins probably due to conformational changes of the proteins adsorbed on the nanoparticle surface, which could increase the binding affinity with the metal ions in the copper complex formation [426]. However, these different conformational changes also influence the biological properties of the proteins, as shown in Figure 64, so that only the proteins immobilized by physisorption on the gold surface, Au-rANG and Au-wtANG, significantly increase the intracellular copper ions concentration thus improving cell migration at short and long time of incubation in comparison to the chemisorbed mutant S28CANG.

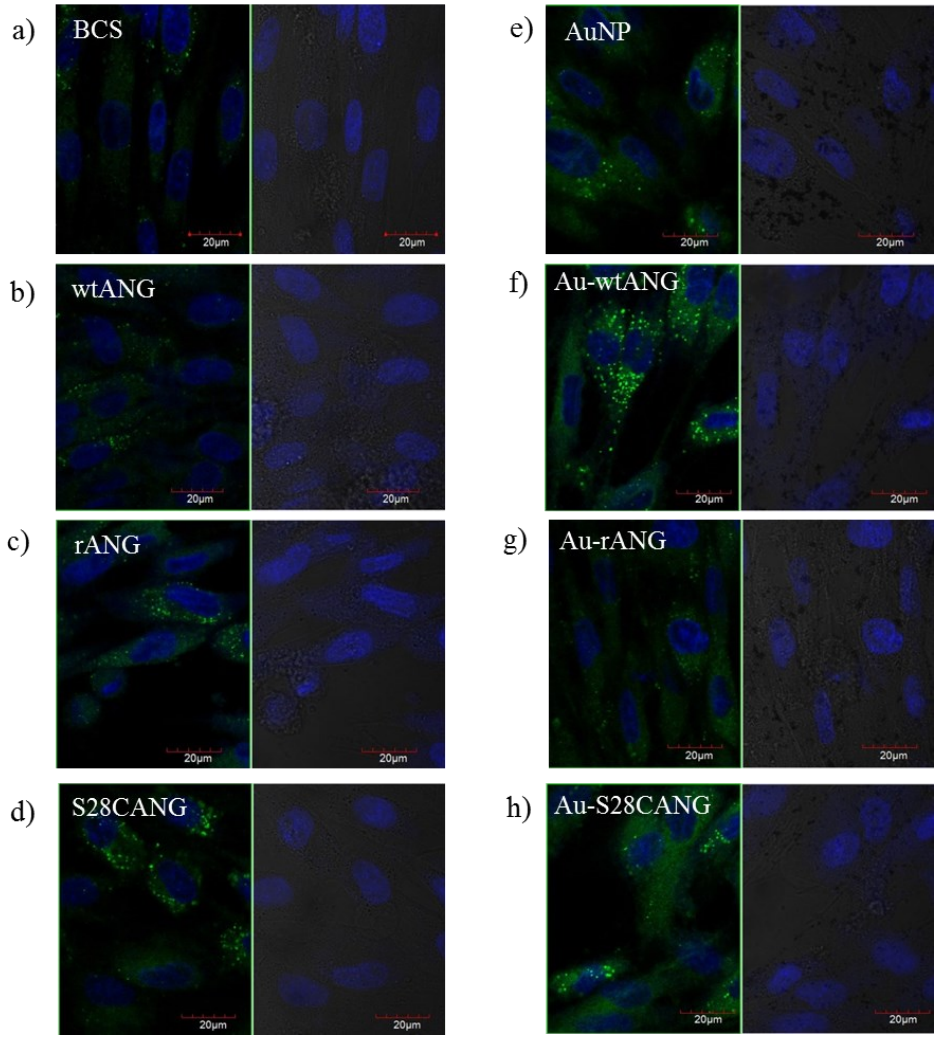

Figure 67- LSM optical bright field and fluorescence (in blue, nuclear staining, $\lambda_{ex/em}$=405/425–450 nm; in green, CS1-copper probe, $\lambda_{ex/em}$=543/550–600 nm) micrographs of HFF1 cells after 1 hr of treatment with a) 50 µM bathocuproinedisulfonate (BCS) as copper chelator; b-c-d) the free proteins, wtANG, S28CANG, rANG at the concentration of $2 \cdot 10^{8}$ M; e-f-g-h) the bare AuNPs and the hybrids at the concentration of $3.2 \cdot 10^{7}$ NP/mL ($4.5 \cdot 10^{-9}$ M) for AuNP, $2.7 \cdot 10^{6}$ NP/mL ($1.1 \cdot 10^{-9}$ M) for Au-wtANG, $1.8 \cdot 10^{6}$ NP/mL ($9.0 \cdot 10^{-10}$ M) for Au-rANG and $2.3 \cdot 10^{6}$ NP/mL ($1.1 \cdot 10^{-9}$ M) for Au-S28CANG, respectively. Scale bar 20 µm.

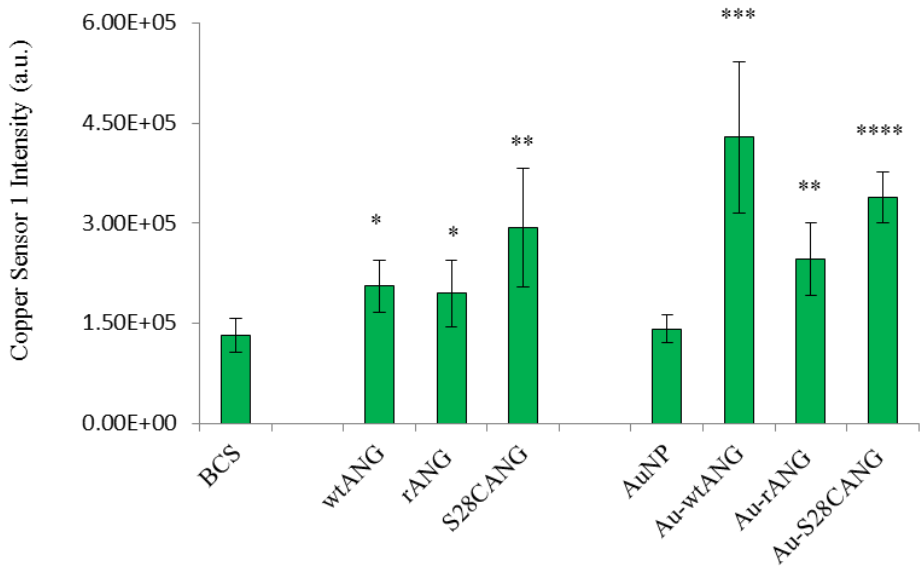

Figure 68- Intensity value of fluorescence corresponding to the CS1 copper probe. Bars represent means ± SEM of at least 5 experiments; (*) = p< 0.05, (**) = p<0.01, (***) = p<0.001, (****) = p<0.0001 vs. BCS (One-way ANOVA).

3.2.2. Cellular response to the hybrid Au-GO-wtANG (PAPER IV)

Cellular experiments on fibroblast HFF1 cell line were carried out to assess the ability of the hybrids Au-GO functionalized with the whole protein wtANG to induce cell migration for potential wound healing treatments. In this regard, MTT assay was firstly carried out to evaluate the HFF1 response in terms of cell viability by treating the cells for 24 hrs with: $1.3 \cdot 10^{6}$ NP/mL ($7 \cdot 10^{-10}$ M) AuNPs; 8.6 μg/mL of GO into the hybrids Au-GO with AuNP at the concentration of $1.4 \cdot 10^{5}$ NP/mL ($2 \cdot 10^{-10}$ M); 6.2 μg/mL of GO into the hybrids Au-GO-wtANG with AuNP at the concentration of $2.1 \cdot 10^{4}$ NP/mL ($6 \cdot 10^{-11}$ M); 10 μg/mL of GO; $5 \cdot 10^{-8}$ M wtANG.

MTT results (Figure 69), in accord with literature data, show that both the synthetized bare AuNPs and GO sheets, don't exhibit cytotoxicity at the tested conditions. Differently, the hybrids Au-GO and Au-GO-wtANG lead to a slight reduction of the cell viability, most likely due to the higher ability of GO, into the hybrid Au-GO, to go across the cell membrane, thus directly reach the intracellular organelles (see section 3.1.2).

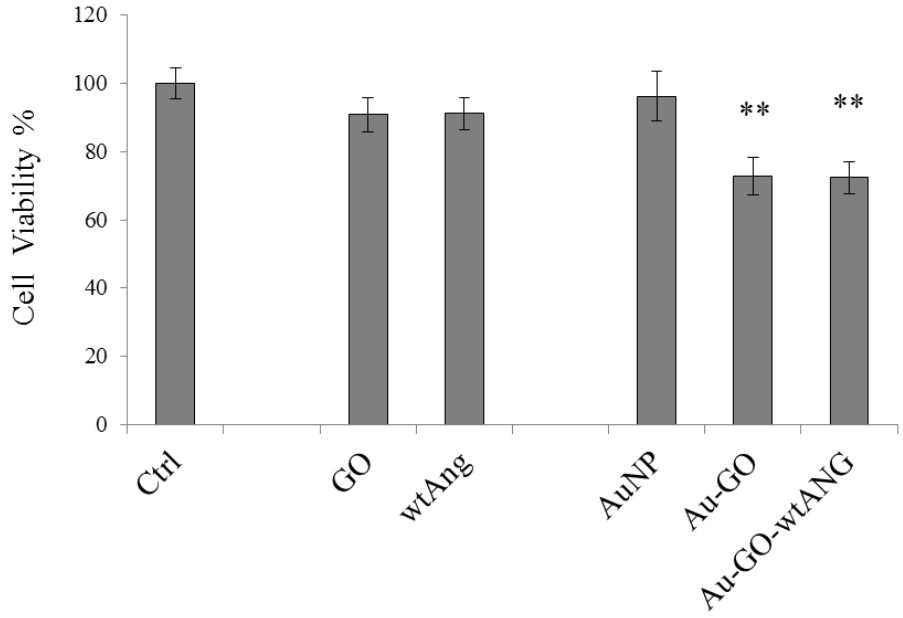

Figure 69- Cell proliferation assay on HFF1 cells treated for 24 hrs with: $1.3 \cdot 10^{6}$ NP/mL ($7 \cdot 10^{-10}$ M) AuNPs; 8.6 μg/mL of GO into the hybrids Au-GO, with AuNP at the concentration of $1.4 \cdot 10^{5}$ NP/mL ($2 \cdot 10^{-10}$ M); 6.2 μg/mL of GO into the hybrids Au-GO-wtANG with AuNP at the concentration of $2.1 \cdot 10^{4}$ NP/mL ($6 \cdot 10^{-11}$ M); 10 μg/mL of GO; $5 \cdot 10^{-8}$ M wtANG. (**) $p<0.01$ vs. Ctrl. (One-wayANOVA).

As to the wound repair properties, wound closure assay was carried out on HFF1 cells treated with the protein-functionalized and un-functionalized Au-GO hybrid, the GO sheets, the free protein wtANG and the bare AuNPs as controls. Optical micrographs were collected at the incubation times of 6 hrs, 24 hrs and 48 hrs and the wound area was calculated by using the MRI Wound Healing Tool on the ImageJ software (Figure 70-71).

Noteworthy, after 6 hrs of incubation, the treatments with wtANG and the bare AuNPs don't exhibit a statistically significant increase of cell migration with respect to the negative control, while the incubation with

GO sheets and both the hybrids Au-GO and the protein-functionalized Au-GO-wtANG significantly reduces the cell migration rate in comparison to the untreated cells. After 24 hrs, in general, all the cellular treatments lead to a comparable percentage of cell migration with respect to the untreated cells except for GO, which seems to impair the HFF1 migration that significantly decreases with respect to the untreated cells. Such an effect is nullified for the hybrid Au-GO-wtANG which exhibits an improved wound closure capability with respect to GO alone. After 48 hrs of treatment, wtANG, as expected, leads to the total closure of the scratch, while for the bare AuNPs the estimated closure is around 98%. GO, does not induce the total closure of the wound area and the calculated percentage of closure is only the 85%. Interestingly the synthetized hybrid Au-GO-wtANG shows a significant enhancement of the wound healing activity with respect to the bare AuNPs, the hybrid Au-GO and the GO alone, thus proving the biological relevance of ANG in the wound repair properties of the synthetized hybrid.

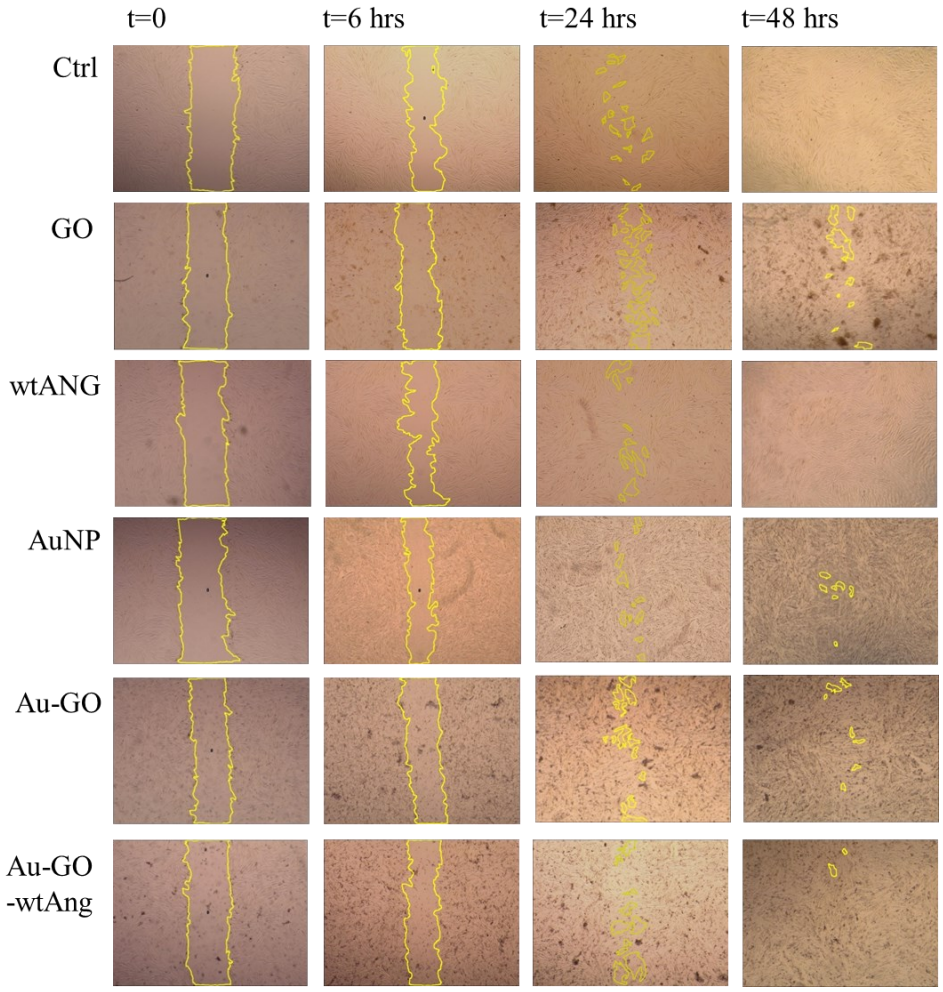

Figure 70- Bright-field optical images of fibroblasts (HFF1) cell line acquired after 6 hrs, 24 hrs and 48 hrs of treatment of HFF1cells with: $1.3 \cdot 10^{6}$ NP/mL ($7 \cdot 10^{-10}$ M) AuNPs; 8.6 µg/mL of GO into the hybrids Au-GO, with AuNP at the concentration of $1.4 \cdot 10^{5}$ NP/mL ($2 \cdot 10^{-10}$ M); 6.2 µg/mL of GO into the hybrids Au-GO-wtANG with AuNP at the concentration of $2.1 \cdot 10^{4}$ NP/mL ($6 \cdot 10^{-11}$ M); 10 µg/mL of GO; $5 \cdot 10^{-8}$ M wtANG.

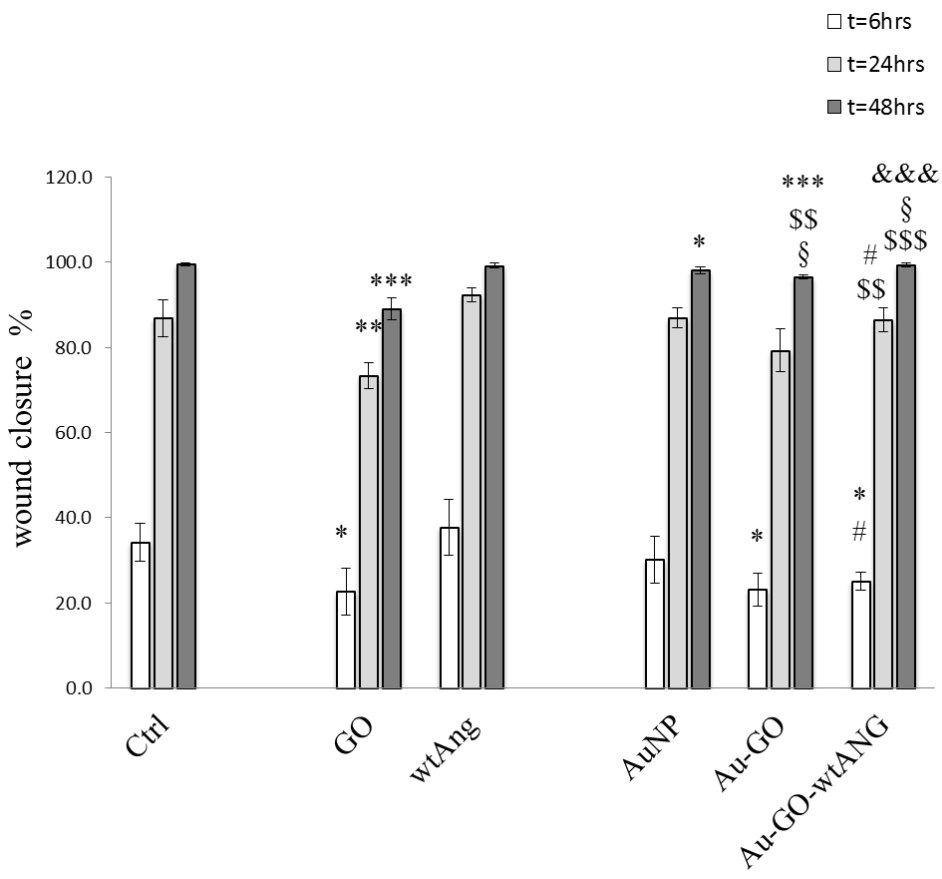

Figure 71- Percentage of wound closure after 6 hrs, 24 hrs and 48 hrs of treatment of HFF1cells with: $1.3 \cdot 10^{6}$ NP/mL ($7 \cdot 10^{-10}$ M) AuNPs; 8.6 µg/mL of GO into the hybrids Au-GO, with AuNP at the concentration of $1.4 \cdot 10^{5}$ NP/mL ($2 \cdot 10^{-10}$ M); 6.2 µg/mL of GO into the hybrids Au-GO-wtANG with AuNP at the concentration of $2.1 \cdot 10^{4}$ NP/mL ($6 \cdot 10^{-11}$ M); 10 µg/mL of GO; $5 \cdot 10^{-8}$ M wtANG. (*) = $p < 0.05$, (**) = $p < 0.01$, (***) = $p < 0.0001$ vs. Ctrl; (#) = $p < 0.05$ vs. wtANG, ($$) = $p < 0.01$, ($$$) = $p < 0.001$ vs. GO, (§) = $p < 0.05$ vs. AuNP; (&&&) = $p < 0.001$ vs. Au-GO n=3 (one-way ANOVA).

Finally, intracellular imaging by laser scanning confocal microscopy, was carried out to assess the cellular internalization of the studied systems

and the interaction with intracellular organelles, namely lysosomes and mitochondria, since the GO and hybrids Au-GO can lead to a significant impairment of their function, as described in the section 3.1.2.

Figure 72 shows the representative confocal microscopy images stained with actin green, lysotracker red, mitotracker deep red and the optical images, of untreated HFF1cells and after 1 hrs of incubation with $1.3 \cdot 10^{6}$ NP/mL ($7 \cdot 10^{-10}$ M) AuNP; 8.6 µg/mL of GO into the hybrids Au-GO, with AuNP at the concentration of $1.4 \cdot 10^{5}$ NP/mL ($2 \cdot 10^{-10}$ M); 6.2 µg/mL of GO into the hybrids Au-GO-wtANG with AuNP at the concentration of $2.1 \cdot 10^{4}$ NP/mL ($6 \cdot 10^{-11}$ M); 10 µg/mL of GO; $5 \cdot 10^{-8}$ M wtANG. The recorded bright field images show small aggregates of AuNPs, as dark spots, while GO sheets are visible as dark blots. The bare AuNPs and the hybrids Au-GO and Au-GO-wtANG are observed inside the cells confirming their efficient access to the intracellular cytosol also reaching the nuclei. As to GO alone, only few aggregates are visible inside the cells thus further proving that the presence of AuNPs into hybrids improve the entrance of the GO sheets into the cells.

The actin staining, confirms the activity of the protein to bind to actin leading to a marked re-organization of the cell cytoskeleton which shows thick actin filament mostly confined along the cellular membrane. On the other hand, thinner filaments of actin are observed after the treatment with GO alone and the hybrid Au-GO. It has been demonstrated, indeed, that GO interacts with F-actin decreasing its assembly and thus impairing the cell cytoskeleton [427]. Interestingly in the presence of the protein such an effect is significantly reduced and dense filaments of actin, homogeneously distribute inside the cells, are clearly observed (Figure 72-

73 a). As to the bare AuNPs no substantial differences, in terms of cytoskeleton re-organization, are shown with respect to the untreated cells.

As to the lysosomal staining (Figure 72-73 b), in the control lysosomes exhibits the characteristic dot distribution, while, as expected, a lysosome enlargement is shown after the treatment with nanosystems, AuNPs, Au-GO and Au-GO-wtANG with respect to the untreated control, thus indicating their accumulation into these organelles that appear significantly activated [428]. Whereas GO and the wtANG show a comparable lysosomal response with respect to the control.

As to the mitochondrial staining (Figure 72-73 c), in the control mitochondria exhibits a rather high distribution and show the characteristic ellipsoidal shape. In general, all the cellular treatments seem to affect the mitochondria function leading to a significant reduction of the signal. However, such an effect is particularly evident in the presence of GO, alone and into the hybrids, Au-GO and Au-GO-wtANG. GO indeed, interacts with the mitochondria of mammalian cells modulating their morphology and function [429].

These findings highlight the maintenance of the biological activity of wtANG immobilized in the nanoplatform Au-GO and its central role in the modulation of the HFF1 biological response to the hybrid Au-GO-wtANG, that only in the presence of ANG shows an improved ability to interact with the cell cytoskeleton, which is involved in the migration of the cells and so enhanced wound healing properties.

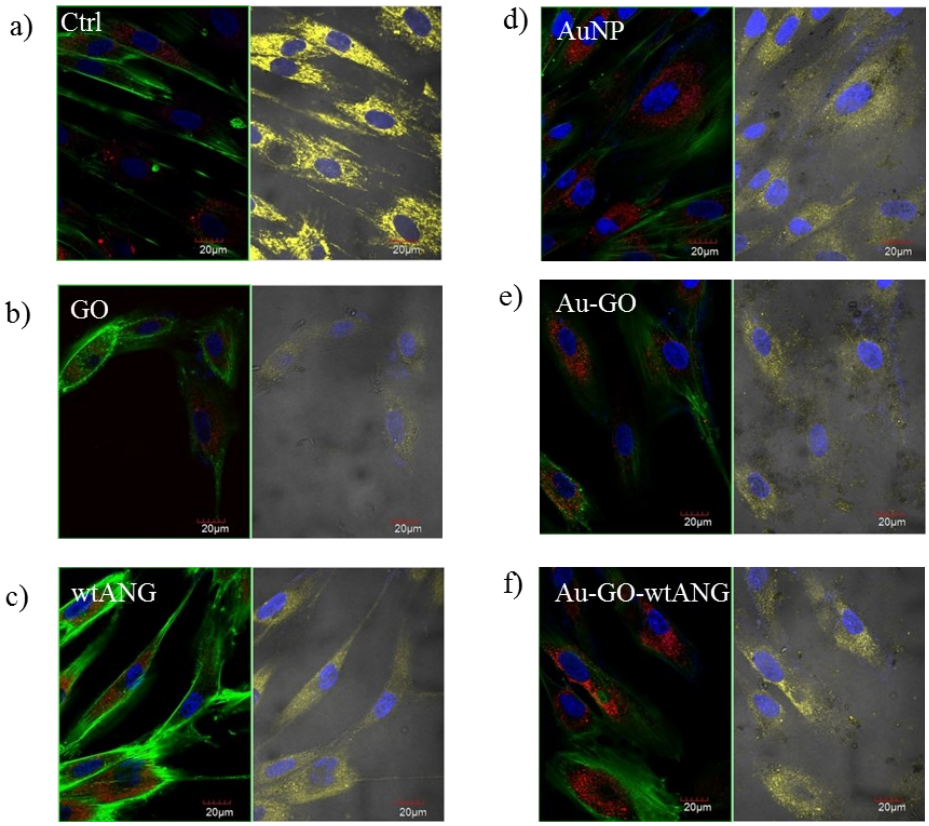

Figure 72- LSM optical bright field and fluorescence (in blue, nuclear staining, $\lambda_{ex/em}$=405/425–450 nm; in green, Actin Green, $\lambda_{ex/em}$= 488/500–530 nm; in red, lysosomal staining $\lambda_{ex/em}$=543/550–600 nm; in yellow, MitoTracker d.r $\lambda_{ex/em}$= 633/650-655nm) micrographs of HFF1 cells after 1 hr of treatment with: $1.3 \cdot 10^{6}$ NP/mL ($7 \cdot 10^{-10}$ M) AuNPs; 8.6 µg/mL of GO into the hybrids Au-GO, with AuNP at the concentration of $1.4 \cdot 10^{5}$ NP/mL ($2 \cdot 10^{-10}$ M); 6.2 µg/mL of GO into the hybrids Au-GO-wtANG with AuNP at the concentration of $2.1 \cdot 10^{4}$ NP/mL ($6 \cdot 10^{-11}$ M); 10 µg/mL of GO; $5 \cdot 10^{-8}$ M wtANG. Scale bar 20 µm.

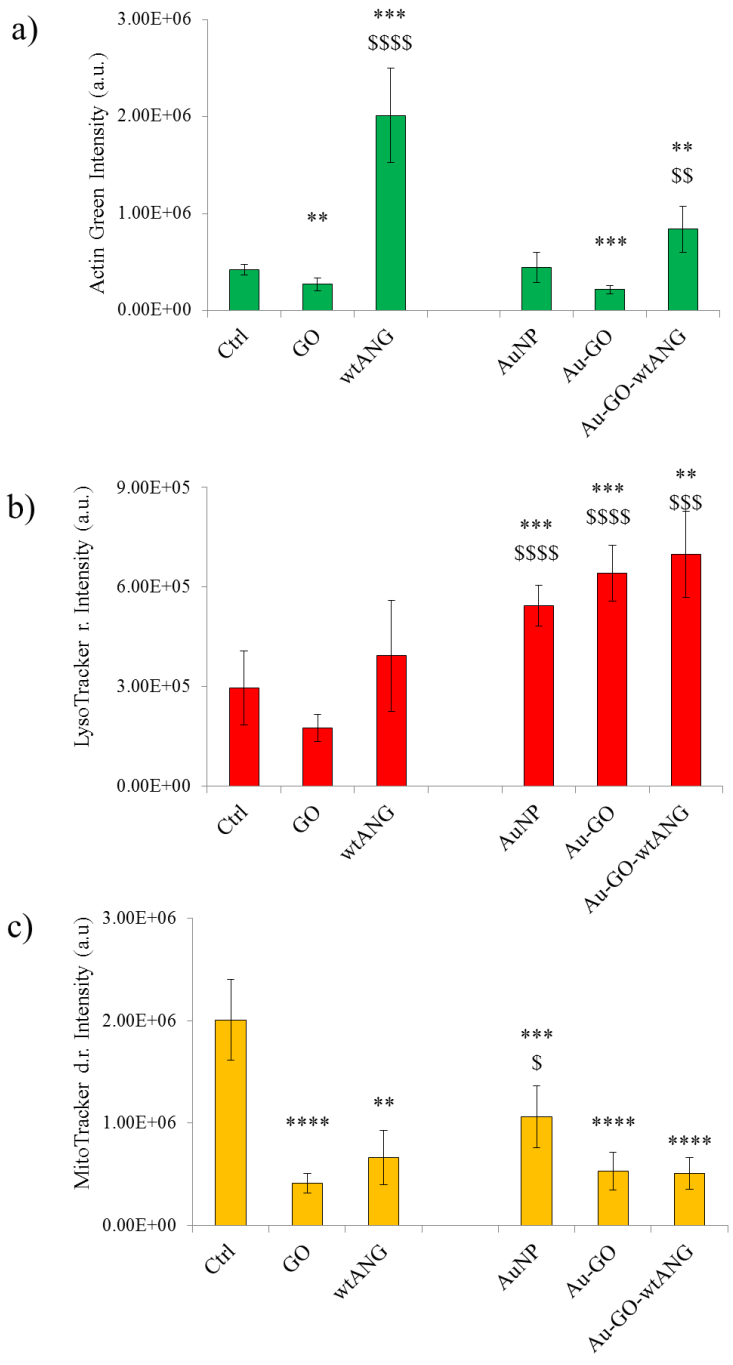

Figure 73- Intensity value of fluorescence corresponding to the a) Actin Green, b) LysoTracker red, c) MitoTracker deep red staining. Bars represent means ±

SEM of at least 5 experiments. (*) $p < 0.05$, (**) $p < 0.01$, (***) $p < 0.001$, (****) $p < 0.0001$ vs. Ctrl; ($) $p < 0.05$, ($$) $p < 0.01$, ($$$) $p < 0.001$, ($$$$) $p < 0.0001$ vs. GO. (One-way ANOVA).

Chapter 4- Materials and Method

4.1 Chemicals

Gold(III) chloride trihydrate, trisodium citrate dihydrate and tris(2-carboxyethyl)phosphine (TCEP) were purchased from Sigma-Aldrich. Ultrapure MilliQ water was used (18.2 mΩ·cm at 25 °C, Millipore). 3-(N-morpholino)-propanesulfonic acid (MOPS) buffer solution (added with 0.003 M KCl and 0.14 M NaCl) was prepared at the concentration of 1 mM and pH was corrected to 7.4.

Glassware was cleaned with aqua-regia rinsing ($HCl:HNO_3$, 1:3 volume ratio) and then washed with MilliQ water before starting the experiments.

All the N-fluorenylmethoxycarbonyl (Fmoc)-protected amino-acids, 2-(1-H-benzotriazole-1-yl)-1,1,3,3-tetramethyluronium tetrafluoroborate (TBTU), used for the ANG peptide synthesis, were obtained from Novabiochem.

N,N-diisopropyl-ethylamine (DIEA), N,N-dimethylformamide (DMF, peptide synthesis grade), 20% piperidine-DMF solution, N-hydroxybenzotriazole (HOBT), triisopropylsilane (TIS), trifluoroacetic acid (TFA), were purchased from Sigma Aldrich.

Small unilamellar vesicles (SUVs) were prepared from 1-palmitoyl-2-oleoylsn-glycero-3-phosphocholine (POPC) and the rhodamine-labelled 1,2-dihexadecanoyl-sn-glycero-3-phosphoethanolamine (Rhod-DHPE), purchased from Avanti Polar Lipids (Alabaster, AL). Phosphate buffer saline (PBS) solution (0.01 M phosphate buffer, containing 0.003 M KCl and 0.14 M NaCl, pH 7.4) was prepared from tablets (Sigma).

The designed primers for ANG protein expression were purchased from Eurofins GWM. The over-expression plasmid (pET22b(+)-Ang), including a codon-optimized gene for ANG, was obtained from Sloning BioTechnology. For the protein expression, yeast extract and glycerol, were purchased from Merck, bacto-peptone from DIFCO, tris(hydroxymethyl)aminomethane (TRIS) from AMRESCO and isopropyl β- D-1-thiogalactopyranoside (IPTG) from VWR, while the other reagents were obtained from Sigma Aldrich at the highest commercially available grade.

Dulbecco's modified eagle medium (DMEM) high glucose, Dulbecco's modified eagle medium (DMEM)-F12, minimal essential Eagle medium (MEME), fetal bovine serum (FBS), streptomycin and L-glutamine were purchased from Sigma Aldrich.

4.2 UV–visible (UV-vis) spectroscopy and dynamic light scattering (DLS) analysis

UV-vis spectroscopy was performed on the aqueous dispersions of AuNPs or Au-GO in quartz cuvettes with 1 and 0.1 cm optical path length on a Perkin Elmer UV-vis spectrometer (Lambda 2S). Particle size analysis were performed by dynamic light scattering (Horiba LB-550) and the results were presented as the mean of at least three measurements.

4.3 Attenuated Total Reflection (ATR) Fourier Transform Infrared (FTIR)

ATR-FT IR spectra were recorded on a Perkin Elmer FT-IR spectrophotometer Spectrum Two, in the range of 400–4000 cm^{-1}. Each spectrum was acquired at a resolution of 4 cm^{-1} (30 scans). AuNPs, the

free peptide $Ang_{60-68}Cys$ and the hybrid Au-$Ang_{60-68}Cys$ were deposited by drop casting on freshly cleaned silicon surfaces and gently dried under a stream of N_2.

4.4 Circular Dichroism (CD)

CD spectra were recorded on a Jasco model 810 spectropolarimeter, in the 195-270 nm wavelength region, at RT and under a constant flow of nitrogen. Spectra were obtained at the scan rate of 50 nm/min and a resolution of 1 nm using quartz cuvettes with 1 or 0.1 cm optical path length as an average of 10 scans.

4.5 Atomic Force Microscopy (AFM)

To register AFM images a drop of the sample was put on freshly cleaved muscovite mica (Ted Pella, Inc.) and incubated at room temperature for 5 minutes. After that, samples were washed with 1 mL of MilliQ, dried under a gentle nitrogen stream and immediately imaged. A Cypher AFM instrument (Asylum Research, Oxford Instruments, Santa Barbara, CA) operating in tapping AC-mode was used. Tetrahedral tips made of silicon and mounted on rectangular 30-μm long cantilevers were purchased from Olympus (AT240TS, Oxford Instruments). The probes had nominal spring constants of 2 N/m and driving frequencies of 70 kHz. Images, with a surface from 1 μm^2, were scanned and the sizes of particles were measured using a free tool in the Asylum Research offline section analysis software.

4.6 Supported lipid bilayer (SLBs) preparation and Fluorescence recovery after photo-bleaching (FRAP) experiment

To prepare small unilamellar vesicles (SUVs), chloroform solution of POPC (5 mg/mL) and Rhod-DHPE (1% w/v) were added to a round-bottom flask. The solvent was evaporated under a gentle N_2 flow to form a uniform thin film on the flask wall. The dried lipid film was emulsified using 10 mM PBS at room temperature and vortexed, to obtain obtaining a lipid vesicles dispersion. This latter was extruded through a 100 nm polycarbonate membrane (13 times), followed by another 13 times through a 30 nm membrane (Avanti Polar Lipids). The obtained SUVs were stored under N_2 and used within 2 weeks, according to the established protocol [430].

To carry out the fluorescence recovery after photobleaching (FRAP) experiment, 5 dishes were cleaned twice, immediately before the analysis, with ultrapure water and 20 minutes of UV ozone treatment, followed by multiple rinsing with MilliQ water and drying under N_2 stream. Subsequently, the dishes were incubated for 30 min with 100 μg/mL of POPC-Rhod in PBS. After this time, the SLBs samples were treated for 30 min with AuNPs, Au-Ang$_{60\text{-}68}$, Au-Ang$_{60\text{-}68}$Cys or Au-Fam-Ang$_{60\text{-}68}$. An untreated SLB-coated dish was used as control.

For the FRAP analysis, time-solved snapshots were acquired as described below. Three images before bleach, then bleaching by using a high intensity (95% power) Ar laser, and other micrographs every 5 seconds up to 2 minutes. By translating the sample stage, an average of three spots per substrate were photobleached in a given experiment.

Fluorescence recovery curves were analysed by ImageJ sofware (FRAP Profiler macro) and the data were normalized to the initial pre-photobleach value. For each sample, the emission recorded from the bleached spots was compared with that obtained from contiguous non-bleached areas.

4.7 Quartz crystal microbalance with dissipation monitoring (QCM-D)

QCM-D sensor crystals (5 MHz) sputter-coated with 50 nm thin silicon oxide were purchased from Q-Sense, Biolin Scientific. QCM-D measurements were carried out in flow mode (100 µL/min) by using a Q-Sense instrument (Biolin Scientific).

The sensor crystals were cleaned by immersion overnight in a sodium dodecyl sulfate (SDS) solution (0.4% w/v in MilliQ water), followed by MilliQ water washing, N_2 blow drying and UV-ozone treatment for the removal of surface organic contamination (two steps of 15 min each with water rinsing in between and at the end).

An additional cleaning was performed by two following steps of rinsing with MilliQ water and PBS in the QCM-D measurement chamber. The fundamental frequency (n = 1, 5 Mhz) and its odd harmonics (n = 3, 5, 7, 9, 11, 13) were monitored as a function of time and the frequency shifts were normalized by dividing for the overtone number. The dissipation changes were also recorded as a function of time.

4.8 Enzymatic activity

Ribonuclease (RNase) assay was performed to attest the maintenance of the biological activity of the mutant S28CANG protein in comparison with the human wtANG.

The ribonucleolytic activity toward tRNA, was determined by measuring the formation of perchloric acid-soluble fragments, following the procedure reported by Shapiro et al. 1987 [431] and modified by Halloway et al. 2001 [363]. Briefly, wtAng, S28CAng (protein concentrations ranging from 0.5 up to 1.5 μg/mL) and tRNA (20 μg/mL) were incubated for 2 hrs at 37 °C in 33 mM MOPS buffer solution added with 33 mM NaCl, at the final volume of 300 μL. Afterwards, samples were diluted with 700 μL of ice-cold 3.4% $HClO_4$ and kept on ice for an additional 10 min. Finally, samples were centrifuged (17,949 RCF, for 10 min) and the absorbance at 262 nm of perchloric acid tRNA soluble fragments was spectroscopically measured.

4.9 Cell cultures

SH-SY5Y neuroblastoma cells were cultured in DMEM-F12 supplemented with 10% FBS, 2 mM glutamine, 100 U penicillin/0.1 mg/mL streptomycin while human glioblastoma cell line (A172) was cultivated in DMEM (n. 30–2002) supplemented with 10% FBS and 100 $\mu g \cdot ml^{-1}$ streptomycin. Human foreskin fibroblasts (HFF1) and human lung fibroblasts (MRC-5) were cultured in DMEM high glucose medium and minimal essential Eagle medium (MEME), respectively, both supplemented with 10% FBS, 4 mM of L-glutamine and 100 U penicillin/0.1 mg/mL streptomycin. Cells were grown in tissue-culture treated Corning® flasks (Sigma-Aldrich, St. Louis, MO) under a humidified atmosphere of air/CO_2 (95:5) at 37°C in an incubator (Heraeus Hera Cell 150C incubator). To induce the differentiation of neuroblsatoma SH-SY5Y, cells were firstly plated at a density of $2.3 \cdot 10^5$ cells/mL in

complete medium for 24 hrs and then were treated for 5 days with 10 μM of retinoic acid in DMEM high glucose.

4.10 Confocal microscopy analysis

Confocal microscopy studies were executed with an Olympus FV1000 confocal laser scanning microscope (LSM), equipped with diode UV (405 nm, 50 mW), multiline Argon (457 nm, 488 nm, 515 nm, total 30 mW), HeNe(G) (543 nm, 1 mW) and HeNe(R) (633 nm, 1 mW) lasers. An oil immersion objective (60xO PLAPO) and spectral filtering systems were used. The detector gain was fixed at a constant value and images were collected, in sequential mode, randomly all through the area of the well. The image analysis was carried out using Huygens Essential software (by Scientific Volume Imaging B.V., The Netherlands). The statistical analysis was performed with ImageJ software and one-way ANOVA test.

To perform the experiments on both SH-SY5Y and MRC-5 cell lines, cells were plated in glass bottom dishes (WillCo-dish®, Willco Wells, B.V.) with 22 mm of glass diameter at a density of $50 \cdot 10^3$ cells per dish in DMEM-F12 or MEME complete medium for 24 hrs. Thereafter, cells were treated with bare AuNPs and the hybrids Au-peptide for 2 hrs, in medium deprived of FBS and stained with nuclear dye Hoechst33342 (1 μg/mL) and LysoTracker deep red ($1.5 \cdot 10^{-11}$ M) before fixing. Cell fixation was performed with high purity 2% paraformaldehyde in PBS, pH = 7.3. Subsequently, cells were permeabilized with 0.5% Triton X-100 supplemented with 0.1% BSA in PBS and then stained with a high-affinity F-actin probe, conjugated to green-fluorescent Alexa Fluor 488 dye (2 drops/mL) .

A172 cells were seeded in glass bottom dishes at a density of $30 \cdot 10^3$ cells per dish in complete medium. After 24 hrs of incubation, cells were treated with AuNPs, the free peptides, the protein and the hybrids in the presence or absence of copper ions for 2 hrs in DMEM high glucose medium without FBS. Thereafter, cells were fixed with 2% paraformaldehyde in PBS, permeabilized and then stained with a Actin Green probe as described above.

As to the HFF1 cells were seeded at a density of $5 \cdot 10^5$ cells/mL in complete medium on 22 mm dishes for LSM (Sigma-Aldrich, St. Louis, MO) for 24h. Cells were incubated with the hybrid Au-ANG samples (at the concentration of $5.6 \cdot 10^7$ nanoparticle/mL) in FBS-deprived medium for 1 hr. Negative controls were prepared by cells treatment with the extracellular copper chelator bathocuproinedisulfonic acid disodium salt (BCS) (50 μM, 3 hrs); positive control cells were instead obtained by cells incubation with bare AuNP or the free proteins. During the last 15 min of the total treatment period, cells were stained with the nuclear dye Hoechst33342, the CS1 probe ($1 \cdot 10^{-6}$ M) of intracellular monovalent copper or LysoTracker red ($1.5 \cdot 10^{-11}$ M) and MitoTracker deep red ($5 \cdot 10^{-10}$ M) for the lysosomal and mitochondrial staining. Cell fixation was performed with high purity 4% paraformaldehyde in PBS. Finally, cells were permeabilizedand stained with Actin Green probe.

4.11 MTT assay

To perform the cytotoxicity assay, cells were plated in two different 96-well plates, at a density of 15 x 10^3 cells per well, in complete medium supplemented with 10% or 15% FBS for HFF1 cells, for 24 hrs. Afterword, cells were treated with the samples for 24 hrs and the

incubation was performed in medium supplemented with 1% FBS. Cytotoxicity was determined at 37°C, by using the the tetrazolium dye 3-(4,5-dimethylthiazol-2-yl)-2,5-diphenyltetrazolium bromide (MTT) [432]. After 2 hrs of incubation, the enzymatic reduction of MTT to the insoluble purple formazan product was detected by dissolving the crystals with 100 μL of dimethyl sulphoxide and thus measuring the absorbance at 569 nm by Varioscan spectrophotometer. The experiments were performed in triplicate and the results are presented as the means ±SEM

4.12 ROS cell and mitochondrial $O_2^{\bullet-}$ production

SH-SY5Y cells were treated with GO, AuNP and Au-GO hybrid systems for 24hrs. Then, cells were stained with 2′,7′-dichlorofluorescein (DCF) (Thermo Fisher Scientific) (total ROS) or MitoSOX (Thermo Fisher Scientific) (mitochondrial $O_2^{\bullet-}$) and analyzed by Varioscan spectrophotometer (λ_{ex}= 493 nm, λ_{em}= 523 nm or λ_{ex}= 510, λ_{em}= 580, respectively). Results are represented as the increase in DCF or MitoSOX signals with respect to controls. Data are presented as the means ± SEM of eight replicas.

4.13 Scratch wound closure assay

HFF1cells were seeded and cultured in growth medium until confluence in 24-well TPP® tissue culture plates. The confluent HFF1 monolayers were scratched and wounded using a universal sterile 200-μL pipette tip and then rinsed with complete medium. Plates were marked immediately after the scratch to ensure that scratches were measured at the same location throughout each experiment. Each well was treated with AuNP or Au-ANG samples in the presence or absence of $1 \cdot 10^{-7}$ M $CuSO_4$

as well as with the free proteins, in DMEM medium supplemented with 1% of FBS. Serial phase contrast images (Leica) of the in vitro wounds were taken immediately after the treatment and then after 6 hrs, 24 hrs and 48 hrs of incubation. The width of the separation wall was measured by using the MRI Wound Healing Tool on the ImageJ software (version 1.50i, NIH).

4.14 Tube formation assay

To perform the tube formation assay, Matrigel matrix (Corning) was thawed at 5 °C overnight and spread over each well (50 µL) of a 96-well plate. The plate was then incubated for 30 min at 37 °C to allow the gel to solidify. Thereafter, HUVEC cells (10,000/well) from passage 4 were seeded in 100 µL of Medium 200, not supplemented with low serum growth supplement (LSGS), untreated and treated with the free proteins wtANG and S28CANG at the concentration of $5 \cdot 10^{-8}$ M, the bare AuNPs and the functionalized Au-wtANG and Au-S28CANG at the concentrations of $6.8 \cdot 10^{6}$ NP/mL ($2.2 \cdot 10^{-9}$ M), $2.9 \cdot 10^{6}$ NP/mL ($1.6 \cdot 10^{-9}$ M), $1.3 \cdot 10^{6}$ NP/mL ($1.0 \cdot 10^{-9}$ M), respectively. After 2 hrs of incubation at 37 °C, the tube structures were observed with a Leika microscope equipped with a digital camera and three bright field images (magnification 4x) were captured for each sample.

Conclusion

In this work, hybrid nanosystems were fabricated to specifically modulate the angiogenic process with potential application in cancer and wound care. Following an approach of increasing complexity, spherical gold nanoparticles (AuNPs) and the hybrid nanoplatform AuNPs-graphene oxide (Au-GO) were synthetized and functionalized with ANG peptides, encompassing the cell-binding site (60-68 sequence) of the protein, using a peptide-mimetic approach to control the angiogenic process or the whole protein, ANG. In particular, we assess the basic Ang_{60-68}, the cysteine-added $Ang_{60-68}Cys$ and the carboxyfluorescein labelled Fam-Ang_{60-68} peptides. As to the whole protein, the physiological protein wtANG, the recombinant rANG with an additional methionine residue at the N-terminal domain and the mutant S28CANG, designed to introduce a thiol-free cysteine residue on the protein, were scrutinized.

The different peptide/proteins were used to create hybrid assemblies with AuNPs through two different approaches. In particular, a prevalent physisorption process, for $Ang_{60-68,}$ Fam-Ang_{60-68}, wtANG and rANG and a mixed physisorption/chemisorption mechanism, resulting in the grafting of $Ang_{60-68}Cys$ and S28CAng molecules to the metal surface of the nanoparticles, owing to the formation of the S-Au high-affinity bonds. The two functionalization methods as well as the charge/steric hindrance effects associated with the Fam moiety, were investigated at the AuNP interface by means of UV-vis spectroscopy in terms of the shifts in the maximum of absorbance and wavelength of the AuNP plasmon peak.

The obtained results revealed different adsorption modes of the molecules triggered by the two physisorption and chemisorption methods. Thus, a "disordered" shell of proteins/peptides was figured around the nanoparticle surface, while an "ordered" arrangement of molecules around AuNPs characterized the chemisorbed systems, due to formation of the strong thiol-gold bonds. On the other hand, an increased contribution of aggregation effects, related to the negatively charged carboxyfluorescein moiety and its steric hindrance was observed for Au-Fam-Ang$_{60-68}$. Whereas, a higher polydispersity of the colloidal dispersion associated with the presence of several size populations due to both aggregation effects and nanoparticle coating was observed for the Au-ANG hybrids.

Such findings were also supported by AFM and DLS measurements, which evidenced a significant and distinctive increase of the AuNP core and the hydrodynamic size related to the two studied functionalization processes.

As to the Au-GO nanoplatform, a novel and simple one-step reduction method was developed for the assembly of graphene oxide and gold nanoparticles and the effective interaction between GO nanosheets and gold colloids was demonstrated by UV-vis spectroscopy. The hybrid Au-GO-wtANG was obtained by physisorption of the protein on the nanoplatform surface and the molecule adsorption was demonstrated by the UV-vis spectra following the red-shift of the plasmon peak, the increase of the FWHM value as well as of the size by DLS measures.

The interaction of the peptide/protein-functionalized hybrids was scrutinised at the bio-interface with system of model membranes and cells, specifically cancer cells (undifferentiated neuroblastoma, SH-SY5Y cell

line; tumour glioblastoma cells, A172) with respect to normal cells (fibroblasts, MRC-5 and HFF1 cell lines; differentiated neuroblastoma d-SH-SY5Y) in terms of cytotoxicity, cellular internalization, biological effects on intracellular organelles (cytoskeleton, lysosomes, mitochondria) cell-migration and tubulogenesis.

The interaction with model membrane systems confirms the effective coating of the nanoparticles with the proteins/peptides, that exhibit a comparable behaviour against the SLBs, both as free-molecules and ANG-adsorbed on the nanoparticle surface.

Cellular experiments on cancer cells, neuroblastoma SH-SY5Y and glioblastoma A172 cells, in comparison to normal fibroblasts and differentiated d-SH-SY5Y, highlighted the cell-specific activity of the synthetized systems. Thus, our results showed promising anti-cancer capabilities, particularly against glioblastoma at short time of incubation, for the hybrids Au-peptide/protein, being able to reduce the viability of these tumour cells in comparison to the free peptide/proteins. Whereas, no cytotoxic effects were observed on normal cells for all the tested conditions. Moreover, the controlled modification of the surface properties, obtained through the two different functionalization approaches, differently modulated the interaction of the biomolecules immobilized on the gold surface and cellular organelles. Thus, a different organization in term of cellular cytoskeleton was observed after the treatment with the three Au-Ang hybrids. Au-Ang$_{60-68}$ more markedly increases the intensity of the actin staining in comparison to the other two hybrids Au-Ang$_{60-68}$Cys and Au-Fam-Ang$_{60-68}$ and the actin filaments were thick and confined to the membrane on neuroblastoma cells. On the other hand, Au-Ang$_{60-68}$Cys strongly impaired the A172 cell cytoskeleton

leading to a significant reduction of the actin signal. Moreover, Au-Ang$_{60-68}$Cys appeared mostly localized on the cellular membrane in both the cell lines, confirming the role of the 60-68 sequence that binds to the cell membrane, thus reducing the cellular internalisation of the gold nanoparticles covalently functionalised with the fragment peptide.

All the nanosystems showed a marked activation of lysosomes indicative of cell internalization and stress effect in all the studied cell lines.

Recognized the essential role of the copper ions in the angiogenesis process and its capability to form complexes with ANG which are able to modulate the cellular expression and the biological functions of angiogenin, ANG- copper (II) complexes were also scrutinized.

CD measurements proved that the Fam unit does not perturb the coordination environment of the Ang$_{60-68}$ peptide in the complex with Cu(II) and further revealed comparable conformational features of the three proteins with minor structural rearrangements of the secondary structure of ANG, that occurred after the addition of copper.

Cellular results highlighted that the copper ions supplementation causes an unmistakable cytoskeleton impairment with an evident reduction of the actin signal on the studied cells. This effect is more appreciable after the treatment with Ang$_{60-68}$-Cu(II) and Fam-Ang$_{60-68}$-Cu(II) complexes on undifferentiated neuroblastoma cell line, thus confirming the ability of copper to modulate the biological behavior of ANG, probably due to the promotion of conformational changes of the peptide structure, that affects the interaction between the biological molecules and the cells.

These results are very promising to modulate the cell cytoskeleton arrangement and could allow for the design of useful nanoplatforms able to control the vessels growth.

As to the hybrids Au-GO, cellular results proved that the AuNPs support the entrance of GO sheets into the cancer cells and revealed an increase of intracellular ROS concentration associated with mitochondrial dysfunctions and enhanced cytotoxic effects on neuroblastoma cells, providing promising potentialities for the medical treatment of cancer disease.

Cellular experiments on human fibroblasts (HFF1 cell line) were performed to scrutinize the proliferation and wound healing properties of the hybrid Au-ANG, both in the absence and the presence of copper ions and of the nanoplatform Au-GO-wtANG. The obtained findings provided evidence of the ability of ANG to bind to extracellular copper, thus increasing its intracellular concentration, while wound closure assay reveals enhanced and rapid wound healing capability of the hybrid assemblies Au-ANG, specifically the physisorbed systems Au-wtANG and Au-rANG, in complex with Cu(II), thus attesting the pivotal role of the metal in the wound healing process. Moreover, tube formation assay on HUVEC cell highlighted the ability of the hybrids Au-wtANG and Au-S28CANG to modulate the angiogenic process.

As to the Au-GO-wtANG nanosystem, a significant improvement of the wound healing activity was observed with respect to the bare AuNPs, the hybrid Au-GO and the GO alone, which, instead, impaired the migration of fibroblast cells also affecting the cell cytoskeleton and the mitochondrial functions. Such data prove the biological relevance of ANG

in the wound repair properties of the synthetized hybrids and are very promising to develop a multifunctional platform for wound care treatment and tissue regeneration applications.

Appendix- Methodology

Techniques for the characterization of nanoparticles

1. UV-vis spectroscopy

UV-visible spectroscopy is an easily available technique extensively used for the characterization of noble metal nanoparticles, like AuNPs, which show distinctive optoelectronic features. Such a technique allows for the detection of the effective nanoparticles surface functionalization with target compounds, since the optical absorption of AuNPs depends on the dielectric properties of the surrounding chemical environment [433] and the UV-vis spectrum of the adsorbed molecules can be modified upon their interaction with the nanoparticle surface [434]. Given that, UV-vis spectroscopy further permits a sensible and rapid quantification of the adsorbed compounds [435]. Moreover, the interaction of nanoparticles with some analytes namely, metals, salts and biomolecules, results in small changes of the aggregation degree of colloidal AuNPs, which causes also a variation of the SPR band. In this respect, UV-vis spectroscopy has been used for the development of several analytical procedures which, based on the observation of changes in the plasmon extinction peak position, allow to quantify metals ions like copper [436], lithium [437], platinum [438] ions, as well as organic compounds such as proteins [439] and nucleic acids [440] within the analysed samples. Colorimetric measures were also used to detect large objects like cells. In this regard, gold nanoparticles functionalized with aptamer sequences were synthetized to specifically interact with targets cells (e.g. cancer cells), causing an increase of the

absorbance and light scattering of the solution [441]. Furthermore, the dependence of the nanoparticle optical properties on their geometric parameters allows the UV-vis spectroscopy to finely determine the shape and the size of the particles [442], but also the stability, as well as the kinetics of nucleation and growth of the nanoparticles [443].

The basic principle behind the UV-vis spectroscopy is the absorption of light in the visible (400-750 nm) and ultraviolet (200-400 nm) ranges, associated with the excitation of electrons from the ground state (S_0) to the higher energy excited states (S_1, S_2 etc.), considering that electrons in either atoms or molecules are distributed between several energy levels and principally reside in the lowest ones [444]. Since these transitions are quantum phenomena and correspond to the absorption of an energy quantum, a photon, the excitation and so the light absorption, can occur only if the introduced energy, $E = h\nu$ derived from the electromagnetic radiation, matches with the difference in energy between the two electronic levels. Such electronic energy levels are described by molecular orbitals, which arise from a combination of atomic orbitals and in particular, the two bonding orbitals σ and π, which contain bonding pairs of electrons and the non-bonding orbital *n,* containing lone pairs of electrons. Whereas, the electronically excited electrons occupy the two anti-bonding orbitals, σ^* and π^*, which are normally empty. Accordingly, possible electron transitions are σ to σ*, n to σ*, n to π*, π to π*, even though the most energetically favoured electron promotion comes from the highest occupied molecular orbital (HOMO) to the lowest unoccupied molecular orbital (LUMO) (Figure 1_a) [445].

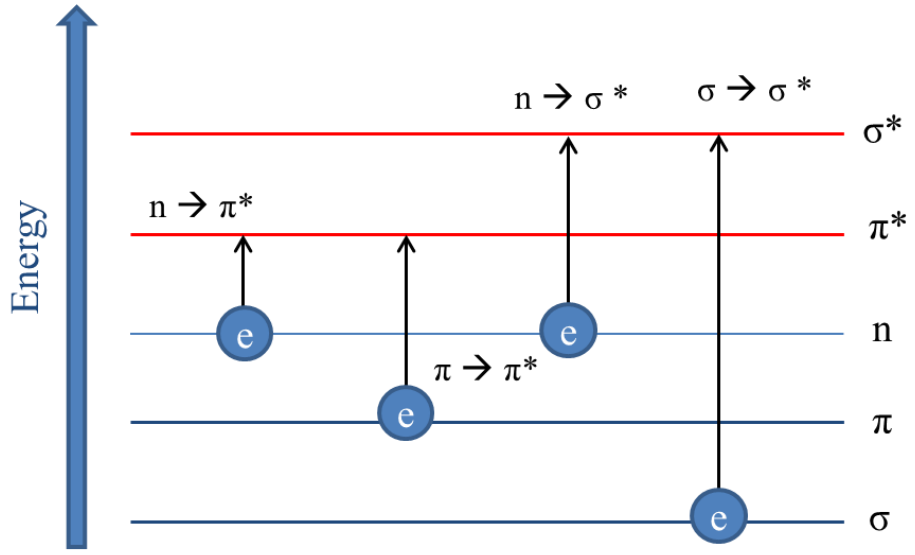

Figure 1$_a$- Possible transitions between bonding and anti-bonding electronic energy states, when the light is absorbed in the UV-vis spectroscopy.

The σ to σ* and n to σ* transitions require high energy and occur in the far UV region, while n to π* and π to π*, which characterize molecules with un-saturated centres, require less energy and a radiation with longer wavelengths. Noteworthy, several inorganic species, in solution, absorb light in the visible region, owing to a process called charge transfer, whereby electrons move from a system, the donor, to an orbital associated with the acceptor, by the energy provided from the visible light [446].

When a radiation with a specific wavelength λ, and intensity I_0 passes through a sample with a known path length *l,* its intensity *I* drops along the pathway in an exponential manner. The amount of light absorbed is expressed as molar absorptivity ε, which measure the characteristic "absorbing power" of a substance and is clearly related to the transition probability at a precise wavelength. The molar absorptivity is the defined by the Lambert–Beer low as follow:

$$\varepsilon = \frac{A}{c \cdot l}$$

where A is the absorbance or optical density, $A = log_{10}\left(\frac{I_0}{I}\right)$, I_0 is the intensity of the incident light, I is the intensity of the light transmitted through the sample and c is the sample concentration in mol/L [447].

Given that each electronic energy level possess its own set of vibrational and rotational levels with discrete energies, the electronic transitions give rise to a combination of rotational and vibrational transitions, which further appear as a continuous absorption band in the UV-vis spectrum, which is usually presented as a plot of A versus the wavelength of irradiation.

2. Atomic force microscopy

Atomic force microscopy (AFM) is a pivotal nanotechnology tool for the characterization of nanomaterials, providing information about the topography as well as mechanical, electrostatic, optical and magnetic properties of their surface [448], offering, in addition, the opportunity to gain three-dimensional images of the nanostructures with high resolution [449]. As to the nanoparticles, AFM is used to determine their shape and size distribution [450], giving also a detailed characterization of the submicron-size molecules, such as proteins and drugs, adsorbed on the nanoparticle surface [451], with a vertical and lateral resolution of 1 and 0.1 nm, respectively [452]. Furthermore, AFM allows for the detection of the nanoparticles mechanical properties, like hardness and elastic modulus, which often deviate from their bulk materials and changes with the size and the surface functionalization [453]. Interestingly, the ability to study the surface properties in a non-invasive way at the nanometre scale, makes AFM useful to also investigate the cell surface and its mechanical response like deformability, cytoadherence and cytoskeleton remodelling, upon the interaction with biomolecules and nanostructures [454, 455] and to monitor dynamic processes such as cell division, growth and movement [456].

AFM system consists of a probe with a sharp tip (height < 5 μm, diameter < 10 nm), generally made of silicon or silicon nitride (Si_3N_4), particularly sensitive to the interactions at the atomic level [457], which is fixed at the end of a micro-machined cantilever, that is around 100-500 μm in length [458]. The position of the probe on the surface sample is controlled by a scanner made of a piezoelectric material, which expands

and contracts when a voltage is applied, thus allowing precise movements of the sample at nanometre resolution, in the x, y and z directions. As the tip interacts with the sample, the cantilever deflects, according to electrostatics, magnetic, capillary and Van der Waal interactions between the tip and the surface. Such a deflection is revealed by a beam laser, which is reflected from the back of the cantilever to position–sensitive detectors, called photodiodes and it is used by a feedback system, to track the surface for imaging and measuring [459]. The feedback mechanism enables also the piezo scanner to maintain the tip either at a constant force above the sample surface thereby monitoring the height deviation, or at a constant height which allows for the deflection force recording.

The interacting force between the tip and the sample surface depends both on the spring constant of the cantilever and the distance with the surface and can be described by the Hooke's low as follow:

$$F = -k \cdot x$$

where F is the force, k is the spring constant and x is the cantilever deflection.

Generally, the cantilever can operate in three different modes: non-contact, contact and tapping mode. The interacting force in each operating mode can be described by a force to displacement curve (Figure 2_a). Thus, weak attractive forces are generated when the distance between the tip and the sample surface is quite large. Such attractive forces increase by reducing the interatomic distance as long as the atoms are so close that the electron clouds start to repulse each other. The interaction force is zero when the interatomic distance reaches 1-2 Å and become entirely repulsive when the atoms are in contact [460].

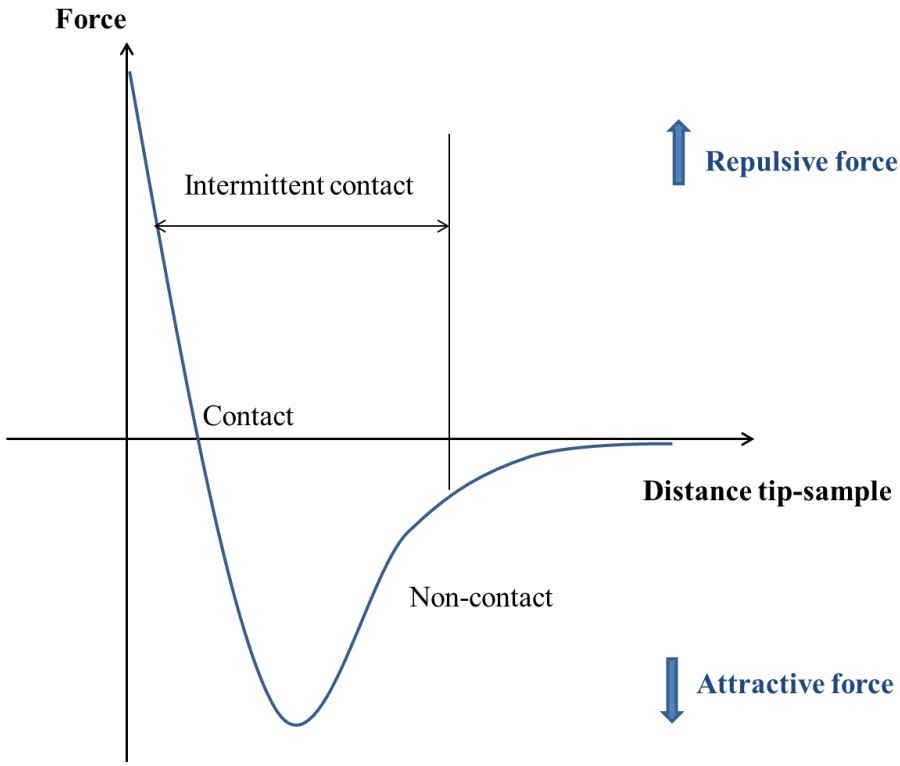

Figure 2$_a$- Interatomic force variation versus distance between the AFM tip and the sample surface

Accordingly, in the non-contact mode, the distance between the sample and the tip is around 50-150 Å to allow the detection of attractive Van der Waals forces. Since these forces are rather weak, the cantilever, which is mounted on a piezo element, is strained to oscillate near its natural resonance frequency. Thus, the amplitude, phase and frequency shifts of the cantilever, given by the attractive interactions generated between the tip and the sample surface, allow to extract the topographical information of the sample [461].

In the contact mode the tip is close to the sample. Such a mode is also known as repulsive mode, owing that repulsive Van del Waals forces

dominate any other attractive force between the tip and the sample surface. Using this mode, the image of the sample is given by operating in either constant height or constant force. Contact mode is generally used to investigate solid sample, since the application of improper force to soft surface could cause reversible but also irreversible deformation of the sample [462].

As to the tapping mode or dynamic mode, it is based on the oscillation of the cantilever induced by an applied voltage on the piezo element [463]. The cantilever oscillation is nearby its resonance frequency, typically in the range of 20-100 nm when the tip is not in contact. During the scanning, the tip alternately touches the sample surface and lifts, at a frequency of 50-500 kcycle/s, causing an energy loss and thereby a variation of the oscillation amplitude according to the topography of the sample [464]. The amplitude variation is detected by both the optical and feedback systems which, by comparing the set values with the measured values, generates an error signal which leads the piezo element to adjust the tip position in order to maintain a constant amplitude and force on the sample. This operating mode is useful to acquire high resolution images of soft samples and overcomes problems like adhesion and friction which usually characterize the contact mode. Thus, it can be applied to image biological structures, such as proteins and nucleic acids [465, 466], but also highly corrugates objects, like cells [467] and for the nanoparticle sizing [468].

3. Dynamic Light Scattering (DLS)

Dynamic Light Scattering is a non-invasive technique typically used to study the physico-chemical properties of macromolecules and nanoparticles in the size range from 1 to 4000 nm. Such a technique allows for the detection of aggregation of proteins, protein-protein interaction studies and in particular nanoparticles analysis [469].

In a typical DLS experiment, the sample is exposed to a laser beam. When the laser encounters the dispersed particles, light scatters in all directions and the intensity of scattered light is measured as a time averaged intensity by an appropriate detector, thus providing useful information on both the molecular weight and radius of gyration of macromolecules. Moreover, the analysis of the intensity fluctuations of the scattered light, caused by the Brownian motion of particles in solution, described as the random movement of particles suspended in a fluid resulting from their collisions with the molecules of solvent, allows for the measurements of the diffusion coefficient (Dτ), which relates to the particle hydrodynamic size, for spherical particle, through the Stokes-Einstein equation:

$$d_{hydrod.} = \frac{kT}{6\pi\eta D_\tau}$$

where $d_{hydrod.}$ is the hydrodynamic diameter, D_τ is the translational diffusion coefficient, μ is the Boltzmann's constant ($1.38 \cdot 10^{-23}$ kg·m^2·s^{-2}·K^{-1}), T is the absolute temperature and η is viscosity.

As it is shown in the equation, the particle diffusion depends on the temperature and the viscosity of the surrounding medium as well as on the size of the particles. To this respect, accurate control of both temperature and solvent viscosity is essential to perform DLS measures. At the beginning of the experiment, when the scattered intensity is related to several time points, the observed values are similar, losing their similarity over the time due to the motion of the particles. At the same temperature and viscosity, "small" particles move rapidly, not adopting specific positions and thereby creating rapid variations in the scattering intensity. On the other hand, "large" particles move rather slowly resulting in similar positions at different time points so that the similarity of the intensities over time persists for long periods.

Moreover, the hydrodynamic diameter is influenced by the ionic strength of the medium as well as by the shape and the surface structure of the particles. As to the ionic strength, ions in the medium affect the particle motion by changing the thickness of the electric double layer, which surrounds the particle surface. In particular, a lower concentration of ions reduces the motion of the particles by increasing the electric layer around them. On the other hand, a higher concentration of ions compresses this electric layer, thereby increasing the diffusion speed of the particles and so reducing the measured value of the hydrodynamic diameter. As to the surface structure, any changes, e.g. the adsorption of molecules and their chemical nature, affects the rate of particle diffusion, thus modifying their hydrodynamic size. In this regard, DLS is an advantageous method to verify the effective coating and functionalization of nanoparticles [470].

4. Laser scanning confocal microscopy

Laser scanning confocal microscopy (LSCM) is an advantageous tool in material sciences, to examine the interaction between substrates and biomaterial [471], process of deposition of biomolecules on selected surfaces [472], as well as to characterize the structure of scaffolds in tissue engineering [473].

Moreover, as a non-invasive technique, it is widely used for biological and medical investigations, proving images of thin optical sections of both living and fixed fluorescently labelled tissues and cells and further allowing for the recording of the 3D representation of the samples by collecting x-y scans along their z axes and processing them with available image manipulation software [474]. Owing to its high both lateral and axial resolution, indeed, confocal microscopy is used for studying the capability of fluorescent molecules as well as of nanosystems to pass through biological barriers such as skin and blood-brain barrier [475, 476], but also for imaging their spatial distribution within cells and tissues [477]. Furthermore, confocal microscopy, allows for the detection of physio and pathological events prompted, in living cells, upon their exposure to physical, chemical, biological and nanomaterials-based agents, like nuclear morphology modification [478], cytoskeleton rearrangement [479], mitochondrial damage [480] and ROS production [481] as well as drugs and nanoparticles lysosomal accumulation [482] and cellular proliferation and viability studies, using multiple labelled specimens. In this respect, several fluorescent probes have been successfully developed to specifically label cellular organelles [483]. For instance, DNA and chromatin can be stained to detect nuclear damage and to measure cell

viability and proliferation, by using 4',6-diamidino-2-phenylindole (DAPI) ($\lambda_{ex/em}$ =358/461 nm) and the bisbenzimide Hoechst dyes ($\lambda_{ex/em}$ =352/461 nm), which externally bind to the AT-rich domains of the double-stranded DNA, thus significantly increasing their fluorescence intensity [484, 485]. Cellular respiration and oxidative damages can be detected by using probes that specifically interact with mitochondria, such as MitoTracker, which is a cationic fluorophores, available in a variety of excitation and emission spectral profile (deep-red $\lambda_{ex/em}$=644/665 nm, red $\lambda_{ex/em}$ =579/599 nm, green $\lambda_{ex/em}$ =490/516 nm), that specifically accumulate into mitochondria in response to their highly negative membrane potential [486]. As to the lysosomes, LysoTracker probes, obtainable at different excitation and emission wavelengths (deep-red $\lambda_{ex/em}$= 647/669 nm, red $\lambda_{ex/em}$ = 577/590 nm, green $\lambda_{ex/em}$ = 504/511 nm) [487], allow for the investigation of the suppression, down or up-regulation of the lysosome activity in the secretory pathways, owing to their high selectivity for acidic organelles [488, 489]. On the other hand, cytoskeleton remodelling can be detected by staining its major protein components, tubulin and actin, by using probe composed of fluorophores linked to taxanes [490] or phalloidines [491] that specifically bind to microtubules and F-actin structures, respectively.

Confocal images are generally recorded in three different modes: epitransmission, using the light scattered from the sample; reflectance, which uses the light reflected by opaque surfaces; epifluorescence by capturing the fluorescent light emitted from the excited sample [471].

LSCM consists of lasers as source of light, sensitive photomultiplier tube detectors (PMTs) and a computer, whereby it is possible to control the scanning mirrors and that allows to display and collect the images. To

obtain confocal images, the coherent light emitted by the laser source is constrained to pass through a spatial filter, the pinhole, positioned in a conjugate plane with a scanning point on the sample. Thus, the filtered light is reflected by a dichromatic mirror in a defined point on the focal plane of the specimen causing the emission of fluorescence, which passes back to the dichromatic mirror and it is focused, as a confocal point, to a second pinhole placed in front of the detector. This configuration ensures that no confocal fluorescence emission, occurring above and below the focal plane, is detected by the photomultiplier thus not contributing to the final image [492]. In view of that, confocal microscopy provides several advantages with respect to the conventional wide field optical epi-fluorescence microscope, including the possibility to control the depth of field, the elimination of background information as well as the ability to collect serial thin (0.5-1.5 μm) optical sections from samples with a thickness up to 50 μm or even more [493].

Moreover, the improved resolution of LSCM offers the possibility to acquire time-lapse images of a single focal plane of the specimen, to study dynamic processes in living cells, like cell division [494], drug and macromolecules trafficking [495] as well as nanoparticle internalization [496]. Time-lapse images of a Z-series, can be further used to produce a four dimensional (4D) data set, which can be viewed by means of several available 4D-viewer programs as a 3D reconstruction at each time point [497].

5. Quartz crystal microbalance with dissipation monitoring (QCM-D)

Quartz crystal microbalance with dissipation monitoring (QCM-D) is an acoustic sensing technique which offers the possibility to measure and characterize, in real-time, both the adsorption of molecules at the interfaces [498] by monitoring the frequency changes of an oscillating quartz sensor [499], and the viscoelastic properties of the layer formed on the sensor surface, by monitoring the dissipation response [500]. Due to its high sensitivity, which allows to reveal mass changes as low as 1 ng/cm^2, its easy operation mode, low cost and the rather small volume of the flow chamber of the QCM-D cell (~ 0.05 mL), that permits the use only few millilitres of sample [501], this technique is an excellent tool to study surface processes.

Based on these advantages, QCM-D has been widely applied to investigate the interaction and adsorption kinetics of proteins [502], polymers [503] and DNA [504] on probing substrates and bio-surface, as well as to assess, in cell biology studies, the interaction between cells and substrate surfaces [505] together with the variation of the cell mechanical properties upon their attachment on the sensor surface [506]. In addition, QCM-D is implemented to measure binding events of colloidal particles on naked or functionalized surface [507], that are critical for their applications, ranging from biological and medical sciences to nanomaterials industrial production [508] and are highly dependent on both the physicochemical properties of the nanostructures, (e.g. surface charge, size and shape) and solution composition (e.g. ionic strength and pH) [509, 510]. Thus, QCM-D studies were carried out to investigate

nanoparticles toxicity and environmental risk by measuring their mobility or deposition kinetics on sensors surface, in natural aqueous environments [499] as well as to provide information about the interaction between nanoparticles and biomolecules for biomedical applications [511]. Besides, owing to the possibility to detect the formation of lipid bilayers on the crystal sensor surface, QCM-D allows for the investigation of the biological mechanism of interaction between nanoparticles or macromolecules and model cell membrane, thereby revealing their propensity to attach or even disrupt the model membrane [512, 513].

The central component of the QCM-D is a quartz crystal with piezoelectric properties, mounted between two metal electrodes through which an alternating electrical potential (AC) is applied, whereby contractions and the expansions of the crystal are induced. The resonance is excited when the AC frequency is close to crystal fundamental frequency (f_0). Such a fundamental frequency depends on the crystal mass and it is typically 5 MHz for a sensor with a thickness of 330 μm. Hence, the adsorption of molecules on its surface induces a variation of the fundamental and harmonic frequencies of the QCM-D sensor, from which it is possible to calculate the loaded mass, thereby using QCM-D as a balance [498]. In 1959, indeed, Sauerbrey demonstrated the linear relationship between the frequency shift and the loaded mass on the crystal as described by the following equation [514]:

$$\Delta m = \frac{C}{n} \cdot \Delta f$$

where C is the mass sensitivity constant ~ -17.7 ng·cm^{-2}·Hz^{-1} for a 5 MHz quartz crystal and n is the number of overtones (n = 1, 3, 5,…). Based on

this equation, the higher is the frequency, the lower is mass absorbed on the sensor surface.

Noteworthy, this equation is applicable only for rigid film evenly deposited on the resonator surface, since the water trapped between the adsorbed species, into a non-rigid film, leads to damping the oscillation frequency of the crystal, owing to frictional dissipative losses in the adsorbed film. As a result, the Sauerbrey equation can underestimate the deposited mass and it is no longer valid [515]. To describe the energy dissipation associated with non-rigid films, another parameter, the dissipation factor D, has been introduced:

$$D = \frac{1}{Q} = \frac{E_{dissipated}}{2\pi E_{stored}}$$

where Q is the quality factor of the crystal, $E_{dissipated}$ is the energy dissipated during the crystal oscillation and E_{stored} is the energy stored in the oscillating system. The variation of D, ΔD, is obtained by measuring the crystal oscillation amplitude decay for the freely oscillating sensor, which depends on both the physical properties of the crystal and the adsorbed film [516]. The frequency of the oscillating decay, f, as a function of time is given by the difference between the resonance frequency f_0 and a reference frequency f_R as follows [498]:

$$f = f_0 - f_R$$

This output frequency f, is fit to an exponentially damped sinusoidal $A(t)$ described by the following equation:

$$A(t) = A_0\, e^{\frac{1}{\tau}} \sin(2\pi f t + \alpha)$$

and the dissipation D is given by:

$$D = \frac{1}{\pi f \tau}$$

Despite that, the two found parameters f and D are insufficient to properly describe the measured responses in terms of physical properties of the system, such as density, thickness and viscoelasticity. Hence, based on the Voigt model, it was developed a theoretical method capable to describe the QCM-D response of Newtonian fluids as described by the equations below [517]:

$$G = G' + G'' = \mu_f + i2\pi f \eta_f = \mu_f\left(1 + i2\pi f \tau_f\right)$$

$$\Delta f = Im\left(\frac{\beta}{2\pi \rho_q l_q}\right)$$

$$\Delta D = -Re\left(\frac{\beta}{\pi f \rho_q I_q}\right)$$

$$\beta = \xi_1 \frac{2\pi f \eta_f - i\eta_f}{2\pi f} \frac{1 - \alpha \exp\left(2\xi_1 h_f\right)}{1 + \alpha \exp\left(2\xi_2 h_f\right)}$$

$$\alpha = \frac{\frac{\xi_1}{\xi_2}\frac{2\pi f \eta_f - i\eta_f}{2\pi f \eta_f} + 1}{\frac{\xi_1}{\xi_2}\frac{2\pi f \eta_f - i\eta_f}{2\pi f \eta_f} - 1}$$

$$\xi_1 = \sqrt{-\frac{(2\pi f)^2 \rho_f}{\mu_f + i2\pi\eta_f}}$$

$$\xi_2 = \sqrt{i\frac{2\pi f \rho_f}{\eta_f}}$$

where G, G', G'' are the shear, storage and loss modulus, μ_f is the elastic shear modulus, η_f is the shear viscosity, ρ_f is the density of the adsorbed film, τ_f is the relaxation time and l_q and h_f are the length and the thickness of the crystal. The value of these parameters can be obtained from the fitting of the Δf and ΔD QCM-D curves with the Voigt model, thus gaining information on both the absorbed mass and the viscoelastic properties of the film. Another model, the Maxwell model, can be used to describe the behaviour of liquid-like samples like polymers, at low shear rates [518].

Generally for nanoparticle dispersions, ΔD is coverege-dependent, since both the particle motion and the solvent coupled to the nanosystems are influcenced by the neighboring nanoparticles; moreover, larger nanoparticles lead to a higher $\Delta D / \Delta f$ ratio signal, due to the major momentum and frictional flow of solvent in compartison with small nanoparticles. Similarly Δf is influenced by the coverage of the sensor surface with the nanoparticles, which affects the number of solvent molecules sourounding the nanosystems and also trapped among them and that contribute to the frequency variation. Thus, at high coverege, crowed particles, which strongly interact with the sensor surface, marckedly interfere each other and the solvent contribution to the frequency shift is hightly significant, therby leading to an overextimation amount of particles adsorbed on the crystal surface. Wherease, at low coverage, for nanoparticles that show a strong contact with the QCM-D crystal surface, the effect of the solvent is not significant and Δf could be considered proportional to the mass deposited on the crystal surface [519]. As to the nanoparticles that weakly interact with the sensor surface, physical models are necessary to describe the QCM-D response [520, 521].

6. Fluorescence recovery after photobleaching (FRAP)

Fluorescence recovery after photobleaching (FRAP) is a fluorescence microscopy technique widely used in biological research to assess the interaction of biomolecules or nanomaterials with a model of cell membranes made of supported lipid bilayers (SLBs) by determining the mobility of the lipids upon the treatment with the studied compounds or even cells [522]. Photobleaching is a phenomenon based on the decreasing of the fluorescence intensity due to the exposition of a fluorophore to a high level of light intensity that in the presence of molecular oxygen causes permanent and irreversible changes of the chemical structure of the fluorophore thus rendering it non-fluorescent [523]. In a usual FRAP experiment, photobleaching, obtained by using a short pulse of laser light, is exploited to turn off a specific area of the sample, typically a SLBs formed on a glass-bottom dish. Hence, the recovery of the fluorescence intensity in the bleached area over time is monitored in order to gain information about the lipid mobility. The intensity fluctuations during the experiment allow to determine a recovery curve (Figure 3_a), from which it is possible to characterize the lipid dynamics, by extracting the half-time recovery value ($t_{1/2}$) and to quantify the fraction of immobile molecules within the bleached area.

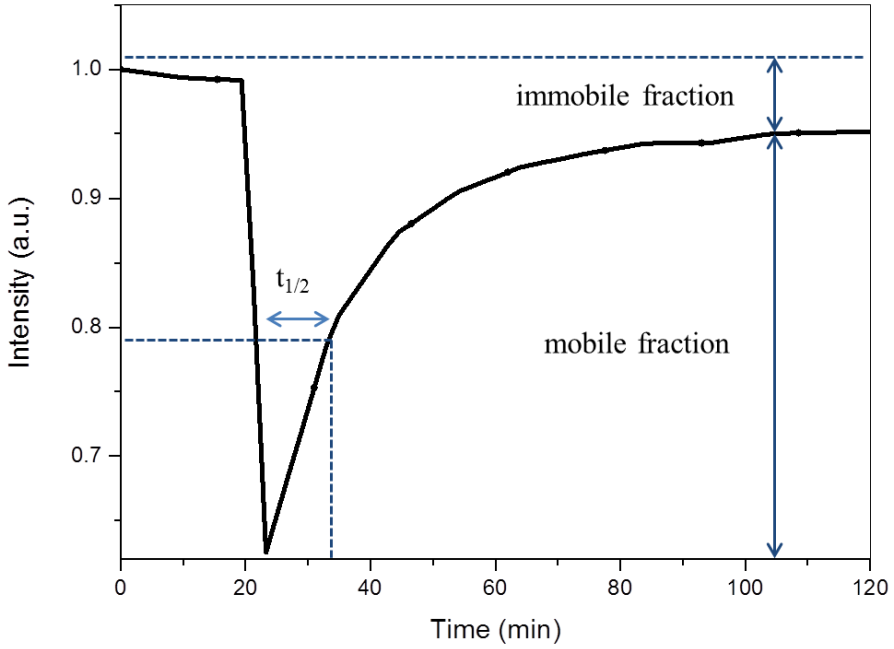

Figure 3$_a$- Recovery curve of a typical FRAP experiment.

Furthermore, the Axelrod model [524] allows to calculate the lipids diffusion coefficient D knowing the diameter of the bleached region of interest (ω) and the $t_{1/2}$ values.

$$D = \frac{0.88\ \omega^2}{4\ t_{1/2}}$$

Hence, molecules that strongly interact with the SLB, or trapped in the lipid bilayer reduce the D value, while soft interactions no significantly change the lipid diffusion with respect to the untreated sample. Accordingly, FRAP experiments provide a general semi-quantitative

estimate of lipid dynamics and can be used to compare several biological conditions.

References

[1] A. Nazir, A. Raggi, B. Corso, N. Minicuci, R. Quintas, D. Sattin, L. De Torres, S. Chatterji, G.B. Frisoni, J.M. Haro, S. Koskinen, A. Martinuzzi, M. Miret, B. Tobiasz-Adamczyk, M. Leonardi, Determinants of Quality of Life in Ageing Populations: Results from a Cross-Sectional Study in Finland, Poland and Spain, Plos One 11(7) (2016).
[2] C. Franceschi, P. Garagnani, C. Morsiani, M. Conte, A. Santoro, A. Grignolio, D. Monti, M. Capri, S. Salvioli, The Continuum of Aging and Age-Related Diseases: Common Mechanisms but Different Rates, Frontiers in Medicine 5 (2018).
[3] R.F. Loeser, Aging and osteoarthritis, Current Opinion in Rheumatology 23(5) (2011) 492-496.
[4] C. López-Ramírez, L. Suarez Valdivia, J. Rodríguez Portal, Causes of Pulmonary Fibrosis in the Elderly, Medical Sciences 6(3) (2018).
[5] K. Heese, Ageing, dementia and society – an epistemological perspective, SpringerPlus 4(1) (2015).
[6] M.S. Kirkman, V.J. Briscoe, N. Clark, H. Florez, L.B. Haas, J.B. Halter, E.S. Huang, M.T. Korytkowski, M.N. Munshi, P.S. Odegard, R.E. Pratley, C.S. Swift, Diabetes in Older Adults, Diabetes Care 35(12) (2012) 2650-2664.
[7] K. Søreide, W.C. Cho, J.R. Aunan, The Biology of Aging and Cancer: A Brief Overview of Shared and Divergent Molecular Hallmarks, Aging and Disease 8(5) (2017).
[8] G.S. Ashcroft, S.J. Mills, J.J. Ashworth, Ageing and wound healing, Biogerontology 3(6) (2002) 337-45.
[9] Y. Cao, Tumorigenesis as a process of gradual loss of original cell identity and gain of properties of neural precursor/progenitor cells, Cell & Bioscience 7(1) (2017).
[10] J. Moriya, T. Minamino, Angiogenesis, Cancer, and Vascular Aging, Front Cardiovasc Med 4 (2017) 65.
[11] M.D. Burkhalter, K.L. Rudolph, T. Sperka, Genome instability of ageing stem cells--Induction and defence mechanisms, Ageing Res Rev 23(Pt A) (2015) 29-36.
[12] R. Yancik, Population aging and cancer: a cross-national concern, Cancer J 11(6) (2005) 437-41.
[13] M.G. Tonnesen, X. Feng, R.A.F. Clark, Angiogenesis in Wound Healing, Journal of Investigative Dermatology Symposium Proceedings 5(1) (2000) 40-46.

[14] C.K. Sen, G.M. Gordillo, S. Roy, R. Kirsner, L. Lambert, T.K. Hunt, F. Gottrup, G.C. Gurtner, M.T. Longaker, Human skin wounds: A major and snowballing threat to public health and the economy, Wound Repair and Regeneration 17(6) (2009) 763-771.
[15] L. Martinengo, M. Olsson, R. Bajpai, M. Soljak, Z. Upton, A. Schmidtchen, J. Car, K. Järbrink, Prevalence of chronic wounds in the general population: systematic review and meta-analysis of observational studies, Annals of Epidemiology 29 (2019) 8-15.
[16] G.H. Lyman, Economics of Cancer Care, Journal of Oncology Practice 3(3) (2007) 113-114.
[17] G. Bor, I.D. Mat Azmi, A. Yaghmur, Nanomedicines for cancer therapy: current status, challenges and future prospects, Therapeutic Delivery 10(2) (2019) 113-132.
[18] M. Parani, G. Lokhande, A. Singh, A.K. Gaharwar, Engineered Nanomaterials for Infection Control and Healing Acute and Chronic Wounds, ACS Applied Materials & Interfaces 8(16) (2016) 10049-10069.
[19] S. Marchesan, M. Prato, Nanomaterials for (Nano)medicine, ACS Medicinal Chemistry Letters 4(2) (2012) 147-149.
[20] L. Yan, X. Chen, Nanomaterials for Drug Delivery, Nanocrystalline Materials2014, pp. 221-268.
[21] G. Schmid, U. Simon, Gold nanoparticles: assembly and electrical properties in 1–3 dimensions, Chem. Commun. (6) (2005) 697-710.
[22] J. Chen, F. Saeki, B.J. Wiley, H. Cang, M.J. Cobb, Z.Y. Li, L. Au, H. Zhang, M.B. Kimmey, X. Li, Y. Xia, Gold nanocages: bioconjugation and their potential use as optical imaging contrast agents, Nano Lett 5(3) (2005) 473-7.
[23] D. Cabuzu, A. Cirja, R. Puiu, A.M. Grumezescu, Biomedical applications of gold nanoparticles, Curr Top Med Chem 15(16) (2015) 1605-13.
[24] P.M. Tiwari, K. Vig, V.A. Dennis, S.R. Singh, Functionalized Gold Nanoparticles and Their Biomedical Applications, Nanomaterials (Basel) 1(1) (2011) 31-63.
[25] P.D. Pietro, G. Strano, L. Zuccarello, C. Satriano, Gold and Silver Nanoparticles for Applications in Theranostics, Curr Top Med Chem 16(27) (2016) 3069-3102.
[26] E. Boisselier, D. Astruc, Gold nanoparticles in nanomedicine: preparations, imaging, diagnostics, therapies and toxicity, Chem Soc Rev 38(6) (2009) 1759-82.
[27] M. Ovais, I. Ahmad, A.T. Khalil, S. Mukherjee, R. Javed, M. Ayaz, A. Raza, Z.K. Shinwari, Wound healing applications of biogenic colloidal

silver and gold nanoparticles: recent trends and future prospects, Appl Microbiol Biotechnol 102(10) (2018) 4305-4318.
[28] R. Bhattacharya, P. Mukherjee, Biological properties of "naked" metal nanoparticles, Adv Drug Deliv Rev 60(11) (2008) 1289-306.
[29] N. Ferrara, A.P. Adamis, Ten years of anti-vascular endothelial growth factor therapy, Nat Rev Drug Discov 15(6) (2016) 385-403.
[30] M.J. Allen, V.C. Tung, R.B. Kaner, Honeycomb carbon: a review of graphene, Chem Rev 110(1) (2010) 132-45.
[31] A.K. Geim, Graphene: status and prospects, Science 324(5934) (2009) 1530-4.
[32] K. Haubner, J. Murawski, P. Olk, L.M. Eng, C. Ziegler, B. Adolphi, E. Jaehne, The route to functional graphene oxide, Chemphyschem 11(10) (2010) 2131-9.
[33] C. Xu, X. Wang, Fabrication of flexible metal-nanoparticle films using graphene oxide sheets as substrates, Small 5(19) (2009) 2212-7.
[34] S. Mukherjee, P. Sriram, A.K. Barui, S.K. Nethi, V. Veeriah, S. Chatterjee, K.I. Suresh, C.R. Patra, Graphene Oxides Show Angiogenic Properties, Adv Healthc Mater 4(11) (2015) 1722-32.
[35] X.W. Tan, B. Thompson, A. Konstantopoulos, T.W. Goh, M. Setiawan, G.H. Yam, D. Tan, K.A. Khor, J.S. Mehta, Application of Graphene as Candidate Biomaterial for Synthetic Keratoprosthesis Skirt, Invest Ophthalmol Vis Sci 56(11) (2015) 6605-11.
[36] Z. Tahergorabi, M. Khazaei, A review on angiogenesis and its assays, Iran J Basic Med Sci 15(6) (2012) 1110-26.
[37] P. Carmeliet, Angiogenesis in health and disease, Nat Med 9(6) (2003) 653-60.
[38] J. Folkman, What is the evidence that tumors are angiogenesis dependent?, J Natl Cancer Inst 82(1) (1990) 4-6.
[39] G. Varricchi, F. Granata, S. Loffredo, A. Genovese, G. Marone, Angiogenesis and lymphangiogenesis in inflammatory skin disorders, J Am Acad Dermatol 73(1) (2015) 144-53.
[40] H.A. Elshabrawy, Z. Chen, M.V. Volin, S. Ravella, S. Virupannavar, S. Shahrara, The pathogenic role of angiogenesis in rheumatoid arthritis, Angiogenesis 18(4) (2015) 433-48.
[41] C.H. Liu, Z. Wang, Y. Sun, J. Chen, Animal models of ocular angiogenesis: from development to pathologies, FASEB J 31(11) (2017) 4665-4681.
[42] E. Falk, Pathogenesis of atherosclerosis, J Am Coll Cardiol 47(8 Suppl) (2006) C7-12.

[43] A. Jazwa, U. Florczyk, A. Grochot-Przeczek, B. Krist, A. Loboda, A. Jozkowicz, J. Dulak, Limb ischemia and vessel regeneration: Is there a role for VEGF?, Vascul Pharmacol 86 (2016) 18-30.
[44] M. Vallon, J. Chang, H. Zhang, C.J. Kuo, Developmental and pathological angiogenesis in the central nervous system, Cell Mol Life Sci 71(18) (2014) 3489-506.
[45] J. Filipowska, K.A. Tomaszewski, L. Niedzwiedzki, J.A. Walocha, T. Niedzwiedzki, The role of vasculature in bone development, regeneration and proper systemic functioning, Angiogenesis 20(3) (2017) 291-302.
[46] R.M. Cabral, P.V. Baptista, Anti-cancer precision theranostics: a focus on multifunctional gold nanoparticles, Expert Rev Mol Diagn 14(8) (2014) 1041-52.
[47] S. Aftab, A. Shah, A. Nadhman, S. Kurbanoglu, S. Aysıl Ozkan, D.D. Dionysiou, S.S. Shukla, T.M. Aminabhavi, Nanomedicine: An effective tool in cancer therapy, International Journal of Pharmaceutics 540(1-2) (2018) 132-149.
[48] K. Huang, H. Ma, J. Liu, S. Huo, A. Kumar, T. Wei, X. Zhang, S. Jin, Y. Gan, P.C. Wang, S. He, X. Zhang, X.J. Liang, Size-dependent localization and penetration of ultrasmall gold nanoparticles in cancer cells, multicellular spheroids, and tumors in vivo, ACS Nano 6(5) (2012) 4483-93.
[49] S. Nazir, T. Hussain, A. Ayub, U. Rashid, A.J. MacRobert, Nanomaterials in combating cancer: therapeutic applications and developments, Nanomedicine 10(1) (2014) 19-34.
[50] T. Cao, P. You, X. Zhou, J. Luo, X. Xu, Z. Zhou, S. Yang, Y. Zhang, H. Yang, M. Wang, Visualization of size-dependent tumour retention of PEGylated nanographene oxide via SPECT imaging, Journal of Materials Chemistry B 4(39) (2016) 6446-6453.
[51] M. Pelin, L. Fusco, C. Martin, S. Sosa, J. Frontinan-Rubio, J.M. Gonzalez-Dominguez, M. Duran-Prado, E. Vazquez, M. Prato, A. Tubaro, Graphene and graphene oxide induce ROS production in human HaCaT skin keratinocytes: the role of xanthine oxidase and NADH dehydrogenase, Nanoscale 10(25) (2018) 11820-11830.
[52] D.G. You, V.G. Deepagan, W. Um, S. Jeon, S. Son, H. Chang, H.I. Yoon, Y.W. Cho, M. Swierczewska, S. Lee, M.G. Pomper, I.C. Kwon, K. Kim, J.H. Park, ROS-generating TiO2 nanoparticles for non-invasive sonodynamic therapy of cancer, Sci Rep 6 (2016) 23200.
[53] M.M. Mihai, M.B. Dima, B. Dima, A.M. Holban, Nanomaterials for Wound Healing and Infection Control, Materials 12(13) (2019).

[54] M. Ramos, L. Ortiz-Jordan, A. Hurtado-Macias, S. Flores, J. Elizalde-Galindo, C. Rocha, B. Torres, M. Zarei-Chaleshtori, R. Chianelli, Hardness and Elastic Modulus on Six-Fold Symmetry Gold Nanoparticles, Materials 6(1) (2013) 198-205.
[55] J. Shang, X. Gao, Nanoparticle counting: towards accurate determination of the molar concentration, Chem Soc Rev 43(21) (2014) 7267-78.
[56] K. Graham, M. Gogins, H. Schreuder-Gibson, Incorporation of Electrospun Nanofibers into Functional Structures, International Nonwovens Journal os-13(2) (2018).
[57] M.H. Oueslati, L.B. Tahar, A.H. Harrath, Catalytic, antioxidant and anticancer activities of gold nanoparticles synthesized by kaempferol glucoside from Lotus leguminosae, Arabian Journal of Chemistry 13(1) (2020) 3112-3122.
[58] J.-G. Leu, S.-A. Chen, H.-M. Chen, W.-M. Wu, C.-F. Hung, Y.-D. Yao, C.-S. Tu, Y.-J. Liang, The effects of gold nanoparticles in wound healing with antioxidant epigallocatechin gallate and α-lipoic acid, Nanomedicine: Nanotechnology, Biology and Medicine 8(5) (2012) 767-775.
[59] C. Dunnill, T. Patton, J. Brennan, J. Barrett, M. Dryden, J. Cooke, D. Leaper, N.T. Georgopoulos, Reactive oxygen species (ROS) and wound healing: the functional role of ROS and emerging ROS-modulating technologies for augmentation of the healing process, Int Wound J 14(1) (2017) 89-96.
[60] S. Liu, T.H. Zeng, M. Hofmann, E. Burcombe, J. Wei, R. Jiang, J. Kong, Y. Chen, Antibacterial activity of graphite, graphite oxide, graphene oxide, and reduced graphene oxide: membrane and oxidative stress, ACS Nano 5(9) (2011) 6971-80.
[61] S. Gurunathan, J.W. Han, A.A. Dayem, V. Eppakayala, J.H. Kim, Oxidative stress-mediated antibacterial activity of graphene oxide and reduced graphene oxide in Pseudomonas aeruginosa, Int J Nanomedicine 7 (2012) 5901-14.
[62] B. Lu, T. Li, H. Zhao, X. Li, C. Gao, S. Zhang, E. Xie, Graphene-based composite materials beneficial to wound healing, Nanoscale 4(9) (2012).
[63] M. Verdanova, B. Rezek, A. Broz, E. Ukraintsev, O. Babchenko, A. Artemenko, T. Izak, A. Kromka, M. Kalbac, M. Hubalek Kalbacova, Nanocarbon Allotropes-Graphene and Nanocrystalline Diamond-Promote Cell Proliferation, Small 12(18) (2016) 2499-509.

[64] Z.-S. Wu, G. Zhou, L.-C. Yin, W. Ren, F. Li, H.-M. Cheng, Graphene/metal oxide composite electrode materials for energy storage, Nano Energy 1(1) (2012) 107-131.
[65] J.H. Kaplan, S. Lutsenko, Copper Transport in Mammalian Cells: Special Care for a Metal with Special Needs, Journal of Biological Chemistry 284(38) (2009) 25461-25465.
[66] J. Jeevanandam, A. Barhoum, Y.S. Chan, A. Dufresne, M.K. Danquah, Review on nanoparticles and nanostructured materials: history, sources, toxicity and regulations, Beilstein Journal of Nanotechnology 9 (2018) 1050-1074.
[67] M.F. Hochella, M.G. Spencer, K.L. Jones, Nanotechnology: nature's gift or scientists' brainchild?, Environmental Science: Nano 2(2) (2015) 114-119.
[68] V.K. Sharma, J. Filip, R. Zboril, R.S. Varma, Natural inorganic nanoparticles – formation, fate, and toxicity in the environment, Chemical Society Reviews 44(23) (2015) 8410-8423.
[69] D. Byun, J. Hong, Saputra, J.H. Ko, Y.J. Lee, H.C. Park, B.-K. Byun, J.R. Lukes, Wetting Characteristics of Insect Wing Surfaces, Journal of Bionic Engineering 6(1) (2009) 63-70.
[70] E.E. Pfündel, G. Agati, Z.G. Cerovic, Optical Properties of Plant Surfaces, Annual Plant Reviews online2018, pp. 216-249.
[71] N. Reznikov, M. Bilton, L. Lari, M.M. Stevens, R. Kröger, Fractal-like hierarchical organization of bone begins at the nanoscale, Science 360(6388) (2018).
[72] V. Prakash Sharma, U. Sharma, M. Chattopadhyay, V.N. Shukla, Advance Applications of Nanomaterials: A Review, Materials Today: Proceedings 5(2) (2018) 6376-6380.
[73] C. Dhand, N. Dwivedi, X.J. Loh, A.N. Jie Ying, N.K. Verma, R.W. Beuerman, R. Lakshminarayanan, S. Ramakrishna, Methods and strategies for the synthesis of diverse nanoparticles and their applications: a comprehensive overview, RSC Advances 5(127) (2015) 105003-105037.
[74] K.B. Cederquist, B. Liu, M.R. Grima, P.J. Dalack, J.T. Mahorn, Laser-fabricated gold nanoparticles for lateral flow immunoassays, Colloids Surf B Biointerfaces 149 (2017) 351-357.
[75] A. Kaganskiy, M. Gschrey, A. Schlehahn, R. Schmidt, J.H. Schulze, T. Heindel, A. Strittmatter, S. Rodt, S. Reitzenstein, Advanced in-situ electron-beam lithography for deterministic nanophotonic device processing, Rev Sci Instrum 86(7) (2015) 073903.

[76] M. Hennes, A. Lotnyk, S.G. Mayr, Plasma-assisted synthesis and high-resolution characterization of anisotropic elemental and bimetallic core-shell magnetic nanoparticles, Beilstein J Nanotechnol 5 (2014) 466-75.
[77] H. Ho, J. Lee, Redispersible drug nanoparticles prepared without dispersant by electro-spray drying, Drug Dev Ind Pharm 38(6) (2012) 744-51.
[78] M.C. Goncalves, Sol-gel Silica Nanoparticles in Medicine: A Natural Choice. Design, Synthesis and Products, Molecules 23(8) (2018).
[79] P. Suchomel, L. Kvitek, R. Prucek, A. Panacek, A. Halder, S. Vajda, R. Zboril, Simple size-controlled synthesis of Au nanoparticles and their size-dependent catalytic activity, Scientific Reports 8(1) (2018).
[80] M. Ethayaraja, K. Dutta, D. Muthukumaran, R. Bandyopadhyaya, Nanoparticle Formation in Water-in-Oil Microemulsions: Experiments, Mechanism, and Monte Carlo Simulation, Langmuir 23(6) (2007) 3418-3423.
[81] D.B. Bharti, A.V. Bharati, Synthesis of ZnO nanoparticles using a hydrothermal method and a study its optical activity, Luminescence 32(3) (2017) 317-320.
[82] T. Klaus, R. Joerger, E. Olsson, C.G. Granqvist, Silver-based crystalline nanoparticles, microbially fabricated, Proceedings of the National Academy of Sciences 96(24) (1999) 13611-13614.
[83] S.S. Shankar, A. Rai, B. Ankamwar, A. Singh, A. Ahmad, M. Sastry, Biological synthesis of triangular gold nanoprisms, Nat Mater 3(7) (2004) 482-8.
[84] N. Ahmad, S. Sharma, V.N. Singh, S.F. Shamsi, A. Fatma, B.R. Mehta, Biosynthesis of Silver Nanoparticles from Desmodium triflorum: A Novel Approach Towards Weed Utilization, Biotechnology Research International 2011 (2011) 1-8.
[85] K. Albert, H.Y. Hsu, Carbon-Based Materials for Photo-Triggered Theranostic Applications, Molecules 21(11) (2016).
[86] N. Venkatesh, Metallic Nanoparticle: A Review, Biomedical Journal of Scientific & Technical Research 4(2) (2018).
[87] S. Bayda, M. Hadla, S. Palazzolo, P. Riello, G. Corona, G. Toffoli, F. Rizzolio, Inorganic Nanoparticles for Cancer Therapy: A Transition from Lab to Clinic, Curr Med Chem 25(34) (2018) 4269-4303.
[88] M.J. Virlan, D. Miricescu, R. Radulescu, C.M. Sabliov, A. Totan, B. Calenic, M. Greabu, Organic Nanomaterials and Their Applications in the Treatment of Oral Diseases, Molecules 21(2) (2016).

[89] M.A. Deshmukh, M.D. Shirsat, A. Ramanaviciene, A. Ramanavicius, Composites Based on Conducting Polymers and Carbon Nanomaterials for Heavy Metal Ion Sensing (Review), Crit Rev Anal Chem 48(4) (2018) 293-304.
[90] C. Buzea, I.I. Pacheco, K. Robbie, Nanomaterials and nanoparticles: Sources and toxicity, Biointerphases 2(4) (2007) MR17-MR71.
[91] S. Alim, J. Vejayan, M.M. Yusoff, A.K.M. Kafi, Recent uses of carbon nanotubes & gold nanoparticles in electrochemistry with application in biosensing: A review, Biosens Bioelectron 121 (2018) 125-136.
[92] H.P. Feng, L. Tang, G.M. Zeng, Y. Zhou, Y.C. Deng, X. Ren, B. Song, C. Liang, M.Y. Wei, J.F. Yu, Core-shell nanomaterials: Applications in energy storage and conversion, Adv Colloid Interface Sci 267 (2019) 26-46.
[93] J. Liang, F. Zeng, M. Zhang, Z. Pan, Y. Chen, Y. Zeng, Y. Xu, Q. Xu, Y. Huang, Green Synthesis of Hyaluronic Acid-based Silver Nanoparticle and Its Enhanced Delivery to CD44+ Cancer Cells, 2015.
[94] Y.J. Kim, B. Jeong, Graphene-Based Nanomaterials and Their Applications in Biosensors, Adv Exp Med Biol 1064 (2018) 61-71.
[95] Z. Dai, H.M. Leung, P.K. Lo, Stimuli-Responsive Self-Assembled DNA Nanomaterials for Biomedical Applications, Small 13(7) (2017).
[96] A.G. Dumanli, Nanocellulose and its Composites for Biomedical Applications, Curr Med Chem 24(5) (2017) 512-528.
[97] Y. Bai, I. Mora-Seró, F. De Angelis, J. Bisquert, P. Wang, Titanium Dioxide Nanomaterials for Photovoltaic Applications, Chemical Reviews 114(19) (2014) 10095-10130.
[98] I. Gehrke, A. Geiser, A. Somborn-Schulz, Innovations in nanotechnology for water treatment, Nanotechnology, Science and Applications (2015).
[99] Y.-H. Li, J. Ding, Z. Luan, Z. Di, Y. Zhu, C. Xu, D. Wu, B. Wei, Competitive adsorption of Pb2+, Cu2+ and Cd2+ ions from aqueous solutions by multiwalled carbon nanotubes, Carbon 41(14) (2003) 2787-2792.
[100] M. Holzinger, A. Le Goff, S. Cosnier, Nanomaterials for biosensing applications: a review, Frontiers in Chemistry 2 (2014).
[101] J. Kuzma, Nanotechnology in animal production—Upstream assessment of applications, Livestock Science 130(1-3) (2010) 14-24.
[102] A. Barras, A. Mezzetti, A. Richard, S. Lazzaroni, S. Roux, P. Melnyk, D. Betbeder, N. Monfilliette-Dupont, Formulation and

characterization of polyphenol-loaded lipid nanocapsules, International Journal of Pharmaceutics 379(2) (2009) 270-277.
[103] M.C.E. Lomer, R.P.H. Thompson, J.J. Powell, Fine and ultrafine particles of the diet: influence on the mucosal immune response and association with Crohn's disease, Proceedings of the Nutrition Society 61(1) (2007) 123-130.
[104] L. Wang, W. Ma, L. Xu, W. Chen, Y. Zhu, C. Xu, N.A. Kotov, Nanoparticle-based environmental sensors, Materials Science and Engineering: R: Reports 70(3-6) (2010) 265-274.
[105] H. Zhang, K.R. Millington, X. Wang, The photostability of wool doped with photocatalytic titanium dioxide nanoparticles, Polymer Degradation and Stability 94(2) (2009) 278-283.
[106] Q. Huang, H. Yu, Q. Ru, Bioavailability and Delivery of Nutraceuticals Using Nanotechnology, Journal of Food Science 75(1) (2010) R50-R57.
[107] B.Y. Kim, J.T. Rutka, W.C. Chan, Nanomedicine, N Engl J Med 363(25) (2010) 2434-43.
[108] K.W. Powers, M. Palazuelos, B.M. Moudgil, S.M. Roberts, Characterization of the size, shape, and state of dispersion of nanoparticles for toxicological studies, Nanotoxicology 1(1) (2009) 42-51.
[109] H. Nakamura, S. Watano, Direct Permeation of Nanoparticles across Cell Membrane: A Review, KONA Powder and Particle Journal 35(0) (2018) 49-65.
[110] P. Aggarwal, J.B. Hall, C.B. McLeland, M.A. Dobrovolskaia, S.E. McNeil, Nanoparticle interaction with plasma proteins as it relates to particle biodistribution, biocompatibility and therapeutic efficacy, Advanced Drug Delivery Reviews 61(6) (2009) 428-437.
[111] A. Woźniak, A. Malankowska, G. Nowaczyk, B.F. Grześkowiak, K. Tuśnio, R. Słomski, A. Zaleska-Medynska, S. Jurga, Size and shape-dependent cytotoxicity profile of gold nanoparticles for biomedical applications, Journal of Materials Science: Materials in Medicine 28(6) (2017).
[112] W. Gao, K. Xu, L. Ji, B. Tang, Effect of gold nanoparticles on glutathione depletion-induced hydrogen peroxide generation and apoptosis in HL7702 cells, Toxicol Lett 205(1) (2011) 86-95.
[113] R. Coradeghini, S. Gioria, C.P. García, P. Nativo, F. Franchini, D. Gilliland, J. Ponti, F. Rossi, Size-dependent toxicity and cell interaction mechanisms of gold nanoparticles on mouse fibroblasts, Toxicology Letters 217(3) (2013) 205-216.

[114] R. Madannejad, N. Shoaie, F. Jahanpeyma, M.H. Darvishi, M. Azimzadeh, H. Javadi, Toxicity of carbon-based nanomaterials: Reviewing recent reports in medical and biological systems, Chemico-Biological Interactions 307 (2019) 206-222.
[115] O. Akhavan, E. Ghaderi, A. Akhavan, Size-dependent genotoxicity of graphene nanoplatelets in human stem cells, Biomaterials 33(32) (2012) 8017-25.
[116] K.L. Aillon, Y. Xie, N. El-Gendy, C.J. Berkland, M.L. Forrest, Effects of nanomaterial physicochemical properties on in vivo toxicity, Advanced Drug Delivery Reviews 61(6) (2009) 457-466.
[117] W.H. De Jong, W.I. Hagens, P. Krystek, M.C. Burger, A.J.A.M. Sips, R.E. Geertsma, Particle size-dependent organ distribution of gold nanoparticles after intravenous administration, Biomaterials 29(12) (2008) 1912-1919.
[118] G. Sonavane, K. Tomoda, K. Makino, Biodistribution of colloidal gold nanoparticles after intravenous administration: effect of particle size, Colloids Surf B Biointerfaces 66(2) (2008) 274-80.
[119] X. Zhang, J. Yin, C. Peng, W. Hu, Z. Zhu, W. Li, C. Fan, Q. Huang, Distribution and biocompatibility studies of graphene oxide in mice after intravenous administration, Carbon 49(3) (2011) 986-995.
[120] A. Verma, F. Stellacci, Effect of Surface Properties on Nanoparticleâ□“Cell Interactions, Small 6(1) (2010) 12-21.
[121] Z. Lu, Y. Qiao, X.T. Zheng, M.B. Chan-Park, C.M. Li, Effect of particle shape on phagocytosis of CdTe quantum dot–cystine composites, MedChemComm 1(1) (2010).
[122] B. Fubini, I. Fenoglio, M. Tomatis, F. Turci, Effect of chemical composition and state of the surface on the toxic response to high aspect ratio nanomaterials, Nanomedicine (Lond) 6(5) (2011) 899-920.
[123] Y. Li, M. Kröger, W.K. Liu, Shape effect in cellular uptake of PEGylated nanoparticles: comparison between sphere, rod, cube and disk, Nanoscale 7(40) (2015) 16631-16646.
[124] Y.-P. Jia, B.-Y. Ma, X.-W. Wei, Z.-Y. Qian, The in vitro and in vivo toxicity of gold nanoparticles, Chinese Chemical Letters 28(4) (2017) 691-702.
[125] K.H. Park, M. Chhowalla, Z. Iqbal, F. Sesti, Single-walled carbon nanotubes are a new class of ion channel blockers, J Biol Chem 278(50) (2003) 50212-6.
[126] C.A. Poland, R. Duffin, I. Kinloch, A. Maynard, W.A.H. Wallace, A. Seaton, V. Stone, S. Brown, W. MacNee, K. Donaldson, Carbon nanotubes introduced into the abdominal cavity of mice show asbestos-

like pathogenicity in a pilot study, Nature Nanotechnology 3(7) (2008) 423-428.
[127] S.G. Elci, Y. Jiang, B. Yan, S.T. Kim, K. Saha, D.F. Moyano, G. Yesilbag Tonga, L.C. Jackson, V.M. Rotello, R.W. Vachet, Surface Charge Controls the Suborgan Biodistributions of Gold Nanoparticles, ACS Nano 10(5) (2016) 5536-5542.
[128] A. Hoshino, K. Fujioka, T. Oku, M. Suga, Y.F. Sasaki, T. Ohta, M. Yasuhara, K. Suzuki, K. Yamamoto, Physicochemical Properties and Cellular Toxicity of Nanocrystal Quantum Dots Depend on Their Surface Modification, Nano Letters 4(11) (2004) 2163-2169.
[129] D.L.J. Thorek, A. Tsourkas, Size, charge and concentration dependent uptake of iron oxide particles by non-phagocytic cells, Biomaterials 29(26) (2008) 3583-3590.
[130] H. Jin, D.A. Heller, R. Sharma, M.S. Strano, Size-Dependent Cellular Uptake and Expulsion of Single-Walled Carbon Nanotubes: Single Particle Tracking and a Generic Uptake Model for Nanoparticles, ACS Nano 3(1) (2009) 149-158.
[131] J. Lin, H. Zhang, Z. Chen, Y. Zheng, Penetration of Lipid Membranes by Gold Nanoparticles: Insights into Cellular Uptake, Cytotoxicity, and Their Relationship, ACS Nano 4(9) (2010) 5421-5429.
[132] B. Wang, L. Zhang, S.C. Bae, S. Granick, Nanoparticle-induced surface reconstruction of phospholipid membranes, Proceedings of the National Academy of Sciences 105(47) (2008) 18171-18175.
[133] N.M. Schaeublin, L.K. Braydich-Stolle, A.M. Schrand, J.M. Miller, J. Hutchison, J.J. Schlager, S.M. Hussain, Surface charge of gold nanoparticles mediates mechanism of toxicity, Nanoscale 3(2) (2011).
[134] A. Pietroiusti, M. Massimiani, I. Fenoglio, M. Colonna, F. Valentini, G. Palleschi, A. Camaioni, A. Magrini, G. Siracusa, A. Bergamaschi, A. Sgambato, L. Campagnolo, Low Doses of Pristine and Oxidized Single-Wall Carbon Nanotubes Affect Mammalian Embryonic Development, ACS Nano 5(6) (2011) 4624-4633.
[135] A.K. Gupta, M. Gupta, Cytotoxicity suppression and cellular uptake enhancement of surface modified magnetic nanoparticles, Biomaterials 26(13) (2005) 1565-73.
[136] A. Sasidharan, L.S. Panchakarla, P. Chandran, D. Menon, S. Nair, C.N.R. Rao, M. Koyakutty, Differential nano-bio interactions and toxicity effects of pristine versus functionalized graphene, Nanoscale 3(6) (2011).
[137] C. Kirchner, T. Liedl, S. Kudera, T. Pellegrino, A. Muñoz Javier, H.E. Gaub, S. Stölzle, N. Fertig, W.J. Parak, Cytotoxicity of Colloidal CdSe and CdSe/ZnS Nanoparticles, Nano Letters 5(2) (2005) 331-338.

[138] J.S. Suk, Q. Xu, N. Kim, J. Hanes, L.M. Ensign, PEGylation as a strategy for improving nanoparticle-based drug and gene delivery, Adv Drug Deliv Rev 99(Pt A) (2016) 28-51.
[139] T.-R. Kuo, C.-F. Lee, S.-J. Lin, C.-Y. Dong, C.-C. Chen, H.-Y. Tan, Studies of Intracorneal Distribution and Cytotoxicity of Quantum Dots: Risk Assessment of Eye Exposure, Chemical Research in Toxicology 24(2) (2011) 253-261.
[140] Y.-J. Gu, J. Cheng, C.-C. Lin, Y.W. Lam, S.H. Cheng, W.-T. Wong, Nuclear penetration of surface functionalized gold nanoparticles, Toxicology and Applied Pharmacology 237(2) (2009) 196-204.
[141] C. Borghouts, C. Kunz, B. Groner, Current strategies for the development of peptide-based anti-cancer therapeutics, Journal of Peptide Science 11(11) (2005) 713-726.
[142] F. Chen, G. Wang, J.I. Griffin, B. Brenneman, N.K. Banda, V.M. Holers, D.S. Backos, L. Wu, S.M. Moghimi, D. Simberg, Complement proteins bind to nanoparticle protein corona and undergo dynamic exchange in vivo, Nature Nanotechnology 12(4) (2016) 387-393.
[143] S. Tenzer, D. Docter, J. Kuharev, A. Musyanovych, V. Fetz, R. Hecht, F. Schlenk, D. Fischer, K. Kiouptsi, C. Reinhardt, K. Landfester, H. Schild, M. Maskos, S.K. Knauer, R.H. Stauber, Rapid formation of plasma protein corona critically affects nanoparticle pathophysiology, Nature Nanotechnology 8(10) (2013) 772-781.
[144] E. Casals, V.F. Puntes, Inorganic nanoparticle biomolecular corona: formation, evolution and biological impact, Nanomedicine (Lond) 7(12) (2012) 1917-30.
[145] S.-T. Yang, Y. Liu, Y.-W. Wang, A. Cao, Biosafety and Bioapplication of Nanomaterials by Designing Protein-Nanoparticle Interactions, Small 9(9-10) (2013) 1635-1653.
[146] W. Xiao, H. Gao, The impact of protein corona on the behavior and targeting capability of nanoparticle-based delivery system, International Journal of Pharmaceutics 552(1-2) (2018) 328-339.
[147] S.L. Hirsh, D.R. McKenzie, N.J. Nosworthy, J.A. Denman, O.U. Sezerman, M.M.M. Bilek, The Vroman effect: Competitive protein exchange with dynamic multilayer protein aggregates, Colloids and Surfaces B: Biointerfaces 103 (2013) 395-404.
[148] P. Huetz, V. Ball, J.C. Voegel, P. Schaaf, Exchange Kinetics for a Heterogeneous Protein System on a Solid Surface, Langmuir 11(8) (1995) 3145-3152.
[149] J. Piella, N.G. Bastús, V. Puntes, Size-Dependent Protein–Nanoparticle Interactions in Citrate-Stabilized Gold Nanoparticles: The

Emergence of the Protein Corona, Bioconjugate Chemistry 28(1) (2016) 88-97.
[150] F. Charbgoo, M. Nejabat, K. Abnous, F. Soltani, S.M. Taghdisi, M. Alibolandi, W. Thomas Shier, T.W.J. Steele, M. Ramezani, Gold nanoparticle should understand protein corona for being a clinical nanomaterial, Journal of Controlled Release 272 (2018) 39-53.
[151] A. Chaudhary, S. Khan, A. Gupta, C.K. Nandi, Effect of surface chemistry and morphology of gold nanoparticle on the structure and activity of common blood proteins, New Journal of Chemistry 40(6) (2016) 4879-4883.
[152] R. García-Álvarez, M. Hadjidemetriou, A. Sánchez-Iglesias, L.M. Liz-Marzán, K. Kostarelos, In vivo formation of protein corona on gold nanoparticles. The effect of their size and shape, Nanoscale 10(3) (2018) 1256-1264.
[153] W. Hu, C. Peng, M. Lv, X. Li, Y. Zhang, N. Chen, C. Fan, Q. Huang, Protein Corona-Mediated Mitigation of Cytotoxicity of Graphene Oxide, ACS Nano 5(5) (2011) 3693-3700.
[154] C. Ge, J. Du, L. Zhao, L. Wang, Y. Liu, D. Li, Y. Yang, R. Zhou, Y. Zhao, Z. Chai, C. Chen, Binding of blood proteins to carbon nanotubes reduces cytotoxicity, Proceedings of the National Academy of Sciences 108(41) (2011) 16968-16973.
[155] F. Benetti, M. Fedel, L. Minati, G. Speranza, C. Migliaresi, Gold nanoparticles: role of size and surface chemistry on blood protein adsorption, Journal of Nanoparticle Research 15(6) (2013).
[156] W. Xiao, J. Xiong, S. Zhang, Y. Xiong, H. Zhang, H. Gao, Influence of ligands property and particle size of gold nanoparticles on the protein adsorption and corresponding targeting ability, International Journal of Pharmaceutics 538(1-2) (2018) 105-111.
[157] J. Folkman, Y. Shing, Angiogenesis, J Biol Chem 267(16) (1992) 10931-4.
[158] H. Gerhardt, VEGF and endothelial guidance in angiogenic sprouting, Organogenesis 4(4) (2008) 241-6.
[159] J.V. Small, T. Stradal, E. Vignal, K. Rottner, The lamellipodium: where motility begins, Trends Cell Biol 12(3) (2002) 112-20.
[160] V.W. van Hinsbergh, P. Koolwijk, Endothelial sprouting and angiogenesis: matrix metalloproteinases in the lead, Cardiovasc Res 78(2) (2008) 203-12.
[161] Z.J. Liu, T. Shirakawa, Y. Li, A. Soma, M. Oka, G.P. Dotto, R.M. Fairman, O.C. Velazquez, M. Herlyn, Regulation of Notch1 and Dll4 by vascular endothelial growth factor in arterial endothelial cells:

implications for modulating arteriogenesis and angiogenesis, Mol Cell Biol 23(1) (2003) 14-25.
[162] R.K. Jain, Molecular regulation of vessel maturation, Nat Med 9(6) (2003) 685-93.
[163] L. Fredriksson, H. Li, U. Eriksson, The PDGF family: four gene products form five dimeric isoforms, Cytokine Growth Factor Rev 15(4) (2004) 197-204.
[164] G. Fitzgerald, I. Soro-Arnaiz, K. De Bock, The Warburg Effect in Endothelial Cells and its Potential as an Anti-angiogenic Target in Cancer, Frontiers in Cell and Developmental Biology 6 (2018).
[165] J.W. Fett, D.J. Strydom, R.R. Lobb, E.M. Alderman, J.L. Bethune, J.F. Riordan, B.L. Vallee, Isolation and characterization of angiogenin, an angiogenic protein from human carcinoma cells, Biochemistry 24(20) (1985) 5480-6.
[166] X. Gao, Z. Xu, Mechanisms of action of angiogenin, Acta Biochim Biophys Sin (Shanghai) 40(7) (2008) 619-24.
[167] Y. Zhai, X. Zhao, J. Sheng, X. Gao, Z. Ou, Z. Xu, Ribonuclease like 5 regulates zebrafish yolk extension by suppressing a p53-dependent DNA damage response pathway, Int J Biochem Cell Biol 65 (2015) 12-9.
[168] K. Kishimoto, S. Liu, T. Tsuji, K.A. Olson, G.F. Hu, Endogenous angiogenin in endothelial cells is a general requirement for cell proliferation and angiogenesis, Oncogene 24(3) (2005) 445-56.
[169] E. Urso, M. Maffia, Behind the Link between Copper and Angiogenesis: Established Mechanisms and an Overview on the Role of Vascular Copper Transport Systems, Journal of Vascular Research 52(3) (2015) 172-196.
[170] J. Kim, Y.M. Lee, H. Kim, D. Park, J. Kim, W.J. Kim, Phenylboronic acid-sugar grafted polymer architecture as a dual stimuli-responsive gene carrier for targeted anti-angiogenic tumor therapy, Biomaterials 75 (2016) 102-111.
[171] M. Hrynyk, J.P. Ellis, F. Haxho, S. Allison, J.A. Steele, S. Abdulkhalek, R.J. Neufeld, M.R. Szewczuk, Therapeutic designed poly (lactic-co-glycolic acid) cylindrical oseltamivir phosphate-loaded implants impede tumor neovascularization, growth and metastasis in mouse model of human pancreatic carcinoma, Drug Des Devel Ther 9 (2015) 4573-86.
[172] Y. Xu, Z. Wen, Z. Xu, Chitosan nanoparticles inhibit the growth of human hepatocellular carcinoma xenografts through an antiangiogenic mechanism, Anticancer Res 29(12) (2009) 5103-9.

[173] X. Yue, Z. Dai, Liposomal Nanotechnology for Cancer Theranostics, Curr Med Chem 25(12) (2018) 1397-1408.
[174] Y. Jin, X. Liang, Y. An, Z. Dai, Microwave-Triggered Smart Drug Release from Liposomes Co-encapsulating Doxorubicin and Salt for Local Combined Hyperthermia and Chemotherapy of Cancer, Bioconjug Chem 27(12) (2016) 2931-2942.
[175] I. Banerjee, K. De, D. Mukherjee, G. Dey, S. Chattopadhyay, M. Mukherjee, M. Mandal, A.K. Bandyopadhyay, A. Gupta, S. Ganguly, M. Misra, Paclitaxel-loaded solid lipid nanoparticles modified with Tyr-3-octreotide for enhanced anti-angiogenic and anti-glioma therapy, Acta Biomater 38 (2016) 69-81.
[176] C.R. Dass, P.F. Choong, Selective gene delivery for cancer therapy using cationic liposomes: in vivo proof of applicability, J Control Release 113(2) (2006) 155-63.
[177] C. Cha, S.R. Shin, N. Annabi, M.R. Dokmeci, A. Khademhosseini, Carbon-based nanomaterials: multifunctional materials for biomedical engineering, ACS Nano 7(4) (2013) 2891-7.
[178] V. Amendola, R. Pilot, M. Frasconi, O.M. Marago, M.A. Iati, Surface plasmon resonance in gold nanoparticles: a review, J Phys Condens Matter 29(20) (2017) 203002.
[179] J. Zuloaga, P. Nordlander, On the Energy Shift between Near-Field and Far-Field Peak Intensities in Localized Plasmon Systems, Nano Letters 11(3) (2011) 1280-1283.
[180] S. Eustis, M.A. el-Sayed, Why gold nanoparticles are more precious than pretty gold: noble metal surface plasmon resonance and its enhancement of the radiative and nonradiative properties of nanocrystals of different shapes, Chem Soc Rev 35(3) (2006) 209-17.
[181] P.K. Jain, K.S. Lee, I.H. El-Sayed, M.A. El-Sayed, Calculated absorption and scattering properties of gold nanoparticles of different size, shape, and composition: applications in biological imaging and biomedicine, J Phys Chem B 110(14) (2006) 7238-48.
[182] M.S. Dresselhaus, G. Dresselhaus, Interband Transitions for Metals in a Magnetic Field, Physical Review 125(2) (1962) 499-508.
[183] V. Amendola, M. Meneghetti, Size Evaluation of Gold Nanoparticles by UV−vis Spectroscopy, The Journal of Physical Chemistry C 113(11) (2009) 4277-4285.
[184] Y. Xia, N.J. Halas, Shape-Controlled Synthesis and Surface Plasmonic Properties of Metallic Nanostructures, MRS Bulletin 30(5) (2011) 338-348.

[185] P. Bradshaw, Light scattering functions for particles used in the determination of smoke plume concentration, Journal of Aerosol Science 6(2) (1975) 147-156.
[186] G.A. Farias, E.F. Vasconcelos, S.L. Cesar, A.A. Maradudin, Mie scattering by a perfectly conducting sphere with a rough surface, Physica A: Statistical Mechanics and its Applications 207(1-3) (1994) 315-322.
[187] Y.Q. He, S.P. Liu, L. Kong, Z.F. Liu, A study on the sizes and concentrations of gold nanoparticles by spectra of absorption, resonance Rayleigh scattering and resonance non-linear scattering, Spectrochimica Acta Part A: Molecular and Biomolecular Spectroscopy 61(13-14) (2005) 2861-2866.
[188] K.L. Kelly, E. Coronado, L.L. Zhao, G.C. Schatz, The Optical Properties of Metal Nanoparticles: The Influence of Size, Shape, and Dielectric Environment, The Journal of Physical Chemistry B 107(3) (2003) 668-677.
[189] Optical Properties of Metal Clusters, 1995.
[190] J.J. Mock, D.R. Smith, S. Schultz, Local Refractive Index Dependence of Plasmon Resonance Spectra from Individual Nanoparticles, Nano Letters 3(4) (2003) 485-491.
[191] S.A. Maier, Plasmonics: Fundamentals and Applications, 2007.
[192] M.J. Pollitt, G. Buckton, R. Piper, S. Brocchini, Measuring antibody coatings on gold nanoparticles by optical spectroscopy, RSC Advances 5(31) (2015) 24521-24527.
[193] M.M. Miller, A.A. Lazarides, Sensitivity of Metal Nanoparticle Surface Plasmon Resonance to the Dielectric Environment, The Journal of Physical Chemistry B 109(46) (2005) 21556-21565.
[194] H. Liao, C.L. Nehl, J.H. Hafner, Biomedical applications of plasmon resonant metal nanoparticles, Nanomedicine (Lond) 1(2) (2006) 201-8.
[195] E.D. Fabrizio, S. Schlücker, J. Wenger, R. Regmi, H. Rigneault, G. Calafiore, M. West, S. Cabrini, M. Fleischer, N.F. van Hulst, M.F. Garcia-Parajo, A. Pucci, D. Cojoc, C.A.E. Hauser, M. Ni, Roadmap on biosensing and photonics with advanced nano-optical methods, Journal of Optics 18(6) (2016).
[196] A. Csáki, G. Maubach, D. Born, J. Reichert, W. Fritzsche, DNA-based Molecular Nanotechnology, Single Molecules 3(5-6) (2002) 275-280.
[197] W. Zheng, H. Li, W. Chen, J. Ji, X. Jiang, Recyclable Colorimetric Detection of Trivalent Cations in Aqueous Media Using Zwitterionic Gold Nanoparticles, Anal Chem 88(7) (2016) 4140-6.

[198] H. Niu, S. Wang, Z. Zhou, Y. Ma, X. Ma, Y. Cai, Sensitive colorimetric visualization of perfluorinated compounds using poly(ethylene glycol) and perfluorinated thiols modified gold nanoparticles, Anal Chem 86(9) (2014) 4170-7.
[199] C. Guarise, L. Pasquato, V. De Filippis, P. Scrimin, Gold nanoparticles-based protease assay, Proc Natl Acad Sci U S A 103(11) (2006) 3978-82.
[200] I. Brigger, C. Dubernet, P. Couvreur, Nanoparticles in cancer therapy and diagnosis, Adv Drug Deliv Rev 54(5) (2002) 631-51.
[201] T.B. Huff, L. Tong, Y. Zhao, M.N. Hansen, J.X. Cheng, A. Wei, Hyperthermic effects of gold nanorods on tumor cells, Nanomedicine (Lond) 2(1) (2007) 125-32.
[202] L. Tong, Y. Zhao, T.B. Huff, M.N. Hansen, A. Wei, J.X. Cheng, Gold Nanorods Mediate Tumor Cell Death by Compromising Membrane Integrity, Adv Mater 19 (2007) 3136-3141.
[203] Z. Ge, Y. Kang, T.A. Taton, P.V. Braun, D.G. Cahill, Thermal Transport in Au-Core Polymer-Shell Nanoparticles, Nano Letters 5(3) (2005) 531-535.
[204] M.S. Yavuz, Y. Cheng, J. Chen, C.M. Cobley, Q. Zhang, M. Rycenga, J. Xie, C. Kim, K.H. Song, A.G. Schwartz, L.V. Wang, Y. Xia, Gold nanocages covered by smart polymers for controlled release with near-infrared light, Nat Mater 8(12) (2009) 935-9.
[205] M.C. Daniel, D. Astruc, Gold nanoparticles: assembly, supramolecular chemistry, quantum-size-related properties, and applications toward biology, catalysis, and nanotechnology, Chem Rev 104(1) (2004) 293-346.
[206] P. Ghosh, X. Yang, R. Arvizo, Z.J. Zhu, S.S. Agasti, Z. Mo, V.M. Rotello, Intracellular delivery of a membrane-impermeable enzyme in active form using functionalized gold nanoparticles, J Am Chem Soc 132(8) (2010) 2642-5.
[207] M. Cardenas, J. Barauskas, K. Schillen, J.L. Brennan, M. Brust, T. Nylander, Thiol-specific and nonspecific interactions between DNA and gold nanoparticles, Langmuir 22(7) (2006) 3294-9.
[208] W. Putzbach, N. Ronkainen, Immobilization Techniques in the Fabrication of Nanomaterial-Based Electrochemical Biosensors: A Review, Sensors 13(4) (2013) 4811-4840.
[209] S. Kumar, J. Aaron, K. Sokolov, Directional conjugation of antibodies to nanoparticles for synthesis of multiplexed optical contrast agents with both delivery and targeting moieties, Nat Protoc 3(2) (2008) 314-20.

[210] E. Pensa, E. Cortés, G. Corthey, P. Carro, C. Vericat, M.H. Fonticelli, G. Benítez, A.A. Rubert, R.C. Salvarezza, The Chemistry of the Sulfur–Gold Interface: In Search of a Unified Model, Accounts of Chemical Research 45(8) (2012) 1183-1192.
[211] Y. Zhao, F. Zhou, H. Zhou, H. Su, The structural and bonding evolution in cysteine–gold cluster complexes, Phys. Chem. Chem. Phys. 15(5) (2013) 1690-1698.
[212] C. Tao, Antimicrobial activity and toxicity of gold nanoparticles: research progress, challenges and prospects, Lett Appl Microbiol 67(6) (2018) 537-543.
[213] I. Chakravarty, R.J. Pradeepam, K. Kundu, P.K. Singh, S. Kundu, Mycofabrication of gold nanoparticles and evaluation of their antioxidant activities, Curr Pharm Biotechnol 16(8) (2015) 747-55.
[214] K. Sztandera, M. Gorzkiewicz, B. Klajnert-Maculewicz, Gold Nanoparticles in Cancer Treatment, Molecular Pharmaceutics 16(1) (2018) 1-23.
[215] S. Balakrishnan, F.A. Bhat, P. Raja Singh, S. Mukherjee, P. Elumalai, S. Das, C.R. Patra, J. Arunakaran, Gold nanoparticle-conjugated quercetin inhibits epithelial-mesenchymal transition, angiogenesis and invasiveness via EGFR/VEGFR-2-mediated pathway in breast cancer, Cell Prolif 49(6) (2016) 678-697.
[216] D. Bartczak, O.L. Muskens, T. Sanchez-Elsner, A.G. Kanaras, T.M. Millar, Manipulation of in vitro angiogenesis using peptide-coated gold nanoparticles, ACS Nano 7(6) (2013) 5628-36.
[217] Y.-J. Roh, C.R. Rho, W.-K. Cho, S. Kang, The Antiangiogenic Effects of Gold Nanoparticles on Experimental Choroidal Neovascularization in Mice, Investigative Opthalmology & Visual Science 57(15) (2016).
[218] Y. Pan, H. Ding, L. Qin, X. Zhao, J. Cai, B. Du, Gold nanoparticles induce nanostructural reorganization of VEGFR2 to repress angiogenesis, J Biomed Nanotechnol 9(10) (2013) 1746-56.
[219] R.R. Arvizo, S. Rana, O.R. Miranda, R. Bhattacharya, V.M. Rotello, P. Mukherjee, Mechanism of anti-angiogenic property of gold nanoparticles: role of nanoparticle size and surface charge, Nanomedicine 7(5) (2011) 580-7.
[220] P. Mukherjee, R. Bhattacharya, P. Wang, L. Wang, S. Basu, J.A. Nagy, A. Atala, D. Mukhopadhyay, S. Soker, Antiangiogenic properties of gold nanoparticles, Clin Cancer Res 11(9) (2005) 3530-4.

[221] Y. Pan, Q. Wu, L. Qin, J. Cai, B. Du, Gold nanoparticles inhibit VEGF165-induced migration and tube formation of endothelial cells via the Akt pathway, Biomed Res Int 2014 (2014) 418624.
[222] S.J. Soenen, B. Manshian, J.M. Montenegro, F. Amin, B. Meermann, T. Thiron, M. Cornelissen, F. Vanhaecke, S. Doak, W.J. Parak, S. De Smedt, K. Braeckmans, Cytotoxic Effects of Gold Nanoparticles: A Multiparametric Study, ACS Nano 6(7) (2012) 5767-5783.
[223] Y. Liu, N. Rogel, K. Harada, L. Jarett, C.H. Maiorana, G.K. German, G.J. Mahler, A.L. Doiron, Nanoparticle size-specific actin rearrangement and barrier dysfunction of endothelial cells, Nanotoxicology 11(7) (2017) 846-856.
[224] S. Kumari, A.K. Badana, M.M. G, S. G, R. Malla, Reactive Oxygen Species: A Key Constituent in Cancer Survival, Biomark Insights 13 (2018) 1177271918755391.
[225] M. Cano Sanchez, S. Lancel, E. Boulanger, R. Neviere, Targeting Oxidative Stress and Mitochondrial Dysfunction in the Treatment of Impaired Wound Healing: A Systematic Review, Antioxidants (Basel) 7(8) (2018).
[226] Z. Zhen, H. Zhu, Structure and Properties of Graphene, Graphene2018, pp. 1-12.
[227] W. Choi, I. Lahiri, R. Seelaboyina, Y.S. Kang, Synthesis of Graphene and Its Applications: A Review, Critical Reviews in Solid State and Materials Sciences 35(1) (2010) 52-71.
[228] P.-G. Ren, D.-X. Yan, X. Ji, T. Chen, Z.-M. Li, Temperature dependence of graphene oxide reduced by hydrazine hydrate, Nanotechnology 22(5) (2011).
[229] H.K. Jeong, M.H. Jin, K.P. So, S.C. Lim, Y.H. Lee, Tailoring the characteristics of graphite oxides by different oxidation times, Journal of Physics D: Applied Physics 42(6) (2009).
[230] S. Stankovich, D.A. Dikin, R.D. Piner, K.A. Kohlhaas, A. Kleinhammes, Y. Jia, Y. Wu, S.T. Nguyen, R.S. Ruoff, Synthesis of graphene-based nanosheets via chemical reduction of exfoliated graphite oxide, Carbon 45(7) (2007) 1558-1565.
[231] J.M. Tour, Top-Down versus Bottom-Up Fabrication of Graphene-Based Electronics, Chemistry of Materials 26(1) (2013) 163-171.
[232] S. Niyogi, E. Bekyarova, M.E. Itkis, J.L. McWilliams, M.A. Hamon, R.C. Haddon, Solution properties of graphite and graphene, J Am Chem Soc 128(24) (2006) 7720-1.

[233] T. Kuilla, S. Bhadra, D. Yao, N.H. Kim, S. Bose, J.H. Lee, Recent advances in graphene based polymer composites, Progress in Polymer Science 35(11) (2010) 1350-1375.
[234] A.T. Smith, A.M. LaChance, S. Zeng, B. Liu, L. Sun, Synthesis, properties, and applications of graphene oxide/reduced graphene oxide and their nanocomposites, Nano Materials Science 1(1) (2019) 31-47.
[235] V. Georgakilas, J.N. Tiwari, K.C. Kemp, J.A. Perman, A.B. Bourlinos, K.S. Kim, R. Zboril, Noncovalent Functionalization of Graphene and Graphene Oxide for Energy Materials, Biosensing, Catalytic, and Biomedical Applications, Chemical Reviews 116(9) (2016) 5464-5519.
[236] W. Gao, Graphene Oxide, 2015.
[237] N. Ahmad, A. Kausar, B. Muhammad, An investigation on 4-aminobenzoic acid modified polyvinyl chloride/graphene oxide and PVC/graphene oxide based nanocomposite membranes, Journal of Plastic Film & Sheeting 32(4) (2016) 419-448.
[238] C. Chung, Y.-K. Kim, D. Shin, S.-R. Ryoo, B.H. Hong, D.-H. Min, Biomedical Applications of Graphene and Graphene Oxide, Accounts of Chemical Research 46(10) (2013) 2211-2224.
[239] J. Shen, Y. Zhu, X. Yang, C. Li, Graphene quantum dots: emergent nanolights for bioimaging, sensors, catalysis and photovoltaic devices, Chem Commun (Camb) 48(31) (2012) 3686-99.
[240] J. Lee, J. Kim, S. Kim, D.-H. Min, Biosensors based on graphene oxide and its biomedical application, Advanced Drug Delivery Reviews 105 (2016) 275-287.
[241] M. Chakrabarti, R. Kiseleva, A. Vertegel, S.K. Ray, Carbon Nanomaterials for Drug Delivery and Cancer Therapy, J Nanosci Nanotechnol 15(8) (2015) 5501-11.
[242] H. Zhao, R. Ding, X. Zhao, Y. Li, L. Qu, H. Pei, L. Yildirimer, Z. Wu, W. Zhang, Graphene-based nanomaterials for drug and/or gene delivery, bioimaging, and tissue engineering, Drug Discov Today 22(9) (2017) 1302-1317.
[243] Y. Zhang, S.F. Ali, E. Dervishi, Y. Xu, Z. Li, D. Casciano, A.S. Biris, Cytotoxicity effects of graphene and single-wall carbon nanotubes in neural phaeochromocytoma-derived PC12 cells, ACS Nano 4(6) (2010) 3181-6.
[244] T. Tojo, M. Ushio-Fukai, M. Yamaoka-Tojo, S. Ikeda, N. Patrushev, R.W. Alexander, Role of gp91phox (Nox2)-containing NAD(P)H oxidase in angiogenesis in response to hindlimb ischemia, Circulation 111(18) (2005) 2347-55.

[245] J. Park, Y.S. Kim, S. Ryu, W.S. Kang, S. Park, J. Han, H.C. Jeong, B.H. Hong, Y. Ahn, B.-S. Kim, Graphene Potentiates the Myocardial Repair Efficacy of Mesenchymal Stem Cells by Stimulating the Expression of Angiogenic Growth Factors and Gap Junction Protein, Advanced Functional Materials 25(17) (2015) 2590-2600.
[246] I. Lasocka, L. Szulc-Dabrowska, M. Skibniewski, E. Skibniewska, W. Strupinski, I. Pasternak, H. Kmiec, P. Kowalczyk, Biocompatibility of pristine graphene monolayer: Scaffold for fibroblasts, Toxicol In Vitro 48 (2018) 276-285.
[247] M. Kalbacova, A. Broz, J. Kong, M. Kalbac, Graphene substrates promote adherence of human osteoblasts and mesenchymal stromal cells, Carbon 48(15) (2010) 4323-4329.
[248] C.S.N.B. Garcia, P.R.M. Rocco, M.M. Morales, Cellular response to mechanical stress, Springer Milan, Milano, 2006, pp. 3-19.
[249] I. Lasocka, E. Jastrzebska, L. Szulc-Dabrowska, M. Skibniewski, I. Pasternak, M.H. Kalbacova, E.M. Skibniewska, The effects of graphene and mesenchymal stem cells in cutaneous wound healing and their putative action mechanism, Int J Nanomedicine 14 (2019) 2281-2299.
[250] F. Gentile, L. Tirinato, E. Battista, F. Causa, C. Liberale, E.M. di Fabrizio, P. Decuzzi, Cells preferentially grow on rough substrates, Biomaterials 31(28) (2010) 7205-12.
[251] X. Zou, L. Zhang, Z. Wang, Y. Luo, Mechanisms of the Antimicrobial Activities of Graphene Materials, Journal of the American Chemical Society 138(7) (2016) 2064-2077.
[252] Y. Tu, M. Lv, P. Xiu, T. Huynh, M. Zhang, M. Castelli, Z. Liu, Q. Huang, C. Fan, H. Fang, R. Zhou, Destructive extraction of phospholipids from Escherichia coli membranes by graphene nanosheets, Nature Nanotechnology 8(8) (2013) 594-601.
[253] N. Kurantowicz, E. Sawosz, S. Jaworski, M. Kutwin, B. Strojny, M. Wierzbicki, J. Szeliga, A. Hotowy, L. Lipinska, R. Kozinski, J. Jagiello, A. Chwalibog, Interaction of graphene family materials with Listeria monocytogenes and Salmonella enterica, Nanoscale Res Lett 10 (2015) 23.
[254] S.K. Singh, M.K. Singh, M.K. Nayak, S. Kumari, S. Shrivastava, J.J.A. Grácio, D. Dash, Thrombus Inducing Property of Atomically Thin Graphene Oxide Sheets, ACS Nano 5(6) (2011) 4987-4996.
[255] T.J. Koh, L.A. DiPietro, Inflammation and wound healing: the role of the macrophage, Expert Rev Mol Med 13 (2011) e23.

[256] T.A. Wilgus, S. Roy, J.C. McDaniel, Neutrophils and Wound Repair: Positive Actions and Negative Reactions, Adv Wound Care (New Rochelle) 2(7) (2013) 379-388.
[257] M. Vinish, W. Cui, E. Stafford, L. Bae, H. Hawkins, R. Cox, T. Toliver-Kinsky, Dendritic cells modulate burn wound healing by enhancing early proliferation, Wound Repair Regen 24(1) (2016) 6-13.
[258] J. Saleem, L. Wang, C. Chen, Immunological effects of graphene family nanomaterials, NanoImpact 5 (2017) 109-118.
[259] R. Shapiro, D.J. Strydom, K.A. Olson, B.L. Vallee, Isolation of angiogenin from normal human plasma, Biochemistry 26(16) (1987) 5141-6.
[260] J. Sheng, Z. Xu, Three decades of research on angiogenin: a review and perspective, Acta Biochim Biophys Sin (Shanghai) 48(5) (2016) 399-410.
[261] N. Thiyagarajan, K.R. Acharya, Crystal structure of human angiogenin with an engineered loop exhibits conformational flexibility at the functional regions of the molecule, FEBS Open Bio 3 (2013) 65-70.
[262] K.R. Acharya, R. Shapiro, S.C. Allen, J.F. Riordan, B.L. Vallee, Crystal structure of human angiogenin reveals the structural basis for its functional divergence from ribonuclease, Proc Natl Acad Sci U S A 91(8) (1994) 2915-9.
[263] N. Russo, R. Shapiro, K.R. Acharya, J.F. Riordan, B.L. Vallee, Role of glutamine-117 in the ribonucleolytic activity of human angiogenin, Proc Natl Acad Sci U S A 91(8) (1994) 2920-4.
[264] N. Russo, V. Nobile, A. Di Donato, J.F. Riordan, B.L. Vallee, The C-terminal region of human angiogenin has a dual role in enzymatic activity, Proc Natl Acad Sci U S A 93(8) (1996) 3243-7.
[265] G.F. Hu, S.I. Chang, J.F. Riordan, B.L. Vallee, An angiogenin-binding protein from endothelial cells, Proc Natl Acad Sci U S A 88(6) (1991) 2227-31.
[266] J. Moroianu, J.F. Riordan, Nuclear translocation of angiogenin in proliferating endothelial cells is essential to its angiogenic activity, Proc Natl Acad Sci U S A 91(5) (1994) 1677-81.
[267] C. Giacomelli, M.L. Trincavelli, C. Satriano, O. Hansson, D. La Mendola, E. Rizzarelli, C. Martini, diamondCopper (II) ions modulate Angiogenin activity in human endothelial cells, Int J Biochem Cell Biol 60 (2015) 185-96.
[268] G.F. Hu, J.F. Riordan, B.L. Vallee, A putative angiogenin receptor in angiogenin-responsive human endothelial cells, Proc Natl Acad Sci U S A 94(6) (1997) 2204-9.

[269] S. Liu, D. Yu, Z.P. Xu, J.F. Riordan, G.F. Hu, Angiogenin activates Erk1/2 in human umbilical vein endothelial cells, Biochem Biophys Res Commun 287(1) (2001) 305-10.
[270] S. Ibaragi, N. Yoshioka, H. Kishikawa, J.K. Hu, P.M. Sadow, M. Li, G.F. Hu, Angiogenin-stimulated rRNA transcription is essential for initiation and survival of AKT-induced prostate intraepithelial neoplasia, Mol Cancer Res 7(3) (2009) 415-24.
[271] Z. Xu, D.M. Monti, G. Hu, Angiogenin activates human umbilical artery smooth muscle cells, Biochem Biophys Res Commun 285(4) (2001) 909-14.
[272] R. Trouillon, D.K. Kang, H. Park, S.I. Chang, D. O'Hare, Angiogenin induces nitric oxide synthesis in endothelial cells through PI-3 and Akt kinases, Biochemistry 49(15) (2010) 3282-8.
[273] J. Sheng, W. Yu, X. Gao, Z. Xu, G.F. Hu, Angiogenin stimulates ribosomal RNA transcription by epigenetic activation of the ribosomal DNA promoter, J Cell Physiol 229(4) (2014) 521-9.
[274] P. Ivanov, M.M. Emara, J. Villen, S.P. Gygi, P. Anderson, Angiogenin-induced tRNA fragments inhibit translation initiation, Mol Cell 43(4) (2011) 613-23.
[275] A. Elkordy, E. Mishima, K. Niizuma, Y. Akiyama, M. Fujimura, T. Tominaga, T. Abe, Stress-induced tRNA cleavage and tiRNA generation in rat neuronal PC12 cells, J Neurochem 146(5) (2018) 560-569.
[276] T.W. Hallahan, R. Shapiro, B.L. Vallee, Dual site model for the organogenic activity of angiogenin, Proc Natl Acad Sci U S A 88(6) (1991) 2222-6.
[277] G.F. Hu, J.F. Riordan, Angiogenin enhances actin acceleration of plasminogen activation, Biochem Biophys Res Commun 197(2) (1993) 682-7.
[278] R.M. Lyons, L.E. Gentry, A.F. Purchio, H.L. Moses, Mechanism of activation of latent recombinant transforming growth factor beta 1 by plasmin, J Cell Biol 110(4) (1990) 1361-7.
[279] M.G. Pyatibratov, A.S. Kostyukova, New insights into the role of angiogenin in actin polymerization, Int Rev Cell Mol Biol 295 (2012) 175-98.
[280] P.A. Janmey, The cytoskeleton and cell signaling: component localization and mechanical coupling, Physiol Rev 78(3) (1998) 763-81.
[281] P. Patwari, R.T. Lee, Mechanical control of tissue morphogenesis, Circ Res 103(3) (2008) 234-43.
[282] A. Mammoto, K.M. Connor, T. Mammoto, C.W. Yung, D. Huh, C.M. Aderman, G. Mostoslavsky, L.E. Smith, D.E. Ingber, A

mechanosensitive transcriptional mechanism that controls angiogenesis, Nature 457(7233) (2009) 1103-8.
[283] J. Blaser, S. Triebel, C. Kopp, H. Tschesche, A highly sensitive immunoenzymometric assay for the determination of angiogenin, Eur J Clin Chem Clin Biochem 31(8) (1993) 513-6.
[284] J. Skog, T. Würdinger, S. van Rijn, D.H. Meijer, L. Gainche, W.T. Curry, B.S. Carter, A.M. Krichevsky, X.O. Breakefield, Glioblastoma microvesicles transport RNA and proteins that promote tumour growth and provide diagnostic biomarkers, Nature Cell Biology 10(12) (2008) 1470-1476.
[285] C.Y. Spong, A. Ghidini, D.M. Sherer, J.C. Pezzullo, M. Ossandon, G.S. Eglinton, Angiogenin: a marker for preterm delivery in midtrimester amniotic fluid, Am J Obstet Gynecol 176(2) (1997) 415-8.
[286] J. Ilzecka, Cerebrospinal fluid angiogenin level in patients with amyotrophic lateral sclerosis, Acta Clin Croat 47(2) (2008) 77-9.
[287] P. Ivanov, E. O'Day, M.M. Emara, G. Wagner, J. Lieberman, P. Anderson, G-quadruplex structures contribute to the neuroprotective effects of angiogenin-induced tRNA fragments, Proc Natl Acad Sci U S A 111(51) (2014) 18201-6.
[288] S.H. Lee, K.W. Kim, K.M. Min, K.W. Kim, S.I. Chang, J.C. Kim, Angiogenin reduces immune inflammation via inhibition of TANK-binding kinase 1 expression in human corneal fibroblast cells, Mediators Inflamm 2014 (2014) 861435.
[289] T. Eleftheriadis, G. Pissas, M. Sounidaki, N. Antoniadis, G. Antoniadi, V. Liakopoulos, I. Stefanidis, Angiogenin is upregulated during the alloreactive immune response and has no effect on the T-cell expansion phase, whereas it affects the contraction phase by inhibiting CD4(+) T-cell apoptosis, Exp Ther Med 12(5) (2016) 3471-3475.
[290] L.V. Hooper, T.S. Stappenbeck, C.V. Hong, J.I. Gordon, Angiogenins: a new class of microbicidal proteins involved in innate immunity, Nat Immunol 4(3) (2003) 269-73.
[291] G. Rajashekhar, A. Loganath, A.C. Roy, Y.C. Wong, Expression and localization of angiogenin in placenta: enhanced levels at term over first trimester villi, Mol Reprod Dev 62(2) (2002) 159-66.
[292] M.J. Greenway, P.M. Andersen, C. Russ, S. Ennis, S. Cashman, C. Donaghy, V. Patterson, R. Swingler, D. Kieran, J. Prehn, K.E. Morrison, A. Green, K.R. Acharya, R.H. Brown, Jr., O. Hardiman, ANG mutations segregate with familial and 'sporadic' amyotrophic lateral sclerosis, Nat Genet 38(4) (2006) 411-3.

[293] W.J. Bradshaw, S. Rehman, T.T. Pham, N. Thiyagarajan, R.L. Lee, V. Subramanian, K.R. Acharya, Structural insights into human angiogenin variants implicated in Parkinson's disease and Amyotrophic Lateral Sclerosis, Sci Rep 7 (2017) 41996.
[294] I.E. Koutroubakis, C. Xidakis, K. Karmiris, A. Sfiridaki, E. Kandidaki, E.A. Kouroumalis, Serum angiogenin in inflammatory bowel disease, Dig Dis Sci 49(11-12) (2004) 1758-62.
[295] S.-C. Pan, L.-W. Wu, C.-L. Chen, S.-J. Shieh, H.-Y. Chiu, Angiogenin expression in burn blister fluid: Implications for its role in burn wound neovascularization, Wound Repair and Regeneration 20(5) (2012) 731-739.
[296] N. Yoshioka, L. Wang, K. Kishimoto, T. Tsuji, G.F. Hu, A therapeutic target for prostate cancer based on angiogenin-stimulated angiogenesis and cancer cell proliferation, Proc Natl Acad Sci U S A 103(39) (2006) 14519-24.
[297] Z. Bokebayev, I. Kukiyev, Z. Shulgau, A. Gulyayev, K. Draganov, [Wound Healing Properties of the Recombinant Human Angiogenin in the Gel Medicinal Form Used as a Treatment in the Model of Planal Musculocutaneous and Linear Wounds], Georgian Med News (276) (2018) 177-182.
[298] M.I. Shabayek, O.M. Sayed, H.A. Attaia, H.A. Awida, H. Abozeed, Diagnostic evaluation of urinary angiogenin (ANG) and clusterin (CLU) as biomarker for bladder cancer, Pathol Oncol Res 20(4) (2014) 859-66.
[299] A.C. Gonzalez, T.F. Costa, Z.A. Andrade, A.R. Medrado, Wound healing - A literature review, An Bras Dermatol 91(5) (2016) 614-620.
[300] B.S. Nayak, S. Sandiford, A. Maxwell, Evaluation of the Wound-healing Activity of Ethanolic Extract of Morinda citrifolia L. Leaf, Evid Based Complement Alternat Med 6(3) (2009) 351-6.
[301] P.-H. Lin, M. Sermersheim, H. Li, P. Lee, S. Steinberg, J. Ma, Zinc in Wound Healing Modulation, Nutrients 10(1) (2017).
[302] U.D.S. Sekhon, A. Sen Gupta, Platelets and Platelet-Inspired Biomaterials Technologies in Wound Healing Applications, ACS Biomaterials Science & Engineering 4(4) (2017) 1176-1192.
[303] M. Hesketh, K.B. Sahin, Z.E. West, R.Z. Murray, Macrophage Phenotypes Regulate Scar Formation and Chronic Wound Healing, Int J Mol Sci 18(7) (2017).
[304] S.V. Pollack, The wound healing process, Clin Dermatol 2(3) (1984) 8-16.

[305] T. Velnar, T. Bailey, V. Smrkolj, The wound healing process: an overview of the cellular and molecular mechanisms, J Int Med Res 37(5) (2009) 1528-42.
[306] C.C. Khoury, F.N. Ziyadeh, Angiogenic factors, Contrib Nephrol 170 (2011) 83-92.
[307] P.J. Keck, S.D. Hauser, G. Krivi, K. Sanzo, T. Warren, J. Feder, D.T. Connolly, Vascular permeability factor, an endothelial cell mitogen related to PDGF, Science 246(4935) (1989) 1309-12.
[308] S.C. Pan, L.W. Wu, C.L. Chen, S.J. Shieh, H.Y. Chiu, Angiogenin expression in burn blister fluid: implications for its role in burn wound neovascularization, Wound Repair Regen 20(5) (2012) 731-9.
[309] S. Balani, L.V. Nguyen, C.J. Eaves, Modeling the process of human tumorigenesis, Nat Commun 8 (2017) 15422.
[310] S. Shimoyama, F. Gansauge, S. Gansauge, G. Negri, T. Oohara, H.G. Beger, Increased angiogenin expression in pancreatic cancer is related to cancer aggressiveness, Cancer Res 56(12) (1996) 2703-6.
[311] S. Shimoyama, M. Kaminishi, Increased angiogenin expression in gastric cancer correlated with cancer progression, J Cancer Res Clin Oncol 126(8) (2000) 468-74.
[312] S. Sadagopan, M.V. Veettil, S. Chakraborty, N. Sharma-Walia, N. Paudel, V. Bottero, B. Chandran, Angiogenin functionally interacts with p53 and regulates p53-mediated apoptosis and cell survival, Oncogene 31(46) (2012) 4835-47.
[313] A. Hartmann, M. Kunz, S. Kostlin, R. Gillitzer, A. Toksoy, E.B. Brocker, C.E. Klein, Hypoxia-induced up-regulation of angiogenin in human malignant melanoma, Cancer Res 59(7) (1999) 1578-83.
[314] H. Pilch, K. Schlenger, E. Steiner, P. Brockerhoff, P. Knapstein, P. Vaupel, Hypoxia-stimulated expression of angiogenic growth factors in cervical cancer cells and cervical cancer-derived fibroblasts, Int J Gynecol Cancer 11(2) (2001) 137-42.
[315] M.L. Jones, C.M. Ewing, W.B. Isaacsa, R.H. Getzenberg, Prostate cancer-derived angiogenin stimulates the invasion of prostate fibroblasts, J Cell Mol Med 16(1) (2012) 193-201.
[316] M. Kulka, N. Fukuishi, D.D. Metcalfe, Human mast cells synthesize and release angiogenin, a member of the ribonuclease A (RNase A) superfamily, J Leukoc Biol 86(5) (2009) 1217-26.
[317] H. Tschesche, C. Kopp, W.H. Horl, U. Hempelmann, Inhibition of degranulation of polymorphonuclear leukocytes by angiogenin and its tryptic fragment, J Biol Chem 269(48) (1994) 30274-80.

[318] S. Landt, K. Mordelt, I. Schwidde, J. Barinoff, S. Korlach, F. Stoblen, W. Lichtenegger, J. Sehouli, S. Kummel, Prognostic significance of the angiogenic factors angiogenin, endoglin and endostatin in cervical cancer, Anticancer Res 31(8) (2011) 2651-5.
[319] M. Vetchy, Biological role of copper as an essential trace element in the human organism, Ceska Slov Farm 67(4) 143-153.
[320] S.C. Leary, D.R. Winge, The Janus face of copper: its expanding roles in biology and the pathophysiology of disease. Meeting on Copper and Related Metals in Biology, EMBO Rep 8(3) (2007) 224-7.
[321] E. Gaggelli, H. Kozlowski, D. Valensin, G. Valensin, Copper homeostasis and neurodegenerative disorders (Alzheimer's, prion, and Parkinson's diseases and amyotrophic lateral sclerosis), Chem Rev 106(6) (2006) 1995-2044.
[322] B.R. McAuslan, W. Reilly, Endothelial cell phagokinesis in response to specific metal ions, Exp Cell Res 130(1) (1980) 147-57.
[323] M. Ziche, J. Jones, P.M. Gullino, Role of prostaglandin E1 and copper in angiogenesis, J Natl Cancer Inst 69(2) (1982) 475-82.
[324] K.S. Raju, G. Alessandri, M. Ziche, P.M. Gullino, Ceruloplasmin, copper ions, and angiogenesis, J Natl Cancer Inst 69(5) (1982) 1183-8.
[325] S. Brem, A.M. Tsanaclis, D. Zagzag, Anticopper treatment inhibits pseudopodial protrusion and the invasive spread of 9L gliosarcoma cells in the rat brain, Neurosurgery 26(3) (1990) 391-6.
[326] D. Yoshida, Y. Ikeda, S. Nakazawa, Quantitative analysis of copper, zinc and copper/zinc ratio in selected human brain tumors, J Neurooncol 16(2) (1993) 109-15.
[327] S.K. Gupta, V.K. Shukla, M.P. Vaidya, S.K. Roy, S. Gupta, Serum trace elements and Cu/Zn ratio in breast cancer patients, J Surg Oncol 46(3) (1991) 178-81.
[328] S. Apelgot, J. Coppey, A. Fromentin, E. Guille, M.F. Poupon, A. Roussel, Altered distribution of copper (64Cu) in tumor-bearing mice and rats, Anticancer Res 6(2) (1986) 159-64.
[329] A. Crowe, C. Jackaman, K.M. Beddoes, B. Ricciardo, D.J. Nelson, Rapid copper acquisition by developing murine mesothelioma: decreasing bioavailable copper slows tumor growth, normalizes vessels and promotes T cell infiltration, PLoS One 8(8) (2013) e73684.
[330] U. Mirastschijski, A. Martin, L.N. Jorgensen, B. Sampson, M.S. Agren, Zinc, copper, and selenium tissue levels and their relation to subcutaneous abscess, minor surgery, and wound healing in humans, Biol Trace Elem Res 153(1-3) (2013) 76-83.

[331] I.T. Cangul, N.Y. Gul, A. Topal, R. Yilmaz, Evaluation of the effects of topical tripeptide-copper complex and zinc oxide on open-wound healing in rabbits, Vet Dermatol 17(6) (2006) 417-23.
[332] T.D. Rae, Undetectable Intracellular Free Copper: The Requirement of a Copper Chaperone for Superoxide Dismutase, Science 284(5415) (1999) 805-808.
[333] R.A. Festa, D.J. Thiele, Copper: an essential metal in biology, Curr Biol 21(21) (2011) R877-83.
[334] E.B. Maryon, S.A. Molloy, A.M. Zimnicka, J.H. Kaplan, Copper entry into human cells: progress and unanswered questions, Biometals 20(3-4) (2007) 355-64.
[335] T.Z. Kidane, R. Farhad, K.J. Lee, A. Santos, E. Russo, M.C. Linder, Uptake of copper from plasma proteins in cells where expression of CTR1 has been modulated, Biometals 25(4) (2012) 697-709.
[336] T.V. O'Halloran, V.C. Culotta, Metallochaperones, an intracellular shuttle service for metal ions, J Biol Chem 275(33) (2000) 25057-60.
[337] F. Martin, T. Linden, D.r.M. Katschinski, F. Oehme, I. Flamme, C.K. Mukhopadhyay, K. Eckhardt, J. Tröger, S. Barth, G. Camenisch, R.H. Wenger, Copper-dependent activation of hypoxia-inducible factor (HIF)-1: implications for ceruloplasmin regulation, Blood 105(12) (2005) 4613-4619.
[338] Y. Jiang, C. Reynolds, C. Xiao, W. Feng, Z. Zhou, W. Rodriguez, S.C. Tyagi, J.W. Eaton, J.T. Saari, Y.J. Kang, Dietary copper supplementation reverses hypertrophic cardiomyopathy induced by chronic pressure overload in mice, J Exp Med 204(3) (2007) 657-66.
[339] Y. Demura, T. Ishizaki, S. Ameshima, S. Okamura, T. Hayashi, S. Matsukawa, I. Miyamori, The activation of nitric oxide synthase by copper ion is mediated by intracellular Ca2+mobilization in human pulmonary arterial endothelial cells, British Journal of Pharmacology 125(6) (1998) 1180-1187.
[340] T. Kishimoto, T. Oguri, D. Ueda, M. Tada, Copper enhances EDNO (endothelium-derived nitric oxide) activity by cultured human vascular endothelial cells, Hum Cell 9(2) (1996) 117-24.
[341] V. Shanbhag, K. Jasmer-McDonald, S. Zhu, A.L. Martin, N. Gudekar, A. Khan, E. Ladomersky, K. Singh, G.A. Weisman, M.J. Petris, ATP7A delivers copper to the lysyl oxidase family of enzymes and promotes tumorigenesis and metastasis, Proc Natl Acad Sci U S A 116(14) (2019) 6836-6841.
[342] M. Landriscina, C. Bagala, A. Mandinova, R. Soldi, I. Micucci, S. Bellum, I. Prudovsky, T. Maciag, Copper induces the assembly of a

multiprotein aggregate implicated in the release of fibroblast growth factor 1 in response to stress, J Biol Chem 276(27) (2001) 25549-57.
[343] G.F. Hu, Copper stimulates proliferation of human endothelial cells under culture, J Cell Biochem 69(3) (1998) 326-35.
[344] D. La Mendola, D. Farkas, F. Bellia, A. Magrì, A. Travaglia, Ö. Hansson, E. Rizzarelli, Probing the Copper(II) Binding Features of Angiogenin. Similarities and Differences between a N-Terminus Peptide Fragment and the Recombinant Human Protein, Inorganic Chemistry 51(1) (2011) 128-141.
[345] F. Soncin, J.D. Guitton, T. Cartwright, J. Badet, Interaction of human angiogenin with copper modulates angiogenin binding to endothelial cells, Biochem Biophys Res Commun 236(3) (1997) 604-10.
[346] D. La Mendola, F. Arnesano, O. Hansson, C. Giacomelli, V. Calo, V. Mangini, A. Magri, F. Bellia, M.L. Trincavelli, C. Martini, G. Natile, E. Rizzarelli, Copper binding to naturally occurring, lactam form of angiogenin differs from that to recombinant protein, affecting their activity, Metallomics 8(1) (2016) 118-24.
[347] J. Turkevich, P.C. Stevenson, J. Hillier, A study of the nucleation and growth processes in the synthesis of colloidal gold, Discussions of the Faraday Society 11 (1951).
[348] X. Huang, M.A. El-Sayed, Gold nanoparticles: Optical properties and implementations in cancer diagnosis and photothermal therapy, Journal of Advanced Research 1(1) (2010) 13-28.
[349] N. Hanžić, T. Jurkin, A. Maksimović, M. Gotić, The synthesis of gold nanoparticles by a citrate-radiolytical method, Radiation Physics and Chemistry 106 (2015) 77-82.
[350] J. Uddin, Terahertz multispectral imaging for the analysis of gold nanoparticles' size and the number of unit cells in comparison with other techniques, International Journal of Biosensors & Bioelectronics 4(3) (2018).
[351] J.R.G. Navarro, M.H.V. Werts, Resonant light scattering spectroscopy of gold, silver and gold–silver alloy nanoparticles and optical detection in microfluidic channels, The Analyst 138(2) (2013) 583-592.
[352] M. Iqbal, G. Usanase, K. Oulmi, F. Aberkane, T. Bendaikha, H. Fessi, N. Zine, G. Agusti, E.-S. Errachid, A. Elaissari, Preparation of gold nanoparticles and determination of their particles size via different methods, Materials Research Bulletin 79 (2016) 97-104.
[353] J.P. Oliveira, A.R. Prado, W.J. Keijok, M.R.N. Ribeiro, M.J. Pontes, B.V. Nogueira, M.C.C. Guimarães, A helpful method for controlled

synthesis of monodisperse gold nanoparticles through response surface modeling, Arabian Journal of Chemistry 13(1) (2020) 216-226.
[354] X. Sun, Z. Liu, K. Welsher, J.T. Robinson, A. Goodwin, S. Zaric, H. Dai, Nano-Graphene Oxide for Cellular Imaging and Drug Delivery, Nano Res 1(3) (2008) 203-212.
[355] J. Li, C.-y. Liu, Ag/Graphene Heterostructures: Synthesis, Characterization and Optical Properties, European Journal of Inorganic Chemistry 2010(8) (2010) 1244-1248.
[356] C. Goldmann, R. Lazzari, X. Paquez, C. Boissière, F. Ribot, C. Sanchez, C. Chanéac, D. Portehault, Charge Transfer at Hybrid Interfaces: Plasmonics of Aromatic Thiol-Capped Gold Nanoparticles, ACS Nano 9(7) (2015) 7572-7582.
[357] M.I. Stockman, Nanoplasmonic sensing and detection, Science 348(6232) (2015) 287-288.
[358] S.C. Patel, S. Lee, G. Lalwani, C. Suhrland, S.M. Chowdhury, B. Sitharaman, Graphene-based platforms for cancer therapeutics, Therapeutic Delivery 7(2) (2016) 101-116.
[359] M.P. Baker, H.M. Reynolds, B. Lumicisi, C.J. Bryson, Immunogenicity of protein therapeutics: The key causes, consequences and challenges, Self Nonself 1(4) (2010) 314-322.
[360] S. D. Skaper, Peptide Mimetics of Neurotrophins and their Receptors, Current Pharmaceutical Design 17(25) (2011) 2704-2718.
[361] N. Trier, P. Hansen, G. Houen, Peptides, Antibodies, Peptide Antibodies and More, Int J Mol Sci 20(24) (2019).
[362] D.L. Mendola, A. Magrì, L.I. Vagliasindi, Ö. Hansson, R.P. Bonomo, E. Rizzarelli, Copper(ii) complex formation with a linear peptide encompassing the putative cell binding site of angiogenin, Dalton Transactions 39(44) (2010).
[363] D.E. Holloway, M.C. Hares, R. Shapiro, V. Subramanian, K.R. Acharya, High-level expression of three members of the murine angiogenin family in Escherichia coli and purification of the recombinant proteins, Protein Expr Purif 22(2) (2001) 307-17.
[364] S.H. Jang, D.K. Kang, S.I. Chang, H.A. Scheraga, H.C. Shin, High level production of bovine angiogenin in E. coli by an efficient refolding procedure, Biotechnol Lett 26(19) (2004) 1501-4.
[365] E.N. Lorenzón, G.F. Cespedes, E.F. Vicente, L.G. Nogueira, T.M. Bauab, M.S. Castro, E.M. Cilli, Effects of Dimerization on the Structure and Biological Activity of Antimicrobial Peptide Ctx-Ha, Antimicrobial Agents and Chemotherapy 56(6) (2012) 3004-3010.

[366] K.S. Siddiqui, A. Poljak, M. Guilhaus, G. Feller, S. D'Amico, C. Gerday, R. Cavicchioli, Role of Disulfide Bridges in the Activity and Stability of a Cold-Active -Amylase, Journal of Bacteriology 187(17) (2005) 6206-6212.
[367] J.F. Riordan, Angiogenin, Methods Enzymol 341 (2001) 263-73.
[368] M.E. Levison, A.S. Josephson, D.M. Kirschenbaum, Reduction of biological substances by water-soluble phosphines: gamma-globulin (IgG), Experientia 25(2) (1969) 126-7.
[369] M. Yu, J. Wu, J. Shi, O.C. Farokhzad, Nanotechnology for protein delivery: Overview and perspectives, Journal of Controlled Release 240 (2016) 24-37.
[370] C. Vericat, M.E. Vela, G. Corthey, E. Pensa, E. Cortés, M.H. Fonticelli, F. Ibañez, G.E. Benitez, P. Carro, R.C. Salvarezza, Self-assembled monolayers of thiolates on metals: a review article on sulfur-metal chemistry and surface structures, RSC Adv. 4(53) (2014) 27730-27754.
[371] P. Mulvaney, Surface Plasmon Spectroscopy of Nanosized Metal Particles, Langmuir 12(3) (1996) 788-800.
[372] L. Caprile, A. Cossaro, E. Falletta, C. Della Pina, O. Cavalleri, R. Rolandi, S. Terreni, R. Ferrando, M. Rossi, L. Floreano, M. Canepa, Interaction of l-cysteine with naked gold nanoparticles supported on HOPG: a high resolution XPS investigation, Nanoscale 4(24) (2012).
[373] A.E. Lanterna, E.A. Coronado, A.M. Granados, When Nanoparticle Size and Molecular Geometry Matter: Analyzing the Degree of Surface Functionalization of Gold Nanoparticles with Sulfur Heterocyclic Compounds, The Journal of Physical Chemistry C 116(11) (2012) 6520-6529.
[374] N. Díaz-Herrera, A. González-Cano, D. Viegas, J.L. Santos, M.-C. Navarrete, Refractive index sensing of aqueous media based on plasmonic resonance in tapered optical fibres operating in the 1.5μm region, Sensors and Actuators B: Chemical 146(1) (2010) 195-198.
[375] C. Zhou, J.-M. Friedt, A. Angelova, K.-H. Choi, W. Laureyn, F. Frederix, L.A. Francis, A. Campitelli, Y. Engelborghs, G. Borghs, Human Immunoglobulin Adsorption Investigated by Means of Quartz Crystal Microbalance Dissipation, Atomic Force Microscopy, Surface Acoustic Wave, and Surface Plasmon Resonance Techniques, Langmuir 20(14) (2004) 5870-5878.
[376] H. Zhao, P.H. Brown, P. Schuck, On the distribution of protein refractive index increments, Biophys J 100(9) (2011) 2309-17.

[377] A. Majzik, L. Fulop, E. Csapo, F. Bogar, T. Martinek, B. Penke, G. Biro, I. Dekany, Functionalization of gold nanoparticles with amino acid, beta-amyloid peptides and fragment, Colloids Surf B Biointerfaces 81(1) (2010) 235-41.
[378] K. Esumi, N. Takei, T. Yoshimura, Antioxidant-potentiality of gold–chitosan nanocomposites, Colloids and Surfaces B: Biointerfaces 32(2) (2003) 117-123.
[379] A. Pudlarz, J. Szemraj, Nanoparticles as carriers of proteins, peptides and other therapeutic molecules, Open Life Sciences 13(1) (2018) 285-298.
[380] T. Kim, C.-H. Lee, S.-W. Joo, K. Lee, Kinetics of gold nanoparticle aggregation: Experiments and modeling, Journal of Colloid and Interface Science 318(2) (2008) 238-243.
[381] S. Basu, S.K. Ghosh, S. Kundu, S. Panigrahi, S. Praharaj, S. Pande, S. Jana, T. Pal, Biomolecule induced nanoparticle aggregation: Effect of particle size on interparticle coupling, Journal of Colloid and Interface Science 313(2) (2007) 724-734.
[382] K. Wagers, T. Chui, S. Adem, Effect of pH on the Stability of Gold Nanoparticles and Their Application for Melamine Detection in Infant Formula, IOSR Journal of Applied Chemistry 7(8) (2014) 15-20.
[383] A. Bikfalvi, Encyclopedic Reference of Vascular Biology & Pathology, Springer Berlin Heidelberg2013.
[384] N.G. Khlebtsov, V.A. Bogatyrev, B.N. Khlebtsov, L.A. Dykman, P. Englebienne, A Multilayer Model for Gold Nanoparticle Bioconjugates: Application to Study of Gelatin and Human IgG Adsorption Using Extinction and Light Scattering Spectra and the Dynamic Light Scattering Method, Colloid Journal 65(5) (2003) 622-635.
[385] A. Zuber, M. Purdey, E. Schartner, C. Forbes, B. van der Hoek, D. Giles, A. Abell, T. Monro, H. Ebendorff-Heidepriem, Detection of gold nanoparticles with different sizes using absorption and fluorescence based method, Sensors and Actuators B: Chemical 227 (2016) 117-127.
[386] X. Huang, Q. Bai, J. Hu, D. Hou, A Practical Model of Quartz Crystal Microbalance in Actual Applications, Sensors (Basel) 17(8) (2017).
[387] C.A. Keller, B. Kasemo, Surface specific kinetics of lipid vesicle adsorption measured with a quartz crystal microbalance, Biophys J 75(3) (1998) 1397-1402.
[388] R.P. Richter, R. Berat, A.R. Brisson, Formation of solid-supported lipid bilayers: an integrated view, Langmuir 22(8) (2006) 3497-505.

[389] S. Tharad, O. Uzulmez, B. Promdonkoy, J.L. Toca-Herrera, Cholesterol Increases Lipid Binding Rate and Changes Binding Behavior of Bacillus thuringiensis Cytolytic Protein, Int J Mol Sci 19(12) (2018).
[390] J. Chen, G. Zhou, L. Chen, Y. Wang, X. Wang, S. Zeng, Interaction of Graphene and its Oxide with Lipid Membrane: A Molecular Dynamics Simulation Study, The Journal of Physical Chemistry C 120(11) (2016) 6225-6231.
[391] S. Liu, T.H. Zeng, M. Hofmann, E. Burcombe, J. Wei, R. Jiang, J. Kong, Y. Chen, Antibacterial Activity of Graphite, Graphite Oxide, Graphene Oxide, and Reduced Graphene Oxide: Membrane and Oxidative Stress, ACS Nano 5(9) (2011) 6971-6980.
[392] J.L. Biedler, S. Roffler-Tarlov, M. Schachner, L.S. Freedman, Multiple neurotransmitter synthesis by human neuroblastoma cell lines and clones, Cancer Res 38(11 Pt 1) (1978) 3751-7.
[393] L.N. Kiseleva, A.V. Kartashev, N.L. Vartanyan, A.A. Pinevich, M.P. Samoilovich, A172 and T98G cell lines characteristics, Cell and Tissue Biology 10(5) (2016) 341-348.
[394] A. Belounis, C. Nyalendo, R. Le Gall, T.V. Imbriglio, M. Mahma, P. Teira, M. Beaunoyer, S. Cournoyer, E. Haddad, G. Vassal, H. Sartelet, Autophagy is associated with chemoresistance in neuroblastoma, BMC Cancer 16(1) (2016) 891.
[395] M. Da Ros, V. De Gregorio, A.L. Iorio, L. Giunti, M. Guidi, M. de Martino, L. Genitori, I. Sardi, Glioblastoma Chemoresistance: The Double Play by Microenvironment and Blood-Brain Barrier, Int J Mol Sci 19(10) (2018).
[396] J. Kovalevich, D. Langford, Considerations for the Use of SH-SY5Y Neuroblastoma Cells in Neurobiology, Neuronal Cell Culture2013, pp. 9-21.
[397] A. Carpentieri, E. Cozzoli, M. Scimeca, E. Bonanno, A.M. Sardanelli, A. Gambacurta, Differentiation of human neuroblastoma cells toward the osteogenic lineage by mTOR inhibitor, Cell Death & Disease 6(11) (2015) e1974-e1974.
[398] H. Teppola, J.R. Sarkanen, T.O. Jalonen, M.L. Linne, Morphological Differentiation Towards Neuronal Phenotype of SH-SY5Y Neuroblastoma Cells by Estradiol, Retinoic Acid and Cholesterol, Neurochem Res 41(4) (2016) 731-47.
[399] M. Stanisstreet, A comparison of the antigens of dorsal and ventral regions of Xenopus neurulae, Acta Embryol Exp (Palermo) (1) (1975) 33-7.

[400] J.J. Tomasek, G. Gabbiani, B. Hinz, C. Chaponnier, R.A. Brown, Myofibroblasts and mechano-regulation of connective tissue remodelling, Nat Rev Mol Cell Biol 3(5) (2002) 349-63.
[401] I.R. Fernandes, F.B. Russo, G.C. Pignatari, M.M. Evangelinellis, S. Tavolari, A.R. Muotri, P.C. Beltrao-Braga, Fibroblast sources: Where can we get them?, Cytotechnology 68(2) (2016) 223-8.
[402] L. Schneider, J. Zhang, Lysosomal function in macromolecular homeostasis and bioenergetics in Parkinson's disease, Molecular Neurodegeneration 5(1) (2010).
[403] X. Ma, Y. Wu, S. Jin, Y. Tian, X. Zhang, Y. Zhao, L. Yu, X.J. Liang, Gold nanoparticles induce autophagosome accumulation through size-dependent nanoparticle uptake and lysosome impairment, ACS Nano 5(11) (2011) 8629-39.
[404] K.J. Bayless, G.A. Johnson, Role of the cytoskeleton in formation and maintenance of angiogenic sprouts, J Vasc Res 48(5) (2011) 369-85.
[405] C.M. Fife, J.A. McCarroll, M. Kavallaris, Movers and shakers: cell cytoskeleton in cancer metastasis, British Journal of Pharmacology 171(24) (2014) 5507-5523.
[406] S. Gurunathan, J.-H. Kim, Biocompatible Gold Nanoparticles Ameliorate Retinoic Acid-Induced Cell Death and Induce Differentiation in F9 Teratocarcinoma Stem Cells, Nanomaterials 8(6) (2018).
[407] P.J. Chueh, R.Y. Liang, Y.H. Lee, Z.M. Zeng, S.M. Chuang, Differential cytotoxic effects of gold nanoparticles in different mammalian cell lines, J Hazard Mater 264 (2014) 303-12.
[408] A.M. Alkilany, C.J. Murphy, Toxicity and cellular uptake of gold nanoparticles: what we have learned so far?, Journal of Nanoparticle Research 12(7) (2010) 2313-2333.
[409] C.J. Murphy, A.M. Gole, J.W. Stone, P.N. Sisco, A.M. Alkilany, E.C. Goldsmith, S.C. Baxter, Gold Nanoparticles in Biology: Beyond Toxicity to Cellular Imaging, Accounts of Chemical Research 41(12) (2008) 1721-1730.
[410] M.M.O. Peña, J. Lee, D.J. Thiele, A Delicate Balance: Homeostatic Control of Copper Uptake and Distribution, The Journal of Nutrition 129(7) (1999) 1251-1260.
[411] L. Perrin, S. Roudeau, A. Carmona, F. Domart, J.D. Petersen, S. Bohic, Y. Yang, P. Cloetens, R. Ortega, Zinc and Copper Effects on Stability of Tubulin and Actin Networks in Dendrites and Spines of Hippocampal Neurons, ACS Chemical Neuroscience 8(7) (2017) 1490-1499.

[412] C.I. Lee, J.H. Perng, H.Y. Chen, Y.R. Hong, J.J. Wang, Undifferentiated Neuroblastoma Cells Are More Sensitive to Photogenerated Oxidative Stress Than Differentiated Cells, J Cell Biochem 116(9) (2015) 2074-85.
[413] M. Arul, A.C. Roslani, S.H. Cheah, Heterogeneity in cancer cells: variation in drug response in different primary and secondary colorectal cancer cell lines in vitro, In Vitro Cellular & Developmental Biology - Animal 53(5) (2017) 435-447.
[414] T. Hohmann, F. Dehghani, The Cytoskeleton-A Complex Interacting Meshwork, Cells 8(4) (2019).
[415] X. Ma, R. Hartmann, D. Jimenez de Aberasturi, F. Yang, S.J.H. Soenen, B.B. Manshian, J. Franz, D. Valdeperez, B. Pelaz, N. Feliu, N. Hampp, C. Riethmüller, H. Vieker, N. Frese, A. Gölzhäuser, M. Simonich, R.L. Tanguay, X.-J. Liang, W.J. Parak, Colloidal Gold Nanoparticles Induce Changes in Cellular and Subcellular Morphology, ACS Nano 11(8) (2017) 7807-7820.
[416] I. Bratic, A. Trifunovic, Mitochondrial energy metabolism and ageing, Biochimica et Biophysica Acta (BBA) - Bioenergetics 1797(6-7) (2010) 961-967.
[417] M. Akbar, M.M. Essa, G. Daradkeh, M.A. Abdelmegeed, Y. Choi, L. Mahmood, B.J. Song, Mitochondrial dysfunction and cell death in neurodegenerative diseases through nitroxidative stress, Brain Res 1637 (2016) 34-55.
[418] H. Zhou, B. Zhang, J. Zheng, M. Yu, T. Zhou, K. Zhao, Y. Jia, X. Gao, C. Chen, T. Wei, The inhibition of migration and invasion of cancer cells by graphene via the impairment of mitochondrial respiration, Biomaterials 35(5) (2014) 1597-607.
[419] M. Lv, Y. Zhang, L. Liang, M. Wei, W. Hu, X. Li, Q. Huang, Effect of graphene oxide on undifferentiated and retinoic acid-differentiated SH-SY5Y cells line, Nanoscale 4(13) (2012).
[420] A.V. Snezhkina, A.V. Kudryavtseva, O.L. Kardymon, M.V. Savvateeva, N.V. Melnikova, G.S. Krasnov, A.A. Dmitriev, ROS Generation and Antioxidant Defense Systems in Normal and Malignant Cells, Oxidative Medicine and Cellular Longevity 2019 (2019) 1-17.
[421] J.M. Reinke, H. Sorg, Wound Repair and Regeneration, European Surgical Research 49(1) (2012) 35-43.
[422] H.E. desJardins-Park, D.S. Foster, M.T. Longaker, Fibroblasts and wound healing: an update, Regenerative Medicine 13(5) (2018) 491-495.

[423] B. Li, J.H. Wang, Fibroblasts and myofibroblasts in wound healing: force generation and measurement, J Tissue Viability 20(4) (2011) 108-20.
[424] G. Borkow, Using Copper to Improve the Well-Being of the Skin, Curr Chem Biol 8(2) (2014) 89-102.
[425] N. Philips, H. Hwang, S. Chauhan, D. Leonardi, S. Gonzalez, Stimulation of Cell Proliferation and Expression of Matrixmetalloproteinase-1 and Interluekin-8 Genes in Dermal Fibroblasts by Copper, Connective Tissue Research 51(3) (2010) 224-229.
[426] P. Satzer, F. Svec, G. Sekot, A. Jungbauer, Protein adsorption onto nanoparticles induces conformational changes: Particle size dependency, kinetics, and mechanisms, Engineering in Life Sciences 16(3) (2016) 238-246.
[427] M.C. Matesanz, M. Vila, M.J. Feito, J. Linares, G. Goncalves, M. Vallet-Regi, P.A. Marques, M.T. Portoles, The effects of graphene oxide nanosheets localized on F-actin filaments on cell-cycle alterations, Biomaterials 34(5) (2013) 1562-9.
[428] X. Ma, Y. Wu, S. Jin, Y. Tian, X. Zhang, Y. Zhao, L. Yu, X.-J. Liang, Gold Nanoparticles Induce Autophagosome Accumulation through Size-Dependent Nanoparticle Uptake and Lysosome Impairment, ACS Nano 5(11) (2011) 8629-8639.
[429] B. Zhang, P. Wei, Z. Zhou, T. Wei, Interactions of graphene with mammalian cells: Molecular mechanisms and biomedical insights, Advanced Drug Delivery Reviews 105 (2016) 145-162.
[430] C. Satriano, S. Svedhem, B. Kasemo, Well-defined lipid interfaces for protein adsorption studies, Phys Chem Chem Phys 14(48) (2012) 16695-8.
[431] R. Shapiro, S. Weremowicz, J.F. Riordan, B.L. Vallee, Ribonucleolytic activity of angiogenin: essential histidine, lysine, and arginine residues, Proc Natl Acad Sci U S A 84(24) (1987) 8783-7.
[432] R. Pauwels, J. Balzarini, M. Baba, R. Snoeck, D. Schols, P. Herdewijn, J. Desmyter, E. De Clercq, Rapid and automated tetrazolium-based colorimetric assay for the detection of anti-HIV compounds, Journal of Virological Methods 20(4) (1988) 309-321.
[433] J. Krajczewski, K. Kołątaj, A. Kudelski, Plasmonic nanoparticles in chemical analysis, RSC Advances 7(28) (2017) 17559-17576.
[434] B.L. Darby, B. Auguié, M. Meyer, A.E. Pantoja, E.C. Le Ru, Modified optical absorption of molecules on metallic nanoparticles at sub-monolayer coverage, Nature Photonics 10(1) (2015) 40-45.

[435] B.L. Baldock, J.E. Hutchison, UV-Visible Spectroscopy-Based Quantification of Unlabeled DNA Bound to Gold Nanoparticles, Anal Chem 88(24) (2016) 12072-12080.
[436] Y. Zhou, S. Wang, K. Zhang, X. Jiang, Visual Detection of Copper(II) by Azide- and Alkyne-Functionalized Gold Nanoparticles Using Click Chemistry, Angewandte Chemie International Edition 47(39) (2008) 7454-7456.
[437] S.O. Obare, R.E. Hollowell, C.J. Murphy, Sensing Strategy for Lithium Ion Based on Gold Nanoparticles, Langmuir 18(26) (2002) 10407-10410.
[438] D. Fan, Q. Zhai, W. Zhou, X. Zhu, E. Wang, S. Dong, A label-free colorimetric aptasensor for simple, sensitive and selective detection of Pt (II) based on platinum (II)-oligonucleotide coordination induced gold nanoparticles aggregation, Biosensors and Bioelectronics 85 (2016) 771-776.
[439] D. Rithesh Raj, S. Prasanth, T.V. Vineeshkumar, C. Sudarsanakumar, Surface plasmon resonance based fiber optic dopamine sensor using green synthesized silver nanoparticles, Sensors and Actuators B: Chemical 224 (2016) 600-606.
[440] R. Elghanian, J.J. Storhoff, R.C. Mucic, R.L. Letsinger, C.A. Mirkin, Selective Colorimetric Detection of Polynucleotides Based on the Distance-Dependent Optical Properties of Gold Nanoparticles, Science 277(5329) (1997) 1078-1081.
[441] C.D. Medley, J.E. Smith, Z. Tang, Y. Wu, S. Bamrungsap, W. Tan, Gold nanoparticle-based colorimetric assay for the direct detection of cancerous cells, Anal Chem 80(4) (2008) 1067-72.
[442] W. Haiss, N.T.K. Thanh, J. Aveyard, D.G. Fernig, Determination of Size and Concentration of Gold Nanoparticles from UV−Vis Spectra, Analytical Chemistry 79(11) (2007) 4215-4221.
[443] M. Herbst, E. Hofmann, S. Forster, Nucleation and Growth Kinetics of ZnO Nanoparticles Studied by in Situ Microfluidic SAXS/WAXS/UV-Vis Experiments, Langmuir 35(36) (2019) 11702-11709.
[444] D.M. Atole, H.H. Rajput, Ultraviolet Spectroscopy and Its Pharmaceutical Applications- a Brief Review, Asian Journal of Pharmaceutical and Clinical Research 11(2) (2018).
[445] K. Wilson, J. Walker, Principles and Techniques of Biochemistry and Molecular Biology, 2010.
[446] R.A. Marcus, Relation between charge transfer absorption and fluorescence spectra and the inverted region, The Journal of Physical Chemistry 93(8) (1989) 3078-3086.

[447] I.D. Campbell, R.A. Dwek, Biological spectroscopy, Benjamin/Cummings Pub. Co., Menlo Park, Calif., 1984.
[448] A. Rao, M. Schoenenberger, E. Gnecco, T. Glatzel, E. Meyer, D. Brändlin, L. Scandella, Characterization of nanoparticles using Atomic Force Microscopy, Journal of Physics: Conference Series 61 (2007) 971-976.
[449] I. Akhtar, M.A. Rehman, W. Choi, S. Kumar, N. Lee, S.-J. Cho, H.-H. Park, K.-H. Park, Y. Seo, Three-dimensional atomic force microscopy for ultra-high-aspect-ratio imaging, Applied Surface Science 469 (2019) 582-592.
[450] O. Couteau, G. Roebben, Measurement of the size of spherical nanoparticles by means of atomic force microscopy, Measurement Science and Technology 22(6) (2011).
[451] R. B, AFM/TEM Complementary Structural Analysis of Surface-Functionalized Nanoparticles, Journal of Physical Chemistry & Biophysics 4(4) (2014).
[452] M. Egger, F. Ohnesorge, A.L. Weisenhorn, S.P. Heyn, B. Drake, C.B. Prater, S.A.C. Gould, P.K. Hansma, H.E. Gaub, Wet lipid-protein membranes imaged at submolecular resolution by atomic force microscopy, Journal of Structural Biology 103(1) (1990) 89-94.
[453] D. Guo, G. Xie, J. Luo, Mechanical properties of nanoparticles: basics and applications, Journal of Physics D: Applied Physics 47(1) (2014).
[454] S. Suresh, Biomechanics and biophysics of cancer cells☆, Acta Materialia 55(12) (2007) 3989-4014.
[455] W. Lam, P. Pravincumar, D.L. Bader, M.M. Knight, Viscoelastic Cell Mechanics and Actin Remodelling Are Dependent on the Rate of Applied Pressure, PLoS ONE 7(9) (2012).
[456] G.E. Fantner, R.J. Barbero, D.S. Gray, A.M. Belcher, Kinetics of antimicrobial peptide activity measured on individual bacterial cells using high-speed atomic force microscopy, Nat Nanotechnol 5(4) (2010) 280-5.
[457] A.D. Ozkan, A.E. Topal, F.B. Dikecoglu, M.O. Guler, A. Dana, A.B. Tekinay, Probe microscopy methods and applications in imaging of biological materials, Semin Cell Dev Biol 73 (2018) 153-164.
[458] D.T. Edwards, T.T. Perkins, Optimizing force spectroscopy by modifying commercial cantilevers: Improved stability, precision, and temporal resolution, J Struct Biol 197(1) (2017) 13-25.
[459] J. Zhong, J. Yan, Seeing is believing: atomic force microscopy imaging for nanomaterial research, RSC Advances 6(2) (2016) 1103-1121.

[460] Y.F. Dufrêne, T. Ando, R. Garcia, D. Alsteens, D. Martinez-Martin, A. Engel, C. Gerber, D.J. Müller, Imaging modes of atomic force microscopy for application in molecular and cell biology, Nature Nanotechnology 12(4) (2017) 295-307.
[461] M. Basso, L. Giarre, M. Dahleh, I. Mezic, Numerical analysis of complex dynamics in atomic force microscopes, Proceedings of the 1998 IEEE International Conference on Control Applications (Cat. No.98CH36104), 1998, pp. 1026-1030.
[462] A. Engel, D.J. Muller, Observing single biomolecules at work with the atomic force microscope, Nat Struct Biol 7(9) (2000) 715-8.
[463] G. Binnig, C.F. Quate, C. Gerber, Atomic Force Microscope, Physical Review Letters 56(9) (1986) 930-933.
[464] T.R. Albrecht, P. Grütter, D. Horne, D. Rugar, Frequency modulation detection using high-Qcantilevers for enhanced force microscope sensitivity, Journal of Applied Physics 69(2) (1991) 668-673.
[465] P.K. Hansma, J.P. Cleveland, M. Radmacher, D.A. Walters, P.E. Hillner, M. Bezanilla, M. Fritz, D. Vie, H.G. Hansma, C.B. Prater, J. Massie, L. Fukunaga, J. Gurley, V. Elings, Tapping mode atomic force microscopy in liquids, Applied Physics Letters 64(13) (1994) 1738-1740.
[466] S. Ido, H. Kimiya, K. Kobayashi, H. Kominami, K. Matsushige, H. Yamada, Immunoactive two-dimensional self-assembly of monoclonal antibodies in aqueous solution revealed by atomic force microscopy, Nat Mater 13(3) (2014) 264-70.
[467] H.G. Hansma, J.H. Hoh, Biomolecular imaging with the atomic force microscope, Annu Rev Biophys Biomol Struct 23 (1994) 115-39.
[468] Y. Ebenstein, E. Nahum, U. Banin, Tapping Mode Atomic Force Microscopy for Nanoparticle Sizing: Tip−Sample Interaction Effects, Nano Letters 2(9) (2002) 945-950.
[469] J. Stetefeld, S.A. McKenna, T.R. Patel, Dynamic light scattering: a practical guide and applications in biomedical sciences, Biophysical Reviews 8(4) (2016) 409-427.
[470] H. Jans, X. Liu, L. Austin, G. Maes, Q. Huo, Dynamic Light Scattering as a Powerful Tool for Gold Nanoparticle Bioconjugation and Biomolecular Binding Studies, Analytical Chemistry 81(22) (2009) 9425-9432.
[471] N.S. Murthy, Techniques for analyzing biomaterial surface structure, morphology and topography, Surface Modification of Biomaterials2011, pp. 232-255.

[472] D. Brabazon, Nanocharacterization Techniques for Dental Implant Development, Emerging Nanotechnologies in Dentistry2012, pp. 307-331.
[473] S. Wang, I.V. Larina, High-resolution imaging techniques in tissue engineering, Monitoring and Evaluation of Biomaterials and their Performance In Vivo2017, pp. 151-180.
[474] N.S. White, Visualization Systems for Multidimensional CLSM Images, Handbook of Biological Confocal Microscopy1995, pp. 211-254.
[475] L. Treuel, X. Jiang, G.U. Nienhaus, New views on cellular uptake and trafficking of manufactured nanoparticles, Journal of The Royal Society Interface 10(82) (2013).
[476] M.A.I. Rasel, S. Singh, T.D. Nguyen, I.O. Afara, Y. Gu, Impact of Nanoparticle Uptake on the Biophysical Properties of Cell for Biomedical Engineering Applications, Scientific Reports 9(1) (2019).
[477] T. Miyashita, Confocal microscopy for intracellular co-localization of proteins, Methods Mol Biol 261 (2004) 399-410.
[478] A.W. Coleman, L.J. Goff, Applications of Fluorochromes to Pollen Biology. I. Mithramycin and 4′,6-Diamidino-2-Phenylindole (Dapi) as Vital Stains and for Quantitation of Nuclear Dna, Stain Technology 60(3) (2009) 145-154.
[479] S.V. Reddy, S. Tauber, B.A. Lauber, K. Paulsen, L.E. Layer, M. Lehmann, S. Hauschild, N.R. Shepherd, J. Polzer, J. Segerer, C.S. Thiel, O. Ullrich, Cytoskeletal stability and metabolic alterations in primary human macrophages in long-term microgravity, Plos One 12(4) (2017).
[480] K. Mitra, J. Lippincott-Schwartz, Analysis of Mitochondrial Dynamics and Functions Using Imaging Approaches, Current Protocols in Cell Biology 46(1) (2010).
[481] J.-K. Jeon, S.-M. Han, J.-K. Kim, Fluorescence imaging of reactive oxygen species by confocal laser scanning microscopy for track analysis of synchrotron X-ray photoelectric nanoradiator dose: X-ray pump–optical probe, Journal of Synchrotron Radiation 23(5) (2016) 1191-1196.
[482] H. Zhou, X. Gong, H. Lin, H. Chen, D. Huang, D. Li, H. Shan, J. Gao, Gold nanoparticles impair autophagy flux through shape-dependent endocytosis and lysosomal dysfunction, Journal of Materials Chemistry B 6(48) (2018) 8127-8136.
[483] I. Johnson, Fluorescent probes for living cells, Histochem J 30(3) (1998) 123-40.
[484] M. Kubista, B. Akerman, B. Norden, Characterization of interaction between DNA and 4',6-diamidino-2-phenylindole by optical spectroscopy, Biochemistry 26(14) (1987) 4545-53.

[485] R.E. Durand, P.L. Olive, Cytotoxicity, Mutagenicity and DNA damage by Hoechst 33342, J Histochem Cytochem 30(2) (1982) 111-6.
[486] M. Poot, Y.Z. Zhang, J.A. Kramer, K.S. Wells, L.J. Jones, D.K. Hanzel, A.G. Lugade, V.L. Singer, R.P. Haugland, Analysis of mitochondrial morphology and function with novel fixable fluorescent stains, J Histochem Cytochem 44(12) (1996) 1363-72.
[487] R.P. Haugland, M.T.Z. Spence, I.D. Johnson, A. Basey, The handbook : a guide to fluorescent probes and labeling technologies, 10th ed., Molecular Probes, Eugene, OR, 2005.
[488] B. Chazotte, Labeling Lysosomes in Live Cells with LysoTracker, Cold Spring Harbor Protocols 2011(2) (2011) pdb.prot5571-pdb.prot5571.
[489] S. Ishii, A. Matsuura, E. Itakura, Identification of a factor controlling lysosomal homeostasis using a novel lysosomal trafficking probe, Scientific Reports 9(1) (2019).
[490] I. Barasoain, J.F. Diaz, J.M. Andreu, Fluorescent taxoid probes for microtubule research, Methods Cell Biol 95 (2010) 353-72.
[491] E. Wulf, A. Deboben, F.A. Bautz, H. Faulstich, T. Wieland, Fluorescent phallotoxin, a tool for the visualization of cellular actin, Proc Natl Acad Sci U S A 76(9) (1979) 4498-502.
[492] N.S. Claxton, T.J. Fellers, M.W. Davidson, Microscopy, Confocal, Encyclopedia of Medical Devices and Instrumentation2006.
[493] V. Rai, N. Dey, The Basics of Confocal Microscopy, Laser Scanning, Theory and Applications2011.
[494] S.K. Balchand, B.J. Mann, P. Wadsworth, Using Fluorescence Microscopy to Study Mitosis, The Mitotic Spindle2016, pp. 3-14.
[495] E.B. Neufeld, K. O'Brien, A.D. Walts, J.A. Stonik, S.J. Demosky, D. Malide, C.A. Combs, A.T. Remaley, Cellular Localization and Trafficking of the Human ABCG1 Transporter, Biology (Basel) 3(4) (2014) 781-800.
[496] A. Jochums, E. Friehs, F. Sambale, A. Lavrentieva, D. Bahnemann, T. Scheper, Revelation of Different Nanoparticle-Uptake Behavior in Two Standard Cell Lines NIH/3T3 and A549 by Flow Cytometry and Time-Lapse Imaging, Toxics 5(3) (2017).
[497] W.A. Mohler, J.G. White, Stereo-4-D reconstruction and animation from living fluorescent specimens, Biotechniques 24(6) (1998) 1006-10, 1012.
[498] M.C. Dixon, Quartz crystal microbalance with dissipation monitoring: enabling real-time characterization of biological materials and their interactions, J Biomol Tech 19(3) (2008) 151-8.

[499] Q. Chen, S. Xu, Q. Liu, J. Masliyah, Z. Xu, QCM-D study of nanoparticle interactions, Advances in Colloid and Interface Science 233 (2016) 94-114.
[500] D. Johannsmann, Studies of Viscoelasticity with the QCM, Piezoelectric Sensors2007, pp. 49-109.
[501] J. Fatisson, R.F. Domingos, K.J. Wilkinson, N. Tufenkji, Deposition of TiO2 nanoparticles onto silica measured using a quartz crystal microbalance with dissipation monitoring, Langmuir 25(11) (2009) 6062-9.
[502] S.J. Fraser, X. Mulet, L. Martin, S. Praporski, A. Mechler, P.G. Hartley, A. Polyzos, F. Separovic, Surface Immobilization of Bio-Functionalized Cubosomes: Sensing of Proteins by Quartz Crystal Microbalance, Langmuir 28(1) (2011) 620-627.
[503] E.F. Irwin, J.E. Ho, S.R. Kane, K.E. Healy, Analysis of Interpenetrating Polymer Networks via Quartz Crystal Microbalance with Dissipation Monitoring, Langmuir 21(12) (2005) 5529-5536.
[504] T.H. Nguyen, M. Elimelech, Adsorption of Plasmid DNA to a Natural Organic Matter-Coated Silica Surface: Kinetics, Conformation, and Reversibility, Langmuir 23(6) (2007) 3273-3279.
[505] Z. Fohlerova, P. Skladal, J. Turanek, Adhesion of eukaryotic cell lines on the gold surface modified with extracellular matrix proteins monitored by the piezoelectric sensor, Biosens Bioelectron 22(9-10) (2007) 1896-901.
[506] C. Galli Marxer, M. Collaud Coen, T. Greber, U.F. Greber, L. Schlapbach, Cell spreading on quartz crystal microbalance elicits positive frequency shifts indicative of viscosity changes, Anal Bioanal Chem 377(3) (2003) 578-86.
[507] I.R. Quevedo, A.L.J. Olsson, N. Tufenkji, Deposition Kinetics of Quantum Dots and Polystyrene Latex Nanoparticles onto Alumina: Role of Water Chemistry and Particle Coating, Environmental Science & Technology 47(5) (2013) 2212-2220.
[508] R.J. Hunter, Foundations of colloid science, 2nd ed., Oxford University Press, Oxford ; New York, 2001.
[509] J.Y. Chen, C.-H. Ko, S. Bhattacharjee, M. Elimelech, Role of spatial distribution of porous medium surface charge heterogeneity in colloid transport, Colloids and Surfaces A: Physicochemical and Engineering Aspects 191(1-2) (2001) 3-15.
[510] E. Rascol, M. Daurat, A. Da Silva, M. Maynadier, C. Dorandeu, C. Charnay, M. Garcia, J. Lai-Kee-Him, P. Bron, M. Auffan, W. Liu, B. Angeletti, J.M. Devoisselle, Y. Guari, M. Gary-Bobo, J. Chopineau,

Biological Fate of Fe(3)O(4) Core-Shell Mesoporous Silica Nanoparticles Depending on Particle Surface Chemistry, Nanomaterials (Basel) 7(7) (2017).
[511] S.H. Brewer, W.R. Glomm, M.C. Johnson, M.K. Knag, S. Franzen, Probing BSA binding to citrate-coated gold nanoparticles and surfaces, Langmuir 21(20) (2005) 9303-7.
[512] R. Richter, A. Mukhopadhyay, A. Brisson, Pathways of Lipid Vesicle Deposition on Solid Surfaces: A Combined QCM-D and AFM Study, Biophysical Journal 85(5) (2003) 3035-3047.
[513] Z.-m. Xiu, Q.-b. Zhang, H.L. Puppala, V.L. Colvin, P.J.J. Alvarez, Negligible Particle-Specific Antibacterial Activity of Silver Nanoparticles, Nano Letters 12(8) (2012) 4271-4275.
[514] Q.B. Xianhe Huang , Jianguo Hu and Dong Hou, A Practical Model of Quartz Crystal Microbalance in Actual Applications, Sensors 17(8) (2017).
[515] C. Lu, A.W. Czanderna, A. Townshend, Applications of piezoelectric quartz crystal microbalances, Analytica Chimica Acta 199 (1987).
[516] M. Rodahl, F. Höök, A. Krozer, P. Brzezinski, B. Kasemo, Quartz crystal microbalance setup for frequency and Q-factor measurements in gaseous and liquid environments, Review of Scientific Instruments 66(7) (1995) 3924-3930.
[517] M.V. Voinova, M. Rodahl, M. Jonson, B. Kasemo, Viscoelastic Acoustic Response of Layered Polymer Films at Fluid-Solid Interfaces: Continuum Mechanics Approach, Physica Scripta 59(5) (1999) 391-396.
[518] A.A. Il'yushin, P.M. Ogibalov, A certain generalization of the Voigt and Maxwell models, Polymer Mechanics 2(2) (1969) 122-124.
[519] E. Tellechea, D. Johannsmann, N.F. Steinmetz, R.P. Richter, I. Reviakine, Model-independent analysis of QCM data on colloidal particle adsorption, Langmuir 25(9) (2009) 5177-84.
[520] A. Pomorska, D. Shchukin, R. Hammond, M.A. Cooper, G. Grundmeier, D. Johannsmann, Positive Frequency Shifts Observed Upon Adsorbing Micron-Sized Solid Objects to a Quartz Crystal Microbalance from the Liquid Phase, Analytical Chemistry 82(6) (2010) 2237-2242.
[521] V.M. Mecea, From Quartz Crystal Microbalance to Fundamental Principles of Mass Measurements, Analytical Letters 38(5) (2005) 753-767.
[522] N. Klonis, M. Rug, I. Harper, M. Wickham, A. Cowman, L. Tilley, Fluorescence photobleaching analysis for the study of cellular dynamics, European Biophysics Journal 31(1) (2014) 36-51.

[523] J. Lippincott-Schwartz, N. Altan-Bonnet, G.H. Patterson, Photobleaching and photoactivation: following protein dynamics in living cells, Nat Cell Biol Suppl (2003) S7-14.
[524] D. Axelrod, D.E. Koppel, J. Schlessinger, E. Elson, W.W. Webb, Mobility measurement by analysis of fluorescence photobleaching recovery kinetics, Biophysical Journal 16(9) (1976) 1055-1069.

List of papers

PAPER I

Lorena M. Cucci, Alessia Munzone, Irina Naletova, Antonio Magrì, Diego La Mendola, and Cristina Satriano. **Gold nanoparticles functionalized with angiogenin-mimicking peptides modulate cell membrane interactions.** Biointerphases 13, 3 (2018); doi: 10.1116/1.5022295.

PAPER II

Lorena M. Cucci, Irina Naletova, Antonio Magrì, Diego La Mendola, Orjan Hansson, Cristina Satriano. **Combined effects of human Angiogenin in the hybrid assembly with gold nanoparticles for wound care.**

PAPER III

Irina Naletova, Lorena M. Cucci, Floriana D'Angeli, Carmelina Daniela Anfuso, Antonio Magrì, Diego La Mendola, Gabriella Lupo and Cristina Satriano. **A Tunable Nanoplatform of Nanogold Functionalised with Angiogenin Peptides for Anti-Angiogenic Therapy of Brain Tumours.** Cancers 11, 9 (2019); doi: 10.3390/cancers11091322.

PAPER IV

Lorena M. Cucci, Irina Naletova, Giuseppe Consiglio and Cristina Satriano. **A hybrid nanoplatform of graphene oxide/nanogold for plasmonic sensing and cellular applications at the nanobiointerface.** Applied Science 9, 676 (2019); doi: 10.3390/app9040676.

PAPER V

Lorena M. Cucci, Giusy Villaggio, Diego La Mendola, Cristina Satriano. **Multifunctional assemblies of Au-GO-ANG for Wound Healing.**

Papers not included in this thesis

PAPER VI

Giuseppe Trapani, Viviana C. L. Caruso, Lorena M. Cucci, Francesco Attanasio, Giovanni Tabbì, Giuseppe Forte, Diego La Mendola, Cristina Satriano**. Graphene oxide nanosheets tailored with aromatic dipeptide nanoassemblies for a tuneable interaction with cell membranes.** Frontiers in Bioengineering and Biotechnology, section Nanobiotechnology (accepted).

PAPER VII

Antonio Magrì, Giovanni Tabbì, Lorena M. Cucci, Cristina Satriano, Adriana Pietropaolo, Gaetano Malgieri, Carla Isernia and Diego La Mendola**. The curious case of opossum prion: a physicochemical study on copper(ii) binding to the bis-decarepeat fragment from the protein N-terminal domain.** Dalton Transactions 48, 17533-17543 (2019); doi: 10.1039/C9DT02510C.

PAPER VIII

Angelo Nicosia, Fabiana Vento, Cristina Satriano, Valentina Villari, Roberto Micali, Lorena M. Cucci, Vanessa Sanfilippo, Placido Mineo. **A smart macromolecular nanobomb for light-triggered blasts in cellular environments.** ACS Applied Nano Materials (2020); doi: 10.1021/acsanm.9b02552.

PAPER IX

Vanessa Sanfilippo, Viviana Caruso, Lorena M. Cucci, Rosanna Inturri, Susanna Vaccaro and Cristina Satriano. **Hyaluronan-metal gold nanoparticle hybrids for targeted tumour cell therapy.** International Journal of Molecular Sciences **(**IJMS) (submitted).

Acknowledgements

I would like to express my gratitude to my supervisor Prof. Cristina Satriano, to the Prof. Diego La Mendola and to all the researchers, post-doc and students that have worked with the Nano-Hybrid-BioInterfaces Lab (NHBIL), during the time of my Ph.D.

My sincere thanks also go to Prof. Orjan Hansson who provided me the opportunity to conduct part of my research activity in his laboratory at the University of Goteborg (Sweden).